Multiphase flow and physicochemical interactions during geological carbon sequestration

A laboratory investigation from micrometer to meter

Malin Haugen

Thesis for the Degree of Philosophiae Doctor (PhD)
University of Bergen, Norway
2024

UNIVERSITY OF BERGEN

Multiphase flow and physicochemical interactions during geological carbon sequestration

A laboratory investigation from micrometer to meter

Malin Haugen

Thesis for the Degree of Philosophiae Doctor (PhD)
at the University of Bergen

Date of defence: 25.04.2024

Year: 2024

Title: Multiphase flow and physicochemical interactions during geological carbon sequestration

Name: Malin Haugen

Print: Skipnes Kommunikasjon / University of Bergen

In the memory of my twin sister Cathrine

Acknowledgements

I would like to acknowledge the research council of Norway for financial support through the "Subsurface Carbonate CO_2 storage and security" Project number 280341, and Centre for Sustainable Subsurface Resources, Project number 33184.

Thank you to my supervisors Prof. Martin A. Fernø and Dr. Bergit Brattekås at the Department of Physics and Technology at the University of Bergen. You have supported me through challenging laboratory tasks and given me the opportunity to work with exciting laboratory modalities. Thank you to the FluidFlower experimental team; Kristoffer Eikehaug, MSc Olav P. Folkvord, Emil Bang Larsen and Prof. Martin Fernø, the DarSIA team; MSc Benyamine Benali, Dr. Jakub W. Both, Dr. Erlend Storvik and Prof. Jan Martin Nordbotten, and Dr. Lluís Saló-Salgado for performing numerical simulations. Also, thank you to Dr. Na Liu for excellent collaboration with the microfluidic experiments, and Dr. Jacquelin E. Cobos Mora for sharing knowledge and support.

A million thanks to my two girls, Christina and Hannah! Thank you for the interest you have shown in the projects, participation in events and patience with long days in the lab. Thank you for giving me something else to think about and for the endless love you have given me. Thank you, Einar, for organizing the family life, supporting me during this work, and for the patience and love you have shown me. I could not have done this without you! Thank you to friends and family for continuous support and motivation during these years. And especially my parents, Oddrun and Harald Haugen, for all your help with the girls, everything in and around the house, continuous love and always believing in me.

Thank you to the staff at the mechanical workshop (Roald Langøen and Charles Thevananth Sebastiampillai) at the Department of Physics and Technology for bringing design ideas into reliable laboratory equipment, for your endless willingness to provide guidance and advice, and for making the time with corona-restrictions easier. Finally, thank you to the wonderful people working in Gullfaks ASD! Thank you for your interest in the projects and for cheering on me all the way to the finish line.

Malin Haugen

Malin Haugen

Summary

Carbon capture and storage (CCS) is a technology that can contribute to reduced greenhouse gas emissions, a stated goal from the world's political leaders. The world's oil production remains consistently high, and while the price of renewable energy is decreasing and accessibility is increasing, complementary technologies are needed among other to handle peaks in energy demand. Carbon dioxide (CO_2) is a greenhouse gas, and the purpose of CCS is to limit emissions of CO_2 into the atmosphere by capturing, transporting, and subsequently storing CO_2 safely. CCS can reduce emissions from existing (hydrocarbon) energy assets and accelerate the development of underground hydrogen storage and low-emission hydrogen production, hence becoming a central aspect of a sustainable energy future.

Geologic carbon storage (GCS) involves storing CO_2 in deep porous formations, where CO_2 becomes less mobile over time by porous media trapping mechanisms. The relative importance of the governing trapping mechanisms depend on both the subsurface conditions (like pressure and temperature) and the length scale the CO_2 flow is studied. Visualization of CO_2 flow in opaque porous systems is valuable to detailly investigate trapping mechanisms and further understand displacement dynamics and migration patterns at various scales; from micrometer (pore) scale to meter (and kilometer) at field scale. Laboratory methodologies that facilitate multiscale investigations of GCS trapping mechanisms have been developed as part of this dissertation. Methodological contributions are described in Chapter 2, whereas salient results are discussed in Chapter 3.

The six scientific contributions included in this dissertation span three length scales (pore, Darcy and room) across six orders of magnitude from micrometer to meter. Pore-scale methods were improved (**Paper 1**) and implemented to study kinetics of calcium dissolution and secondary precipitation (**Paper 2**). GCS-related mineralization processes were subsequently reversed, and dissolution of calcium carbonate is studied at pore- (**Paper 2**) and Darcy-scale (**Paper 3**), respectively.

Trapping mechanisms during GCS naturally relates to multiphase flow in porous media. Pore scale visualization of GCS was complemented by *in situ* tracking of flow at larger scales to provide more information. Positron emission tomography (PET) imaging was used in **Paper 4**, where a method for explicit CO_2 tracking in an opaque rock sample was detailed. CO_2 was labelled with a short-lived radioactive isotope, and flow of CO_2 explicitly

captured during viscous displacement. During injection into a storage reservoir (e.g., an aquifer), CO_2 mixes and dissolves in formation water. The density of the (partially) CO_2-saturated aqueous phase is higher than the formation water, which initiates convective mixing processes. Such (gravity-dominated) processes cannot generally be studied at the Darcy-scale. Hence, the *FluidFlower concept* was developed, to enable detailed laboratory studies on convective mixing and structural/stratigraphic, residual and solubility trapping during meter-scale CO_2 injection and storage (**Paper 5** and **Paper 6**).

Summary – Norwegian

Karbonfangst og lagring (CCS) er ein teknologi som kan medverke til reduserte klimagassutslepp; eit uttalt mål frå verdas politiske leiarar. Oljeproduksjonen i verda er vedvarande høg og, medan prisen på fornybar energi synk og tilgangen aukar, trengs komplementære teknologiar blant anna for å handtere toppane i etterspørsel av energi. CO_2 er ein drivhusgass, og formålet med CCS er å redusere utslepp av CO_2 til atmosfæren; ved at CO_2 fangast, transporterast og lagrast trygt. CCS kan redusere utslepp frå eksisterande (fossile) energiressursar, støtte rask oppskalering av lågutslepp hydrogenproduksjon og industrielle prosesser, samt mogleggjere at noko CO_2 kan fjernast frå atmosfæren gjennom bioenergi og direkte luftfangst.

Geologisk karbonlagring (GCS) inneber å lagre CO_2 i djupe porøse formasjonar, og nyttegjer seg av kjende prinsipp i fleirfasestraum der injisert CO_2 blir mindre mobil over tid grunna ulike lagringsmekanismar. Den relative viktigheita av dominerande lagringsmekanismar avheng av forholda i undergrunnen (til dømes trykk og temperatur) og avstandane CO_2 strøymer over (lengdeskala). Visualisering av CO_2-strøyming, også i ugjennomsiktige porøse medie, er viktig for å detaljert kunne undersøke fangst- og lagringsmekanismar. Målet er å forstå fortrengingsdynamikk og migrasjonsmønster på fleire ulike lengdeskalaer; frå mikrometer (pore-skala) til meter (og kilometer) på felt-skala. Gjennom denne avhandlinga er det utvikla laboratoriemetodar som mogleggjer detaljerte undersøkingar av multiskala GCS-lagringsmekanismar. Metodiske bidrag blir skildra i kapittel 2, medan dei viktigaste resultata diskuterast i kapittel 3.

Dei seks vitskaplege bidraga som er inkludert i denne avhandlinga omhandlar forsking utført på tre lengdeskalaer: pore-, Darcy- og rom-skala. Til saman spenner arbeidet over seks storleiksordenar: frå mikrometer til meter. Pore-skala metodar vart forbetra (**Artikkel 1**) og brukt for å studere kinetikk i kalsiumoppløysning og sekundær utfelling (**Artikkel 2**). Mineralisering relatert til GCS vart reversert og oppløysing av kalsiumkarbonat studert på både pore- (**Artikkel 2**) og Darcy-skala (**Artikkel 3**).

GCS-lagringsmekanismar er knytt til fleirfaseflyt i porøse medie, og visualisering av væskestraum *in-situ* kan gi verdifull informasjon på fleire skalaer. I **Artikkel 4** vart positronemisjonstomografi (PET) nytta for å eksplisitt følgje straumen av CO_2 gjennom ei ugjennomsiktig kjerneprøve. CO_2 vart merka med ein radioaktiv isotop, og dynamikken i væskestraumen kunne avbildast med høg tidoppløysing og romleg presisjon. CO_2 løyser seg i formasjonsvatnet under og etter injeksjon i eit lagringsreservoar. Tettleiken til (delvis) CO_2-metta vatn er høgare enn tettleiken til formasjonsvatnet; dermed startar

konvektive blandingsprosessar. Slike (gravitasjonsdrivne) prosessar kan generelt ikkje studerast på Darcy-skala og gjennom standardisert kjerneanalyse. Derfor vart *FluidFlower-konseptet* utvikla. FluidFlower og tilknytt metodologi mogleggjer detaljerte studie av konvektiv blanding og lagringsmekanismar som strukturell/stratigrafisk fanging, samt residuell og løyselegheitssfanging, under og etter CO_2-injeksjon på meter-skala (**Artikkel 5** og **Artikkel 6**).

Table of contents

List of scientific papers

1. **Haugen M.,** Benali B., Føyen T.L., Song W., Fernø M.A. & Brattekås B. (2023a). *Calcite-functionalized micromodels for pore-scale investigations of CO_2 storage security*, presented at the 2021 International Symposium of the Society of Core Analysts (*peer-reviewed*), E3S Web of Conferences, 366. https://doi.org/10.1051/e3sconf/202336601004

2. Liu N., **Haugen M**., Benali B., Landa-Marbán D., & Fernø M.A. (2023a). *Pore-scale kinetics of calcium dissolution and secondary precipitation during geological carbon storage*. *Chemical Geology*, 641. https://doi.org/10.1016/j.chemgeo.2023.121782

3. **Haugen M.**, Folkvord O.P., Veien T., Fernø M.A., & Brattekås, B. (2023b). *Multi-scale dissolution dynamics for carbon sequestration in carbonate rock samples*. Gas Science and Engineering, 119. https://doi.org/10.1016/j.jgsce.2023.205139

4. Brattekås B. and **Haugen M**. (2020). *Explicit tracking of CO_2-flow at the core scale using micro-Positron Emission Tomography (μPET)*, J. of Natural Gas Sci and Eng, 77. https://doi.org/10.1016/j.jngse.2020.103268

5. **Haugen M**., Saló-Salgado L., Eikehaug K., Benali B., Both J.W., Storvik E., Folkvord O., Juanes R., Nordbotten J.M. & Fernø M.A. (2024). *Physical variability in meter-scale laboratory CO_2 injections in faulted geometries*, Transp. Porous Med. https://doi.org/10.1007/s11242-023-02047-8

6. Fernø M.A., **Haugen M**., Eikehaug K., Folkvord O., Benali B., Both J.W., Storvik E., Nixon C.W., Gawthrope R.L., Nordbotten J.M. (2023). *Room-Scale CO_2 Injections in a Physical Reservoir Model with Faults*. Transp. Porous Med. https://doi.org/10.1007/s11242-023-02013-4

Additional Scientific Contributions

Citation of these additional scientific contributions are indicated in blue throughout the dissertation.

Liu N., **Haugen M.**, Benali B., Landa-Marbán D. & Fernø M.A. (2023b). *Pore-scale spatiotemporal dynamics of microbial-induced calcium carbonate growth and distribution in porous media*. International Journal of Greenhouse Gas Control, 125. https://doi.org/10.1016/j.ijggc.2023.103885

Haugen M., Brattekås B. & Fernø M.A. (2023c). *Multimodal Visualization of Calcium Carbonate ($CaCO_3$) in the Pore Space of a Micromodel*. In: Médici, E.F., Otero, A.D. (Eds), Album of Porous Media: Structure and Dynamics (pp. 95-95). Cham: Springer International Publishing. https://doi.org/10.1007/978-3-031-23800-0_77

Brattekås B., Fernø M.A., **Haugen M**., Føyen T.L., Steinsbø M., Graue A., Brekke N., Adamsen T.C.H., Rygh C.B & Espedal H. (2023). *Of Rats and Rocks: using pre-clinical PET imaging facilities in core analysis.* Presented at the 2021 International Symposium of the Society of Core Analysts (peer-reviewed). *E3S Web of Conferences,* 366. https://doi.org/10.1051/e3sconf/202336601011

Saló-Salgado L., **Haugen M.**, Eikehaug K. Fernø M.A., Nordbotten J.M. & Juanes R. (2023). *Direct Comparison of Numerical Simulations and Experiments of CO_2 Injection and Migration in Geologic Media: Value of Local Data and Forecasting Capability*. Transp. Porous Med. https://doi.org/10.1007/s11242-023-01972-y

Eikehaug K., **Haugen M**., Folkvord O., Benali B., Bang Larsen E., Tinkova A., Rotevatn A., Nordbotten J.M., Fernø, M.A. (2024). *Engineering meter-scale porous media flow experiments for quantitative studies of geological carbon sequestration*, Transp. Porous Med. https://doi.org/10.1007/s11242-023-02025-0

Eikehaug K., **Haugen M**., Benali B., Alcorn Z.P., Rotevatn A., Nordbotten J.M. & Fernø M.A. (2023). *Geological Carbon Storage at the University of Bergen, Norway*. In: Médici, E.F., Otero, A.D. (Eds) Album of Porous Media: Structure and Dynamics (pp. 46-46). Cham: Springer International Publishing. https://doi.org/10.1007/978-3-031-23800-0_34

Both J.W., Benali B., Folkvord O., **Haugen M.**, Storvik E., Fernø M.A. & Nordbotten J.M. (2023a). *Image Analysis of the International FluidFlower Benchmark Study Dataset (v1.0)*. Zenodo. https://doi.org/10.5281/zenodo.7515038

Benali B., Føyen T.L., Alcorn Z.P., **Haugen M**., Gauteplass J., Kovscek A.R. & Fernø M.A. (2022). *Pore-scale Bubble Population Dynamics of CO_2-Foam at Reservoir Pressure. Int. J. of Greenhouse Gas Control, 114*. https://doi.org/10.1016/j.ijggc.2022.103607

Exhibition and posters

Our porous world. Exhibition at the University Museum, Bergen, 2022-04-01 – 2023-01-20. https://www.uib.no/en/researchcommunication/153199/our-porous-world, accessed 2023-09-28.

Haugen M., Brattekås B., Fernø M.A. Dos and don'ts when developing a system for microbially induced calcite precipitation in micromodels. Poster at *Microfluidics and Energy Symposium*; 2021-04-29 – 2021-04-30.

Føyen T.L., **Haugen M.,** Benali B., Fernø M.A. CO_2 Mobility Control by Foam at the Pore Level. *Interpore*; 2020-08-31 – 2020-09-04.

1. Theory and background

1.1 Energy and environmental perspective

Today there is little doubt that increasing carbon dioxide (CO_2) concentration in the atmosphere leads to global warming and that urgent action is required to mitigate subsequent climate changes and its consequences. One of the Sustainable Development Goals (SDGs) which was agreed upon by the United Nations in 2015 was SDG number 13, to *take urgent action to combat climate change and its impacts* (UN General Assembly, 2015). The Paris Agreement was also adopted in 2015 by the international community. It provides a roadmap for climate actions that will reduce emissions by a collective agreement to limit the global temperature rise to well below 2 ºC above pre-industrial levels (COP21, 2015). This global focus and effort are important since climate change does not take national borders into consideration.

Together with increasing wealth and world population growth, the global energy demand is increasing. According to the Sustainable Development scenario by the International Energy Agency (IEA, 2021), the electricity demand is expected to increase by about 60% until 2040 (IEA, 2020). Even though the share of renewable energy is increasing, fossil fuels are still the dominating energy source in the world. Transition to low-carbon energy is therefore essential to be able to achieve climate and energy goals. Carbon, capture, and storage represent a bridging technology to combat climate change in the transition towards a zero-carbon society until the cost of renewable energy solutions is further reduced, and the technologies have high enough capacity and can handle peak-demand.

1.1.1 The role of CCUS in the energy transition

Carbon, capture, utilization, and storage (CCUS) is identified to play a major role in the energy transition in multiple ways (IEA, 2020; IEA, 2021), including: 1) The option to retrofit carbon capture technologies to existing fossil-fueled power plants to avoid lock-in of emissions during their lifetime. This is especially important in Asia, where there is a young fleet of coal-based power plants which are expected to be operating for decades to come. 2) As the share of renewable energy is increasing, a portfolio of solutions to cover the short-and long-term seasonal variations in energy supply is needed. CCUS-equipped power plants represent a supplement to the variable renewable energy sources. 3) In combination with bioenergy, carbon capture technologies can enable

power plants with negative emissions and thereby support sectors where it is harder to obtain net-zero emissions (like cement production). As part of the energy transition, CO_2 related to hydrogen production from natural gas could also be stored in safe subsurface locations, and thereby be a supplement to the variable renewable energy sources (IEA, 2021). Experience from CO_2 storage could potentially accelerate development of underground hydrogen storage and be a central aspect of a sustainable energy future (Krevor et al., 2023).

1.2 Geological CO_2 storage

Geologic CO_2 storage (GCS) is storage of captured CO_2 into appropriate geological formations deep into the subsurface. Options for CO_2 storage locations include active or abandoned oil and gas fields, saline aquifers, and coal seams (IPCC, 2005). Several criteria must be fulfilled for this operation to be successful: 1) Injectivity in the desired storage formation, meaning that the rock must be porous and permeable, and the formation needs to have a sufficient volume to avoid pressure buildup during injection. 2) Reliable containment of the injected CO_2, meaning that the structural and/or stratigraphic trap is sealing with no/limited risk of leakage of CO_2 to the surface or to portable aquifers. 3) Surveillance program must be in place to monitor the CO_2 for several years to make sure the CO_2 is permanently stored.

Currently there are two ongoing CO_2 storage projects in Norway; Sleipner since 1996 and Snøhvit since 2008 with totally about 1.7 million tonnes (Mt) CO_2 injected per year (Eiken et al., 2011). A third project, the Northern Lights, is planned to start injecting in 2024, with a storage capacity of 1.5 Mt CO_2 per year in the first phase of the project (Northern Lights JV DA, 2023). Number of CO_2 sequestration projects are increasing world-wide, with a dedicated CO_2 storage capacity which could reach over 420 Mt CO_2 per year by 2030, but many more are required to reach the goal of storing 1200 Mt CO_2 per year by 2030 which is called for in the Net Zero Emissions Scenario (IEA, 2023).

1.2.1 Flow physics and trapping mechanisms

Most CO_2 storage projects involve injection in formations deep enough (>800 m) to exceed the critical point in the CO_2 phase diagram (Figure 1) where CO_2 is in supercritical state (Eiken et al., 2011; Nordbotten & Celia, 2011). This means that CO_2 has both gas-like properties (viscosity) and liquid-like properties (density). With increasing depth, the

density increases and associated reduction in relative volume the CO_2 occupies (Figure 2) provide efficient utilization of underground storage space (IPCC, 2005). However, the density of the injected CO_2 is still lower than the in-situ fluids in the saline aquifer and CO_2 will therefore rise to the base of the seal due to buoyancy forces (Benson & Cole, 2008).

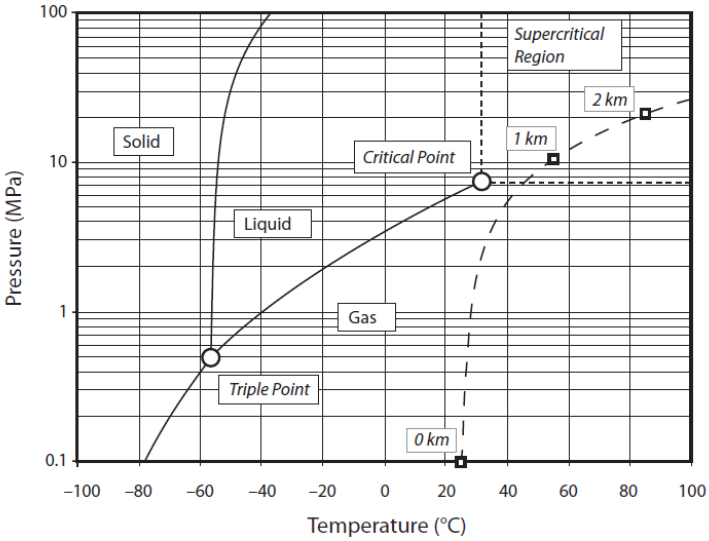

Figure 1: Phase diagram for pure CO_2, including dashed line representing typical conditions as a function of depth below land surface (Nordbotten & Celia, 2011).

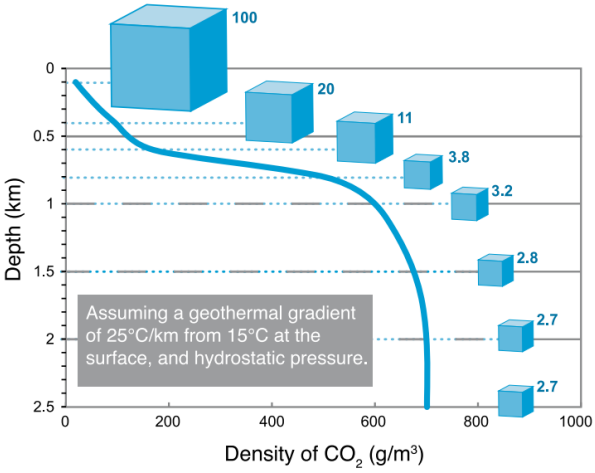

Figure 2: Change in density and volume of CO_2 as a function of depth below land surface for a typical geothermal gradient (IPCC, 2005). The CO_2 density increases rapidly at approximately 800 m depth when it reaches supercritical stage, with associated reduction in volume (represented by blue cubes). After about 1500 m depth, the density and relative volume is almost constant.

During geologic storage of CO_2, it is essential that the buoyant CO_2 is trapped after injection to minimize risk of leakage into shallower formations. Over time the injected CO_2 become less mobile by several porous media trapping mechanisms (Figure 3), with increasing storage security (IPCC, 2005): 1) *Structural trapping* (related to folding and faulting of reservoir rocks) *or stratigraphic trapping (*related to deposition of the reservoir rocks, like channels or rivers) where a thick layer of fine-textured rock provide an effective permeability and capillary barrier constraining the CO_2 from upward migration. 2) *Residual trapping,* or capillary trapping, is related to pore-scale trapping of CO_2 droplets during two-phase flow. 3) *Solubility trapping*, related to CO_2 partially dissolving in brine, creating CO_2-saturated brine with increased density which sink towards the bottom of the aquifer, aided by the development of gravity dominated fingers. 4) *Mineral trapping*, related to trapping as part of solid precipitation.

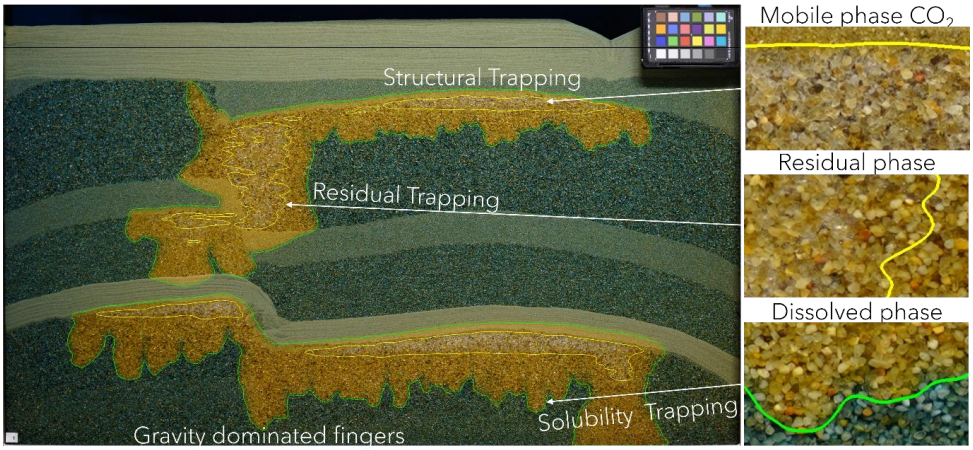

*Figure 3: Trapping mechanisms of CO_2 in the subsurface. Image created using the meter scale methodology presented in section 2.3. Gaseous and aqueous forms of CO_2 are visible due to pH-sensitive dyes added to the formation water. Contours are obtained through image processing using DarSIA (Nordbotten et al., 2023), dividing the phases in dissolved CO_2 (green contours) and CO_2 as gas phase (yellow contours). Further details about the image processing and use of the quantitative data can be found in **Paper 5** and **Paper 6**.*

CO_2 and water are initially immiscible at pressure and temperature conditions expected for GCS, meaning that the pressure needed to inject CO_2, the rate at which the leading edge of the CO_2 plume moves, and the fraction of the pore space filled with CO_2 are all determined by multiphase flow relationships (Bear, 1972). For CO_2 sequestration, three particular important consequences of the multiphase flow behavior were identified by Benson & Cole (2008): 1) The fraction of the pore space which can be filled with CO_2 is

limited by flow dynamics and capillary pressure resulting from the interactions of multiphase flow, 2) CO_2 mobility is limited during the post-injection period, and 3) seals have two mechanisms for trapping CO_2; low permeability resulting in very slow flow rates even at high pressure, and small pores which have a very high capillary entry pressure, causing the sealing rock to allow water to pass but block CO_2 unless the pressure exceeds the capillary entry pressure.

Buoyancy-driven CO_2 migration is determined by intrinsic rock and fluid properties (e.g., porosity, permeability, fluid-density, and viscosity), and distribution and properties of geological structures such as faults and fracture networks. Faults are discontinuities that form at a wide range of scales, and can act as conduits or barriers for flow, and generally have directionally dependent flow properties (Bastesen & Rotevatn, 2012). Large sealing faults control storage site geometries and compartmentalization, while networks of small faults and fractures may affect reservoir flow and seal integrity (Ogata et al., 2014).

Properties of the fracture network (e.g., topology, connectivity, permeability) that constitute the damage zone around faults as they evolve (Nixon et al., 2020) are particularly important for the flow of CO_2. Accurately identifying and predicting CO_2 flow behavior in the subsurface is necessary for the development of GCS. Understanding the interplay between multiphase flow and fault evolution is of particular importance, however; only faults larger than seismic resolution can be mapped from subsurface seismic data. Using geologically analogous outcrops and dedicated laboratory experiments to investigate smaller structures associated with faults is important. Well-designed experiments and new experimental methods may shed light on flow and sealing properties, and contribute to understanding of fault evolution during CO_2 injection.

1.2.2 Geochemical reactive transport

GCS has mostly targeted sandstone formations, however, to achieve ambitious emission goals it is also necessary to utilize the large storage capacity in carbonate formations. *Sandstone* consists mainly of the most resistant minerals quartz and feldspar and are often cemented with carbonate minerals. *Carbonate* rocks are a class of sedimentary rocks which consists of mainly carbonate minerals, and the two major types are limestone and dolomite. The combination of chemical components in rock and fluids makes carbonate reservoir susceptible to changes during CO_2 injection. Geochemical reactive transport is related to both solubility trapping and mineral trapping mechanisms (section 1.2.1).

Geochemical reactions (Table 1) can lead to both dissolution of primary minerals and precipitation of secondary minerals, causing changes in formation porosity and permeability (Kharaka et al., 2006). The rate of these reactions depends on several parameters: pressure, temperature, salinity, brine composition and pH (Baines & Worden, 2004; Chang et al., 2017).

Once CO_2 is injected in a geological formation, it will partially dissolve in the formation brine and develop carbonic acid (H_2CO_3), which dissociates to hydrogen ions (H^+) and bicarbonate ions (HCO_3^-) (Eq.1-2, Table 1). This causes the pH of the aqueous phase to decrease (Morais et al., 2016), typically from near neutral to below pH 4 (Benson & Cole, 2008), or down to pH 1 if the injected CO_2 stream contains NO_2 and SO_2 (Ellis et al., 2010). The reduced pH further promotes geochemical reactions and lead to dissolution of calcium carbonate $(CaCO_3)$ minerals in the cement (sandstone) and/or the host rock (carbonate) (Eq.3-4, Table 1). This will rapidly buffer the pH and thus make the brine less acid (Gaus, 2010). The dissolved bicarbonate ions (HCO_3^-) could react with available cations (e.g., $Ca^{2+}, Mg^{2+}, Fe^{2+}$) present in the aqueous phase and precipitate secondary carbonate minerals at neutral to alkaline pH (Eq.5-7, Table 1) (Benson & Cole, 2008; Oelkers et al., 2008).

Table 1: Geochemical interactions leading to dissolution and re-precipitation

Description	**Chemical process**		**pH change**
Acidification of aqueous phase:	$CO_2(aq) + H_2O \leftrightarrow H_2CO_3$ $H_2CO_3 \leftrightarrow H^+ + HCO_3^-$	[Eq.1] [Eq.2]	decrease
Calcium carbonate dissolution:	$CaCO_3 + H^+ \leftrightarrow Ca^{2+} + HCO_3^-$ $CaCO_3 + H_2O \leftrightarrow Ca^{2+} + HCO_3^- + OH^-$	[Eq.3] [Eq.4]*	increase
Precipitation of secondary minerals**:	$HCO_3^- + Ca^{2+} \leftrightarrow CaCO_3 + H^+$ $HCO_3^- + Mg^{2+} \leftrightarrow MgCO_3 + H^+$ $HCO_3^- + Fe^{2+} \leftrightarrow FeCO_3 + H^+$	[Eq.5] [Eq.6] [Eq.7]	decrease

* Equilibrium of calcium precipitation in water
** Examples of secondary minerals: Calcium carbonate ($CaCO_3$), magnesite ($MgCO_3$) and siderite ($FeCO_3$).

1.2.3 Bio-geochemical precipitation of calcium carbonate

Precipitation of calcium carbonate minerals due to geochemical reactions is a CO_2 trapping mechanism where CO_2 is stored as part of minerals (cf. section 1.2.2). But utilization of geochemical precipitation of calcium carbonate have also been considered as a potential plugging agent in many environmental and engineering applications, including (but not limited to) rehabilitating constructing materials (De Muynck et al., 2010; Ortega-Villamagua et al., 2020; Siddique & Chahal, 2011), constraining contaminated groundwater (Fujita et al., 2010) and reducing the environmental risk from leakage of sequestered CO_2 (Celia et al., 2005; Mitchell et al., 2010; Watson & Bachu, 2009). These applications utilize a method referred to as microbial-induced calcium carbonate precipitation (MICP) through bio-geochemical reactions.

The process of MICP is naturally occurring because bacterial species in many environments (including the subsurface) modify the local environment as a result of their metabolite releases. Bacteria like *Sporosarcina Pasteurii* produce urease enzymes for hydrolyzing urea $(CO(NH_2)_2)$ into ammonium (NH_4^+) and carbonate ions (CO_3^{2-}) in the aqueous phase, causing increased pH of the surrounding solution (Mitchell et al., 2010; Siddique & Chahal, 2011). As discussed in section 1.2.2, the presence of calcium ions (Ca^{2+}) in this alkaline environment promotes chemical precipitation of calcium carbonate ($CaCO_3$) due to elevated supersaturation of the ions (Mitchell et al., 2010). Details about *Sporisarcina Pasteurii* and reactions involved in hydrolyzing urea can be found in **Paper 1**, and it confirmed that to enhance $CaCO_3$ precipitation in the lab, only urea and calcium must be added in addition to active bacteria, while ammonium and calcium carbonate are the products.

Calcium carbonate can crystallize into different polymorphs during bio-geochemical precipitation, seen as minerals in nature. This includes calcite, vaterite and aragonite, and two hydrated polymorphs in addition to several amorphous calcium carbonate (ACC) phases (Krajewska, 2018). According to Ostwald's step rule, the least stable ACC form first, then transforms to thermodynamically more stable polymorphs (Mullin, 2001) with calcite as the most stable molecular structure (Rodriguez-Blanco et al., 2011). For high supersaturation values calcite is initially formed as ACC before transforming to more stable vaterite and calcite (Zhang et al., 2018), while lower supersaturation leads directly to calcite precipitation (Van Paassen, 2009).

Pore-scale properties of $CaCO_3$ precipitates (i.e., crystal size, morphology, and distribution in porous media) can strongly affect the sealing efficiency and plugging strength of the MICP application. Pore structure and operational parameters (like pressure and cell number) influence the supersaturated state in the pores, which strongly impact the kinetics of nucleation and growth of $CaCO_3$ crystals (Yoon et al., 2019).

2. Multiscale laboratory methods

The GCS success heavily relies on our understanding of fluid flow in subsurface formations, and fundamental understanding across length scales contributes to updated predication tools for improved accuracy in forecasting long-term CO_2 storage security. The complexity of multiphase porous media behavior, especially in the GCS context, requires a comprehensive and multifaceted laboratory toolbox. This chapter details laboratory methodologies developed as part of this dissertation that spans a wide range of scales; from *micro scale* (**Paper 1** and **2**, section 2.1) where the fundamental interactions occur, *Darcy scale* (**Paper 3** and **4**, section 2.2) to characterize bulk and multiphase flow behavior, to *meter scale* (**Paper 5** and **6**, section 2.3) to include important trapping mechanisms. The linkage between the length scales (Figure 4) facilitates detailed investigations of multiscale GCS trapping and flow mechanisms.

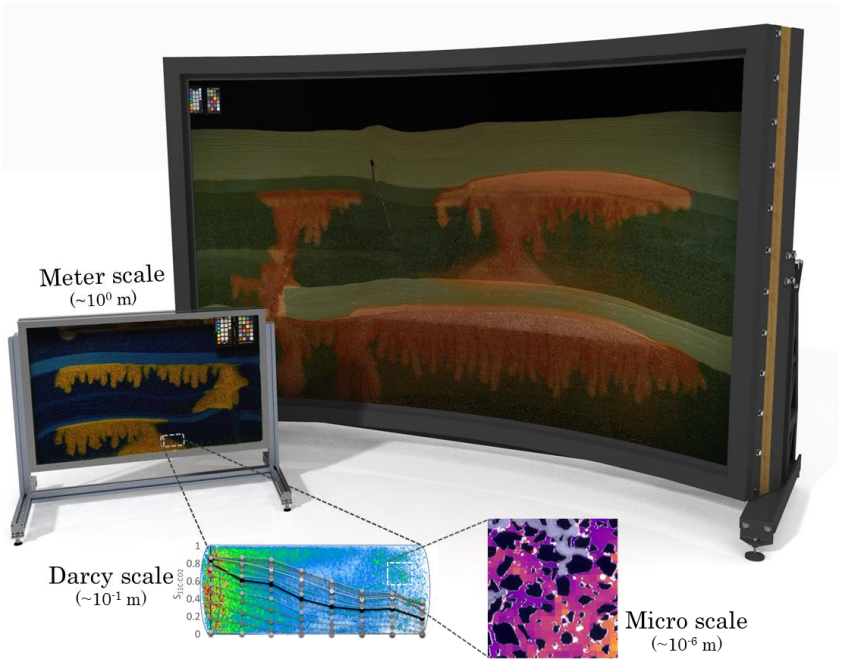

Figure 4: Laboratory methodologies used/developed to quantify multiphase flow and physicochemical interactions from micro scale (~10^{-6}) to Darcy scale (10^{-1}) to meter scale (~10^{0} meter). At micro scale, dynamic pore-scale processes were captured with a microscope, here showing CO_2 in a $CaCO_3$ functionalized micromodel initially filled with labeled brine. At Darcy scale, PET (and µCT) was used to capture flow dynamics in cores, here with labeled CO_2 gas injected (from left) into a core sample. Meter scale flow dynamics were acquired with camera through time lapse imaging, here showing CO_2 injected in FluidFlower rigs, turning the labelled brine to warmer colors when CO_2 dissolves in it.

The laboratory methods for all three scales (Figure 4) rely on imaging of pore scale dynamics with a range of modalities. Labeling of fluid phases enables post image processing and quantification of data to obtain more than just nice images. Overview of fluid labeling used in this research is presented in Table 2.

Table 2: Labelled phases used to quantify pore scale dynamics

Labelled phase	Micro scale	Darcy scale	Meter scale
Fluorescent brine	Paper 1		
Fluorescent brine (pH sensitive)	Paper 2		
Brine (pH sensitive)			Paper 5 and 6
Brine (radioactive)		Paper 3 and 4	
Gaseous CO_2 (radioactive)		Paper 4	

2.1 Micro scale

To resolve the complexities within large scale CO_2 storage, it is essential to understand the fundamentals at the micro scale. For this work micro scale is defined as single and multiple pores, and is interchangeably referred to as pore-scale. Detailed studies of pore-scale flow dynamics are possible with a microfluidic set-up. Microfluidics is a well-established method with a broad applicability, including low-carbon solutions (Datta et al., 2023).

The micro scale experimental set-up designed, built, and used in this study is detailed in **Paper 1** (Figure 5). Chemically resistant materials enable experiments using abrasive fluids, hydrogen, and CO_2. Reactive flow has been identified to be of key importance to accurately model fluid flow and forecast GCS security (Kazemifar et al., 2015), and includes mechanisms of mineral dissolution and precipitation (cf. section 1.2.2). Key system features include a custom-built holder for pressure and temperature control of the porous media (the micromodel) with a porous pattern based on thin section from a natural sandstone (Figure 6). Time-lapsed images of multiphase dynamics are possible with a microscope placed directly above the micromodel, and the motorized stage enables high resolution images of the whole porous network. Two *select valves* allow rapid switching (with minimal dead volume) for controlled injection of different fluids. This feature reduces unwanted fluid mixing before entering the pore space and is especially important when working with bio-geochemical reactions. A *switch valve* is used to inject a low volume (e.g., bacteria solutions or expensive pH sensitive fluorescence tracer) directly into the flow line with high precision.

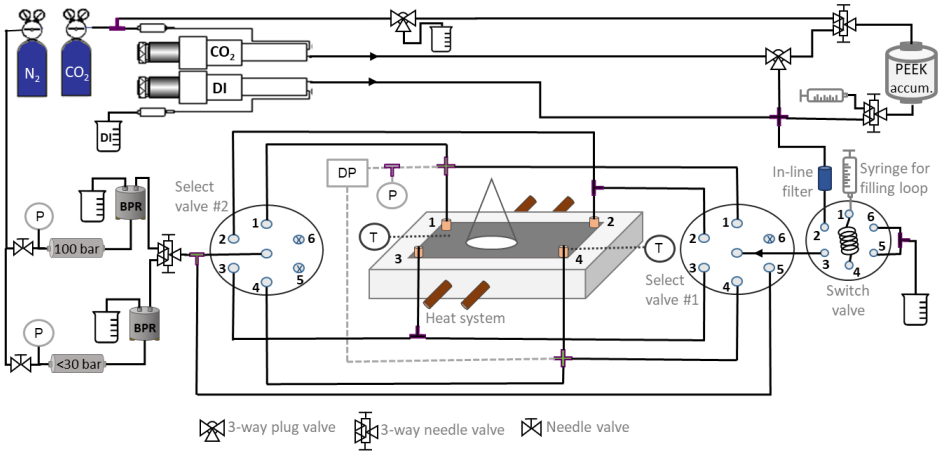

Figure 5: Schematic of the experimental set-up for pore-scale visualization of multiphase flow using microfluidics. Main features include an in-house designed micromodel holder (middle) with direct flow line connections to the four flow ports underneath the micromodel, high precision plunger pump and a microscope with automatic scanning stage. Low volume fluids (typically between 10 – 1000 µL) could be added to the flow line through the switch valve, and two select valves makes it possible to design experiments with different injection/production configurations. Modified from ***Paper 1****.*

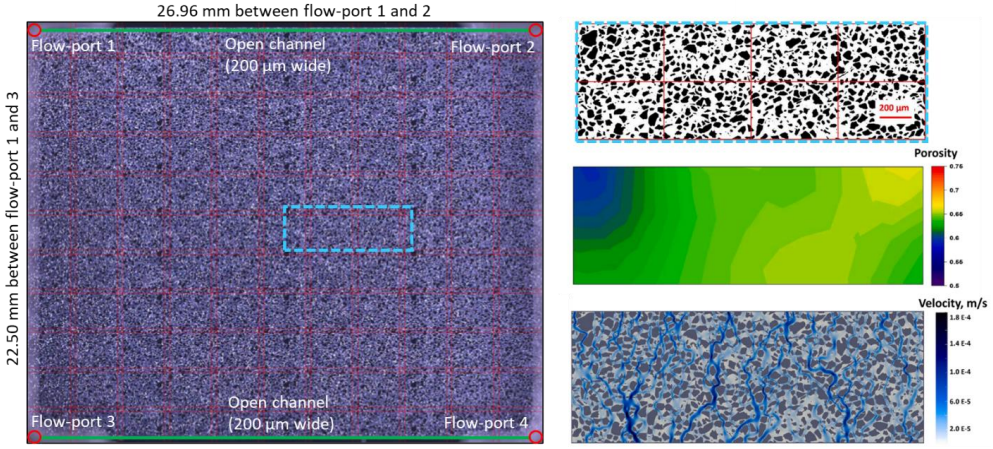

Figure 6: <u>Left</u>: Full-model image of the micromodel including dimensions. Black are silica grains and blue are the pore-space (1.1 µL). The full-model image is generated from individual images automatically captured by the microscope software, stitched together to one image. The four flow-ports and the two open-channel fractures are highlighted. A pattern generated from thin sections of natural sandstone (blue rectangle) is repeated 36 times to create the porous network in the micromodel. Figure from ***Paper 1****. <u>Right:</u> A zoom-in of the unique porous pattern (blue rectangle), shown as a binary image at the top, with corresponding porosity distribution map in the middle and simulation of steady-state flow velocity magnitude at the bottom. Figure from Liu et al., 2023b.*

The micro scale set-up has two light sources (cold light LED and fluorescence) for aqueous phase labelling, for instance during reactive flow studies (c.f. section 1.2.2) or bio-geochemical precipitation of calcium carbonate (c.f. section 1.2.3). In **Paper 1** a fluorescence (FL) dye was used to investigate dynamic changes in mineral structure during the precipitation process (Figure 7). In **Paper 2**, the aqueous phase was labeled with pH sensitive FL tracer (Figure 8) to visualize local pH changes.

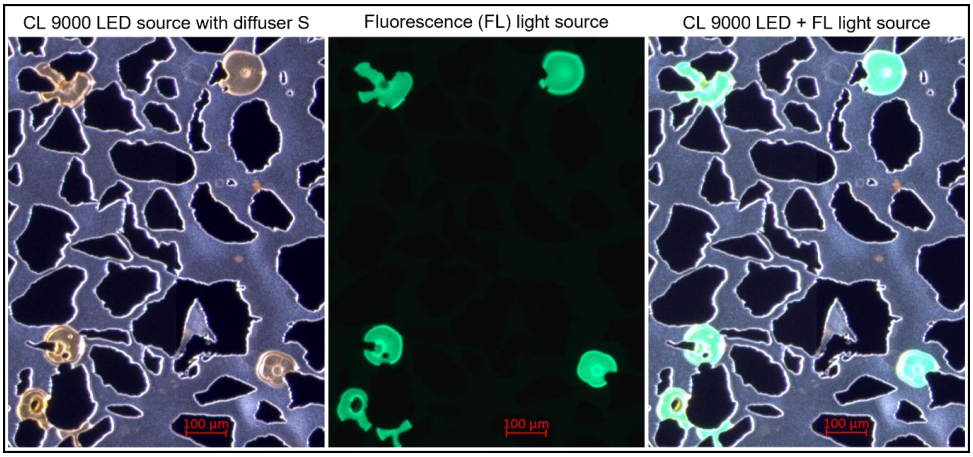

Figure 7: Multimodal pore-scale visualization of calcium carbonate ($CaCO_3$) using the MICP process described in section 1.2.3. The cementation solution contained fluorescence tracer (0.10 wt % Fluorescein sodium salt) to precipitate $CaCO_3$ minerals. After the precipitation process the FL tracer is displaced by deionized water. Internal mineral structure and $CaCO_3$ quantification is possible with image analysis. This approach is of great value for studies of pore-scale reactive flow, and as a tool to determine CO_2 storage security in carbonate formations. Figure from (Haugen et al., 2023c).

Calcium-functionalized micromodels enable mechanistic studies related to CO_2 storage security in formations consisting of/rich in carbonate minerals. Calcium carbonate minerals are precipitated in the pore space (**Paper 2**) for detailed reactive flow studies that maintain integrity of the pore space (except dissolved minerals), supplementing fabricated microchannels in a naturally occurring mineral substrate where reactive flow studies are performed at atmospheric pressure (Song et al., 2014).

Minerals generated with bio-geochemical precipitation of calcium carbonate can crystallize in different polymorphs (c.f. section 1.2.3) with different degree of stability. Raman spectroscopy has been implemented to identify amorphous $CaCO_3$, vaterite and calcite (detailed in Liu et al., 2023b). The impact of pore structure and operational parameters (like pressure and cell number) was largely unknown until this set-up unlocked improved understanding and predictability of porous bio-geochemical

precipitation of calcium carbonate. This could aid development of efficient upscaled MICP models and is thus necessary for different applications (Liu et.al. 2023b).

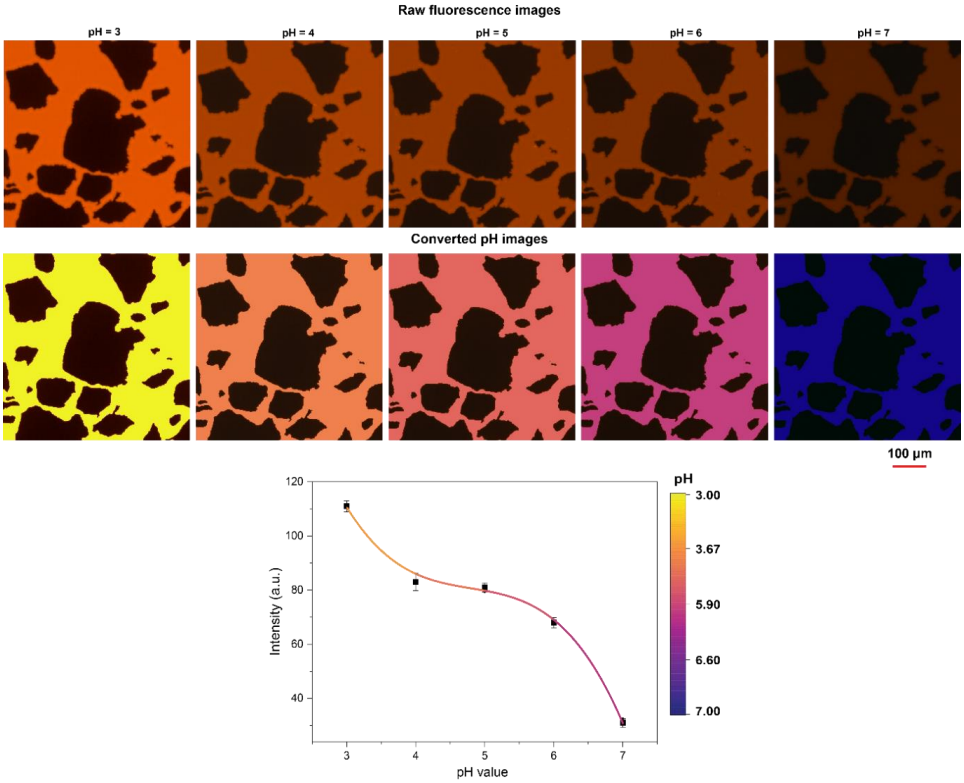

*Figure 8: pH sensitive fluorescent tracer added to brine, or buffers in this case, to create a calibration curve (bottom) to covert raw microscope images (first row) to pH images of the pore space (second row). Figure from **Paper 2**.*

2.2 Darcy scale

Darcy scale analysis is important for characterizing the interaction between injected CO_2 and storage formation during GCS, for instance permeability (and thereby injectivity) changes and geochemical reactions associated with injection of CO_2. If reservoir cores are not available, outcrop cores from analogous formations (i.e., sandstone, chalk, limestone, or shale) may be used to probe mechanistic behavior and map the parameter space in the laboratory. The effect of fractures, small-scale heterogeneities, and local reactive processes should be studied with advanced laboratory methods to access flow parameters and other GCS mechanisms at Darcy and sub-Darcy length scales. The

findings are a necessary input to numerical simulations, aiming to establish large-scale behavior of CO_2 migration.

Positron emission tomography (PET) imaging is primarily used in medicine for accurate cancer diagnosis but is also an increasingly important tool for geoscience research (e.g., Brattekås et al., 2020 and Fernø et al., 2015a). PET imaging is non-invasive and able to visualize multiphase fluid flow dynamics in rocks with excellent signal-to-noise ratios (Fernø et al., 2015b), independent of experimental temperature and pressure conditions, rock properties and mineralogy. Pre-clinical PET (µPET) imaging has shorter distance between the scanned object and detector elements compared to clinical PET scanners and provides higher spatial resolution for geoscience research (e.g., Ebadi et al., 2022 and Brattekås et al., 2023).

The Darcy scale experimental set-up (Figure 9) used in this study includes a custom-made core holder attached to the mechanical arm for accurate field-of-view positioning, pumps for radioactive gas and liquid injections at elevated pressures and an accumulator for effluent production and handling, as detailed in **Paper 4.**

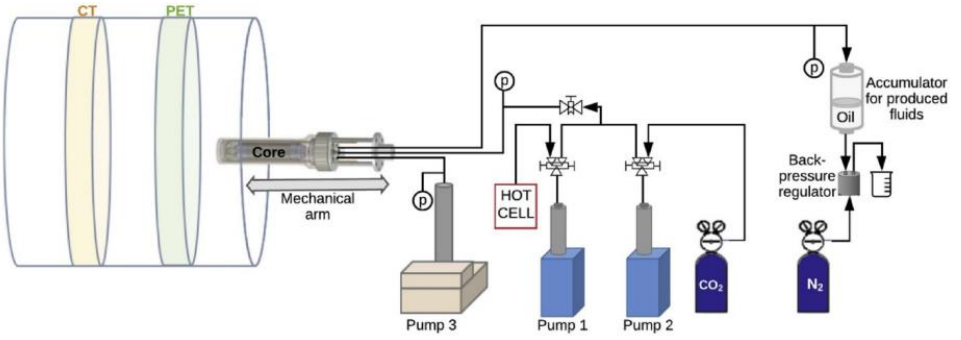

*Figure 9: Schematic of the experimental set-up used for PET imaging of radiolabeled CO_2 and brine injections. Pre-clinical PET-CT scanner enables in-situ visualization of radiolabeled fluids. Figure from **Paper 4**.*

This system presents a recent advancement in pore scale dynamic imaging of CO_2 flow, where µPET and radioactive tracers are used to obtain quantitative and qualitative dynamic saturation development at Darcy and sub-core scale at elevated pressure. Explicit imaging of dense CO_2 is possible with the ^{11}C isotope ($t_{1/2}$ of 20.4 minutes, see Taddei and Pike, 2019) and brine with ^{18}F isotope ($t_{1/2}$ of 109.8 minutes, see Jacobsen and Chen, 2010). Use of µPET for Darcy scale imaging during water injection is exemplified below (Figure 10).

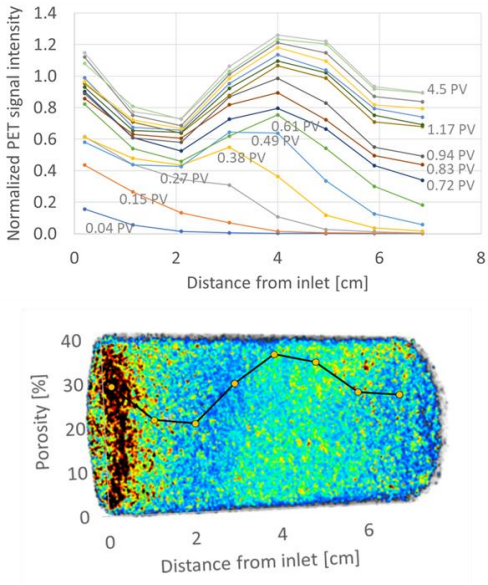

*Figure 10: Top: Saturation profiles for labeled brine injected in a (brine-saturated) carbonate core after experiment with co-injection of CO_2 and brine. Bottom: The porosity (after 4.5 PV injected) is derived from the PET signal distribution (top) and overlayed a 3D image of the core. The high-porosity region identified in the middle illustrates that PET imaging provides insight into spatial fluid flow distribution in the core. Figure from **Paper 3**.*

2.3 Meter scale

Subsurface features and structural complexities relevant for GCS (e.g. layered fining- or coarsening upwards sequences, pinch-outs, folds, and faults) cannot satisfactorily be studied at Darcy scale. Hence, larger length scales are required to accurately determine the influence of said features on the migration pattern and convective mixing of the injected CO_2. The FluidFlower experimental flow rigs (Eikehaug, 2024) enable repeatable meter scale, multiphase, quasi two-dimensional flow on complex, yet representative geological geometries in a laboratory setting with high-accuracy data acquisition. Hence, it represents an opportunity to corroborate numerical GCS simulations (Saló-Salgado et al., 2023) or to evaluate the predictive skills of the GCS modeling and simulation community (Flemisch et al., 2023).

A range of FluidFlower flow cells have been designed for different purposes: smaller A4-format versions for educational purposes, table-top versions (0.9 m length · 0.6 m height, **Paper 5**) for repeatability studies and rapid prototyping/parameter space investigations; and a room-scale version (3 m length · 2 m height, **Paper 6**) for increased geometric

complexity and convective mixing studies. The two latter versions rely on the same conceptual experimental set-up (Figure 11), where the studied geological geometries are constructed in the void space between the front and back panel using unconsolidated sands (described below). The flow cells have no-flow boundaries at the bottom and the sides, whereas the top is open and in contact with atmospheric pressure. Perforations for injection/production and pressure monitoring are placed based on experimental design, but some are fixed: the bottom row (F1-F3) is used for injecting fluids to reset the system, enabling repeated experiments in the same geometry; the *inflow* port maintains a constant water level; the always-open *overflow* port allows excess fluids to exist the system. In addition to the flow cell, the experimental set-up consists of numerous valves, a mass flow controller (MFC) to enable equal mass of CO_2 injected in repeated experiments, a gas trap to mitigate unwanted air injected into the rig during re-setting the fluids between CO_2 injections, a camera with time-lapse function, and a ColorChecker used to calibrate colors in time lapse images towards a constant color palette.

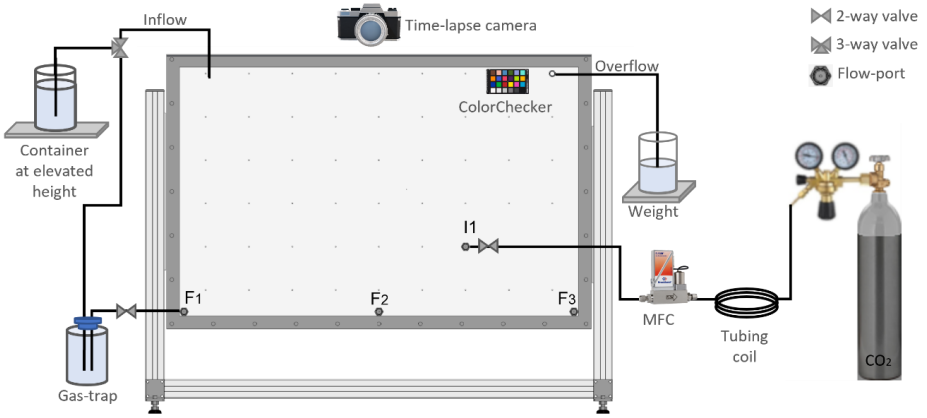

Figure 11: Schematic set-up of the FluidFlower experimentally concept/set-up. Fluids are injected through gravity (container at elevated height) or using a pump. During flushing and resetting of the geometry, the flush-ports (F1 – F3) are utilized, and as a preventive measure to avoid unwanted air in the rig, a gas-trap is included. For gas injection, the set-up consists of a CO_2 calibrated mas flow controller, CO_2 canister with pressure regulator and a coil of tubing to mitigate pressure fluctuations caused by the gas regulator. Inflow through a loose tubing end and outflow through an always-open port provide a constant hydraulic head and provide information about volume displaced if logged. Camera with time lapse function is used to acquire high resolution images of the dynamics, and the ColorChecker ensures correction of colors during image analysis to mitigate changes in illumination. Figure from ***Paper 5****.*

Unconsolidated sands with different grain-size distributions and flow properties are used to build geologic geometries for GCS research. Textural (width, length, and sphericity) and petrophysical (porosity, absolute permeability, endpoint relative permeability to gas

and water, and capillary entry pressure) sand properties are measured (detailed in **Paper 5**). Dry sand is manually poured into the water-filled void between the front and back panels. Faults and large dipping angle features are created with *angle tools* by manipulating the sand during pouring (see Figure 12). Procedures to construct geometries are further detailed in **Paper 5**.

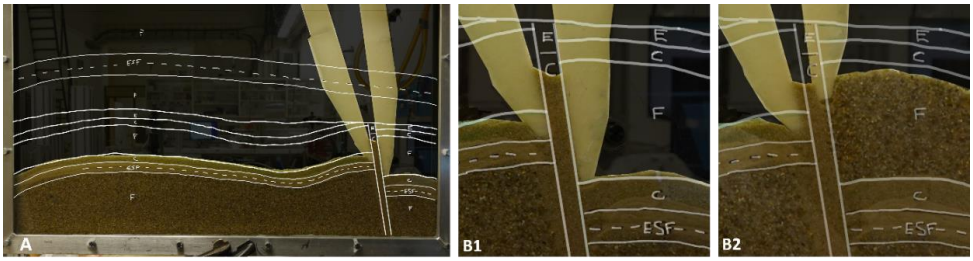

Figure 12: Example of how to build features in the table-top FluidFlower by pouring sand from the top and into the water-filled flow-rig. A: The geological geometry is drawn on the transparent front panel. In this example the sand adjacent to the fault is different from within the fault, and two white angle-tools separate them. B1 and B2: Details from fault construction. The fault and adjacent facies are deposited in a layer-by-layer approach to match the planned geometry. The angle tool represents the boundary of the fault, and the sand on the side of the fault replaces the angle tool as it is lifted to maintain the shape of the fault. Figure from ***Paper 5****.*

The gaseous and aqueous forms of CO_2 are distinguished by use of pH-sensitive dyes. The porous media is initially fully saturated with an aqueous pH-indicator mix, referred to as *formation water*. The CO_2 is injected as a dry gas and will partially partition into the formation water and form *CO_2 saturated water*, and reduce the pH of the formation water and thereby change its color. Three different pH-indicator mixes (Figure 13) were used to evaluate the visual impact for tracking CO_2 gas migration (as absence of color) and CO_2 saturated water. The results show that it is important with large color contrast to separate the phases, and because gaseous CO_2 can only be identified as absent of color, the color of the sand also impacts the color contrasts.

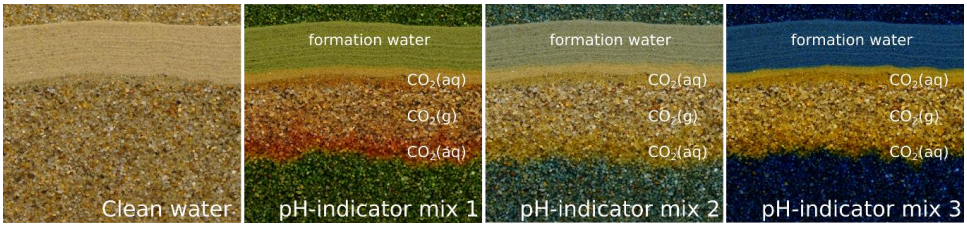

Figure 13: Illustration of different pH-indicator mixes used in the experiments with how their colored response is to gaseous and dissolved CO_2 as supposed to the formation water. From left to right: Image of a layered sand formation saturated with clean water; same formation but saturated with pH-indicator mixes 1-3 in the presence of CO_2. Details about fluid composition can be found in ***Paper 5****.*

The in-house image analysis software DarSIA (Nordbotten et al., 2023; Both et al., 2023a, Both et al., 2023b) transforms the high-resolution time lapse image sequences into physical data to quantify key parameters and the variability between repeated experiments. DarSIA includes preprocessing tools that: align images and project them (or areas of interest) to a two-dimensional Cartesian coordinate grid; correct for the curved surface of the room-scale FluidFlower; account for light fluctuations; and, perform white balance and color corrections based on the attached ColorChecker (further detailed in **Paper 6**). A corrected representation of each image allows tracking of fluid migration as differences to a baseline image.

DarSIA enables quantitative description of the multiphase flow based on a range of assumptions (detailed in **Paper 6**), and an algorithmic phase which essentially consists of thresholding both in terms of color and signal intensity. Two suitable monochromatic color channels are selected (depending on the used pH-indicator mix cf. Figure 13) to first identify CO_2 in the aqueous phase, and then map gaseous CO_2. Variable light reflections for each sand layer are accounted for (see **Paper 5** and **Paper 6**) to achieve an accurate phase segmentation (Figure 14).

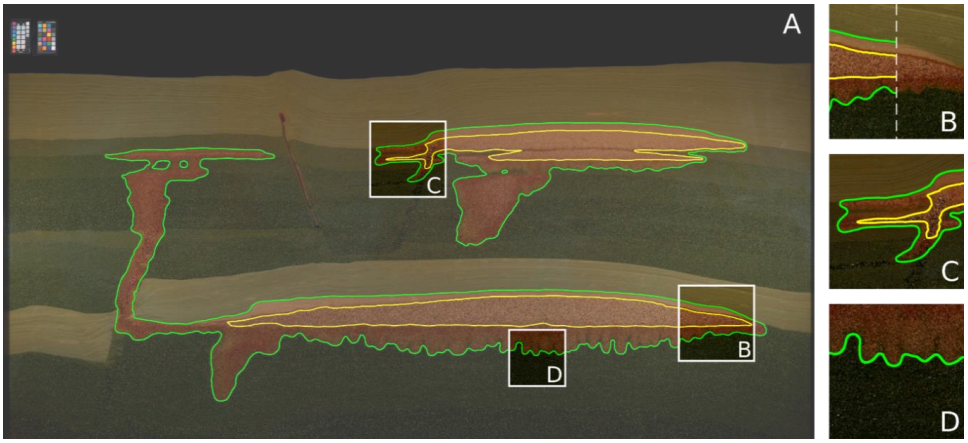

*Figure 14: Resulting phase segmentation of formation water, CO_2-saturated water and free gas using DarSIA. Free gas has yellow contours, and CO_2-saturated water has green contours. Figure from **Paper 6**.*

3. Results and discussion

The multiscale experimental methodologies detailed in Chapter 2 facilitate a wide range of experimental designs, well suited to study the complex systems of physicochemical interactions and multiphase flow during GCS. This chapter discusses selected results from reactive transport and flow dynamics at different length scales. The discussed results demonstrate the variety of research performed and emphasize the importance of local flow variations in porous media.

3.1 Reactive transport in pores and cores

Mechanistic understanding of mineral dissolution-precipitation during CO_2 injection is of key importance to accurately model fluid flow and forecast GCS security (Lu et al., 2013). The injected CO_2 perturbates the natural geochemical equilibrium by increasing the CO_2 partial pressure and reducing the pH of the formation water, and thereby initiate dissolution of carbonate minerals in the near wellbore area. The formation of bicarbonate can also increase the aqueous phase pH downstream to trigger secondary carbonate precipitation (Oelkers et al., 2008) (cf. section 1.2.2).

CO_2 sequestration in carbonate formations subsequently causes mineral dissolution and development of reactive flow patterns. Aspects related to precipitation and dissolution of calcium carbonate minerals are studied at multiple length scales; pore scale spatiotemporal dynamics of microbial-induced calcium carbonate precipitation (**Paper 1** and Liu et al., 2023) and dissolution of calcite minerals at pore and Darcy scale in **Paper 2** and **Paper 3** respectively.

3.1.1 Physicochemical and biological factors influencing $CaCO_3$ precipitation

Laboratory characterization of $CaCO_3$ nucleation and growth kinetics in porous media is important for GCS: to maintain injectivity the crystals deposited by microbial-induced calcium carbonate precipitation (MICP) should be small in the near wellbore area, while for mitigation of potential leakage pathways larger crystals should form in fractures and faults. The effects of hydrodynamics and supersaturation on the MICP (Liu et al., 2023) was studied at elevated pore pressures with *Sporosarcina pasteurii* stains, utilizing the micro scale experimental set-up presented in section 2.1. Physicochemical and biological

factors like system pressure, concentration of cementation reagents, and cell numbers were systematically evaluated for their influence on crystal nucleation and growth in porous media. It was found that 1) crystal size and pore-scale distribution were influenced by local supersaturation (controlled by bacterial cell numbers and variation in cementation concentration), and 2) local pore-scale hydrodynamics (controlled by local pore structure) influenced the crystal nucleation and growth both in a single pore and in the whole porous network (cf. Figure 6). Crystal nucleation and growth tended to start in the low velocity regions (Figure 15), whereas high-velocity regions like fractures and faults induced growth of large crystals. The experimental results, quantitatively corresponding with precipitation kinetic theory, may be used for model validation towards MICP implementation at larger scales.

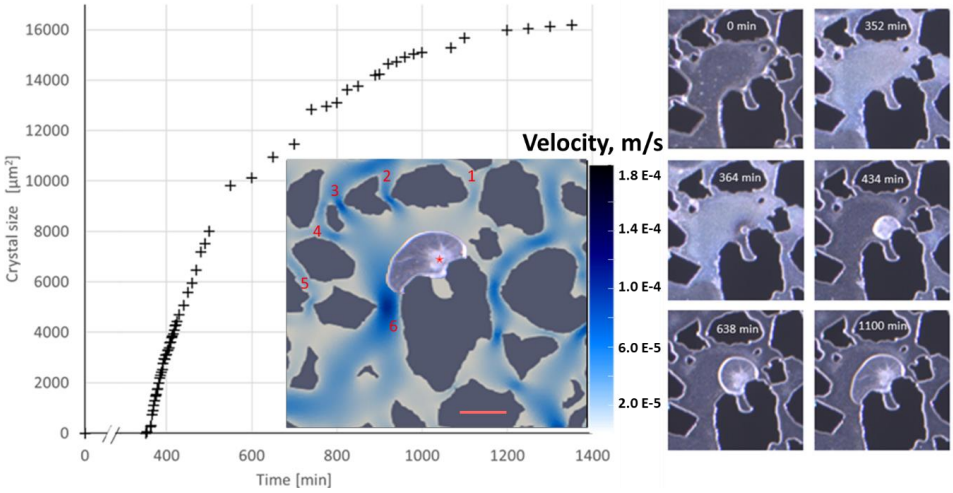

Figure 15: Plot of $CaCO_3$ crystal size over time (from high resolution time-lapse images) at 30 ˚C and 19 bar. Insert: Background colors are image of a crystal overlayed a simulated velocity field without crystals. Scale bar is 100 µm. Image series: Development of different $CaCO_3$ polymorphs; from ACC precipitates as white floc (0 min) to a spherical $CaCO_3$ crystal nucleates (364 min) and continue to grow towards nearby pores with less flow resistance (pore throat 6 in insert). Figure from Liu et al., 2023b.

3.1.2 Aqueous phase pH during $CaCO_3$ dissolution

Injected CO_2 will partially dissolve in the aqueous phase and reduce its pH, leading to geochemical reactive transport within the porous media. Dynamic reaction-induced $CaCO_3$ dissolution was observed both at the pore-scale (**Paper 2**) and at the Darcy-scale (**Paper 3**), where the aqueous phase pH decreased when mixed with CO_2 during primary drainage (pH 3.8, Eq.1 Table 1) or during co-injection (pH 4.3, Eq. 2 Table 1). At both

length scales, the acidic aqueous phase reacted with calcium carbonate crystals to initiate the dissolution process, leading to formation of bicarbonate ions and subsequent re-increase the aqueous phase pH (cf. Eq. 3 and 4, Table 1).

The pore-scale pH change was quantified using water-soluble pH sensitive fluorescence dye in the pore space prior to injection of supercritical CO_2. At Darcy scale pH was measured on the effluent production at the outlet. Time lapse imaging of pore-scale dynamics enabled quantification of the linear relationship between dissolution rate and the aqueous phase pH in the pore. An inverse relationship between aqueous phase pH and carbonate crystal size was also observed, where dissolution occurred at low pH and precipitation was associated with an elevated pH (Figure 16). The same trend was observed at Darcy scale (Figure 17), indicating that the same mechanisms were active at larger scale.

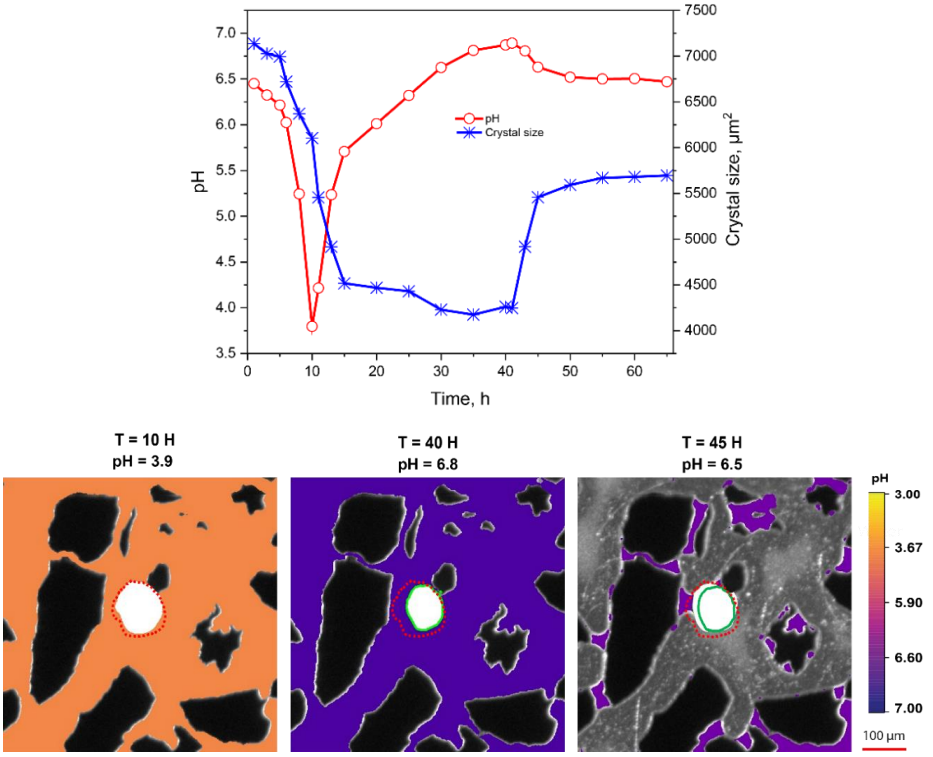

Figure 16: Carbonate dissolution and secondary precipitation during primary drainage scCO₂ injection at the pore scale. Top: The correlation between local pH and crystal size shows that the size reduction followed the aqueous phase pH towards its minimum (3.8) over the first 10 hours. The dissolution reaction consequently buffered (increased) the aqueous phase pH, reducing the carbonate dissolution rate and stabilizing the carbonate crystal size after about 40 hours. Secondary precipitation was observed (increasing crystal size) until 50 hours, coinciding with reduction of aqueous phase pH (from ~ 6.9 to 6.5). Bottom: Calibrated

fluorescence intensity images (based on Figure 8) show development in crystal size during the dissolution-precipitation processes for three pH values (initial crystal size indicated by red dotted line); at pH 3.9 (after 10 hours), at pH 6.8 (after 40 hours); and at pH 6.5 (45 hours, with crystal size from 40 hours indicated with green line). Figure from ***Paper 2****.*

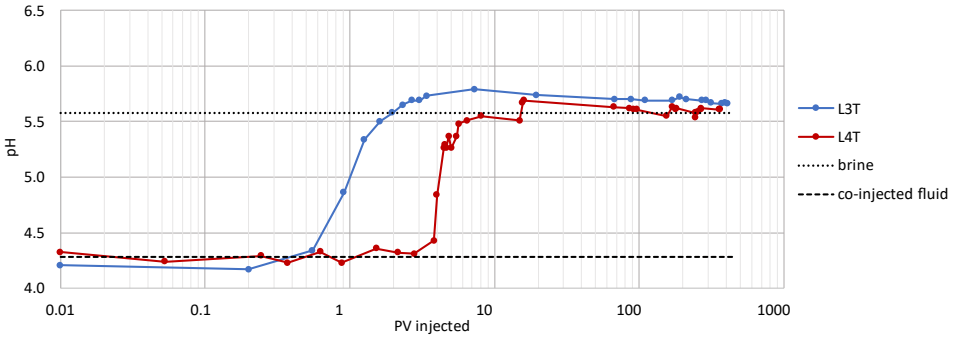

Figure 17: Development in effluent pH during co-injection of brine and CO_2 in fractured cores. Note the logarithmic scale. The open fracture cores (represented by L3T) show a pH increase before 1 pore volume (PV) injected, compared to tight fracture cores (represented by L4T) with increased pH after 3.5 PV injected. Both cores show a slight reduction in aqueous phase pH after about 10 – 20 PV injected, which could indicate secondary precipitation. This figure with additional cores (L2T and L5T) can be found in ***Paper 3****.*

3.1.3 Porosity changes by $CaCO_3$ dissolution and secondary precipitation

Mineral dissolution and precipitation influence multiphase flow during GCS by changing the morphology, porosity, and permeability of the rock. Using carbonate-functionalized micromodels, **Paper 2** investigates pore-scale dynamics of carbonate dissolution in porous media. **Paper 3** investigates dissolution dynamics at sub-core and Darcy scale using limestone core samples.

At the pore-scale the injected CO_2 reduced the pH of the aqueous phase, initializing the dissolution process (Figure 18). After 10 hours, about 12.5 % of the carbonate minerals (primarily those located close to the inlet) were dissolved, resulting in increased porosity and gas saturation. After 40 hours, secondary precipitation and mineralization enhanced the crystal saturation and subsequently reduction in gas saturation. It was further observed that the newly formed minerals were susceptible to dissolution or detachment from the pores from the flux of injected CO_2. Reduction of crystal saturation in the inlet area reduced the capillary pressure (changed pore morphology) and increased the gas saturation, while secondary carbonate precipitation and CO_2 mineralization in the outlet area increased the crystal saturation. These results were also comparable to single pore observations, detailed in **Paper 2**.

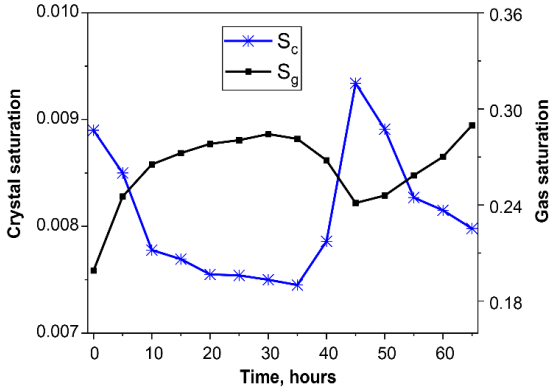

Figure 18: Changes in carbonate crystal saturation within the entire pore network during primary drainage supercritical CO_2 injection. The crystal saturation are obtained from pixel-based calculations under the assumption that each crystal pixel fill the entire height of the pore space (30 µm). Figure from ***Paper 2****.*

The spatial distribution of $CaCO_3$ crystals in the pore network could be determined using the micro-scale experimental set-up (cf. section 2.1), highlighting the dynamics of CO_2-water-mineral interactions in a porous media. It was observed that the continuous flow of CO_2 could change the distribution of crystals and thus change the porosity, permeability, and flow patterns.

Darcy scale co-injection of CO_2 and brine in whole and fractured limestone cores, utilizing the experimental set-up presented in section 2.2, revealed structural changes due to carbonate dissolution (**Paper 3**). Sub-core dissolution and secondary precipitation regimes were studied from high-resolution imaging of structure (µCT) and flow (µPET). Impedance factor is defined as the relation between absolute permeability pre- and post-dissolution. The fractured systems fell into two impedance-based categories: decreased (≤ 1.0) for cores with open fracture, and increased (> 1.0) for cores with tight fracture.

For the cores with open fracture, the impedance factor ranged from 0.3 to 1.0, implying geometric change in the pre-existing fracture plane. There were, however, some differences among these cores: The core with impedance factor of 0.3 (L1T) increased its fracture plane porosity with an averaged 13%, compared to 5.5% in the rock matrix (Figure 19, left side). Although dissolution occurred in most of the pore space, post-dissolution flow occurred exclusively in the fracture plane (Figure 20, left side). The core with impedance factor of 1.0 (L3T) also had porosity increased both in and around the fracture plane due to dissolution, but the Darcy scale permeability pre- and post-dissolution did not change: The change in porosity for the fracture area was largest in the first 3 cm of the core length, with an average of 7%, while in the middle and outlet of the

core it was averaged 5% (Figure 19, right side). However, for this core, the µPET post-dissolution quantified flow both inside and outside of the pre-existing fracture plane, hence, the anticipated reactive flow discrimination to the pre-existing fracture plane did not occur (Figure 20, right side).

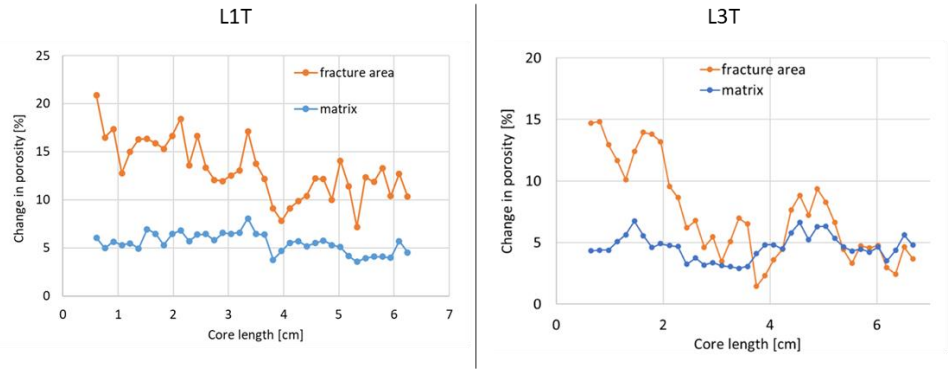

*Figure 19: Quantitative profiles of porosity change after co-injection in the open fracture cores L1T and L3T. Porosity changes by dissolution in the fracture area (orange curve) and matrix (blue curve) after co-injection, visible by µCT. Regions where the two curves differ suggest that more dissolution occurred outside of the fracture plane. Figures from **Paper 3**.*

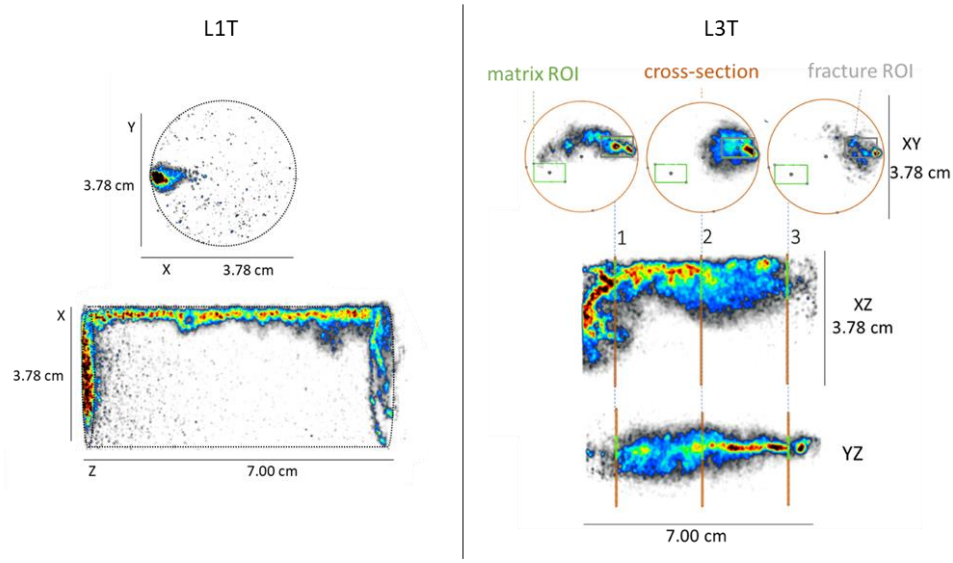

*Figure 20: µPET visualization of flow localization through limestone cores after co-injection from left to right. Both cores initially have an open fracture through the longitudinal side of the core. Warmer colors represent higher PET signal density. Figures from **Paper 3**.*

In cores with tight fractures and in the whole cores, the impedance factor increased (permeability decreased post-dissolution), indicating that reactive flow and dissolution occurred outside the fracture plane. For the core with impedance factor of 1.5 (L5T), it

was observed conical dissolution with development of small wormholes across the cross-sectional area, showing that the reactive flow was not restricted to the fracture plane (Figure 21).

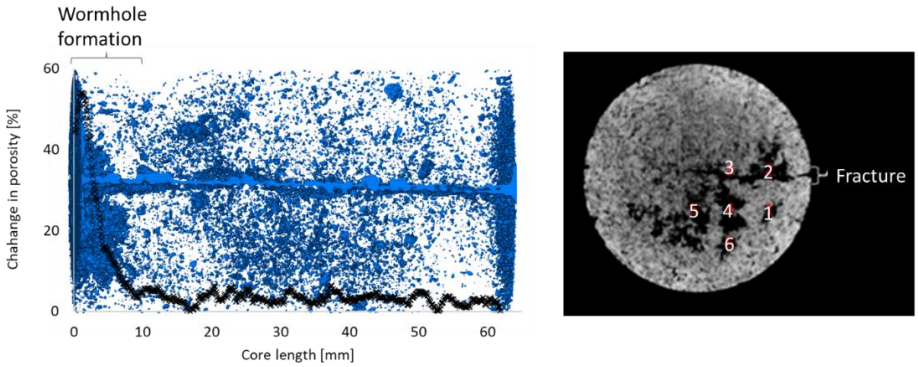

Figure 21: Post-dissolution changes in rock structure in the fractured core L5T. Left: A 3D rendering of µCT images shows global dissolution (void > 50 µm, blue), but mainly at inlet (left side) and outlet (right side). Compact-conical dissolution and formation of multiple wormholes was observed at the inlet. A porosity profile with difference between pre- and post-dissolution is shown in black, overlaying the 3D image of the core porosity: up to 60% change was observed in the first 10 mm of the core, with minor changes (about 5%) in the remaining core. Right: 2D µCT image (XY-plane) 1.5 mm from the inlet (where conical dissolution was not dominant) showing the fracture plane and six wormholes: Smaller wormholes (1, 3-6) formed outside of the fracture plane, while the most prominent wormhole (2) extended 13.5 mm (20% of the core length) in proximity to the fracture. Further details in ***Paper 3.***

Whole limestone cores mimicked the behaviour of tight fractured cores, with increasing impedance factor after co-injection, and generally demonstrated a nonuniform porosity distribution with local areas of low porosity (relative to the surrounding rock matrix). The low-porosity area aligned with reduced water flow in core L4 (Figure 22), and the high-porosity area coincided with a preferential flow path of radioactive water (higher PET signal). Cementation was not observed in any of the cores prior to co-injection, and quantitative analysis suggest that the core was partially clogged by calcite particles from dissolution downstream, or it could be re-precipitation of calcium carbonate as observed in **Paper 2**.

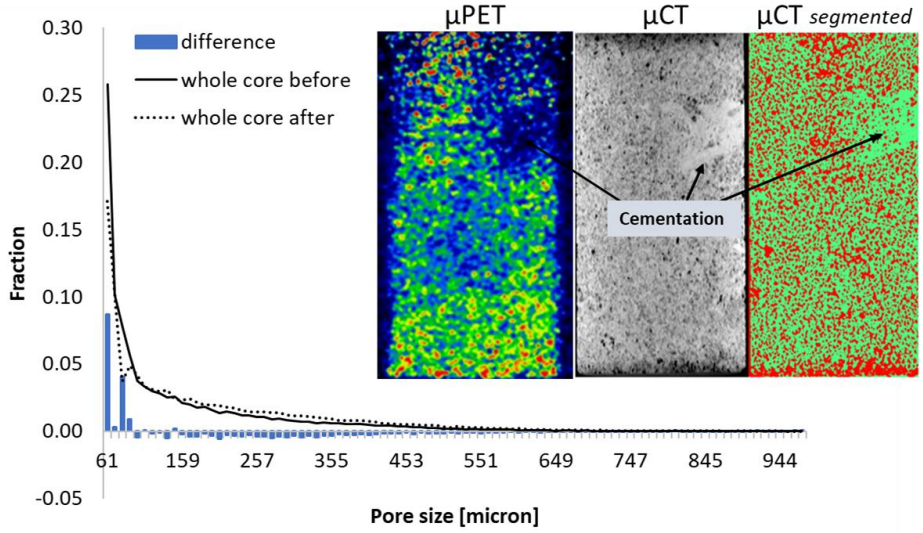

*Figure 22: Plot: Quantitative comparison of the pore size distribution before (core L2) and after co-injection (core L4). The difference between pore sizes before and after co-injection shows reduction in number of small pores and increase in number of medium and larger pores (negative difference values), meaning that dissolution and precipitation processes may have increased the size of some pores while clogging smaller pores by fines during transport or re-precipitation of calcium carbonate minerals. Inset: Multi-modal imaging of water distribution (µPET) and rock structure (µCT) in the XZ plane (core L4). From both modalities it can be observed a low-porosity region in the matrix, represented by low water content (dark blue) region in the 'µPET' image, and high-density (bright) region in the 'µCT' image. For the 'segmented µCT' image, the pore sizes were below image resolution (red pores and green matrix). The water saturation was generally higher (warmer colors) in the inlet region (bottom part of image) compared with the outlet region, attributed to Darcy-scale dissolution heterogeneity. Figure from **Paper 3**.*

3.2 Flow dynamics during CO_2 sequestration

The focus of minerals and sub-Darcy scale calcium carbonate dissolution for **Papers 1-3** now shifts to multiphase flow and GCS displacement processes for **Papers 4-6**. Dynamic Darcy scale multiphase flow is quantified in **Paper 4**, while meter scale CO_2 migration patterns and GCS storage mechanisms are studied in **Paper 5 and 6**.

3.2.1 Flow propagation and CO_2 storage potential at Darcy scale

Unsteady state water injection (imbibition) and CO_2 gas injection (drainage) were performed at elevated pressure conditions, visualized with µPET (cf. section 2.2). Short-lived radioisotopes were used to label brine (^{18}F) and CO_2 (^{11}C) to explicitly track each

phase during single phase injection (Figure 23). Displacement heterogeneities and local permeability variations were observed from *in situ* imaging and dynamic spatially resolved fluid saturations (Figure 23, top). During injection of gaseous CO_2 (Figure 23, middle), radial permeability variations was observed to influence the brine-CO_2 displacement; CO_2 predominantly displaced brine from the higher-permeability outer parts of the core. An initial storage capacity of 66% (of the pore volume) after primary drainage was quantified through sub-core analysis, and secondary imbibition promoted capillary trapping of CO_2, and is proposed to be the most effective method to ensure security during CO_2 storage (Qi et al., 2009). Access to local and dynamic fluid saturations showed that the presence of CO_2 restricted brine flow in higher-permeability areas (Figure 23, bottom), improving sweep efficiency and promoting a nearly ideal Darcy scale displacement. Residually trapped CO_2 was evenly distributed in the pore space, occupying 40% of the pore volume.

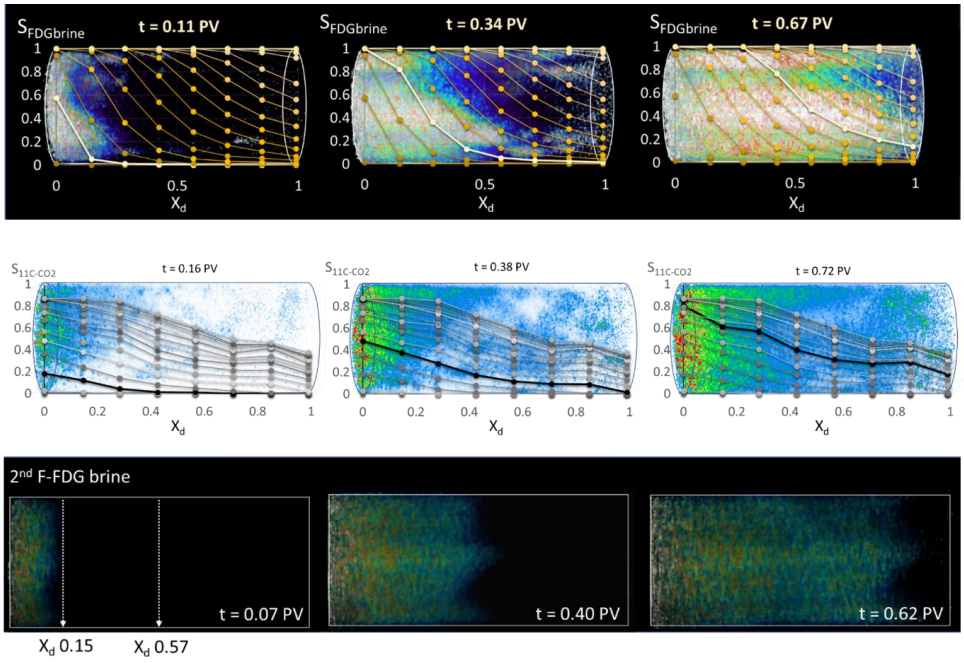

Figure 23: Dynamic saturation development during single phase injection of radioactive labeled fluids through a cylindrical chalk core sample. Injection from left to right. Top row is miscible brine displacement by ^{18}F-FGD labelled brine, revealing displacement heterogeneities from the non-uniform fluid front, middle row is injection of gaseous CO_2 labeled with the radioisotope ^{11}C, with breakthrough after 0.5 PV injected, and bottom is secondary brine injection with ^{18}F-FDG labeled brine, revealing a nearly ideal core-scale displacement. Top and middle row are qualitative 3D PET images of the core saturation overlaid by quantitative 1D profiles derived from the PET signal. Warmer colors represent stronger PET signal. Figures from ***Paper 4****.*

Imaging of dynamic CO_2 flow improves determination of basic flow parameters and saturation functions, which are essential input to numerical simulations of CO_2 migration during GCS. The results indicate positive aspects related to GCS; the secondary imbibition process distributed CO_2 evenly in the pore space and increased utilization of the storage capacity, and the residually trapped CO_2 will over time dissolve in the aqueous phase and loose buoyancy due to increasing density (cf. section 3.2.2).

3.2.2 CO_2 migration patterns at meter scale

One of the benefits with the FluidFlower rigs (cf. section 2.3) is the ability to observe GCS trapping mechanisms and flow (e.g., convective mixing) that cannot be studied at smaller length scales. The meter scale experiments also enabled increased degree of complexity within the same geometry. Another key feature of the FluidFlower rigs is the ability to establish a physical *ground truth* for simulation studies by performing repeated experiments with operationally identical CO_2 injection and initial conditions in the same geological geometry (without having to re-build the geometry).

The 10 CO_2 injection experiments in a table-top FluidFlower rig all followed a similar migration pattern, described below with reference to Figure 24 (details in **Paper 5**): The gaseous CO_2 injected in the lower port (I1) quickly dissolved in the formation water and changed the colour of the pH-indicator, making it possible to generate the contours using image processing with DarSIA (cf. section 2.3). When the injection continued, the gaseous CO_2 migrated upwards until reaching the *Lower seal* above, accumulating in the anticlinal trap (contour 1 – light blue). Gravitational fingers developed under the gas accumulation when CO_2 injection in port 1 stopped (contour 2 – dark blue).

Migration from the second CO_2 injection port (I2) was initially characterized with a gas accumulation in a small anticlinal trap (contour 3-light green). When the gas reached the spill point, buoyancy forces caused the gas to continue through the *Upper E* layer and upwards until it reached the *Top Regional seal* (contour 4-dark green). Gas migrated stepwise upwards under the sealing unit and sequentially filled the upper anticlinal trap. Meanwhile, the gravitational fingers below the lower gas accumulation grew (contour 2-5); after the second injection ceased (contour 5-pink) fingers developed below the *Top Regional seal* (contour 6-red). The fingers moved laterally when reaching the Upper C layer, before some continued into the *Middle F* layer below.

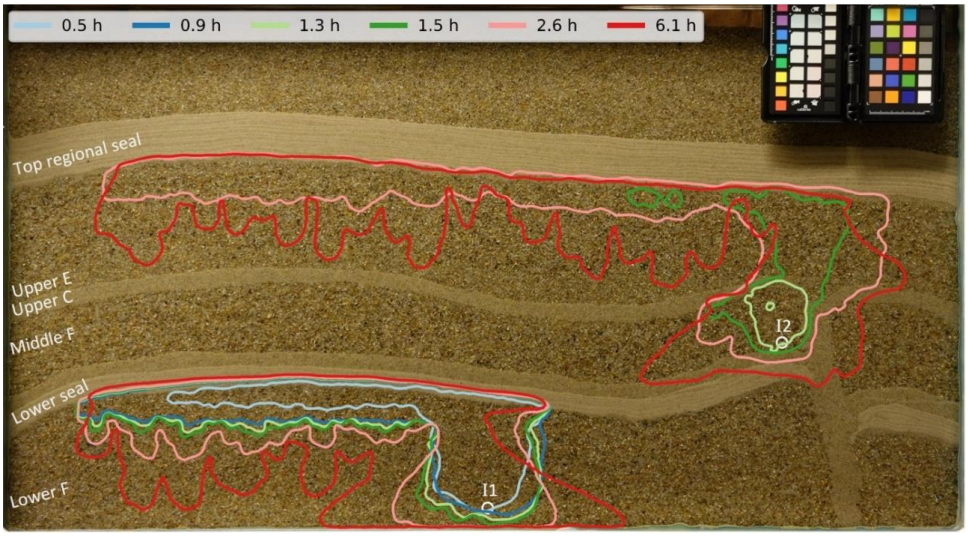

*Figure 24: Development of CO_2 migration pattern in one of the table-top FluidFlower geometries (Albus) during experiment AC10, representing the general pattern observed for all 10 experiments in this geometry. The colored contours represent the distribution of gaseous and aqueous CO_2 at various times: with 0.9 hours representing end of first injection (I1), and 2.6 hours representing end of second injection (I2). Figure from **Paper 5**.*

Repeatability between CO_2 injection experiments was investigated based on the hypothesis that increased reservoir complexity tends to reduce the degree of physical reproducibility. For five operationally identical CO_2 injections (labelled C1 to C5) were performed, where two cycles (C1 and C5) had known inconsistencies (detailed in **Paper 6**) and not included in the discussion of repeatability below C1.

The constructed geological geometry may be divided into three boxes (A, B' and D) with increasing degree of complexity (Figure 25, detailed in **Paper 6**). Development in physical overlap in Box A were divided into four intervals:

i. *Pre-spilling interval:* from injection start until the gas column height exceeded the anticlinal spill-point (< 4 hours), with increasing overlap until maximum of 97%.
ii. *Gravitational fingers interval:* 4-30 hours, characterized by development of pronounced gravitational fingers from the gas accumulation in the anticlinal trap and convective mixing. Overlap reduced to 79 %, dominated by difference in number of fingers and individual finger dynamic.
iii. *Dissolution-driven flow interval:* 30-70 hours, until the gravitational fingers reached the no-flow boundary below, causing the fingers to move lateral and

merge as the gas accumulation dissolved and hence pulled aqueous phase into Box A from the surrounding regions. Overlap increased to > 95%.

iv. *Homogenization interval:* from 70-120 hours, with only minor movement of the aqueous phases confined in Box A. Characterized by a constant overlap of > 95%.

The observations above show that the homogeneous region (Box A) overall had a very good reproducibility between cycles C2, C3 and C4. Box B' includes the heterogeneous fault, and generally follows the same overall trend, including the four intervals described above. One major difference between the cycles was, however, the gravitational fingers interval; variation in spill times resulted in initially reduced overlap with slight variation in fault migration and displacement patterns. In Box D, the development was delayed compared to Box A and Box B' due to the later CO_2 injection start-up in the upper injection port. but follow the same overall trend; initially increasing overlap, then slight reduction due to development of fingers and convective mixing, before increasing overlap through homogenization.

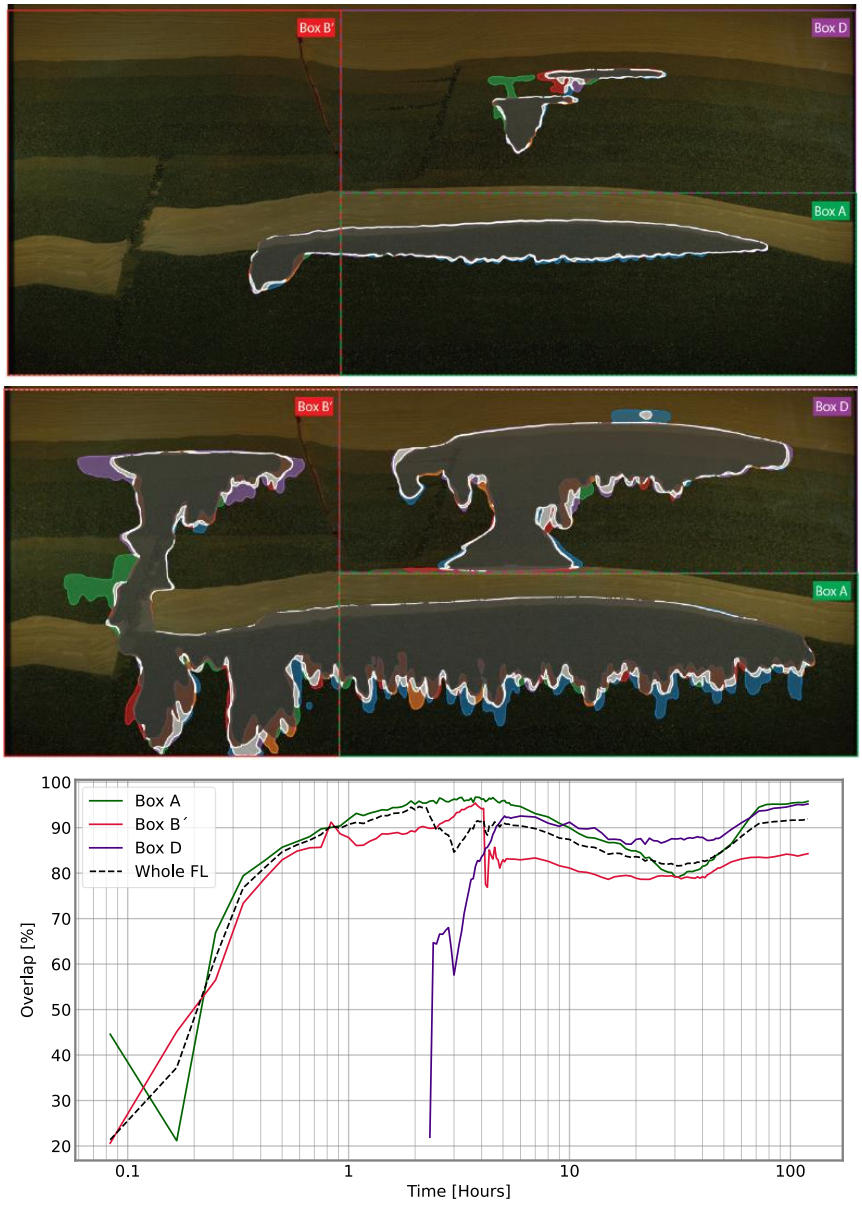

Figure 25: Top and middle show snapshots of CO_2 injection in five identical experiments (C1-C5), showing the degree of physical overlap and location of Box A, Box B' and Box D with increasing geological complexity. Spatially distributed overlaps are overlayed the geological geometry which is initially filled with water including pH-sensitive dye. The color scheme is as follows: blue, orange, green, red, purple is unique C1, C2, C3, C4 or C5 respectively, grey is overlap of C2+C3+C4; brown is combination of all runs with at least one of C2, C3 or C4, and white is other combinations Top image is from the 'pre-spilling interval' before CO_2 reached the anticlinal spill-point (at 3.8 hours), middle image is from the 'gravitational-fingers interval' (at 14 hours), and bottom show degree of overlap for run C2, C3 and C4 in Box A (green line), Box B' (red line), Box D (purple line) and in the whole geometry (dashed line). Figure from ***Paper 6****.*

3.2.3 Impact of local flow variations in porous media

The impact of local hydrodynamic span across all studied length scales, and its importance have been seen in various processes. To illustrate the variety in impact and importance of local flow, a few examples are given below.

Pore scale study (**Paper 2**) of three different aqueous solutions showed that local dissolution rate of calcium carbonate minerals increased linearly with flow velocity (cf. Figure 6, lower right corner). In addition to the aqueous phase pH and flow velocity, the presence of free CO_2 phase (either injected or exsolved from dissolution) also influenced the local dissolution rate by effectively shielding the engulfed crystals (Figure 26). This means that the stability of crystals improves over time if engulfed by CO_2, which inhibit dissolution and thus is positive for the usage of MICP as a mitigation technology for CO_2 leakage during GCS or CO_2 storage in carbonate formations.

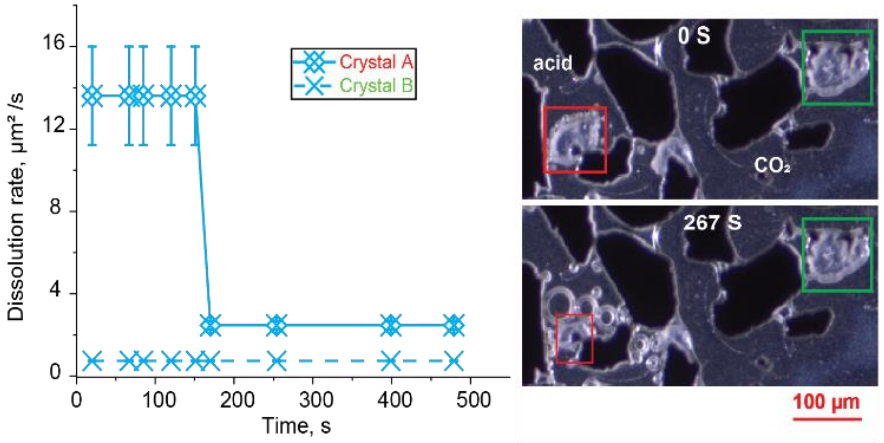

*Figure 26: Left: Plot of calcium carbonate crystal dissolution with (crystal B) and without (crystal A) shielding from CO_2 gas Right: Time series images of CO_2 exsolution from the crystal surface which developed shielding and hence reduction in dissolution rate for crystal A. The presence of a free CO_2 phase reduced the reactive surface area and hinders mass transport at the solid-liquid interface. Figure from **Paper 2**.*

Darcy scale flow variations in porous media have been investigated using both core-samples and performing a zoom-in of FluidFlower experimental results. Tracing fluids through outcrop cores using µPET visualized and quantified how different fracture properties changed the local flow and its impact on the reactive flow processes (**Paper 3**). Two-phase injection in cores with open fractures led to increased injectivity from dissolution in or around the fracture plane, while the injectivity decreased in cores with tight fractures (hence, the reactive flow was not limited to the fracture plane, and

development of conical dissolutions and wormholes were observed). Decreased injectivity was also observed in whole cores, where matrix cementation was identified by µCT and confirmed to affect fluid flow by µPET (cf. section 3.1.3).

Meter scale study of CO_2 injection in faulted geometries showed how Darcy scale faults impacted local flow and migration of CO_2 from micrometer to meter: At the pore scale it was observed differences in capillary entry pressure for CO_2 gas into the overlayed sand layer, that varied with how the sand was deposited. Vertical deposited sand in a fault resulted in higher capillary entry pressure compared to horizontally deposited layers (**Paper 5**). At the meter scale, different fault heterogeneities impacted the larger scale CO_2 migration, and unexpected oscillating CO_2 spilling event occurred from an anticline for all 5 repeated experiments, c1-c5 in Figure 27. Pulsation behaviour of buoyant gas accumulation have been observed in the literature (details in **Paper 6**), and the impact from the observed phenomenon here need a systematic evaluation before it can be generalized. However, it illustrates the importance of local flow at scales from micrometer to meter.

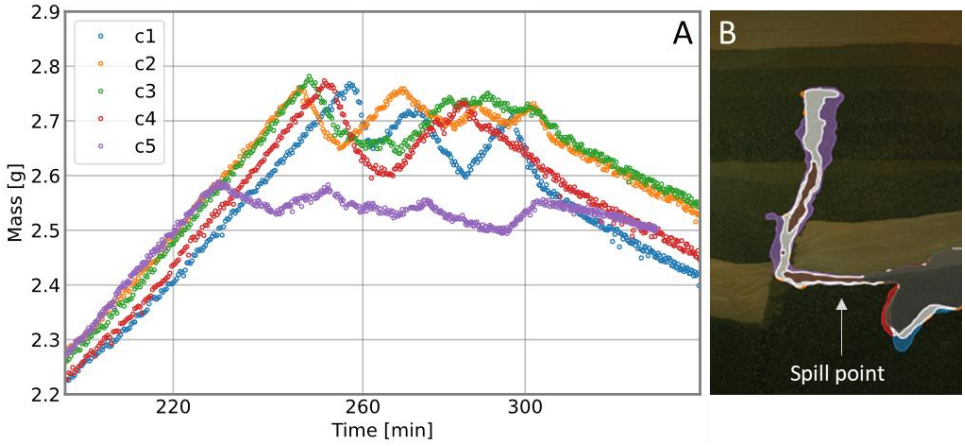

Figure 27: Oscillating CO_2 leakage from an anticline spill point into a heterogeneous fault. The mobile gas trapped under an anticline (to the right of image B) spilled and flowed into the bottom of the fault. When the gas migrated upwards in the high permeable fault zone it displaced the resident aqueous phase downwards. The inflow of the aqueous phase ultimately blocked the upwards migration of gas because the localized pathway at the inlet of the fault could not accommodate the combination of upwards gas flow and downwards water flow. Then the migration of gas was hindered, the anticline gas column again increased due to the continuous CO_2 injection. The process repeated itself (figure A) until CO_2 injection ceased (after about 300 min), seen as decreasing mass of mobile gas as the gas column height was reduced due to dissolution. Figures from **Paper 6**.

4. Conclusions and Future Perspectives

This thesis enlightens multiscale laboratory methods and investigations on multiphase flow and physicochemical interactions during geological carbon sequestration. The main findings from the scientific contributions are repeated below in addition to future research perspectives.

4.1 Conclusions

Laboratory methods spanning length scales over six orders of magnitude have been improved or developed, and link experimental protocols between micro scale, Darcy scale and meter scale. These protocols enable quantitative investigations of temporal pore scale processes, multiphase flow dynamics and porous media mixing processes using optical imaging and PET.

Understanding multiscale reactive transport in the context of CO_2 sequestration is essential for accurate modelling of subsurface fluid flow to enable long term safe storage. **Paper 1** - **3** focus on minerals and sub-Darcy scale calcium carbonate dissolution, with main conclusions listed below:

- Study of microbial-induced calcium carbonate growth and distribution at the pore scale identified that hydrodynamics and supersaturation determine crystal nucleation and growth in porous systems.
- Dissolution of calcium carbonate caused buffering of the aqueous phase which consequently slowed down the dissolution rate before eventually re-precipitation of minerals were observed at elevated pH.
- Local flow of CO_2 influence the pore-scale distribution of calcium carbonate crystals, and, hence, determine changes in the porosity, permeability, and flow pattern.
- At the Darcy scale, after co-injection of CO_2 and brine, it was observed increased injectivity in cores with pre-existing open fractures (with dissolution in or around the fracture plane confirmed with *in-situ* imaging), and decreasing injectivity in cores with pre-existing tight fractures (with dissolution across the core cross-section confirmed by *in-situ* imaging). Decreased injectivity was also observed for whole cores, with identified cementation in the matrix as a proposed mechanism for injectivity reduction.

Multiphase flow dynamics during CO_2 sequestration was the focus of **Paper 4 – 6**, with main conclusions listed below:

- Access to local and dynamic fluid saturation from µPET visualization showed evenly distributed residual trapping of CO_2, occupying 40% of the pore volume, after secondary imbibition followed CO_2 gas injection.
- When increasing the laboratory scale from Darcy to meter scale (with FluidFlower flow cells) it enables study of CO_2 trapping mechanisms and flow otherwise not possible, like convective mixing and development of gravitational fingers as the density of CO_2 saturated water is higher than the initial aqueous phase.
- 10 repeated CO_2 injection experiments in a table-top FluidFlower rig all followed a similar migration pattern with both residual, structural and solubility trapping of CO_2 in a geologic geometry mimicking GCS related features.
- Study of repeatability between CO_2 injection experiments in the room-scale FluidFlower confirmed the hypothesis that increased reservoir complexity tends to reduce the degree of physical reproducibility. This complexity could be related to increasing degree of complexity in fault properties, which have a large impact on multiphase flow in the reservoir,
- The experimental results show that impact of local hydrodynamics span across all the studied porous media length scales. Illustrating the importance of having laboratory set-up to study and quantify multiphase flow mechanisms at a wide range of scales to be utilized in simulations of CO_2 migration during GCS.

4.2 Future Perspective

In addition to the scientific contributions included in this thesis, the developed methods have already been actively used within research in a wide range of applications in the Reservoir Physics research group at the University of Bergen, for pore scale both related to hydrogen storage (Lysyy et al., 2022) and CO_2 foam for mobility control (Benali et al., 2022). At the pore scale a further investigation on the influence of surface properties on dissolution rate of calcium carbonate crystals should be conducted. The current analysis focuses on hydrophilic carbonate crystals, but it should be investigated how a mixed wet surface would influence the dissolution rate. The obtained knowledge and MICP methodology could be transferred to Darcy scale utilizing the experimental set-up in section 2.3.

For the meter scale application (FluidFlower) a wide range of projects are performed or in planning, including seal integrity, changed formation water chemistry and salinity, and MICP applications. The high-resolution images acquired from the FluidFlower experimental set-up where detection of grains (and thus pores) is possible, make it a viable method to implement features which have been studied on e.g., micro-scale, into a larger scale. In addition is the 11th Society of Petroleum Engineers Comparative Solution Project (11th SPE CSP) based on the recent forecasting and validation study (Flemisch et al., 2023), where **Paper 6** details the experimental results that the simulations are compared to. The CSP project (Nordbotten et al., 2023b) is motivated by the simulation challenges associated with CO_2 storage operations in geological settings, developing simulations of realistic complexity. Performing "live" CO_2 injection experiments at exhibitions and public events have demonstrated the unique possibility for enhancing public understanding and acceptance about CO_2 storage, trapping mechanisms and security.

5. Abbreviations

CCUS	Carbon, Capture, Utilization and Storage
GCS	Geologic Carbon Storage
µCT	micro-Computerized Tomography
µPET	micro-Positron Emission Tomography
PET	Positron Emission Tomography
IEA	International Energy Agency
SDG	Sustainable Development Goals
ACC	Amorphous Calcium Carbonate
pH	potential of Hydrogen
FL	Fluorescence
CL	Cold Light
DI	Deionized Water
PV	Pore Volume
BPR	Back Pressure Regulator
MFC	Mas Flow Controller
DarSIA	Darcy Scale Image Analysis
SPE	Society of Petroleum Engineers
CSP	Comparative Solution Project

6. Nomenclature

CO_2	carbon dioxide
$CaCO_3$	calcium carbonate
H_2CO_3	carbonic acid
H^+	hydrogen ion
OH^-	hydroxide ion
NH_4^+	ammonium ion
CO_3^{2-}	carbonate ion
HCO_3^-	bicarbonate ion
Ca^{2+}	calcium ion
Mg^{2+}	magnesium ion
Fe^{2+}	iron ion
$MgCO_3$	magnesite
$FeCO_3$	siderite
H_2O	water
$CO(NH_2)_2$	urea
˚C	degrees Celsius
^{18}F-FDG	18F-Fluorodeoxyglucose, glucose analog and radiopharmaceutical (water soluble)
^{11}C	Radioactive isotope of carbon (used to trace gaseous CO_2)
$t_{1/2}$	half-life, the time it takes to decrease the original level of radioactivity by 50%

7. References

Citation of additional scientific contributions (page 9-10) are written in blue.

Baines, S., & Worden, R. (2004). The long-term fate of CO2 in the subsurface: Natural analogues for CO2 storage. *Geological Society of London Special Publications, 233*, 59-85. https://doi.org/10.1144/GSL.SP.2004.233.01.06

Bastesen, E., & Rotevatn, A. (2012). Evolution and structural style of relay zones in layered limestone–shale sequences: insights from the Hammam Faraun Fault Block, Suez rift, Egypt. *Journal of the Geological Society, 169*(4), 477-488. https://doi.org/10.1144/0016-76492011-100

Bear, J. (1972). *Dynamics of Fluids in Porous Media*: American Elsevier Publishing Company. ISBN: 9780444001146

Benali, B., Føyen, T. L., Alcorn, Z. P., Haugen, M., Gauteplass, J., Kovscek, A. R., & Fernø, M. A. (2022). Pore-scale bubble population dynamics of CO2-foam at reservoir pressure. *International Journal of Greenhouse Gas Control, 114*. https://doi.org/10.1016/j.ijggc.2022.103607

Benson, S. M., & Cole, D. R. (2008). CO2 Sequestration in Deep Sedimentary Formations. *Elements, 4*(5), 325-331. https://doi.org/10.2113/gselements.4.5.325

Both J.W., Benali B., Folkvord O., Haugen M., Storvik E., Fernø M.A., Nordbotten J.M. (2023a). Image Analysis of the International FluidFlower Benchmark Study Dataset (v1.0). Zenodo. https://doi.org/10.5281/zenodo.7515038

Both, J.W., Storvik, E., Nordbotten, J.M., Benali, B. (2023b). DarSIA v1.0 (Version v1.0). Zenodo. https://doi.org/10.5281/zenodo.7515016

Brattekås, B., Gauteplass, J., Brekke, N., Fernø, M. A., & Ersland, G. (2020). Unlocking multimodal PET-MR synergies for geoscience. *Advances in Water Resources*, 142. https://doi.org/10.1016/j.advwatres.2020.103641

Brattekås B., Fernø M.A., Haugen M., Føyen T.L., Steinsbø M., Graue A., Brekke N., Adamsen T.C.H., Rygh C.B, Espedal H. (2023). Of Rats and Rocks: using pre-clinical PET imaging facilities in core analysis. Presented at the 2021 International Symposium of the Society of Core Analysts (peer-reviewed). E3S Web of Conferences, 366. https://doi.org/10.1051/e3sconf/202336601011

Celia, M. A., Bachu, S., Nordbotten, J. M., Gasda, S. E., & Dahle, H. K. (2005). - Quantitative estimation of CO2 leakage from geological storage: Analytical models, numerical models, and data needs. *Greenhouse Gas Control Technologies 7* (pp. 663-671). Oxford: Elsevier Science Ltd. https://doi.org/10.1016/B978-008044704-9/50067-7

Chang, C., Zhou, Q., Oostrom, M., Kneafsey, T., & Mehta, H. (2017). Pore-scale Supercritical CO2 Dissolution and Mass Transfer under Drainage Conditions. *Advances in Water Resources, 100*, 67–81. https://doi.org/10.1016/j.advwatres.2016.12.003

COP21. (2015). The Paris Agreement adopted at the UN Climate Change Conference in Paris. Accessible at: https://unfccc.int/process-and-meetings/the-paris-agreement/the-paris-agreement

Datta, S. S., Battiato, I., Fernø, M. A., Juanes, R., Parsa, S., Prigiobbe, V., Santanach-Carreras, E., Song, W., Biswal, S.L., Sinton, D. (2023). Lab on a chip for a low-carbon future. *Lab on a Chip, 23*(5), 1358-1375. https://doi.org/10.1039/D2LC00020B

De Muynck, W., De Belie, N., & Verstraete, W. (2010). Microbial carbonate precipitation in construction materials: A review. *Ecological Engineering, 36*(2), 118-136. https://doi.org/10.1016/j.ecoleng.2009.02.006

Ebadi, M., Armstrong, R. T., Mostaghimi, P., Wang, Y. D., Alqahtani, N., Amirian, T., ... Koroteev, D. (2022). Predictive Soft Computing Methods for Building Digital Rock Models Verified by Positron Emission Tomography Experiments. *Water Resources Research*, 58(11). https://doi.org/10.1029/2021WR031814

Eikehaug K., Haugen M., Folkvord O., Benali B., Bang Larsen E., Tinkova A., Rotevatn A., Nordbotten J.M., Fernø, M.A. (2024). Engineering meter-scale porous media flow experiments for quantitative studies of geological carbon sequestration, *Transp. Porous Med*. https://doi.org/10.1007/s11242-023-02025-0

Eiken, O., Ringrose, P., Hermanrud, C., Nazarian, B., Torp, T. A., & Høier, L. (2011). Lessons learned from 14 years of CCS operations: Sleipner, In Salah and Snøhvit. *Energy Procedia, 4*, 5541-5548. https://doi.org/10.1016/j.egypro.2011.02.541

Ellis, B. R., Crandell, L. E., & Peters, C. A. (2010). Limitations for brine acidification due to SO2 co-injection in geologic carbon sequestration. *International Journal of Greenhouse Gas Control, 4*(3), 575-582. https://doi.org/10.1016/j.ijggc.2009.11.006

Fernø, M. A., Hauge, L. P., Uno Rognmo, A., Gauteplass, J., & Graue, A. (2015a). Flow visualization of CO2 in tight shale formations at reservoir conditions. *Geophysical Research Letters, 42*(18), 7414-7419. https://doi.org/10.1002/2015GL065100

Fernø, M. A., Gauteplass, J., Hauge, L. P., Abell, G. E., Adamsen, T. C. H., & Graue, A. (2015b). Combined positron emission tomography and computed tomography to visualize and quantify fluid flow in sedimentary rocks. *Water Resources Research*, 51(9), 7811-7819. https://doi.org/10.1002/2015WR017130

Flemisch, B., Nordbotten, J. M., Fernø, M.A, Juanes, R., Both, J. W., Class, H., . . . Zhang, Z. (2023). The FluidFlower Validation Benchmark Study for the Storage of CO_2. *Transport in porous media*. https://doi.org/10.1007/s11242-023-01977-7

Fujita, Y., Taylor, J. L., Wendt, L. M., Reed, D. W., & Smith, R. W. (2010). Evaluating the Potential of Native Ureolytic Microbes To Remediate a 90Sr Contaminated Environment. *Environmental Science & Technology, 44*(19), 7652-7658. https://doi.org/10.1021/es101752p

Gaus, I. (2010). Role and impact of CO2–rock interactions during CO2 storage in sedimentary rocks. *International Journal of Greenhouse Gas Control, 4*(1), 73-89. https://doi.org/10.1016/j.ijggc.2009.09.015

Haugen, M., Brattekås, B., & Fernø, M.A (2023c). Multimodal Visualization of Calcium Carbonate ($CaCO_3$) in the Pore Space of a Micromodel. In E. F. Médici & A. D. Otero (Eds.), *Album of Porous Media: Structure and Dynamics* (pp. 95-95). Cham: Springer International Publishing. https://doi.org/10.1007/978-3-031-23800-0_77

IEA. (2020). *The role of CCUS in low-carbon power systems*. IEA, Paris, License: CC BY 4.0. Accessible at: https://www.iea.org/reports/the-role-of-ccus-in-low-carbon-power-systems

IEA. (2021). *Net Zero by 2050*. IEA, Paris, License: CC BY 4.0. Accessible at: https://www.iea.org/reports/net-zero-by-2050

IEA. (2023). *Tracking Clean Energy Progress 2023*. IEA, Paris, License: CC BY 4.0. Accessible at: https://www.iea.org/reports/tracking-clean-energy-progress-2023

IPCC. (2005). *Special Report on Carbon Dioxide Capture and Storage, Chapter 5: Underground geological storage, p. 195-276*. Accessible at: https://www.ipcc.ch/report/carbon-dioxide-capture-and-storage/

Jacobson, O., & Chen, X., (2010) PET Designated Flouride-18 Production and Chemistry, *Current Topics in Medicinal Chemistry, 1*0 (11). https://dx.doi.org/10.2174/156802610791384298

Kazemifar, F., Blois, G., Kyritsis, D., & Christensen, K. (2015). Quantifying the flow dynamics of supercritical CO2–water displacement in a 2D porous micromodel using fluorescent microscopy and microscopic PIV. *Advances in Water Resources*. https://doi.org/10.1016/j.advwatres.2015.05.011

Kharaka, Y. K., Cole, D. R., Hovorka, S. D., Gunter, W. D., Knauss, K. G., & Freifeld, B. M. (2006). Gas-water-rock interactions in Frio Formation following CO2 injection: Implications for the storage of greenhouse gases in sedimentary basins. *Geology, 34*(7), 577-580. https://doi.org/10.1130/g22357.1

Krajewska, B. (2018). Urease-aided calcium carbonate mineralization for engineering applications: A review. *Journal of Advanced Research, 13*, 59-67. https://doi.org/10.1016/j.jare.2017.10.009

Krevor, S., de Coninck, H., Gasda, S. E., Ghaleigh, N. S., de Gooyert, V., Hajibeygi, H., . . . Swennenhuis, F. (2023). Subsurface carbon dioxide and hydrogen storage for a sustainable energy future. *Nature Reviews Earth & Environment, 4*(2), 102-118. https://doi.org/10.1038/s43017-022-00376-8

Liu N., Haugen M., Benali B., Landa-Marbán D., and Fernø M.A. (2023b). Pore-scale spatiotemporal dynamics of microbial-induced calcium carbonate growth and distribution in porous media. *International Journal of Greenhouse Gas Control*, 125. https://doi.org/10.1016/j.ijggc.2023.103885

Lu, P., Fu, Q., Seyfried, W. E., Hedges, S. W., Soong, Y., Jones, K., & Zhu, C. (2013). Coupled alkali feldspar dissolution and secondary mineral precipitation in batch systems – 2: New experiments with supercritical CO2 and implications for carbon sequestration. *Applied Geochemistry, 30*, 75-90. https://doi.org/10.1016/j.apgeochem.2012.04.005

Lysyy, M., Ersland, G., & Fernø, M.A (2022). Pore-scale dynamics for underground porous media hydrogen storage. *Advances in Water Resources, 163*, 104167. https://doi.org/10.1016/j.advwatres.2022.104167

Mitchell, A. C., Dideriksen, K., Spangler, L. H., Cunningham, A. B., & Gerlach, R. (2010). Microbially Enhanced Carbon Capture and Storage by Mineral-Trapping and Solubility-Trapping. *Environmental Science & Technology, 44*(13), 5270-5276. https://doi.org/10.1021/es903270w

Morais, S., Liu, N., Diouf, A., Bernard, D., Lecoutre, C., Garrabos, Y., & Marre, S. (2016). Monitoring CO2 invasion processes at the pore scale using Geological Labs on Chip. *Lab Chip, 16*. https://doi.org/10.1039/C6LC00830E

Mullin, J. W. (2001). *Crystallization* (4th ed. ed.). Oxford: Butterworth-Heinemann. https://doi.org/10.1016/B978-0-7506-4833-2.X5000-1

Nixon, C. W., Nærland, K., Rotevatn, A., Dimmen, V., Sanderson, D. J., & Kristensen, T. B. (2020). Connectivity and network development of carbonate-hosted fault damage zones from western Malta. *Journal of Structural Geology, 141*, 104212. https://doi.org/10.1016/j.jsg.2020.104212

Nordbotten, J. M, Benali, B., Both, J., Brattekas, B., Storvik, E., & Fernø, M. A (2023). DarSIA: An Open-Source Python Toolbox for Two-Scale Image Processing of Dynamics in Porous Media. *Transp Porous Med.* https://doi.org/10.1007/s11242-023-02000-9

Nordbotten, J. M., & Celia, M. A. (2011). Geological Storage of CO2: Modeling Approaches for Large-Scale Simulation. John Wiley and Sons Ltd. ISBN: 9780470889466.

Nordbotten, J. M., Fernø, M. A., Flemisch, B., Kovscek, A. R., and Lie, K-A. (2023b) The 11th Society of Petroleum Engineers Comparative Solution Project: Problem Definition. *SPE J*. (In Press)

Northern Lights JV DA. (2023) About the Longship project. Accessible at: https://norlights.com/about-the-longship-project/

Oelkers, E. H., Gislason, S. R., & Matter, J. (2008). Mineral Carbonation of CO2. *Elements, 4*(5), 333-337. https://doi.org/10.2113/gselements.4.5.333

Ogata, K., Senger, K., Braathen, A., & Tveranger, J. (2014). Fracture corridors as seal-bypass systems in siliciclastic reservoir-cap rock successions: Field-based insights from the Jurassic Entrada Formation (SE Utah, USA). *Journal of Structural Geology, 66*, 162-187. https://doi.org/10.1016/j.jsg.2014.05.005

Ortega-Villamagua, E., Gudiño-Gomezjurado, M., & Palma-Cando, A. (2020). Microbiologically Induced Carbonate Precipitation in the Restoration and Conservation of Cultural Heritage Materials. *Molecules, 25*(23), 5499. https://www.mdpi.com/1420-3049/25/23/5499

Qi, R., LaForce, T. C., & Blunt, M. J. (2009). Design of carbon dioxide storage in aquifers. *International Journal of Greenhouse Gas Control, 3*(2), 195-205. https://doi.org/10.1016/j.ijggc.2008.08.004

Rodriguez-Blanco, J. D., Shaw, S., & Benning, L. G. (2011). The kinetics and mechanisms of amorphous calcium carbonate (ACC) crystallization to calcite, viavaterite. *Nanoscale, 3*(1), 265-271. https://doi.org/10.1039/C0NR00589D

Saló-Salgado L., Haugen M., Eikehaug K. Fernø M.A., Nordbotten J.M., Juanes R. (2023). Direct Comparison of Numerical Simulations and Experiments of CO_2 Injection and Migration in Geologic Media: Value of Local Data and Forecasting Capability. *Transp. Porous Med*. https://doi.org/10.1007/s11242-023-01972-y

Siddique, R., & Chahal, N. K. (2011). Effect of ureolytic bacteria on concrete properties. *Construction and Building Materials, 25*(10), 3791-3801. https://doi.org/10.1016/j.conbuildmat.2011.04.010

Song, W., de Haas, T. W., Fadaei, H., & Sinton, D. (2014). Chip-off-the-old-rock: the study of reservoir-relevant geological processes with real-rock micromodels. *Lab on a Chip*, 14(22), 4382-4390. https://doi.org/10.1039/C4LC00608A

Taddei, C., & Pike, V. W. (2019). [11C]Carbon monoxide: advances in production and application to PET radiotracer development over the past 15 years. *EJNMMI Radiopharmacy and Chemistry*, 4(1), 25. https://doi.org/10.1186/s41181-019-0073-4

UN General Assembly (2015). Transforming our world: the 2030 Agenda for Sustainable Development. *A/RES/70/1*. Accessible at: https://www.un.org/en/development/desa/population/migration/generalassembly/docs/globalcompact/A_RES_70_1_E.pdf

Van Paassen, L. A. (2009). *Biogrout, ground improvement by microbial induced carbonate precipitation.* Doctoral thesis, TUDelft. http://resolver.tudelft.nl/uuid:5f3384c4-33bd-4f2a-8641-7c665433b57b

Watson, T. L., & Bachu, S. (2009). Evaluation of the Potential for Gas and CO2 Leakage Along Wellbores. *SPE Drilling & Completion, 24*(01), 115-126. https://doi.org/10.2118/106817-pa

Yoon, H., Chojnicki, K. N., & Martinez, M. J. (2019). Pore-Scale Analysis of Calcium Carbonate Precipitation and Dissolution Kinetics in a Microfluidic Device. *Environmental Science & Technology, 53*(24), 14233-14242. https://doi.org/10.1021/acs.est.9b01634

Zhang, W., Ju, Y., Zong, Y., Qi, H., & Zhao, K. (2018). In Situ Real-Time Study on Dynamics of Microbially Induced Calcium Carbonate Precipitation at a Single-Cell Level. *Environmental Science & Technology, 52*(16), 9266-9276. https://doi.org/10.1021/acs.est.8b02660

8. Papers

Paper 1

Calcite-functionalized micromodels for pore-scale investigations of CO_2 storage security

Malin Haugen[1,*], *Benyamine* Benali[1], *Tore* Føyen[1,2], *Wen* Song[3], *Martin* A. Fernø[1], and *Bergit* Brattekås[1]

[1]Department of Physics and Technology, University of Bergen, Norway
[2]SINTEF Industry, Norway
[3]Hildebrand Department of Petroleum and Geosystems Engineering, University of Texas at Austin, USA

Abstract. Carbon capture and subsequent storage (CCS) is identified as a necessity to achieve climate commitments. Permanent storage of carbon dioxide (CO_2) in subsurface saline aquifers or depleted oil and gas reservoirs is feasible, but large-scale implementation of such storage has so far been slow. Although sandstone formations are currently most viable for CO_2 sequestration, carbonates play an important role in widespread implementation of CCS; both due to the world-wide abundancy of saline aquifers in carbonate formations, and as candidates for CO_2-EOR with combined storage. Acidification of formation brine during CO_2 injection cause carbonate dissolution and development of reactive flow patterns. Using calcite-functionalization of micromodels we experimentally investigate fundamental pore-scale reactive transport dynamics relevant for carbonate CO_2 storage security. Calcite-functionalized, two-dimensional and silicon-based, pore scale micromodels were used. Calcite precipitation was microbially induced from the bacteria *Sporosarcina pasteurii* and calcite grains were formed *in-situ*. This paper details an improved procedure for achieving controlled calcite precipitation in the pore space and characterizes the precipitation/mineralization process. The experimental setup featured a temperature-controlled micromodel holder attached to an automatic scanning stage. A high-resolution microscope enabled full-model (22x27 mm) image capture at resolution of 1.1 µm/pixel within 82 seconds. An in-house developed image-analysis python script was used to quantify porosity alterations due to calcite precipitation. The calcite-functionalized micromodels were found to replicate natural carbonate pore geometry and chemistry, and thus may be used to quantify calcite dissolution and reactive flow at the pore-scale.

1 Introduction

Commitments to reach climate goals require us to reduce greenhouse gas concentrations in the atmosphere. Carbon capture, utilization, and storage (CCUS) is identified to play a critical role in achieving these goals. In the Clean Technology Scenario presented by IEA, CCUS is the third-largest contributor (13%) to the cumulative emission reduction until 2060 [1]. Among other, CO_2 can be stored in deep saline aquifers within sandstone or carbonate formations. However, two of the possible risk aspects related to CO_2 storage are the potential for leakage to the surface and, for carbonate formations, dissolution of the reactive calcite rock minerals. The storage potential in carbonate reservoirs is large, but the reactive transport and mechanisms must be accounted for.

Biomineralization is the formation of minerals by living organisms. Microbial induced calcite precipitation (MICP) has been researched in conjunction with different engineering applications, for instance within construction engineering to seal fracture or strengthen concrete [2], for enhanced oil recovery [3, 4], to constrain contaminated groundwater [5], for cementation of unconsolidated porous media [6], and for CO_2 sequestration by reduction of permeability in fractured rock to potential seal leakage paths in the near well area and/or in the cap-rock [7-9].

Precipitation of calcium carbonate ($CaCO_3$) is controlled by four key factors: (1) concentration of calcium (Ca^{2+}) from the cementation solution, (2) concentration of dissolved inorganic carbon as produced by ureolysis, see equation 1-5 in section 2.2, (3) pH value, and (4) availability of nucleation sites [10]. $CaCO_3$ precipitation is dependent on presence of sufficient calcium and carbonate ions to ensure that the ion activity product exceeds the solubility product, making the system oversaturated and precipitation of calcium carbonate is likely. Microbial metabolic activity influence key factor no. 2 and 3, and also no. 4 by function as nucleation site [2]. Calcium carbonate is a common element found in many rocks, such as chalk and marble, it is also the main component in shells, pearls, and corals. $CaCO_3$ can crystallize in different polymorphs, seen as minerals in the nature. This includes calcite, vaterite and aragonite, with calcite as the most stable, and two hydrated polymorphs in addition to several amorphous calcium carbonate (ACC) phases [11]. Vaterite is the least thermodynamically stable polymorph and transforms rapidly to calcite or aragonite in aqueous solutions. According to Ostwald's rule of stages, metastable polymorphs are first formed and then transform into thermodynamically more stable polymorphs [12]. For high supersaturation values it is reported that calcite is initially precipitated as the hydrous form of ACC (tens to hundreds of nanometers) which are subsequently transformed into spherical vaterite and later calcite, while lower supersaturation values lead to direct calcite precipitation [13, 14].

A bacteria often used for studying MICP in the laboratory is the soil bacteria *Sporosarcina pasteurii* [3, 15-18]. In this research these bacteria have also been utilized, with the goal to build upon work by Song et al. 2018 [18] and present an improved procedure to functionalize the pore space in a micromodel with $CaCO_3$ and enable recording of continuous full-model images. A micromodel is a device with a porous pattern from a

* Corresponding author: malin.haugen@uib.no

representative rock matrix etched into a silicon wafer before an optical transparent glass plate is bonded on top. It has four fluid flow ports, one in each corner, with an open fracture connecting two pairs of flow ports (Fig. **1**). This device enable direct study of microscale interactions between fluids and rocks. By functionalizing micromodels with an existing pore-network made of silica grains, it is possible to both precipitate and dissolve $CaCO_3$ minerals and still re-use the micromodel afterwards. This starting point is therefore of great interest during study of fundamental pore-level reactive transport dynamics that determine CO_2 storage security in carbonate formations. MICP in micromodels have also been studied by Wang [19, 20], where, among other, the effect of bacterial cells was studied as well as evolution of shape and size of the $CaCO_3$ precipitates during the MICP process. In this paper we are adding quantification of change in porosity due to $CaCO_3$ precipitation and pressure development throughout experiments.

The experimental set-up was designed to facilitate flow experiments at pressures between 0-120 bars and temperatures between 25-40 °C. Because of the dependency on the biological process, it is important to regulate the temperature to adjust the growth rate of the bacteria. Further, the tubing and valves included in the set-up provide a low, constant, dead volume. The possibility of independent injection and production from each of the four ports in the micromodel, combined with injection of bacterial solution through a loop with constant volume provide excellent experimental conditions. The result is a permeable porous model with carbonate grains distributed throughout the whole pore volume.

By utilizing an in-house built program, we can calculate change in porosity, and among other, identify area of representative elementary volume. The utilized microscope has an automatic scanning stage and a fluorescence module, which enable us to capture the complete porous network (22x27 mm) with resolution of 1.1 µm/pixel. This paper starts with an overview of the micromodel and bacteria utilized to functionalize the micromodel with calcium carbonate. Then, the experimental set-up and equipment is described, followed by the experimental procedures. Results in the form of images, porosity development due to in-situ $CaCO_3$ precipitation and relevance to CO_2 sequestration are presented, before concluding remarks.

2 Materials and methods

2.1 Micromodel

Direct study of microscale interactions between fluids and rocks at elevated reservoir temperature and pressure were enabled by microfluidic devices, further referred to as micromodels. The micromodels consist of two parts, an optical transparent borosilicate glass plate bonded on top of a silicon wafer with etched pattern of a representative porous rock matrix. The state-of-the-art etching method provides a two-dimensional porous system with representative pore-scale geometry with vertical grain walls, sharp edges, and a hydrophilic surface.

The porous network is based on thin sections from natural sandstone, a rock type widely used in laboratory flow experiments for enhanced oil recovery and/or CO_2 storage. Dead-end and isolated pores in the thin section were modified in the micromodel to enable flow across the whole pattern, resulting in higher micromodel porosity and permeability compared to the natural sandstone sample. A unique porous network (6.74 x 2.50 mm) was extracted from the thin section and etched in the silicon wafer with a constant depth of 30 µm. The unique pore pattern was repeated 36 times (4 x 9), resulting in a total porous network which is 27.0 x 22.5 mm large (Fig. **1**). The grains are discontinuous and irregularly shaped, providing flow tortuosity. In each corner, a port through the silicon wafer can connect the pore network to external fluid flow tubes. Two open channels between ports improve flow communication and sweep of the pore space. Further details about design and production procedures can be found in [21] and [22].

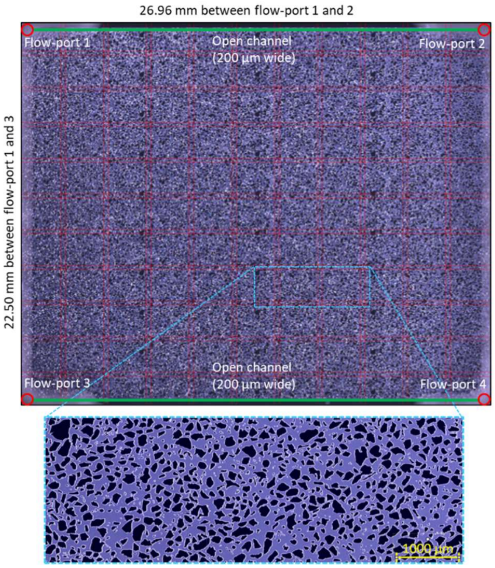

Fig. 1. Full-model image of a micromodel including dimensions. The four flow-ports and the two open-channel fractures between two pairs of ports are highlighted. A pattern generated from thin sections of natural sandstone is repeated 36 times to create the micromodel porous network. A zoom-in of the repeated pattern is highlighted in blue. The full-model image is generated from 121 individual images automatically captured by the microscope software with 10% overlap (shown in red dotted lines), stitched together to one image.

Micromodel properties are listed in Table **1**, as previously reported by Benali et.al (2021) [23]. Stitched full-model images were analyzed to determine grain size distribution, pore throat length distribution (defined as the shortest pore space distance between two neighboring grains) and porosity. Porosity was quantified to 0.61 based on amount of pore space to the total area (grains + pore space) and the total micromodel pore volume (PV) was 11.1 µL. Fig. **2** shows the distribution of grains and pore throat length in the micromodel. Average grain size is calculated to 6 464 μm^2 and average pore throat length is 41 µm, with the shortest pore throat being 0.7 µm with square or rectangular cross-section.

Table 1. Micromodel properties

Parameter	Value
Width	27.0 mm
Length	21.4 mm
Depth	30 µm
Porosity	0.61
Pore volume	11.1 µL
Permeability	2.97 D
Repetition of pattern	36
Grain size	0.5 - 78 366 μm^2
Pore throat length	0.7 - 194 µm

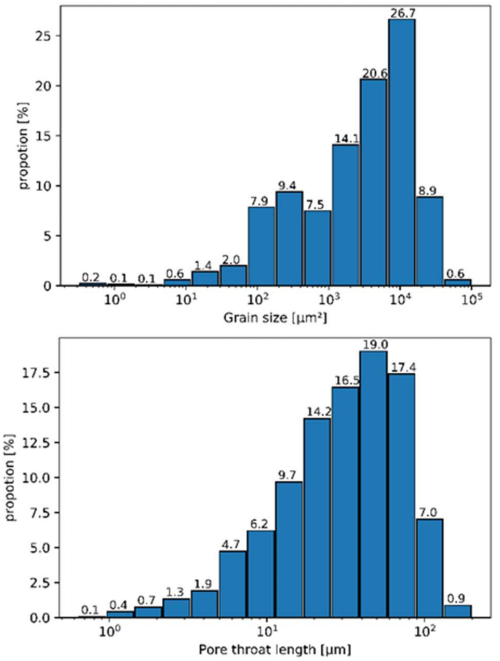

Fig. 2. Distribution of grain size (top) and pore throat length (bottom) in one of the 36 pore network repetitions which make up the micromodel.

The work presented here describes the experimental set-up and method to functionalize micromodels with calcium carbonate grains utilizing bacteria. This enables experimental investigations of fundamental pore-scale reactive transport dynamics in carbonate rocks.

2.2 Sporosarcina pasteurii bacteria

To functionalize micromodels with calcium carbonate for pore-scale investigations of CO_2 storage security, microbially induced calcite precipitation (MICP) by urea hydrolysis have been utilized. The bacteria *Sporosarcina pasteurii*, formerly *Bacillus pasteurii,* (Miquel 1889) DSM33 [24] are urease positive [25] and have a known ability to enable calcite precipitation [15] and growth on solid surfaces [2, 3]. The bacterial cells are gram positive, motile and rod shaped with size in the range of 0.5-1.2 x 1.3-4.0 µm [25]. This is an aerobic bacteria with optimum growth temperature and pH of 30 ºC and 9, respectively [25].

The MICP process has been studied by several researchers and the following equations (Eq.1-5) have typically been used to describe this process [2, 7, 17, 26]. The bacteria enable hydrolysis of urea ($CO(NH_2)_2$) into ammonia (NH_3) and carbonic acid (H_2CO_3), see Eq.1. In solution this leads to production of (OH^-) and accumulation of ammonium (NH_4^+). As a result of increasing (OH^-) concentration, the pH in the microenvironment is increasing (Eq. 2 and 3), and subsequently causes carbonic acid to be converted to bicarbonate (HCO_3^-) and further to carbonate ions (CO_3^{2-}) (Eq.4). When calcium ions (Ca^{2+}) are added to the solution, the increasing pH also leads to precipitation of calcium carbonate ($CaCO_3$) [3, 7] when the solution is supersaturated with calcium- and carbonate- ions (Eq.5). Precipitation of calcium carbonate can occur in the bulk phase, or on the bacteria cell wall because it is negatively charged and will therefore attract the positive charged calcium ions [2, 16]. If the bacterium is covered in calcium carbonate the cell will die as nutrient transfer is prevented [2, 26].

$$CO(NH_2)_2 + 2H_2O \xrightarrow{urease} 2NH_3 + H_2CO_3 \quad (1)$$

$$2NH_3 + 2H_2O \leftrightarrow 2NH_4^+ + 2OH^- \quad (2)$$

$$H_2CO_3 + 2OH^- \leftrightarrow HCO_3^- + H_2O + OH^- \quad (3)$$

$$HCO_3^- + H_2O + OH^- \leftrightarrow C0_3^{2-} + 2H_2O \quad (4)$$

$$Ca^{2+} + CO_3^{2-} \rightarrow CaCO_3(s) \quad (5)$$

Details about preparing bacteria and fluids, and procedure for functionalization of micromodels are described in section 2.4.

2.3 Experimental set-up

A schematic of the experimental set-up for *in situ* visualization of calcite-functionalized micromodels is presented in Fig. **3**. The system also contains equipment to inject CO_2 or CO_2-saturated fluids for pore-scale investigations of CO_2 storage security at elevated reservoir pressure and temperature (see section 3.3). To facilitate injection of these fluids, the set-up is designed with all tubes and equipment (except autoclave-valves) in materials which are chemical compatible with these fluids. Polyether ether ketone (PEEK) has been found to resist all the chemicals and fluids used in this work and is therefore the main material used in this design.

On the inlet side of the micromodel, a high precision plunger pump (Quizix 5000-2.5K) is operated in independent mode and used for injection of water and CO_2. There is also an option to inject CO_2 into an in-house PEEK accumulator (30 ml) for CO_2-saturated fluids. As mentioned in section 2.1, the smallest pore throat in the micromodel is calculated to be 0.7 µm. To avoid injection of unwanted particles, like dust, that clogs up the micromodel, all fluids were filtered prior to use and flow

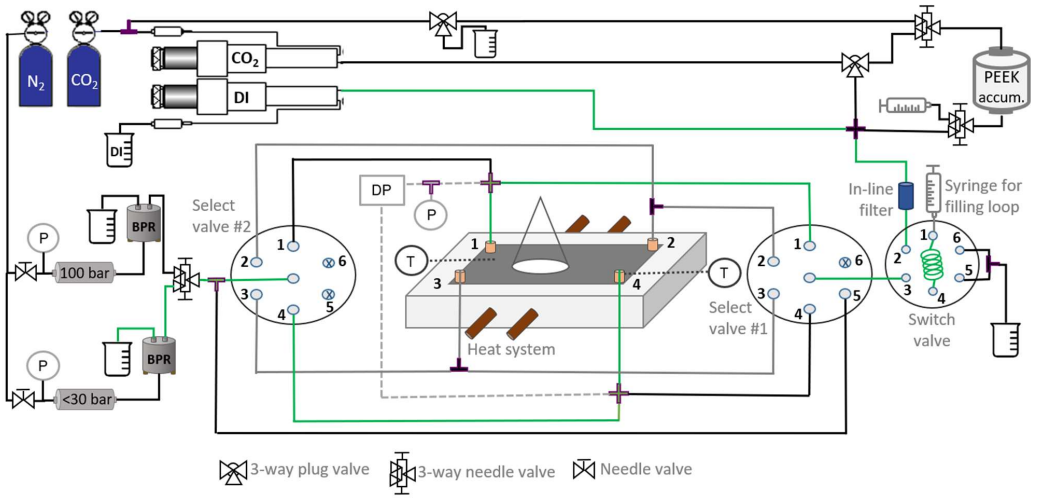

Fig. 3. Schematic of the experimental set-up for calcite-functionalization of micromodels. During injection of bacterial- or cementation solution, tubing marked in green were open/connected. Fluids were injected into a 1.0 ml loop in the switch valve and chased by DI from a pump. The micromodel was placed directly under a microscope, enabling in-situ visualization of $CaCO_3$ precipitation in the pore space. All tubing and tee/cross (purple) are in PEEK from Idex.

through a 0.5 µm inline filter assembly (Idex, A-431) prior to entering the micromodel.

The low pore volume (11.1 µL) makes it important to have a constant system dead-volume to ensure that fluids enter the micromodel when anticipated. This is achieved by utilizing two 6-ports select valves (Idex, MXP7970-000), one at inlet and one at the outlet. When valves #1 and #2 are connected to the fluid-flow-ports (Fig. **3**) it is possible to designate injection and production ports with a single mouse-click. When changing injection fluid, both select valves were set to position 5 for the fluids to by-pass the micromodel until pressure stabilized. During calcite generation experiments small amounts of different fluids will be injected into the model at various times. To facilitate variable fluid injection without air entering the tubes, a two-position switch valve (Idex, 9725) is included in the design. The switch valve has two positions: load and inject. At "load" position, fluids from the pump flow into port 2, via port 3 and to Select Valve #1. A coiled tube (referred to as "loop", see Fig. **3**) with a constant volume could then be filled with e.g. bacteria-solution using a luer-lock syringe. At "inject" position, flow from the pump is rooted through the loop and into Select Valve #1. Other valves used in the set-up are Autoclave valves as described in Fig. **3**.

The system is pressurized by two back pressure regulators (Equilibar), where one is kept at 100 bars for high pressure experiments, and one at lower pressure depending on experimental design. The pressure differential between inlet and outlet is logged with differential pressure transmitter (APLISENS PRE-28 SMART) with a measuring range of 0-2.5 bar and a static pressure limit of 250 bar. In addition, absolute pressure transmitter (ESI), with a range from 0-250 bar, is connected to flow port 1.

The micromodel-holder in the middle of Fig. **3** is designed and machined in-house from PEEK material. It consists of four drilled holes, made with a 10-32 coned drill, which is aligned with the fluid-flow-ports underneath the micromodel, two Omega temperature probes close to port number 1 and 4, and tracks for two 1/8-inch copper tubing for heating of the micromodel by circulation of warm water. Fluid flow tubes are connected to the micromodel-holder by finger tight fittings 10-32

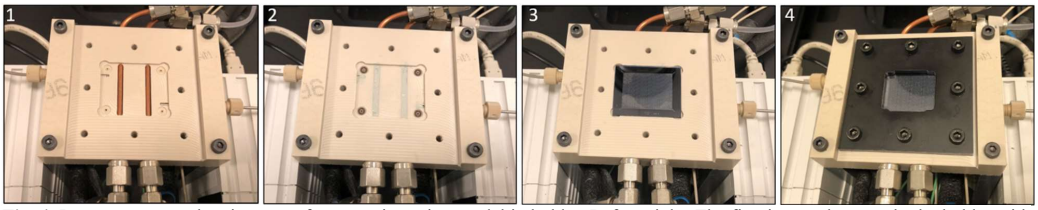

Fig. 4. Image sequence showing steps for mounting micromodel in holder. Left to right: The first image shows only the holder with machined groove for the micromodel, O-rings around the four fluid-flow-ports, two temperature gauges and copper tubing for the heating system. In the second image, the O-rings are in place and thermal paste are covering the temperature gauges and copper tubing to ensure optimal heat transfer. In the third image, the micromodel is in place and in the fourth image the black-painted aluminum plate is placed on-top of the micromodel and tightened with 0.20 Nm force. When everything is in place, the system can be pressurized to 150 bar.

coned (Idex, F-120X) screwed directly into the four drilled holes in the PEEK holder. Mounting of micromodel in the holder is shown in detail in Fig. **4**.

As indicated by the cone in Fig. **3**, the micromodel-holder is placed directly underneath a microscope to enable *in situ* visualization of calcite generation and subsequent investigation of CO_2 storage in carbonate formations. The microscope is a Zeiss, Axio Zoom.V16 Microscope with two light sources: a cold-light (CL 9000 LED) source with diffuser S, and a fluorescence (FL) module. It has an automatic scanning-stage which enables high-resolution imaging of the entire micromodel within 82 seconds (with the CL 9000 LED source) and automatic stitching of the images to a full-model image. When generating images with both the CL 9000 LED source and one FL light channel for each tile, a full-model image is acquired within 293 seconds.

2.4 Experimental procedure

2.4.1 Preparation of fluids

Bacterial growth medium and cementation solution (reactant) were prepared as described by [18]:

Bacterial growth medium: 47g of brain heart infusion broth (BHI Broth, 53286 Sigma-Aldrich) was mixed with 900 ml of deionized (DI) water, obtained from Milli-DI synthesis system including 0.2 µm filter (172-5109, Merck). Then the solution was sterilized in 15 minutes at 121 °C in an autoclave before cooled to ~30 °C. Next, a concentrated urea solution was added to make a 2 wt. % urea broth. This was achieved by mixing 20g of urea into 100 mL of DI water. Before injecting this urea solution into the growth medium, it was filtered through a 0.2 µm syringe filter (514-0061, VWR). The finished growth medium (BHI+U) was also filtered through the syringe filter prior to adding bacteria.

Reactant was prepared by mixing urea (urea, U5378, Sigma-Aldrich) and calcium chloride (calcium chloride dehydrate, 31306, Sigma-Aldrich) in DI water. As for the growth medium, the reactant was filtered through a 0.2 µm syringe filter prior to use to minimize the risk of small particles entering the micro-model.

2.4.2 Cultivation of bacteria

Bacterium *Sporosarcina pasteurii* DSM 33 [24] were received freeze-dried from DSMZ GmbH supplier and cultivated as follows: First the pellet was removed from the sealed glass and added to 0.5 ml growth medium where it was allowed to rehydrate for 30 minutes. Second, 0.2 ml of the bacterial solution was moved to a centrifuge tube containing 10 ml growth medium and placed in a heating cabinet at 30 ºC for 24 hours. Growth was detected after 24 hours, but the procedure was repeated one more time by adding 0.2 ml of the bacterial solution into a new centrifuge tube with 10 ml growth medium and stored in 30 ºC for another 24 hours. After 24 hours, sufficient bacterial growth was observed, and the bacterial solution was ready to be used. Every 7 days, 0.2 ml of bacterial solution is moved to a new centrifuge tube containing 10 ml growth medium to prevent death of bacteria. In case bacteria die, an inventory of glycerol stock was prepared by adding 0.2 ml of bacterial solution and 0.2 ml of 30 % glycerol into 6 pendlorf microtubes for long term storage at -80 ºC.

2.4.3 Calcite-functionalization of micromodels

The experimental set-up (Fig. **3**) is designed to withstand pressure up to 150 bar, but the MICP process was performed at atmospheric pressure or slightly elevated pressure conditions (25 bars). The latter based on experience of when all CO_2 generated from the bacterial metabolism during settling time is completely dissolved in aqueous phase, to mitigate gas-filled pores that influence fluid flow. As the MICP process is developing to be utilized in more extreme environment [27], studying this process at elevated pressures is relevant. Several factors impact the precipitation of calcium carbonate during the MICP process and variables can be adjusted depending on the goal. Details about the experimental procedure used to generate calcium carbonate in a micromodel are explained below.

1. Initial conditions.

The micromodel is initially filled with deionized water (DI). DI is miscibly displaced by bacterial growth medium before 20 µl (2 PV) bacterial solution is injected at 6 µl/min (flow port 3 as inlet and 2 as outlet). 2 PV bacteria solution is consistent with results by Wang et.al (2018) [19], who have reported that bacterial suspension was homogeneously distributed in a microfluidic chip after 1.25 PV injected.

2. Bacterial growth in pore space.

Tubing used for bacterial solution are flushed with sterile bacterial growth medium before the micromodel is shut in. This enables time for bacteria to grow, settle and attach to the pore walls.

3. Prepare for injection of cementation solution.

Cementation solution is loaded in the loop of the switch valve and injected through the bypass next to flow port 1 (with both select-valves at position 1). When the bypass is filled with cementation solution, flow is routed at 1 µl/min to flow-port 1 in the micromodel, and flow port 2 is used as outlet.

4. Cementation solution into micromodel.

After the dead-volume from bypass to flow-port 1 has been injected, the outlet flow-port is changed from 2 to 4. *In situ* growth of calcium carbonate is visualized using a high-resolution microscope with automatic scanning stage, enabling full-model images of 1.1 µm/pixel within 82 seconds or 293 seconds if one FL channel is included.

2.5 Quantification of porosity

Changes in porosity from $CaCO_3$ precipitation were quantified from image analysis (using an in-house python script) on sub-sections during time-lapse imaging, and in the entire pattern for the last time step, see section 3.

Two different light sources (CL 9000 LED and FL) were available for in-situ imaging of the micromodel, each with its own method for calculating the area of precipitated $CaCO_3$ minerals. With the CL 9000 LED light source, calcium carbonate minerals appear white and can be quantified with simple segmentation. The white reflection edge around each silica grain were omitted from

the areal calculations by subtracting the initial image (experiment A). When both light sources were utilized, two approaches were developed, depending on when the FL tracer was injected: 1) displace the aqueous phase with a FL tracer after the MICP process. In the FL light image, the $CaCO_3$ minerals then appear as shades from green to black, where black minerals were interpreted as occupying the whole height in the micromodel; 2) include a FL tracer in the cementation solution during the MICP process. Calcite minerals then appear orange with the CL9000 LED light source (Fig.**6**, B.1). If the FL tracer is replaced with aqueous phase after the MICP process, only $CaCO_3$ minerals are visible in the FL light image. By combining threshold CL 9000 LED and FL images, the result contains the area of all precipitated $CaCO_3$ (Experiment B).

Porosity changes over time can be studied by dividing the full-model images into sub-sections (experiment A). This is achieved by adding the total silica grain area to the calcium carbonate area for each timestep, then normalizing against initial white areas related to reflections around silica grains and bacterial aggregation or potential biofilm. With this approach we mitigate areas related to white reflections which otherwise would impact the porosity as the software/script identify all white colors as porosity. The final fraction of calcite minerals in the pore space was calculated as total calcite grains area divided by the total area of each image, both in the sub-sections and the full-model image. Some calcite grains (part of a whole grain) appear transparent and were not detected by the software. Hence, the calculated calcite fraction is expected to be lower than the real fraction.

3 Results and discussion

3.1 Experimental conditions

Two experiments, with the same bacterial culture and procedure, constitute the experimental results in this study. The pore space bacterial settling times were different between the two experiments (Table **2**), but the initially high pH and bacterial movement observed indicated that they were in the active phase of the bacterial growth curve, performing ureolysis, see section 2.2. The procedure to generate calcite in the micromodel is presented in section 2.4. All experimental conditions for the two experiments are listed in Table **2**.

Table 2. Properties of bacterial- and cementation solution of experiments included in this paper.

Experiment	A	B
Properties of bacterial solution		
OD600	~0.6 *	~0.6 *
Initial pH	~ 9.2 *	~ 9.2 *
PV injected	2	2
Injection rate [µl/min]	6	6
Growth time in micromodel [h]	7	21
Temperature [°C]	31	30
Pressure [bar]	25	atm
Properties of cementation solution		
Urea [M]	1	0.5
$CaCl_2$ [M]	1	0.5
Injected [µl]	244.2	221.8
PV injected	22.0	20.0
Injection rate [µl/min]	1	1
Temperature [°C]	31	30
Initial pressure [bar]	25	atm
Pressure when pump stopped [bar]	50	10
FL included	No	Yes

** Based on measurements on three bacterial solutions made with the same procedure/volumes*

During cementation solution injection (experiment A) the injection and differential pressure across the micromodel increased rapidly after 4.2 PV injected (Fig. **5**), possibly related to large amount of calcium carbonate precipitated. The PV injected increased linearly until the injection pump reached 50 bars (after 22.0 PV injected) due to blockage of the outlet tubing. Continued calcium carbonate growth was observed after injection stopped, reducing the porosity of the pore space (detailed later). For experiment B, the observed pressure behavior was similar.

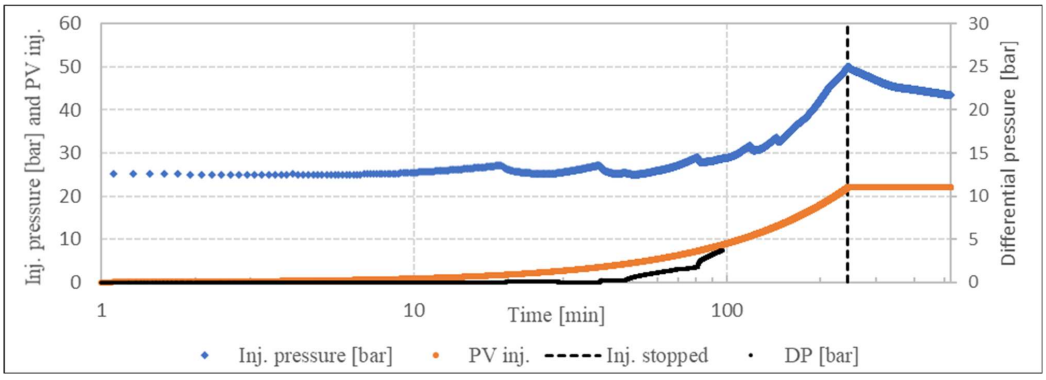

Fig. 5. Injection pressure (blue, left y-axis), differential pressure (black, right y-axis) and pore volumes injected (orange, left y-axis) during injection of cementation solution in experiment A. Injection stopped when the injection pressure reached 50 bars, indicated with vertical dashed line; measurements of differential pressure stopped at 3.7 bars because of limitation in measuring range. Calcite precipitation occurred both during injection and in a period afterwards.

3.2 Calcite precipitation

3.2.1 Single pore

The calcium carbonate grains have a variety of shapes, ranging from square/cubic, spherical to irregular (Fig. **6**). Calcite grains precipitated both close to pore walls and in the pore center, and in some cases calcite grains encapsulated silica grains. The *in-situ* development of calcium carbonate through the MICP process was further studied utilizing a fluorescence module that revealed color differences between minerals. Black calcite grains were interpreted as filling the entire height in the pores space (30 µm) and block flow. The internal structure of other minerals was visible in the FL image, in contrast to images generated with CL 9000 LED. Hence, combining FL and CL 9000 LED images have a large potential in characterizing the development of calcite minerals.

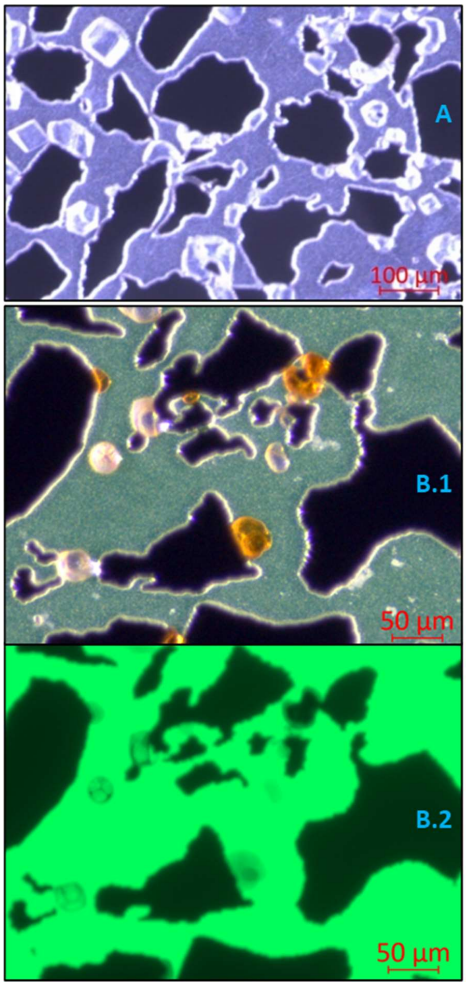

Fig. 6. Top image (A) show example of grains from experiment A, while bottom two (B) show image from experiment B generated with CL 9000 LED light source in B.1 and with FL light source in B.2.

3.2.2 Sweep/areal

The *Sporosarcina pasteurii* bacteria perform urease when settling in the micromodel, prior to injection of cementation solution. During this process, the pH is increasing and subsequently leads to carbonate ions being present in the pore space fluids. When calcium ions are added to the micromodel, calcium carbonate precipitate when the solution is supersaturated with these ions. To study the development of calcium carbonate in more detail, the micromodel is divided in three subsets (Fig. **7**). The change in porosity due to calcium carbonate precipitation (Fig. **8**) was calculated using segmented images (described in section 2.5). The fraction of calcium carbonate (area of $CaCO_3$ / area of image) is summarized in Table **3**. The procedure was compared with manual measurement (using a functionality in the Zeiss software) of the total calcium carbonate grain area divided by total area in the final image (at 520 minutes) in subset 1.

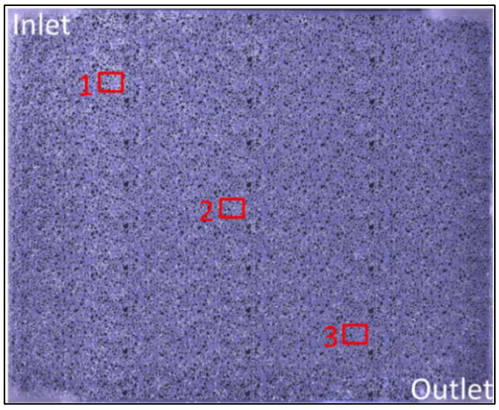

Fig. 7. Full-model image at the end of experiment A (520 min), including subset 1, 2 and 3.

Table 3. Summary of $CaCO_3$ fractions for experiment A.

Method	Area	$CaCO_3$ fraction
Polygons in Zeiss	Subset 1	0.15
Python script	Subset 1	0.13
Python script	Subset 2	0.04
Python script	Subset 3	0.02
Python script	Full-model	0.04

The development of calcium carbonate in subset 1 is detailed in Fig. **9**. Coinciding with cementation solution entering the inlet-flow-port, a small white irregularly-shaped $CaCO_3$ precipitate (< 30 µm^2) formed close to inlet and reached subset 1 after 1.4 min (0.1 PV injected). The initial porosity reduction (Fig. **8**) for subset 1 relates to these irregularly-shaped $CaCO_3$ precipitates, also seen in the image at 5 minutes in Fig. **9**. The amount of $CaCO_3$ precipitates were relatively constant until 19.3 min of injection (1.7 PV injected), when a small number of additional larger (~60-100 µm^2) irregularly-shaped $CaCO_3$ precipitates formed. Some of the irregularly-

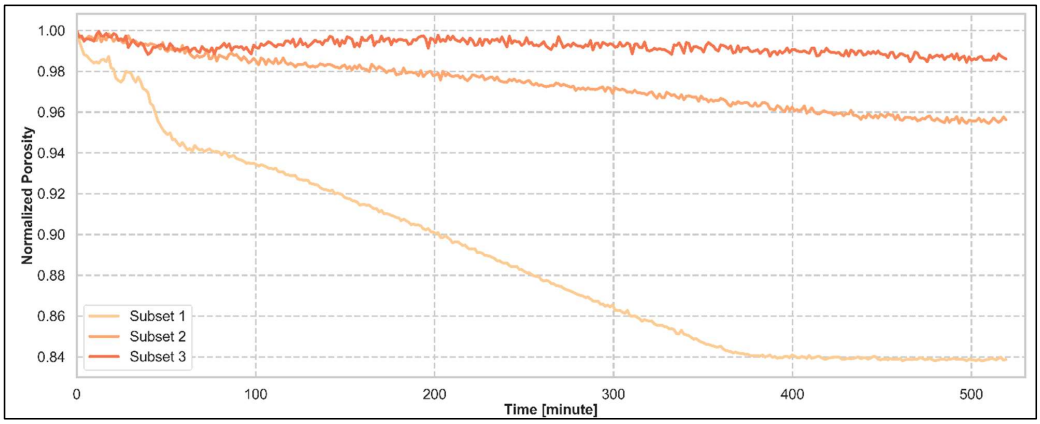

Fig. 8. Development of normalized porosity ($\Phi/\Phi_{initial}$) in each of the three subsets in experiment A. Porosity (Φ) in each timestep was calculated as: $\Phi = 1 - (areal_{silica\ grains} + areal_{CaCO_3})/total\ area$.

shaped $CaCO_3$ precipitates continued to grow at apparently random places in the pore space, located mainly in the middle/right side in the field of view where the pores were largest. These precipitates dissolved as

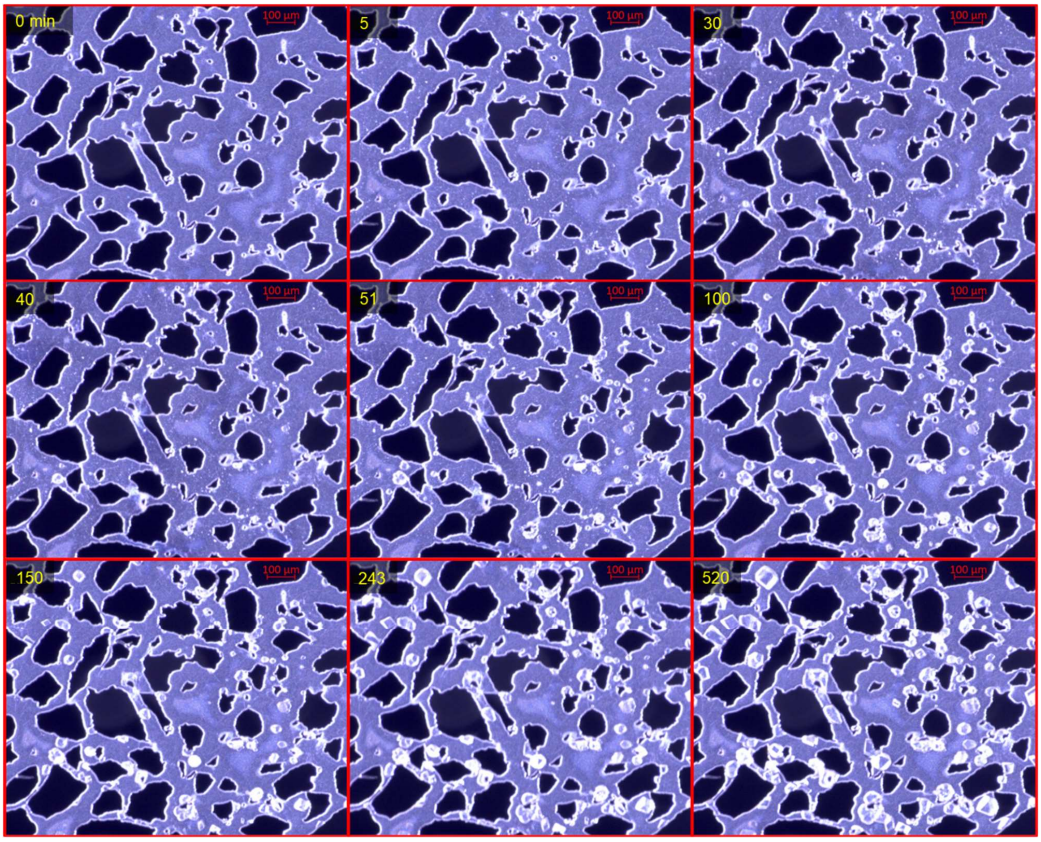

Fig. 9. Calcium carbonate precipitation in subset 1 of experiment A (Fig. **7**) at different timesteps. Yellow number represent minutes from cementation solution entering the micromodel from the top left corner. This equal to PV injected until the pump stopped after 244 minutes.

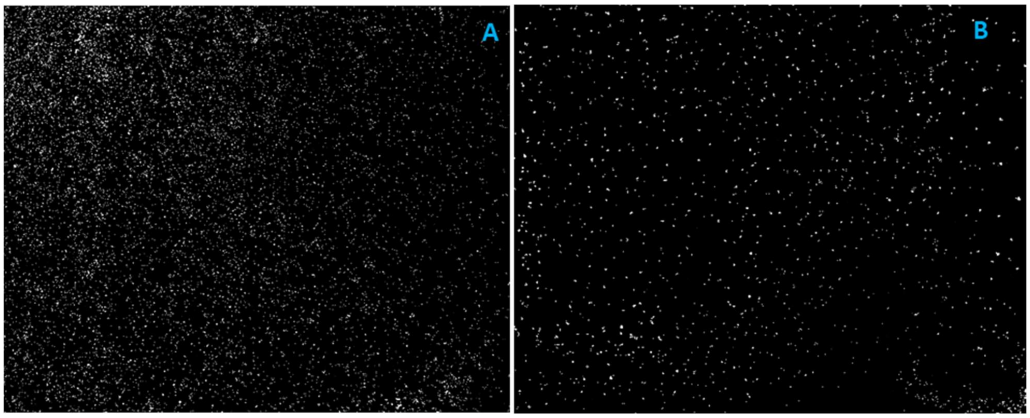

Fig. 10. Segmented images showing grains of calcium carbonate after experiment A to the left and experiment B to the right. For experiment A, the injection is at top left and outlet is bottom right, for experiment B it is opposite, with inlet at bottom right corner and outlet at top left. Width and height of both images are 24.9 mm and 19.9 mm respectively.

larger $CaCO_3$ crystals (spherical or rhombohedral) formed. These observations are consisted with findings from Wang et. al (2019) [20], reporting irregularly-shaped $CaCO_3$ dissolving in a circular trend with increasing radius outwards from the growing crystals. They further assumed that the rhombohedral crystals were calcite, spherical crystals were vaterite, and irregularly-shaped precipitates were amorphous $CaCO_3$ precipitates [20].

For the first 81 minutes, precipitating grains were predominantly spherical and/or irregularly shaped (not square or cubical). These continue to grow, but additional grains forming from this time were mainly square or cubical, with a larger area compared with the spherical grains. This change in grain precipitation coincided with a steeper slope in the differential pressure (Fig. **5**). After 244 minutes the cementation solution injection stopped (22.0 PV injected), but the calcite minerals continued to grow until 378 min. Final $CaCO_3$ fraction in subset 1 was 0.13 (Python script) or 0.15 (manual polygons drawn around all calcite minerals in the Zeiss software), confirming that the Python script could satisfactorily capture porosity reduction.

Many parameters influence the precipitation of calcium carbonate, and concentration of calcium chloride in the cementation solution is one of them. Compared to experiment A, the concentrations of calcium chloride and urea were reduced by 50% in experiment B. From the literature it is expected that lower concentration enables the cementation solution to spread out better in the pore space because the reaction is slowed down. Even though the final $CaCO_3$ fraction in subset 1 (experiment A) was 0.13, the full-model fraction was only 0.04. This indicates an uneven distribution of the carbonate minerals throughout the micromodel, and it is also visible in the left section of Fig. **10**. In experiment B the full-model $CaCO_3$ fraction was calculated to 0.006, it appears to be more evenly distributed, as seen in Fig. **10**.

3.2.3 Multiphase effects

A product of bacterial respiration and urea hydrolysis is CO_2. The dissolved CO_2 form carbonic acid ($H_2O + CO_2$) and precipitates as a part of calcite (see eq 1-5), but also function as a buffer where it slows down the increasing pH as ammonia is produced by the urease [15]. At atmospheric pressure conditions some of the CO_2 develop into bubbles occupying relatively large areas in the pore volume. Because of the low injection rate, these bubbles impacted saturation distribution in the micromodel (Fig. **11**). As the permeability was reduced from precipitation of $CaCO_3$, the pore-pressure increased, and the bubble area reduced. Once a bubble was removed by dissolution in the aqueous phase, $CaCO_3$ precipitated in the area previously occupied by a bubble. It is expected that the change in pore-pressure, and hence CO_2 solubility, has an impact on the local pH value. This should be further studied by adding a pH sensitive FL tracer to the system.

3.3 Relevance to CO_2 sequestration

CO_2 sequestration in carbonate formations causes acidification of the brine and subsequent carbonate dissolution and development of reactive flow patterns. CO_2 is also a reaction product from the dissolution of calcium carbonate. Depending on the solubility and saturation of CO_2 in the pore fluid, it will go into solution or become bubbles that can eventually form a free gas phase. Song et al. 2018 presented the phenomena with a gas phase shielding carbonate minerals from dissolution as “grain engulfment” [18]. The functionalized micromodel in Experiment A was pressurized to 100 bars before CO_2 saturated HCl was injected. Fig. **12** shows CO_2 bubbles generated around $CaCO_3$ minerals during pore-level dissolution. Experiments with full model images of this dynamic reactive flow are ongoing.

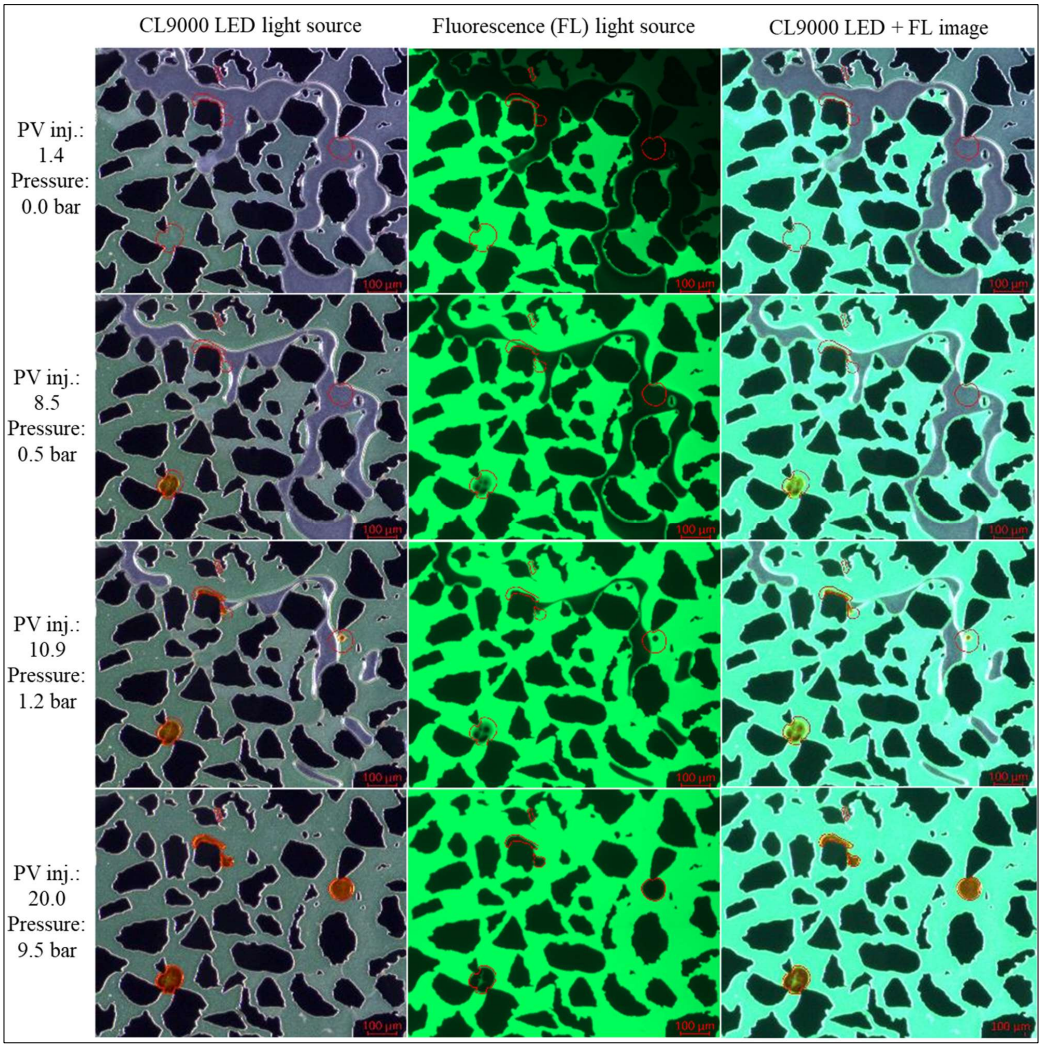

Fig. 11. Image sequence of calcium carbonate precipitation in a subset of experiment B. Pore volume injected is from cementation solution entering the micromodel in the bottom right corner (outside this field of view). Time step from top to bottom row of images are 15 min, 95 min, 122 min and 242 min, respectively. Pump stopped at 222 min (20 PV inj.). Red polygons are drawn in the Zeiss program based on image at 242 min.

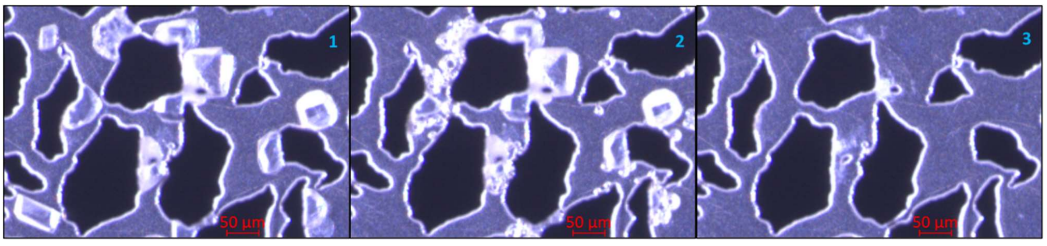

Fig. 12. Image sequence of $CaCO_3$ dissolution due to injection of CO_2 saturated HCl into a micromodel at 100 bars. Image 1) is from the functionalized micromodel in Experiment A, 2) show CO_2 bubbles as the minerals dissolve and 3) is after all the minerals have been dissolved.

4 Conclusions

Calcite-functionalization of micromodels was investigated to enable experimental investigation of fundamental pore-scale reactive transport dynamics; eventually determining carbonate CO_2 storage security. The system is very sensitive to external factors, and small procedural changes may result in large variations in results. Throughout this study we have demonstrated that bacteria are still active at 25 bar pore-pressure, and precipitation of calcium carbonate minerals occur at elevated pressures. To obtain the best conditions for segmenting of images, it is optimal to have the system under pressure and thereby limit gas-bubbles caused by the metabolism of bacteria.

This experimental set-up and methodology provide a unique method for studying the MICP process, where quantification of full-model calcite porosity development over time is demonstrated. This work also demonstrates that a micromodel can be functionalized with calcium carbonate minerals within a few days. Full-model images and elevated pressures provide the opportunity to support several research opportunities and investigations of fundamental pore-scale reactive transport dynamics:

- Carbon sequestration and dissolution of calcium carbonate
- Water weakening of chalk
- Injection rate dependency
- pH dependency using a pH sensitive FL tracer

MICP is a complex, biochemical process, and future work is planned to include a pH sensitive fluorescence tracer to improve understanding in how pH is changed throughout the different steps and how it influences the precipitation process. This focus aligns with future opportunities presented by Tang et. al (2020) [27] and would build upon work done by Zehner et.al (2020) [28] by introducing the FL tracer in a micromodel with representative pore scale geometry.

During injection of cementation solution, a significant proportion of the bacteria are flushed out, as have also been reported previously [19]. This could lead to preliminary clogging of outlet tube and thereby limit amount of Ca^{2+} injected into the pore space. Future work is therefore planned with increased diameter of the outlet tube, expecting to increase calcite fraction in experiment equal to B.

Nomenclature and abbreviations

CCS	Carbon, capture and storage
CO_2	Carbon dioxide
MICP	Microbially induced calcite precipitation
BHI	Brain Heart Infusion
BHI+U	Brain Heart Infusion including urea
DI	Deionized water
OD600	Optical density measured at a wavelength of 600 nm
PEEK	Polyether ether ketone
$CaCO_3$	Calcium carbonate
$CO(NH_2)_2$	Urea
$CaCl_2$	Calcium chloride
NH_3	Ammonia
NH_4^+	Ammonium
H_2CO_3	Carbonic acid
HCO_3^-	Bicarbonate
CO_3^{2-}	Carbonate ions
Ca^{2+}	Calcium ions
FL	Fluorescent
CL 9000 LED	Cold-light source with diffuser S
Φ	Porosity
HCl	Hydrochloric acid
H_2O	Water

This work was supported by Norwegian Research Council under project 280341. The authors thank Dhanasekaran Sivakumaran for assistance in cultivating bacteria, and Tove Skogmo Folkestad and Sonja Ljostveit for autoclaving the bacterial growth medium at Haukeland University Hospital.

References

1. IEA, *The Role of CO2 Storage.* (2019).
2. W. De Muynck, N. De Belie, and W. Verstraete, *Microbial carbonate precipitation in construction materials: A review,* Ecological Engineering, **36**(2): p. 118-136 (2010)
3. F.G. Ferris, et al., *Bacteriogenic Mineral Plugging,* Journal of Canadian Petroleum Technology, **36**(09): p. 5 (1996)
4. J. Wu, et al., *Microbially induced calcium carbonate precipitation driven by ureolysis to enhance oil recovery,* RSC Advances, **7**(59): p. 37382-37391 (2017)
5. Y. Fujita, et al., *Evaluating the Potential of Native Ureolytic Microbes To Remediate a 90Sr Contaminated Environment,* Environmental Science & Technology, **44**(19): p. 7652-7658. (2010)
6. F.D. Meyer, et al., *Microbiologically-Induced Soil Stabilization: Application of Sporosarcina pasteurii for Fugitive Dust Control*, Geo-Frontiers, Vol. 2011, p.4002-4011 (2011)
7. A.C. Mitchell, et al., *Microbially Enhanced Carbon Capture and Storage by Mineral-Trapping and Solubility-Trapping.* Environmental Science & Technology, **44**(13): p. 5270-5276 (2010)
8. A. Phillips, et al., *Potential CO2 Leakage Reduction through Biofilm-Induced Calcium Carbonate Precipitation,* Environmental Science & Technology, **47**: p. 142-149 (2013)

9. A.B. Cunningham, et al., *Microbially enhanced geologic containment of sequestered supercritical CO2,* Energy Procedia, **1**(1): p. 3245-3252 (2009)
10. F. Hammes, and W. Verstraete*, *Key roles of pH and calcium metabolism in microbial carbonate precipitation.* Reviews in Environmental Science and Biotechnology, **1**(1): p. 3-7 (2002)
11. B. Krajewska, *Urease-aided calcium carbonate mineralization for engineering applications: A review.* Journal of Advanced Research, **13**: p. 59-67 (2018)
12. J.W. Mullin, *Crystallization*, 4th ed., Oxford: Butterworth-Heinemann (2001)
13. W. Zhang, et al., *In Situ Real-Time Study on Dynamics of Microbially Induced Calcium Carbonate Precipitation at a Single-Cell Level,* Environmental Science & Technology, **52**(16): p. 9266-9276 (2018)
14. L.A. Van Paassen, *Biogrout, ground improvement by microbial induced carbonate precipitation*, in *TU Delft, Applied Sciences*, TU Delft: The Netherlands (2009)
15. S. Stocks-Fischer, J.K. Galinat, and S.S. Bang, *Microbiological precipitation of CaCO3.* Soil Biology and Biochemistry, **31**(11): p. 1563-1571 (1999)
16. G.E. Mountassir, et al., *Hydrodynamic coupling in microbially mediated fracture mineralization: Formation of self-organized groundwater flow channels,* Water Resources Research, **50**(1): p. 1-16 (2014)
17. C. Wu, et al., *Microbially induced calcite precipitation along a circular flow channel under a constant flow condition,* Acta Geotechnica, **14**(3): p. 673-683 (2019)
18. W. Song, et al., *Mechanisms of Multiphase Reactive Flow using Biogenically Calcite-Functionalized Micromodels,* Lab on a Chip, **18**, (2018)
19. Y. Wang, et al., *A microfluidic chip and its use in characterising the particle-scale behaviour of Microbial-Induced Carbonate Precipitation (MICP),* Géotechnique, **69** (2018)
20. Y. Wang, et al., *Microscale Visualization of Microbial-Induced Calcium Carbonate Precipitation Processes,* Journal of Geotechnical and Geoenvironmental Engineering, **145**: p. 04019045 (2019)
21. M. Buchgraber, et al., *Creation of a dual-porosity micromodel for pore-level visualization of multiphase flow,* Journal of Petroleum Science and Engineering, **86-87**: p. 27-38 (2012)
22. M. Buchgraber, A.R. Kovscek, and L.M. Castanier, *A Study of Microscale Gas Trapping Using Etched Silicon Micromodels,* Transport in Porous Media, **95**(3): p. 647-668 (2012)
23. B. Benali, et al. *[Preprint] Pore-scale Bubble Population Dynamics of CO2-Foam at Reservoir Pressure.* https://essoar.org (2021)
24. J.H. Yoon, et al., *Sporosarcina aquimarina sp. nov., a bacterium isolated from seawater in Korea, and transfer of Bacillus globisporus (Larkin and Stokes 1967), Bacillus psychrophilus (Nakamura 1984) and Bacillus pasteurii (Chester 1898) to the genus Sporosarcina as Sporosarcina globispora comb. nov., Sporosarcina psychrophila comb. nov. and Sporosarcina pasteurii comb. nov., and emended description of th.* International Journal of Systematic and Evolutionary Microbiology, **51**(3): p. 1079-1086 (2001)
25. P. De Vos, G.M. Garrity, and D.H. Bergey, *Bergey's manual of systematic bacteriology: Vol. 3 : The Firmicutes*. 2nd ed. Vol. 3., New York: Springer (2009)
26. M.S. Reddy, *Biomineralization of calcium carbonates and their engineered applications: a review,* Frontiers in Microbiology, **4**(314) (2013)
27. C.-S. Tang, et al., *Factors affecting the performance of microbial-induced carbonate precipitation (MICP) treated soil: a review.* Environmental Earth Sciences, **79**(5): p. 94 (2020)
28. J. Zehner, et al., *Microbial-induced calcium carbonate precipitation: an experimental toolbox for in situ and real time investigation of micro-scale pH evolution,* RSC Advances, **10**(35): p. 20485-20493 (2020)

Paper 2

Chemical Geology 641 (2023) 121782

Contents lists available at ScienceDirect

Chemical Geology

journal homepage: www.elsevier.com/locate/chemgeo

Pore-scale kinetics of calcium dissolution and secondary precipitation during geological carbon storage

Na Liu [a,*], Malin Haugen [a], Benyamine Benali [a], David Landa-Marbán [b], Martin A. Fernø [a,b]

[a] Department of Physics and Technology, University of Bergen, Allégaten 55, 5007 Bergen, Norway
[b] Energy & Technology, NORCE Norwegian Research Centre AS, Nygårdsgaten 112, 5008 Bergen, Norway

ARTICLE INFO

Editor: Dr. Oleg Pokrovsky

Keywords:
Carbonate dissolution
CO_2 exsolution
Mineralization
Surface reactive area
Hydrodynamics
GCS

ABSTRACT

Geological carbon storage (GCS) in deep underground formations presents a significant opportunity to mitigate anthropogenic emissions of carbon dioxide in the context of climate change. The injected carbon dioxide may acidify the formation brine and dissolve carbonate minerals in the storage formations. Understanding the dynamics of carbonate dissolution at reservoir conditions is crucial for assessing the integrity and stability of reservoir rocks. Using carbonate-functionalized micromodels we investigate the pore-scale dynamics of carbonate dissolution and shed light on the interplay between surface reactions and mass transfer with relevance for geological carbon storage. Our experimental observations reveal the complex interplay between carbon dioxide exsolution/mineralization and mineral dissolution/precipitation during injection. Local chemical reactions and hydrodynamics impact the dissolution rate, whereas the presence of a free carbon dioxide phase can impede carbonate dissolution. Hence, we provide new experimental data that enhance our fundamental understanding of coupled geochemical GCS reactions that can augment the development of accurate and reliable constitutive models that assess leakage risks and the stability of mitigation techniques such as microbial-induced carbonate precipitation.

1. Introduction

Geological carbon storage (GCS) may mitigate anthropogenic carbon dioxide (CO_2) emissions and contribute to achieve Net-Zero Carbon emissions by 2050 (Pachauri and Reisinger, 2007). Captured carbon dioxide is injected into deep subsurface geological storage sites, such as saline aquifers and depleted hydrocarbon reservoirs, where the CO_2 is permanently stored through a range of trapping mechanisms acting at different length and time scales. Dissolution trapping occurs when the injected CO_2 partly dissolves into the aqueous phase, and the dissolution rate is influenced by the reservoir temperature, pressure and brine salinity (Chang et al., 2017). The aqueous phase acidity increases during the dissolution process (Morais et al., 2016), and the purity of the injected CO_2 stream determines the pH of carbonated formation brine, which can reach highly acidic levels as low as 1 in the presence of NO_2 and SO_2 (Ellis et al., 2010). Consequently, geochemical interactions occur between the acidic aqueous phase and carbonate minerals within the storage formation, potentially inducing mineral dissolution that could affect CO_2 plume migration and increase the risk of leakage (Deng et al., 2013; Deng et al., 2015).

To mitigate such risks, microbial-induced calcium carbonate precipitation (MICP) has been suggested as a mitigating technology that forms hydraulic barriers in pre-existing or new CO_2 leakage pathways (Cunningham et al., 2014; Phillips et al., 2013). However, the introduction of CO_2 into the system could significantly lead to the abrasion of calcite crystals (Mitchell et al., 2013). To estimate the MICP sealing integrity, kinetic studies of carbonate mineral dissolution at reservoir conditions are essential (Mitchell et al., 2013). Moreover, these studies should be performed at timescales where the CO_2 is mobile (Cunningham et al., 2011). Numerous studies have been performed to understand $CaCO_3$ dissolution rates pertaining to CO_2 geological storage under various conditions of temperature, pressure, pH and salinity (Kaufmann and Dreybrodt, 2007; Liu and Dreybrod, 1997; Morse, 2018; Yoon et al., 2019). The intricate mass transfer dynamics within porous media play a pivotal role in influencing the thickness of the diffusion boundary layer at the liquid-solid interface (Liu and Dreybrod, 1997). Notably, during instances of low injection velocities, the weak shear forces from the flow result in diminished acid mass transfer at the interface. This, in turn, leads to mass transfer regimes taking precedence over the dissolution process due to lower mass transfer rates compared to reaction rates.

* Corresponding author.
E-mail address: Na.Liu@uib.no (N. Liu).

https://doi.org/10.1016/j.chemgeo.2023.121782
Received 19 June 2023; Received in revised form 11 October 2023; Accepted 12 October 2023
Available online 15 October 2023

Furthermore, the wettability of $CaCO_3$ determines the thickness of the water film present on the solid surface, and the dissolution rates have been validated to be linearly dependent on this thickness (Buhmann and Dreybrodt, 1985). Consequently, the kinetics of $CaCO_3$ dissolution in porous media was governed by a plethora of parameters including pH, porous media characteristics, flow velocity, and the intrinsic properties of $CaCO_3$ precipitates (Molins et al., 2014).

However, the underpinning physics and geochemical interactions that form the basis for current understanding of the interplay between pH, flow velocity, and porous media have not been sufficiently validated against experimental data. Micromodels are commonly employed to acquire fundamental insights into physical behaviors, thereby facilitating the development of more precise and robust upscaled constitutive models designed for the continuum scale (Morse et al., 2007). However, conventional micromodels fashioned from materials like glass, silicon, or polymeric, often lack the capacity to faithfully represent real rock mineralogy, and thus are limited in their description of reactive transport (Yoon et al., 2019; Yoon et al., 2012). The functionalization of micromodels for desired chemical and surface characteristics has emerged as an appealing avenue for investigating reactive transport and interfacial phenomena using microfluidics (Haugen et al., 2023b; Xu and Balhoff, 2022).

Within this investigation, we employed carbonate-functionalized micromodels wherein in situ $CaCO_3$ precipitates were generated through the utilization of MICP technology (Liu et al., 2023). This approach allowed us to scrutinize the intricate mechanisms of $CaCO_3$ dissolution within porous media, accentuating the interplay between surface reactions and mass transfer. Our study aims to bridge the gap between simulation and experiment, enabling a more accurate understanding of the complex processes involved in carbonate dissolution within the GCS context. We focus our analysis at the pore-scale, and highlight the importance of local hydrodynamics on reactive transport. New experimental data was provided that shed light on the coupled kinetics of carbonate precipitation and dissolution during CO_2 injection. Our mechanistic approach enables validation and development of more precise and robust constitutive models for the continuum scale studies of MICP as a GCS leakage mitigation technology.

2. Experimental section

2.1. Fluids

To reduce the $CaCO_3$ reactivity within the water phase before CO_2 injection, a low salinity brine (1.12 mmol/L Ca^{2+}) was used instead of pure water. The concentration of Ca^{2+} was calculated based on the solubility of $CaCO_3$ in pure water at test conditions (100 bar, 35 °C) (Coto et al., 2012). Buffer solutions with equal concentrations of phosphoric, acetic and boric acids (see Table 1) were titrated with sodium hydroxide to adjust the pH between 3.0 and 7.0. Carbonated water (CO_2-saturated water) was made by mixing CO_2 with distilled water at elevated pressure (20 barg above test pressure) and room temperature. The carbonated water was equilibrated using a PEEK accumulator for seven days. The pH of carbonated water was calculated to 3.11 based on the CO_2 solubility in water from an improved model (Duan and Sun, 2003). A 'strong' and a 'weak' acid solution (see Table 1) containing different concentrations of HCl acid were used to evaluate the effect of pH on dissolution rate.

Table 1
Summary of fluid properties.

Solutions	Composition	Concentration [mM]	pH
Brine	Calcium chloride ($CaCl_2{\cdot}H_2O$, 31,306, Sigma-Aldrich)	1.12	6.78
Buffer solutions	Phosphoric, acetic and boric acid (Sigma-Aldrich)	40	3, 4, 5, 6, 7
	Sodium hydroxide (NaOH, > 98% pellets, Sigma-Aldrich)	–	
CO_2-saturated water	Carbon dioxide gas (CO_2, >99.99 mol%)	1340 [a]	3.11
	Distilled water	–	
'Weak' acid	Hydrochloric acid (HCl, ACS reagent, 37%, Sigma-Aldrich)	27.54	1.56
'Strong' acid	Hydrochloric acid (HCl, ACS reagent, 37%, Sigma-Aldrich)	138.04	0.86

[a] calculated based on CO_2 solubility.

2.2. Micromodel and experimental setup

Pore-scale dissolution and precipitation kinetics were studied using a high-pressure microfluidic device with a realistic pore network based on a thin section from a natural sandstone (Liu et al., 2023). The pore network contains 36 (4 columns × 9 rows) repetitions of a unique pore pattern, with an overall porosity of 0.61 and permeability of 2.97 Darcy. The microfluidics has four injection ports and two distribution channels (connecting port 1 to 2, and port 3 to 4) allowing fluid injection and/or production through the pore network (Fig. 1). Dynamic pore-scale processes were captured with a Zeiss fluorescent microscope (Axio Zoom. V16, Zeiss) with a motorized scanning stage. Pore pressure was controlled by a high precision plunger pump (Quizix Q5000–10 K), and a back pressure regulator (EB1ZF1 Equilibar Zero Flow) connected to a pressurized 1 L nitrogen cylinder at 100 bar. Temperature was kept constant at 35 ± 0.5 °C by circulating warm water through internal copper tubes in the chip holder. A more detailed description of the experimental setup is found elsewhere (Benali et al., 2022; Haugen et al., 2023a).

2.3. Fluorescence imaging

The aqueous phase pH changes during $scCO_2$ drainage were visualized and quantified using a fluorescent pH indicator (pHrodo™ Red, ThermoFisher). The fluorescent intensity has an inverse functional relationship with pH; low intensity at alkaline conditions, and increases as the pH decreases (Scientific, 2022). The fluorescence intensity was calibrated to visualize and quantify CO_2 mass transfer at the pore scale (Fig. 2). For calibration, each buffer solution mixing with 8 μmol/L dye was injected into the micromodel at experimental conditions (100 barg and 35 °C) for >50 PVs. Continuous scans were taken for 24 h with intervals of 20 min and the average fluorescent intensity was calculated. During imaging, both light intensity and exposure time were kept constant. The plot of pH and intensity shows the calibration relationship fits the following equation with adjusted r-squared (R^2) of 0.998, consistent with previous measurements (Chang et al., 2016; Chang et al., 2017). Therefore, the pH value of the aqueous phase was quantified from the fluorescence images with a maximum uncertainty of ±0.75. Note that the fluorescence-pH relationship is only calibrated for pH range 3.0 to 7.0, and cannot accurately represent aqueous phase pH outside this range.

$$Fluorescence\ intensity = 624.52 - 268.75pH + 55.06pH^2 - 3.82pH^3 \quad (1)$$

2.4. Image analysis

Pore network images were captured using a microscope equipped with both brightfield and fluorescence channels. The whole pore network, comprising a total of 121 distinct images, was acquired in 277 s. These images, depicting the pore network in both fluorescence and brightfield channels, were continuously recorded during the injection of CO_2 and acid solutions. For enhanced analysis, translucent crystals were manually assigned a red colour. Extraction of the red-colored crystals was accomplished using a Python script employing the HSV colour thresholder in OpenCV. The size of crystals was calculated by multiplying the number of pixels containing crystals with the pixel area

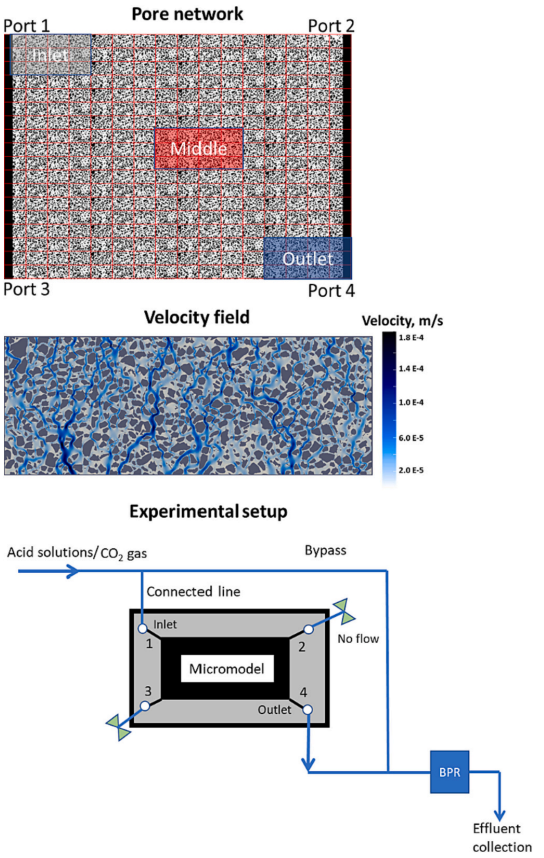

Fig. 1. Pore network and experimental setup. Top row: The pore network of micromodel was constructed based on a thin section obtained from an authentic sandstone rock sample. The porous pattern constitutes 36 repetitions (arranged in a 4 × 9 configuration) of a smaller unique pattern, which was split into 16 columns and 18 rows for measurement of local crystal/gas saturation and porosity. The pore network was divided into 288 units (18 rows × 16 columns). Three areas of interest (AOIs) were defined: inlet, middle and outlet. Each AOI contained 12 units (3 rows × 4 columns), with comparable pore structure and porosity (inlet: 0.628; middle: 0.641; outlet: 0.623). Middle row: A simulation was performed to visualize the magnitude of steady-state flow velocity within the small unique pattern, excluding the presence of crystals (confer to https://daavid00.github.io/pymm/examples.html#image for details on the simulation setup). Bottom row: A simplified schematic of the experimental setup illustrates the intended flow into the pore network.

resolution (19.18 μm^2/pixel).

Crystal saturation (S_c) was quantified by dividing the crystal size by the pore space. We assume that crystals occupy the entire pore depth and possess a horizontal area as depicted in the 2D segmented images, causing an overestimation of crystal size. For the fluorescence channel image, a two-class separation was performed using the Multi-Otsu algorithm from the scikit-image library (Van der Walt et al., 2014): the grains/CO_2 phase and the water phase (fluorescent tracer). CO_2 saturation (S_g) was then computed as the ratio of the pore space minus the water phase and crystals to the total pore space.

2.5. Experimental procedure

The experimental procedure consists of the following four main steps:

1. Microbial induced carbonate precipitation (MICP): $CaCO_3$ crystals were formed in the pore network via the uratolytic pathway – *Sporosarcina pasteurii* stains produce urease enzymes for hydrolysis of urea, promoting the chemical precipitation of $CaCO_3$. The experimental procedure is detailed in our previous work (Haugen et al., 2023b; Liu et al., 2023; Song et al., 2018).
2. Enabling flow through the pore network: Subsequent to the MICP process, the microfluidic device was disconnected from the setup and placed in a weak acid to open clogged injection and production ports. The pore network remained undisturbed and partly filled with $CaCO_3$ precipitates from step 1 above. Once reconnected, approximately 10 pore volumes (PVs) of brine were injected from port 1 to 2, and port 3 to 4 to remove residual weak acid and bacterial solutions in the ports, near-port pores and channels.
3. Pressurization: The brine saturated pore network was pressurized to operating pressure (100 barg) with brine injection (50 μL/min) through bypass lines against a back pressure regulator. The pressure was controlled by the back pressure regulator at the outlet.
4. Drainage process: Key parameters for six drainage experiments are summarized below (see Table 2) and may be divided into two categories: dissolution mechanisms (Exp M1) and dissolution kinetics (Exp K1-K4). Carbonate dissolution mechanisms were studied during primary drainage with supercritical CO_2 ($scCO_2$) over a period of 67 h. Kinetic studies (K1-K4) used CO_2-saturated acid solutions (saturated at 120 barg), and injection was maintained until all the crystals in the pore network were dissolved.

The flow and reaction dynamics in the pore network were visualized by the high-resolution fluorescent microscope system, described below.

3. Results and discussions

3.1. Mechanistic study of carbonate dissolution and precipitation during $scCO_2$ injection

3.1.1. Dynamic reaction-induced carbonate crystal dissolution in a single pore

Reaction-induced carbonate dissolution was studied in single pore initially filled with brine (Fig. 3). The aqueous phase pH decreased during primary drainage with increasing gas saturation (S_g), and the acidic brine reacted with the carbonate crystal to initiate the dissolution process; the formation of bicarbonate ions (HCO_3^-) increased the local aqueous phase pH and restricted further dissolution. The aqueous phase pH reached its minimum (3.52) after 9 h, coinciding with the maximum (554 μm^2/h) crystal dissolution rate. As the crystal size decreased due to the dissolution process, the pH increased from its minimum and regained initial pH values – with a corresponding reduction in the dissolution rate. The pH of brine was inversely correlated with S_g and increased due to the reaction of carbonate dissolution, which produced HCO_3^- and CO_3^{2-}. The dissolution rate scaled linearly with the aqueous phase pH.

The CO_2 mass transfer was dominated by $scCO_2$ dissolution in the brine and convection of dissolved CO_2 ($dsCO_2$) in the pore network (Chang et al., 2016). The $scCO_2$ dissolution is determined by the CO_2 partial pressure and system temperature (Kordač and Linek, 2008), whereas convection of $dsCO_2$ was strongly influenced by local hydrodynamics and carbonate dissolution (Dhar et al., 2022). The solubility of $scCO_2$ in brine was 0.2 M, corresponding to an aqueous phase pH of 3.5 (Duan and Sun, 2003). The interfacial area dominated the propagation of CO_2 in the pore network at early times ($\leq$ 8 h), and the pore network tortuosity (Grogan et al., 1988; Rezk et al., 2022) increased the diffusive

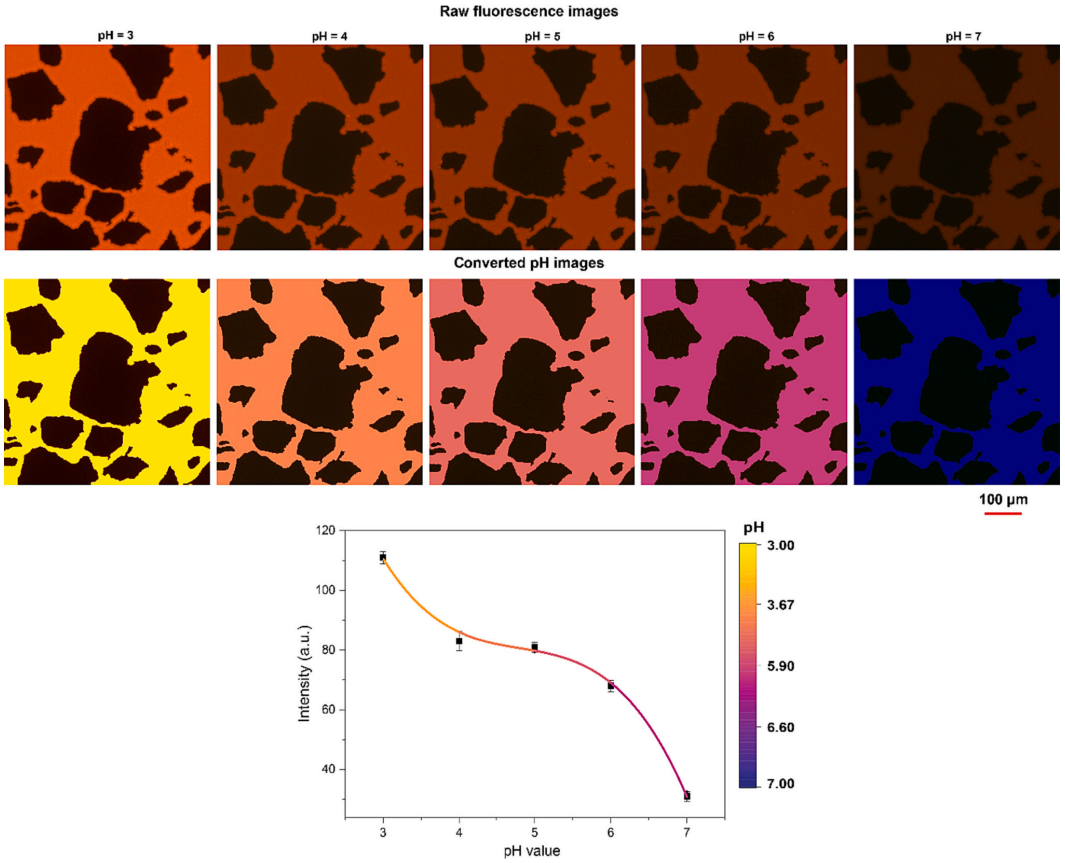

Fig. 2. Calibration between pH and fluorescent intensity for the pHrodo™ Red dye at concentration of 8 µmol/L. Top row: Raw fluorescence images showing the reduction in fluorescence intensity with increasing pH between 3.0 and 7.0. Bottom row: Converted pH images using the pH-fluorescence intensity calibration. Bottom graph: The calibration between fluorescence intensity and pH plotted using the Plasma colormap that scale linearly with fluorescence intensity and pH values calculated from Eq. (1). Error bars represent standard deviations. (For interpretation of the references to colour in this figure legend, the reader is referred to the web version of this article.)

Table 2
Summary of all drainage experiments. All injection test used the same flow velocity (2.03 mm/min), pore pressure (100 barg) and constant temperature (35 °C).

Exp. #	$S_{crystal, inital}$ [b]	Injection fluid (aqueous phase pH)	Figures
M1 [a]	$8.9 \bullet 10^{-2}$	$scCO_2$ (3.50)	Figs. 2-5
K1	$0.93 \bullet 10^{-2}$	CO_2-saturated 'strong' acid (0.86)	Figs. 6, 7
K2	$1.6 \bullet 10^{-2}$	$scCO_2$ (3.50) + CO_2-saturated 'strong' acid (0.86)	Figs. 6, 7
K3	$1.0 \bullet 10^{-2}$	CO_2-saturated 'weak' acid (1.56)	Fig. 6
K4	$1.1 \bullet 10^{-2}$	CO_2-saturated deionized water (3.11)	Fig. 8

[a] capillary number [log C_a]: −3.65.
[b] initial crystal saturation [fraction of pore volume].

loss; unsaturated CO_2-brine was observed in the field of view (FOV). The interfacial area increased with increasing S_g, and the minimum aqueous phase pH (pH = 3.52) coincided with the highest dissolution rate (see Fig. 3). The reduction of $dsCO_2$ during carbonate dissolution (because dissolution uses H^+ from the reaction $dsCO_2 + H_2O = HCO_3^- + H^+$) perturbated the solubility equilibrium, enabling further diffusive CO_2 mass transfer from the surrounding gas phase into the brine. A temporary reduction of S_g was observed (5.6 percentage points between 10 and 11 h), corroborating that carbonate dissolution increases pH and reduces S_g. The changes in brine composition and ionic strength (i.e. increasing Ca^{2+} and HCO_3^- ions) also influenced the CO_2 displacement with brine in the pore network (Cao et al., 2015). The flow of CO_2 was preferentially through high permeable areas with less flow resistance, consistent with previous work (Kazemifar et al., 2016; Zhang et al., 2011).

Understanding the mechanisms of mineral dissolution-precipitation caused by CO_2 injection is of key importance to accurately model fluid flow and forecast GCS security (Lu et al., 2013). The injection of CO_2 perturbates the natural geochemical equilibrium by increasing the CO_2 partial pressures and reducing the pH of formation water, and thereby initiating the dissolution of carbonate minerals in the near wellbore region. Formation of bicarbonate can also increase the aqueous phase pH downstream to trigger secondary carbonate precipitation (Oelkers et al., 2008). The dissolution and precipitation of minerals influence multiphase flow properties during carbon storage by changing the morphology, porosity, and permeability of the porous rock medium. Our pore-scale observations (Fig. 4) show that the size reduction followed

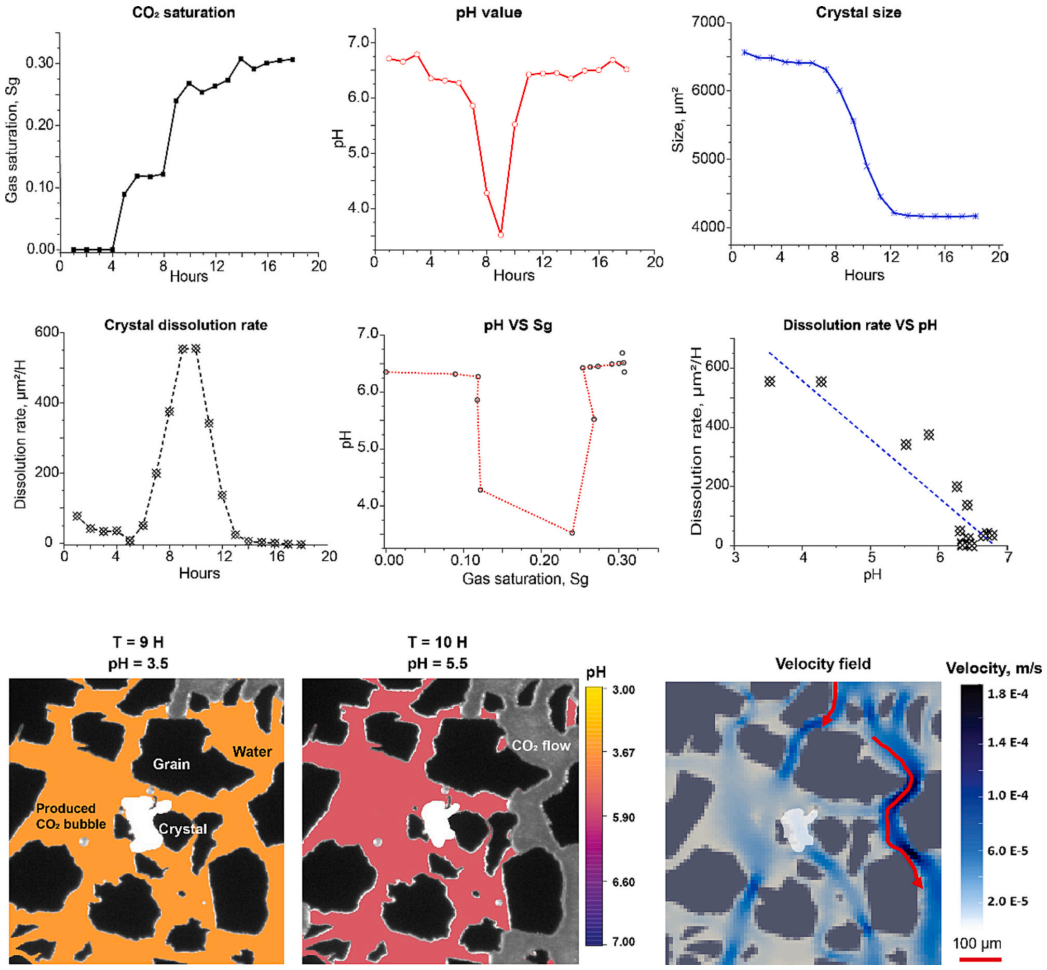

Fig. 3. Dynamic reaction-induced carbonate crystal dissolution in a single pore during primary drainage $scCO_2$ injection. Top row: Plots of gas saturation (S_g), aqueous phase pH and crystal size. Middle row: Temporal crystal dissolution rate, pH-S_g relationship and the dissolution rate versus aqueous phase pH. $T = 0$ h aligns with initial CO_2 invasion of the entire pore network (not FOV) during primary drainage $scCO_2$ injection. Each side of the squared FOV is 500 pixels from the crystal center, and the aqueous phase pH was calculated ($\pm$ 0.03) using the average FOV fluorescence intensity. Bottom row: Visualization of the pore-level gas mass transfer and carbonate dissolution during primary drainage $scCO_2$ injection using calibrated fluorescence images (aqueous phase pH 3.5 and 5.5). Simulated steady-state FOV flow velocity field (Liu et al., 2023), where the red lines indicate the migration of $scCO_2$ during drainage coinciding the high velocity regions. (For interpretation of the references to colour in this figure legend, the reader is referred to the web version of this article.)

the aqueous phase pH towards its minimum (3.8) over the first 10 to 15 h. The dissolution reaction consequently buffered the aqueous phase pH, reducing the carbonate dissolution rate and stabilizing the carbonate crystal size after approximately 40 h. Secondary precipitation was then observed (increasing crystal size) until 50 h, coinciding with a reducing of aqueous phase pH (from >6.9 to 6.5) caused by the invasion of $scCO_2$ in FOV or by increased precipitation of secondary carbonate phases with time.

Carbonate dissolution and precipitation were strongly coupled in the pore, with an inverse relationship between pH and carbonate crystal size; dissolution occurred in a low pH environment, whereas precipitation was associated with an elevated pH. The invasion of $scCO_2$ triggered secondary carbonate precipitation in the pore, explained by the following aspects: the elevated concentration of $dsCO_2$ in brine promoted hydrolysis of H_2CO_3, increasing CO_3^{2-} and H^+ ions in the solution; the dissolution of carbonate increased the concentration of Ca^{2+} and CO_3^{2-} ions in the aqueous phase and increased the pH - which in turn facilitated the $CaCO_3$ precipitation; the solubility of $CaCO_3$ decreased as the salinity and ion strength changed during dissolution, resulting in a high supersaturation; continuous $scCO_2$ injection induced water evaporation from the brine in the vicinity of the carbonate crystal, leading to salt precipitation (Miri and Hellevang, 2016). Hence, secondary carbonate precipitation was controlled by the local aqueous phase pH, carbonate species concentrations and supersaturation state, consistent with previous work (Hellevang et al., 2019; Lu et al., 2013; Zhu and Lu, 2009).

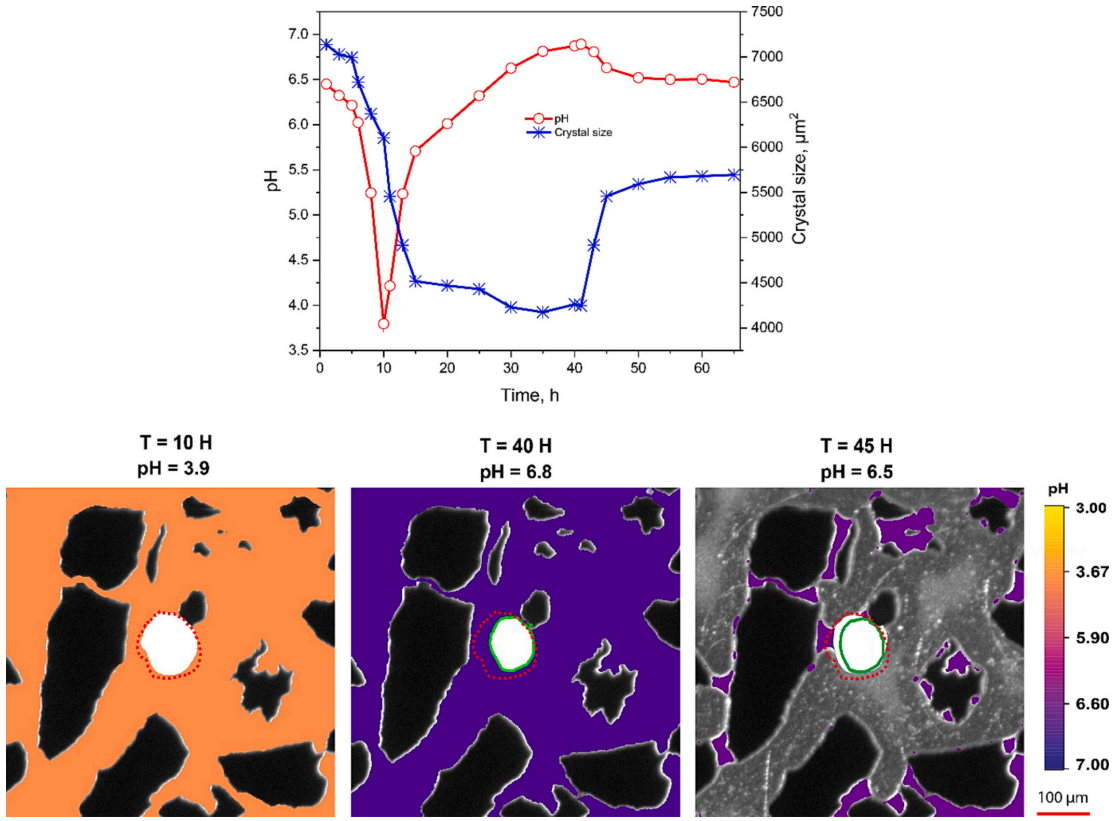

Fig. 4. Carbonate dissolution and secondary precipitation processes during primary drainage $scCO_2$ injection. Top: The relationship between local pH and crystal size. Bottom row: Calibrated fluorescence intensity images show the development in crystal size during the dissolution-precipitation processes for three pH values; at pH 3.9 (after 10 h, initial crystal size indicated with red, dotted line); at pH 6.8 (after 40 h); at pH 6.5 (45 h, crystal size at 40 h indicated with green line). Hence, the size of the carbonate crystal initially decreased (up to 40%) due to dissolution, then increased due to secondary precipitation process as a result of pore-level perturbation of the surrounding aqueous solution that deposited carbonate material onto the crystal surface. Note: From 35 h, the pH measurement was out of calibration range (i.e., pH > 7), underestimating the pH value. (For interpretation of the references to colour in this figure legend, the reader is referred to the web version of this article.)

3.2. The presence of CO_2 exsolution and mineralization

The injected CO_2 may, under certain conditions, change its state in the subsurface through two main transformation pathways: CO_2 exsolution refers to evaporation of gaseous CO_2 from a liquid solution, with the associated bubbles or gas pockets forming in a liquid (Al-Amshawee et al., 2021; Allison et al., 2021); whereas CO_2 mineralization refers to the process when the CO_2 phase converts into stable carbonate compounds (Gadikota, 2021). At the pore-scale (Fig. 5) we observed that both CO_2 exclusion and mineralization may co-occur in porous media. Exsolution was observed when the $dsCO_2$ concentration exceeded the CO_2 solubility limit, and a free CO_2 phase exsolved from the supersaturated aqueous phase. CO_2 bubbles nucleated at the carbonate crystal surfaces in regions with low (< 4.0) pH, explained by the following aspects: i. the low pH environment initiated carbonate dissolution and reduced local CO_2 solubility; ii. the increased concentrations of HCO_3^- and CO_3^{2-} shifted the equilibrium of H_2CO_3 hydrolysis via Le Chatelier's principle (Le Chatelier, 1884), leading to supersaturation due to increased $dsCO_2$ at the interface between the crystal and surrounding brine; iii. the rough carbonate crystal surfaces provided ideal nucleation sites for the CO_2 exsolution process.

Isolated injected CO_2 bubbles were encapsulated with carbonate minerals when they reacted with calcium cations in the water film covering the crystal (Fig. 5). This phenomenon, known as 'CO_2 mineral trapping' (Bachu et al., 1994), has significant potential for GCS applications as it can effectively immobilize CO_2 for long periods of time. The precipitation process was sustained by upstream carbonate dissolution, creating neutral or even alkaline environments and availability of calcium cations in the solution around the bubble (refer to the images located in the bottom row of Fig. 5).

Overall, these findings provide valuable insights into the mechanisms underlying CO_2 mineral trapping and suggest potential pathways for enhancing the effectiveness of geological carbon storage strategies. The CO_2 transformation processes occur in the pore during CO_2 injection, affecting reservoir properties such as porosity and permeability, and ultimately influencing the transport and mobility of CO_2 in the porous media (Xu et al., 2017). The transformation of the injected CO_2 in GCS reservoirs could strongly influence the permeability of the rock and fluid paths and a better understanding of transform mechanisms will improve predictions of the long-term CO_2 storage safety.

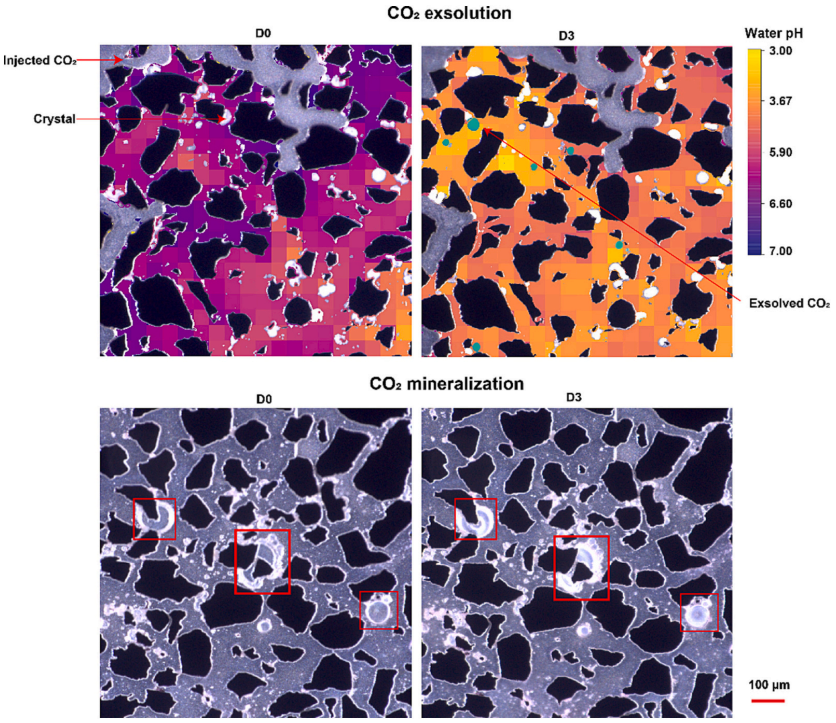

Fig. 5. Transformation of CO_2 in the pore network: CO_2 exsolution and mineralization. Top row: Calibrated fluorescence intensity images (1000 pixels) display the local pH variations during the carbonate dissolution and gas exsolution processes. The initial pH (FOV average pH 6.7) decreased to 3.9 (FOV average) after three days, dissolving the carbonate crystals. During the carbonate dissolution, CO_2 bubbles nucleated and grew on the crystal surfaces. The bubbles preferentially nucleated in regions with low pH. Bottom row: the mineralization process of trapped CO_2 bubbles (red squares). The precipitation of carbonate started at the gas-water interface and grew towards the center of CO_2 bubble to form hollow $CaCO_3$ microspheres. Note: The pH measurement was out of calibration range (i.e., pH > 7) after 10 h and local pH values were therefore not achievable for the mineralization process. (For interpretation of the references to colour in this figure legend, the reader is referred to the web version of this article.)

3.3. Porosity changes by dissolution and secondary precipitation

Geochemical reactions that cause carbonate dissolution/precipitation can occur during CO_2 injection, leading to temporal changes in the pore morphology, local flow velocities and porosity. Carbonate dissolution was initially observed in the entire pore network (Fig. 6) due to low pH of the aqueous phase. Initially, the injection of CO_2 caused a decrease in the pH of the aqueous phase, initiating the dissolution of carbonate crystals. After 10 h of injection, approximately 12.5% of the carbonates underwent dissolution primarily at the inlet, leading to an increase in porosity and S_g. After 40 h, secondary precipitation and CO_2 mineralization enhanced the overall carbonate saturation (S_c). Isolated CO_2 bubbles reacted with calcium cations and formed new minerals, causing a reduction in S_g. The newly formed minerals, however, were susceptible to dissolution or detachment from the pores due to the flow of CO_2. The carbonate dissolution increased local porosity (and permeability), enhancing CO_2 mobility during injection and accelerating further geochemical reactions. The dissolution reactions increased the aqueous phase pH locally, leading to secondary $CaCO_3$ precipitation that reduced porosity (and permeability). The relationship between crystal saturation (S_c) and gas saturation (S_g) for the entire pore network, as depicted in the bottom images presented in Fig. 6 shows reduced S_c (up to 25%) in the inlet region that lowered the capillary pressure (changed pore morphology) and increased S_g. Secondary carbonate precipitation and CO_2 mineralization in the outlet regions lead to the increase of S_c (45 h). After 67 h, crystals located near the inlet (port 1) and outlet (port 4) underwent either dissolution or detachment from the pore due to the injection of CO_2. The results were comparable to single pore observations (see Fig. 3): the injection of CO_2 caused the reduction of the aqueous phase pH and initiated carbonate crystal dissolution; the dissolution reaction in the inlet enlarged the pore throats and increased porosity locally; over time, secondary precipitation and CO_2 mineralization became the dominating geochemical reactions (predominantly in the outlet), leading to increasing S_c. The spatial distribution of crystal in the pore network highlights the dynamics of CO_2-water-mineral interactions in porous media, where the continuous flow of CO_2 could cause changes in the distribution of crystals, ultimately influencing the porosity, permeability, and fluid flow, particularly in near wellbore regions.

The comprehensive assessments above shed light on the compounded processes of CO_2-water–mineral interactions during CO_2 injection, and their coupling to multiphase flow in subsurface reservoirs in the context of carbon storage in carbonate-mineral rich formations. These geochemical reactions, including carbonate dissolution, secondary precipitation, CO_2 exsolution and mineralization can change the morphology, porosity, permeability, and wettability of the storage formation and influence storage efficiency, injectivity and safety.

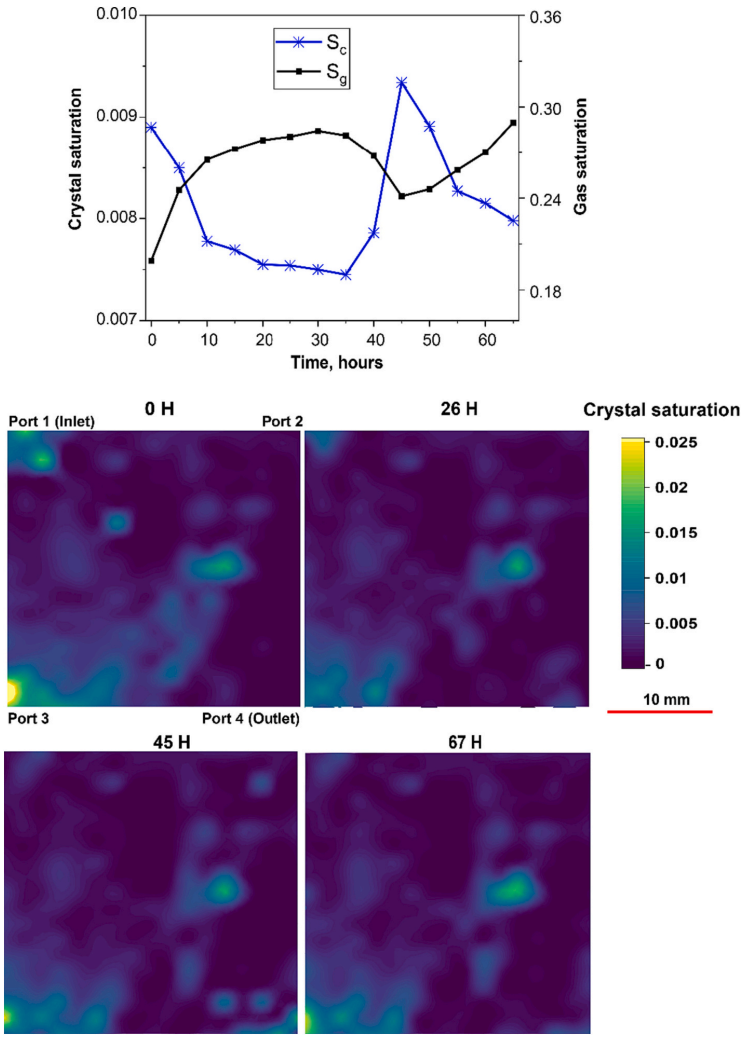

Fig. 6. Carbonate crystal saturation changes (entire pore network) during primary drainage $scCO_2$ injection (Exp M1). Top row: Crystal saturation (S_c) and gas saturation (S_g) as a function of time. Bottom row: Spatial distribution (contour plots) of local crystal saturation over time. Note: The pixel-based S_c was calculated under the assumption that each crystal pixel fills the entire pore space height (30 μm) and should be considered as an upper bound.

3.4. Kinetics of carbonate dissolution in the pore network

The $CaCO_3$ dissolution kinetics in porous media are primary dominated by surface-controlled chemical reactions and mass transfer resistance (Kaufmann and Dreybrodt, 2007; Liu and Dreybrod, 1997; Morse, 2018; Yoon et al., 2019). At the solid–fluid interface, the following parallel reactions (Plummer et al., 1978) occur:

$$CaCO_3 + H^+ \overset{k_1}{\rightarrow} Ca^{2+} + HCO_3^- \quad (2)$$

$$HCO_3^- + H^+ \overset{k_2}{\leftrightarrow} H_2CO_3 \overset{k_3}{\leftrightarrow} dsCO_2 + H_2O \quad (3)$$

where the rate coefficient k_i (i.e., k_{1-3}) is temperature dependent.

Carbonate dissolution (Reaction 2) is solely influenced by the concentration of H^+ ions (a_{H+}) in aqueous phase, and the aqueous phase pH equals to -log(a_{H+}). On the other hand, hydrolysis of H_2CO_3 (Reaction 3) depends on the CO_2 partial pressure and temperature (Kaufmann and Dreybrodt, 2007). As k_i remained constant in this study, the carbonate dissolution was primarily influenced by the aqueous phase and the CO_2 partial pressure. Determining parameters for the dissolution rate are directly linked to experimental operating conditions including aqueous phase pH, flow velocity, interface area, and pore geometry. These conditions allow for a systematic and controlled investigation of porous media dissolution kinetics (Fig. 7 **A**).

The average carbonate dissolution rate in the entire pore network decreased linearly with increasing pH, with a strong correlation between the rate of dissolution and a_{H+} (Fig. 7 **B**). This suggests that pH plays a significant role in controlling the (averaged) dissolution rate of the entire pore network, consistent with our claim that the chemical reaction at the solid-fluid interface (Reaction 2) is the primary mechanism

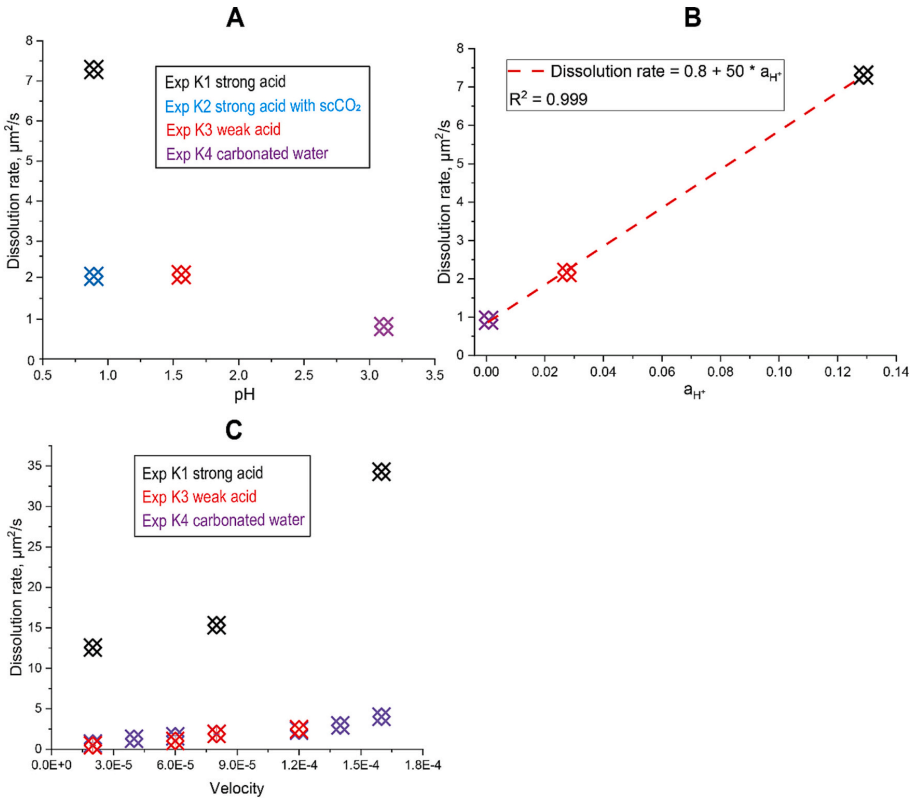

Fig. 7. Carbonate dissolution rate as a function of aqueous phase pH, H^+ concentration (a_{H+}) and local flow velocity. Detailed information regarding the experimental conditions is available in Table 2. Plot A: The dissolution rate is reduced with increasing aqueous phase pH, where the lowest pH (0.86, Exp K1) showed the highest dissolution rate (7.31 $\mu m^2/s$). The presence of a free $scCO_2$ phase (Exp K2) reduced the dissolution rate by 70% relative to the same pH (0.86, Exp K1), discussed more below. Plot B: The experimentally verified linear relationship between the dissolution rate and a_{H+} in porous media. Plot C: Dissolution rate as a function of local flow velocity increased linearly for three different aqueous phase pH values. Note that the flow velocity field was simulated without the presence of carbonate crystals (Landa-Marbán, 2023; Liu et al., 2023). The dissolution rate used was the average for the entire pore network for each experiment (K1-K4).

for carbonate dissolution in porous media. Locally in single pores, however, the miscible displacement of formation water (by the injected acid solutions) enabled transport of H^+ ions across the liquid-solid interface to contact the crystal surface. Hence, local hydrodynamics plays a crucial role for the mass transfer at the liquid-solid interface (Liu and Dreybrod, 1997). The local flow velocities strongly affect the shear stress and transfer of H^+ at the interface (Lv et al., 2021), resulting in locally varying dissolution rates in the pore network. We observed that the dissolution rate increased linearly with flow velocity for three different aqueous phase pH values (Fig. 7 **C**). Higher velocities induced higher shear stress and enhanced the mass transfer at the interface to accelerate the dissolution process. Hence, the mass transfer at the interface between the liquid and solid phases is essential for the local (single pore) dissolution process. Furthermore, the crystal surface was hydrophilic and coated with a water film (depicted in the upper-right images of Fig. 8), emphasizing the importance of mass transfer at the interface because hydrophilic surfaces may reduce the transport of H^+ ions to the crystal surface.

3.5. Effect of a free CO_2 phase on carbonate dissolution

The CO_2 phase (either injected or exsolved) determined the local dissolution rate by effectively blocking the diffusion of H^+ in the solid-liquid interface through a protective shield for engulfed crystals (Fig. 8). The exsolved CO_2 bubbles consistently nucleated at the surface of crystal, merged and engulfed the crystal to reduce the dissolution rate by almost 90%. The merging of CO_2 bubbles eventually led to partial detachment from the crystal surface, thereby allowing the dissolution process to resume at a higher rate. The dissolution rate reduction suggested that the presence of CO_2 bubbles also decreased the reactive surface area and the reaction rate (Song et al., 2018). Comparatively, the dissolution rate of crystals in the aqueous phase was initially much higher than that of crystals within the CO_2 phase, a distinction captured in the bottom images of Fig. 8. As depicted in the upper-right images of Fig. 8, the crystals exhibited hydrophilic properties and were covered with a water film (even when fully engulfed by a CO_2 phase). The water film facilitated the re-establishment of a chemical equilibrium between H^+, H_2CO_3 and $CaCO_3$ contributing to further inhibit dissolution. The presence of exsolved CO_2 led to an elevation in both the CO_2 partial pressure and the concentration of HCO_3^- within the solution. In addition, the a_{H^+} in the isolated water film on engulfed carbonate crystals decreased with reaction, leading to an increased aqueous phase pH surrounding the crystal and decreased dissolution rate.

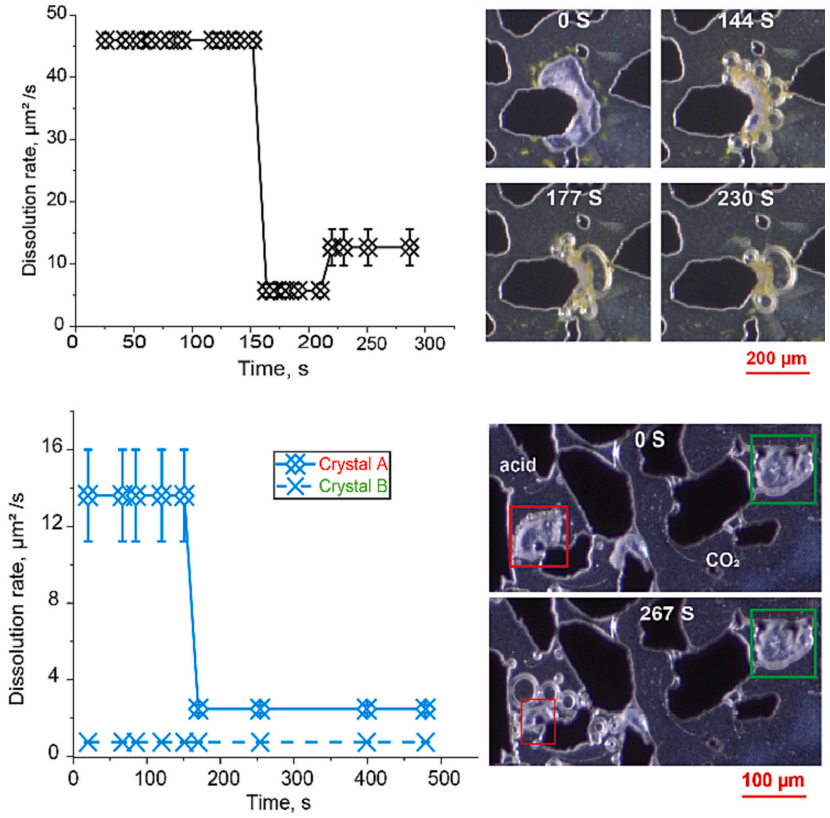

Fig. 8. Plots of crystal dissolution rate with and without the protection from CO_2 and time-series images of CO_2 exsolution from the crystal surface. Top: The high initial dissolution rate (45.95 μm^2/s) was reduced to 5.71 μm^2/s due to CO_2 exsolution from the crystal surface in the presence of a 'strong' acid (Exp K1). Bottom: The dissolution rate of crystal A (red square) was initially 13.61 μm^2/s, almost 20 times higher than of crystal B (green square, 0.74 μm^2/s) (Exp K2). The dissolution rate for crystal A decreased when the crystal was engulfed by exsolved CO_2 bubbles. (For interpretation of the references to colour in this figure legend, the reader is referred to the web version of this article.)

3.6. Pore geometry affecting the dissolution pattern

Local crystal saturation (and hence, porosity) and reactive surface area changed during injection of carbonated water (Fig. 9). The produced reactant ions (i.e., HCO_3^- and Ca^{2+}) upstream increased the aqueous phase pH and shifted the chemical equilibrium for downstream dissolution reactions. With increasing local porosity (due to dissolved crystals), the injected aqueous phase bypassed the low-permeable regions with remaining $CaCO_3$ crystals. Surface reaction (Reaction 2), as opposite to mass transfer, controlled the dissolution process ($t \leq 200$ min) because a separate CO_2 phase (from exsolution or injection) was not present; corroborated with the linear decrease in crystal number (and porosity) in the pore network (**Fig. S1**). The process became mass transfer-controlled ($t > 200$ min), with decreased dissolution rate because the tortuous pore geometry induced mass transfer resistance.

The spatially dependent dissolution rate demonstrated the strong coupling between reactive surface area and hydrodynamics on the dissolution process (plots in Fig. 9). Initially, the inlet area dissolution rate was higher than that in middle and outlet area due to the low pH value. After 100 min, > 90% of inlet area crystals were dissolved, associated with increased local porosity and improved water injectivity. The larger outlet A_{rs} (2.4 times larger than the middle) resulted in a higher dissolution rate. After 200 min, most crystals in the inlet and middle were dissolved, and the dissolution rate approached zero. The outlet dissolution was low (89% reduction from onset), but nonzero, due to residual crystals located in low-velocity zones. The upstream dissolution increased dissolved species and decreased the aqueous phase pH, resulting in reduction of the reaction rate in the middle and outlet areas relative to the inlet. A larger reactive surface area at the outlet promoted a higher dissolution rate. This observation aligns with previous findings (Yang et al., 2018; Yoon et al., 2012), highlighting that the dissolution rate scaled linearly with the available reactive surface area for Reaction 2. Crystals positioned in high-velocity zones dissolved first, whereas residual crystals predominantly accumulated in low-velocity zones near the outlet. These findings emphasize the influence of local flow velocity and available reactive surface area for $CaCO_3$ dissolution in the presence of carbonated water.

4. Conclusions

Our experimental pore-scale observations of carbonate dissolution kinetics show the interplay between CO_2 exsolution/mineralization and mineral dissolution/precipitation during CO_2 injection. These couped processes directly impact key GCS reservoir properties (e.g., porosity and permeability), and determine local transport and mobility of CO_2 in a storage formation. Furthermore, we observed that the $CaCO_3$

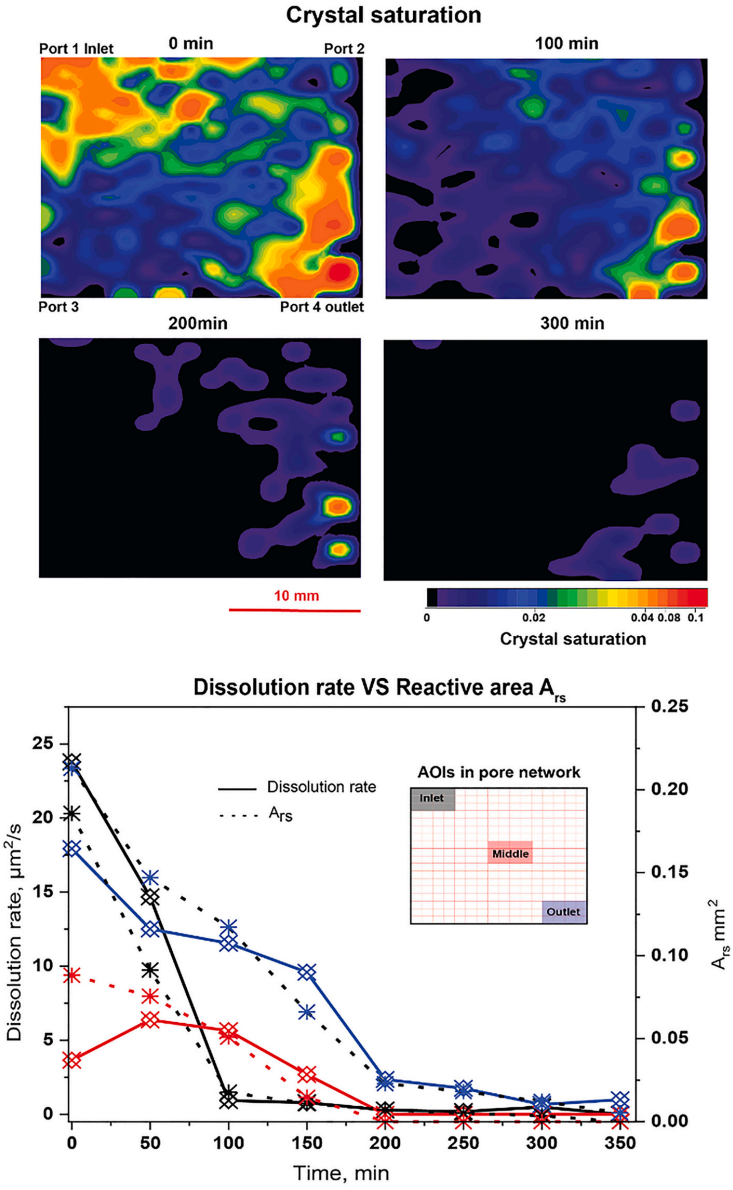

Fig. 9. Temporal changes of local crystal saturation (S_c), dissolution rate and reactive surface area (A_{rs}) during carbonated water injection (Exp K4). Top: The spatially distributed averaged unit S_c shown for four times: 0 min: at the onset, inlet and outlet regions have the highest crystal saturation; 100 min: the inlet S_c was reduced by 84% by dissolution, with an associated porosity increased by 3.7%. Outlet S_c, in comparison, was reduced by 50% where large crystals were only partly dissolved; 200 min: most of the crystals were dissolved, with some larger crystals remaining (right side); 300 min: only a few crystals located in narrow pores with low velocity and reduced mass transfer were observed. Bottom: Development in the average dissolution rate and reactive surface area (A_{rs}) for three areas of interest (see inset). Note: A_{rs} calculations use the perimeter of crystals multiplied by the depth of micromodel (30 μm). To illustrate the S_c changes more clearly, contour lines in plots were smoothed with a parameter of 9.84E-4, and spatially distributed crystal number and size in the pore network are presented in **Fig. S2**.

dissolution rate was significantly influenced by local chemical reactions and hydrodynamics. The dissolution rate increased with the reactive surface area and decreased with the pH of the aqueous phase, and the mass transfer in the diffusion boundary layer at the solid-liquid interface was controlled by local hydrodynamics. The presence of a free CO_2 phase (injected or exsolved) impedes the carbonate dissolution by reducing the reactive surface area and blocking the mass transport in the interface.

The MICP process as a mitigation technology for GCS leakage is susceptible to dissolution by CO_2-acidified brine, influencing its sealing

integrity near wellbores. The stability of MICP sealing may, however, improve over time if the carbonate crystals located in the low permeable area or the crystals become engulfed by CO_2 gas that inhibit dissolution. Hence, we argue that the coupled dissolution/precipitation processes, including the CO_2 exsolution process (releasing a mobile and buoyant CO_2 phase), needs to be considered when evaluating GCS leakage risk scenarios.

Our analysis focuses on hydrophilic carbonate crystals via the ureolytic pathway (using *Sporosarcina pasteurii* stains), resulting in a high dissolution rate due to the water film. To gain a more comprehensive understanding, further investigation is necessary to examine the influence of surface properties of crystals on the dissolution rate.

Declaration of Competing Interest

The authors declare that they have no known competing financial interests or personal relationships that could have appeared to influence the work reported in this paper.

Data availability

Data will be made available on request.

Acknowledgements

The authors would like to thank UiB engineer Kristoffer Eikehaug for preparing buffer solutions used in the work. Thanks to Dr. Jacquelin Elizabeth Cobos Mora for the knowledge sharing on chemical reactions. We acknowledge financial support from the Research Council of Norway under the following projects: Subsurface Carbonate CO_2 Storage and Security (project no. 280341), Hydrogen Storage in Subsurface Porous Media - Enabling Transition to Net-Zero Society (project no. 325457), and Centre for Sustainable Subsurface Resources (project no. 331841).

Appendix A. Supplementary data

Supplementary data to this article can be found online at https://doi.org/10.1016/j.chemgeo.2023.121782.

References

Al-Amshawee, S., et al., 2021. Roughness and wettability of biofilm carriers: a systematic review. Environ. Technol. Innov. 21, 101233.
Allison, C.M., Roggensack, K., Clarke, A.B., 2021. Highly explosive basaltic eruptions driven by CO2 exsolution. Nat. Commun. 12 (1), 217.
Bachu, S., Gunter, W., Perkins, E., 1994. Aquifer disposal of CO2: hydrodynamic and mineral trapping. Energy Convers. Manag. 35 (4), 269–279.
Benali, B., et al., 2022. Pore-scale bubble population dynamics of CO2-foam at reservoir pressure. Int. J. Greenhouse Gas Control 114.
Buhmann, D., Dreybrodt, W., 1985. The kinetics of calcite dissolution and precipitation in geologically relevant situations of karst areas: 1. Open system. Chem. Geol. 48 (1–4), 189–211.
Cao, S., Jung, J., Hu, J., 2015. CO2-brine displacement in geological CO2 sequestration: microfluidic flow model study. Appl. Mech. Mater. 752-753, 1210–1213.
Chang, C., et al., 2016. Pore-scale supercritical CO2 dissolution and mass transfer under imbibition conditions. Adv. Water Resour. 92, 142–158.
Chang, C., Zhou, Q., Oostrom, M., Kneafsey, T.J., Mehta, H., 2017. Pore-scale supercritical CO2 dissolution and mass transfer under drainage conditions. Adv. Water Resour. 100, 14–25.
Coto, B., Martos, C., Peña, J.L., Rodríguez, R., Pastor, G., 2012. Effects in the solubility of CaCO3: Experimental study and model description. Fluid Phase Equilib. 324, 1–7.
Cunningham, A.B., et al., 2011. Reducing the risk of well bore leakage of CO2 using engineered biomineralization barriers. Energy Procedia 4, 5178–5185.
Cunningham, A.B., et al., 2014. Wellbore leakage mitigation using engineered biomineralization. Energy Procedia 63, 4612–4619.
Deng, H., et al., 2013. Modifications of carbonate fracture hydrodynamic properties by CO2-acidified brine flow. Energy Fuel 27 (8), 4221–4231.
Deng, H., Fitts, J.P., Crandall, D., McIntyre, D., Peters, C.A., 2015. Alterations of fractures in carbonate rocks by CO2-acidified brines. Environ. Sci. Technol. 49 (16), 10226–10234.
Dhar, J., Meunier, P., Nadal, F., Méheust, Y., 2022. Convective dissolution of carbon dioxide in two- and three-dimensional porous media: the impact of hydrodynamic dispersion. Phys. Fluids 34 (6), 064114.
Duan, Z., Sun, R., 2003. An improved model calculating CO2 solubility in pure water and aqueous NaCl solutions from 273 to 533 K and from 0 to 2000 bar. Chem. Geol. 193 (3), 257–271.
Ellis, B.R., Crandell, L.E., Peters, C.A., 2010. Limitations for brine acidification due to SO2 co-injection in geologic carbon sequestration. Int. J. Greenhouse Gas Control 4 (3), 575–582.
Gadikota, G., 2021. Carbon mineralization pathways for carbon capture, storage and utilization. Communicat. Chem. 4 (1), 23.
Grogan, A., Pinczewski, V., Ruskauff, G.J., Orr, F., 1988. Diffusion of CO2 at reservoir conditions: models and measurements. SPE Reserv. Eng. 3 (01), 93–102.
Haugen, M., et al., 2023a. Calcite-functionalized micromodels for pore-scale investigations of CO 2 storage security. E3S Web Conf. 366, 01004.
Haugen, M., Brattekås, B., Fernø, M., 2023b. Multimodal Visualization of Calcium Carbonate (CaCO3) in the Pore Space of a Micromodel. In: Médici, E.F., Otero, A.D. (Eds.), Album of Porous Media: Structure and Dynamics. Springer International Publishing, Cham, p. 95.
Hellevang, H., Wolff-Boenisch, D., Nooraiepour, M., 2019. Kinetic Control on the Distribution of Secondary Precipitates during CO2-Basalt Interactions, E3S Web of Conferences.
Kaufmann, G., Dreybrodt, W., 2007. Calcite dissolution kinetics in the system CaCO3–H2O–CO2 at high undersaturation. Geochim. Cosmochim. Acta 71 (6), 1398–1410.
Kazemifar, F., Blois, G., Kyritsis, D.C., Christensen, K.T., 2016. Quantifying the flow dynamics of supercritical CO2–water displacement in a 2D porous micromodel using fluorescent microscopy and microscopic PIV. Adv. Water Resour. 95, 352–368.
Kordać, M., Linek, V., 2008. Dynamic measurement of carbon dioxide volumetric mass transfer coefficient in a well-mixed reactor using a pH Probe: analysis of the salt and supersaturation effects. Ind. Eng. Chem. Res. 47 (4), 1310–1317.
Landa-Marbán, D., 2023. daavid00/pymm: Release 2023.10 (v2023.10).
Le Chatelier, H.L., 1884. A general statement of the laws of chemical equilibrium. Comptes Rendus 99, 786–789.
Liu, Z., Dreybrod, W., 1997. Dissolution kinetics of calcium carbonate minerals in H2O-CO2 solutions in turbulent flow: the role of the diffusion boundary layer and the slow reaction H2O + CO2 → H+ + HCO3−. Geochim. Cosmochim. Acta 61 (14), 2879–2889.
Liu, N., Haugen, M., Benali, B., Landa-Marbán, D., Fernø, M.A., 2023. Pore-scale spatiotemporal dynamics of microbial-induced calcium carbonate growth and distribution in porous media. Int. J. Greenhouse Gas Control 125, 103885.
Lu, P., et al., 2013. Coupled alkali feldspar dissolution and secondary mineral precipitation in batch systems – 2: New experiments with supercritical CO2 and implications for carbon sequestration. Appl. Geochem. 30, 75–90.
Lv, H., et al., 2021. Liquid flow and mass transfer behaviors in a butterfly-shaped microreactor. Micromachines (Basel) 12 (8).
Miri, R., Hellevang, H., 2016. Salt precipitation during CO2 storage—a review. Int. J. Greenhouse Gas Control 51, 136–147.
Mitchell, A.C., et al., 2013. Microbial CaCO3 mineral formation and stability in an experimentally simulated high pressure saline aquifer with supercritical CO2. Int. J. Greenhouse Gas Control 15, 86–96.
Molins, S., et al., 2014. Pore-scale controls on calcite dissolution rates from flow-through laboratory and numerical experiments. Environ. Sci. Technol. 48 (13), 7453–7460.
Morais, S., et al., 2016. Monitoring CO2 invasion processes at the pore scale using geological labs on chip. Lab Chip 16 (18), 3493–3502.
Morse, J.W., 2018. Chapter 7. the kinetics of calcium carbonate dissolution and precipitation. In: Richard, J.R. (Ed.), Carbonates: Mineralogy and Chemistry. De Gruyter, pp. 227–264.
Morse, J.W., Arvidson, R.S., Lüttge, A., 2007. Calcium carbonate formation and dissolution. Chem. Rev. 107 (2), 342–381.
Oelkers, E.H., Gislason, S.R., Matter, J., 2008. Mineral carbonation of CO2. Elements 4 (5), 333–337.
Pachauri, R.K., Reisinger, A., 2007. IPCC Fourth Assessment Report. IPCC, Geneva, p. 2007.
Phillips, A.J., et al., 2013. Potential CO2 Leakage Reduction through Biofilm-Induced Calcium Carbonate Precipitation. Environ. Sci. Technol. 47 (1), 142–149.
Plummer, L., TML, W., DL, P., 1978. The Kinetics of Calcite Dissolution in CO2-Water Systems at 5O to 60OC and 0.0 to 1.0 ATM CO2.
Rezk, M.G., Foroozesh, J., Abdulrahman, A., Gholinezhad, J., 2022. CO2 diffusion and dispersion in porous media: review of advances in experimental measurements and mathematical models. Energy Fuel 36 (1), 133–155.
Scientific, T., 2022. pHrodoTM Red, Succinimidyl Ester (pHrodoTM Red, SE).
Song, W., Ogunbanwo, F., Steinsbø, M., Fernø, M.A., Kovscek, A.R., 2018. Mechanisms of multiphase reactive flow using biogenically calcite-functionalized micromodels. Lab Chip 18 (24), 3881–3891.
Van der Walt, S., et al., 2014. Scikit-image: image processing in Python. PeerJ 2, e453.
Xu, J., Balhoff, M., 2022. Dissolution-After-Precipitation (DAP): a simple microfluidic approach for studying carbonate rock dissolution and multiphase reactive transport mechanisms. Lab Chip 22.
Xu, R., Li, R., Ma, J., He, D., Jiang, P., 2017. Effect of mineral dissolution/precipitation and CO2 exsolution on CO2 transport in geological carbon storage. Acc. Chem. Res. 50 (9), 2056–2066.
Yang, Y., et al., 2018. Retraction of the dissolution front in natural porous media. Sci. Rep. 8 (1), 5693.
Yoon, H., Valocchi, A.J., Werth, C.J., Dewers, T., 2012. Pore-scale simulation of mixing-induced calcium carbonate precipitation and dissolution in a microfluidic pore network. Water Resour. Res. 48 (2).

Yoon, H., Chojnicki, K.N., Martinez, M.J., 2019. Pore-scale analysis of calcium carbonate precipitation and dissolution kinetics in a microfluidic device. Environ. Sci. Technol. 53 (24), 14233–14242.
Zhang, C., Oostrom, M., Grate, J.W., Wietsma, T.W., Warner, M.G., 2011. Liquid CO2 displacement of water in a dual-permeability pore network micromodel. Environ. Sci. Technol. 45 (17), 7581–7588.
Zhu, C., Lu, P., 2009. Alkali feldspar dissolution and secondary mineral precipitation in batch systems: 3. Saturation states of product minerals and reaction paths. Geochim. Cosmochim. Acta 73 (11), 3171–3200.

Paper 3

119 (2023) 205139

Contents lists available at ScienceDirect

Gas Science and Engineering

journal homepage: www.journals.elsevier.com/gas-science-and-engineering

Multi-scale dissolution dynamics for carbon sequestration in carbonate rock samples

Malin Haugen, Olav Parelius Folkvord, Torunn Veien, Martin A. Fernø, Bergit Brattekås *

Department of Physics and Technology, University of Bergen, Norway

A B S T R A C T

Carbon dioxide (CO_2) sequestration in porous, sedimentary reservoirs is a key technology to mitigate emissions of anthropogenic CO_2 and curb irreversible climate change. The abundance of carbonate formations, both as saline aquifers and hydrocarbon reservoirs, makes future CO_2 storage in carbonate formations highly likely. The weak carbonic acid that forms when CO_2 dissolves in water will, however, interact with highly reactive carbonate. Preferential flow paths may form during dissolution or calcite precipitation may reduce injectivity - both processes significantly impacting reservoir sweep efficiency. Hence, understanding the dynamics of the dissolution processes and their influence on flow properties is necessary to safely store CO_2 in carbonate formations. Darcy and sub-Darcy scale dissolution kinetics were here assessed in carbonate core plugs with and without pre-existing highly permeable pathways, during multiphase flow and under relevant storage conditions.

Darcy-scale dissolution and precipitation data (injectivity changes, effluent analysis and mass loss) confirmed that CO_2 and brine co-injections altered the carbonate rock structure on Darcy scale, but could not determine the cause of change. Multi-modal imaging was applied to independently quantify structural changes with computed tomography (CT) and aqueous flow characteristics with positron emission tomography (PET), thereby determining injectivity dependence on local flow patterns. Formation of high permeability pathways, which was expected due to rock dissolution, was only observed in cores with pre-existing open fractures, where reactive flow was limited to the fracture plane. A good correlation between the two imaging modules was found: areas of higher porosity yielded a low-density CT signal (i.e. high number of voids present) and a high PET signal density (i.e. large volume of traced fluid present). Loss of injectivity suggested local changes in the flow pattern due to blocking of pore throats by moving particles or secondary precipitation or mineralization of dissolved ions. High-resolution PET imaging revealed cementation, that was also visible using micro-CT, hence determining sub-Darcy local flow obstructions that led to decreased Darcy scale injectivity. Multi-modal imaging, where core characteristics, such as large vugs and cementation, can be independently determined by complementary modalities, may therefore be a useful tool to quantify reactive flow and resulting dissolution in rock samples.

1. Introduction

Carbon capture and storage (CCS), where CO_2 is permanently stored in geological structures, has been identified as a proven technology to reduce carbon emissions to the atmosphere. The captured and injected CO_2 can be trapped in the reservoir by (mechanisms listed with increased storage security): structural or stratigraphic barriers (physical trapping); as immobile droplets (residual trapping); dissolved in the aqueous phase (solubility trapping); and as a solid part of precipitates (mineral trapping) (IPCC, 2005). Geological storage sites for CO_2 injection include depleted oil and gas reservoirs and saline aquifers, both in sandstone and carbonate formations (IPCC, 2005). Injection of CO_2 for enhanced oil recovery (CO_2-EOR) has been widely implemented in both sandstone and carbonate since the 1970s (Laboratory, 2010). CO_2-EOR with simultaneous storage of CO_2 in the reservoir may be an important contributor to fast upscaling of carbon sequestration (Alcorn et al., 2022). Saline aquifer storage has mostly targeted sandstone formations; however, to achieve ambitious emission goals, utilization of the vast storage capacity in carbonate formations is also necessary.

Carbonate is a class of highly reactive sedimentary rocks mainly consi

sting of carbonate minerals, where the two major types are limestone and dolomite. Limestone, used in this study, mainly consists of different crystal forms of calcium carbonate ($CaCO_3$), with carbonate formation brines often containing NaCl, $CaCl_2$ and $MgCl_2$ (Oelkers et al., 2008). The combination of chemical components in rock and fluids makes carbonates susceptible to structural changes, where both dissolution and re-precipitation of carbonate minerals may occur during CO_2 injection for geological sequestration (Benson and Cole, 2008). Dissolution and development of highly conductive (wormholes) or blocked pathways have implications for large-scale deployment of CCS in carbonates. Wormholes can increase near-well injectivity, but a network of connecting wormholes can cause conformance issues between wells that reduce sweep efficiency and CO_2 storage potential (Larkin and Creel,

* Corresponding author.
E-mail address: Bergit.Brattekas@uib.no (B. Brattekås).

https://doi.org/10.1016/j.jgsce.2023.205139
Received 5 June 2023; Received in revised form 22 September 2023; Accepted 29 September 2023
Available online 30 September 2023

2008; Smith et al., 2006).

Dissolution mainly occurs when injected CO2 dissolves in the aqueous phase, develops carbonic acid and reduces the aqueous phase pH. At neutral to alkaline pH, mineral trapping is expected to occur by the formation of carbonate minerals from the available cations in the present brine [8, 9]. Minto et al. (2017) reported several possible mechanisms for re-precipitation, including: 1) occurrence of supersaturated fluid due to mixing with higher pH water trapped in stagnant pores, and 2) decrease in $CaCO_3$ solubility due to pressure reduction as fluids are transported through a porous medium. Depending on the flow conditions, precipitated minerals (fines) can either remain in place or be transported with the flowing fluids. Minerals may re-precipitate when flowing through a porous medium; consequently blocking pores or preferential flow paths.

1.1. A short summary of experimental work on the Darcy scale

Darcy scale investigations are necessary to investigate flow implications from carbonate dissolution. In addition to being reactive, carbonates are often heterogeneous with a high porosity, low matrix permeability and natural fractures. Carbonate core samples can be homogenous or heterogeneous, and fluid transport during and after dissolution and re-precipitation is strongly influenced by local rock structure. Several authors have experimentally verified the dependence of dissolution on core structure; e.g. in (Al-Khulaifi et al., 2019; Maheshwari et al., 2013) where uniform dissolution was observed in homogeneous limestone, while wormholes formed in more heterogeneous samples. Highly conductive wormholes were also observed in vuggy limestone during carbonated brine injection, while uniform dissolution was observed in relatively homogenous marly dolostones (Hommel et al., 2018; Smith et al., 2013). Luhmann et al. (2014) used x-ray computed tomography (CT) to visualize carbonated brine injection in dolomite core plugs at reservoir conditions (100 °C and 150 bars) and found that dissolution patterns were rate-dependent: conductive wormholes at high (47 cm/h) injection rate, narrow wormholes at intermediate (5 cm/h) rates, and cone-shaped dissolution at low (0.5 cm/h) injection rates.

Single-phase reactive transport (carbonated brine as the only flowing phase) occurs far from the injection well, where CO_2 and brine in equilibrium forms a single phase. The injected CO_2 and formation brine (with and without CO_2 saturation) may co-exist closer to the well during CO_2 injection. Single-phase and two-phase reactive dissolution experiments performed in Estaillades limestone (Ott et al., 2015) resulted in wormhole formation during single-phase injection (injection rate 1 cm/h) and compact dissolution during co-injection (injection rate 120 cm/h, but equal Damkohler and Péclet numbers to single-phase injections). Compact dissolution was explained by capillary forces, causing CO_2 to preferentially occupy small wormholes forming at the inlet end of the core plug (Ott et al., 2015). Free CO_2 is not reactive, hence preventing further growth of the wormholes. Luquot and Gouze (Luquot et al., 2009) pre-mixed and injected different fractions of CO_2 and brine into limestone core plugs at a temperature of 100 °C and a system pressure of 120 bar. Four flow experiments were conducted, where the CO_2 fractions varied between 6 and 83%. Injection rates ranged between 108 ml/h (high CO_2 fraction) to 57 cm/h (low CO_2 fraction), and the results indicated that uniform dissolution occurred at low CO_2 fractions and wormholes at higher CO_2 fractions.

The experimental efforts in this paper focus on the relationship between carbonate dissolution and Darcy-scale structural changes. First, CO_2 and brine were co-injected in whole (un-fractured) limestone cores and structural changes and implications for flow were analyzed. Second, CO_2 and brine were co-injected in the same core material with added heterogeneity (fractures). Two fracture systems were studied: *open fracture cores* (longitudinal fracture with large, irregular aperture mimicking a pre-existing wormhole) and *tight fracture cores* (longitudinal fracture with small and uniform fracture aperture). The different dissolution regimes were analyzed based on global measurements, and in some cores *in-situ* visualization was utilized for improved understanding. High-resolution imaging encompassing both structure (micro-CT) and flow (micro-PET) gave access to sub-core dissolution and secondary precipitation regimes.

2. Methods and materials

2.1. Fluids

Fluid properties used during the experiments are listed in Table 1. The CO_2 fraction used during co-injections was 80%, representative of the near wellbore area where the aquifer is saturated with CO_2 with the presence of a free CO_2 phase. A previous study found that a CO_2 fraction of 80% resulted in the formation of highly conductive flow channels and 20% CO_2 in uniform dissolution (Luquot et al., 2009)..

2.2. Carbonate core samples

Cylindrical Edwards limestone core plugs were drilled from larger blocks, gently washed with distilled water and dried at 60 °C for two weeks. The Early Cretaceous carbonate rocks were sourced from West Texas. Previous work characterized the Edwards limestone core material, and reported a trimodal pore size distribution containing microporosity and vugs (Fernø et al., 2015). The carbonate rock is mainly composed of calcium carbonate mineral ($CaCO_3$) and is highly reactive. Both whole (five cores) and fractured systems (five cores) were studied (see Table 2). A Brazilian test fracturing procedure (Brattekås et al., 2020) was used to create different fracture types: *open fractures* (longitudinal fracture with large, irregular aperture) and *tight fractures* (longitudinal fracture with narrow and uniform fracture aperture). The fracturing procedure creates natural fractures with significant local heterogeneity. The Brazilian test blade determined the fracture type (Brattekås et al., 2020), where L1T, L2T and L3T were classified as *open* and L4T and L5T as *tight*. Visual inspections of the core exterior and mass loss during fracturing (1 g of rock particles removed from the core during fracturing for open fractures, 0.5 g for tight) confirmed the fracture type (Figure A5). Matrix permeabilities were in the range of 20–50 mD for the cores used in this study. Initial fracture conductivity varied significantly within the open fracture cores due to local heterogeneities (Table 2). Variations were also observed in tight fractures, mainly due to additional measures taken in core L5T to promote flow in the fracture interior (silicon strips were mounted along the core to close fracture edges).

2.3. Experimental set-up and procedure

The cores were saturated with brine (Table 1) under vacuum, and porosity (Table 2) was determined gravimetrically. Absolute permeability (Table 2) was measured during single-phase injection of the same brine at different volumetric rates and calculated using Darcy's law, where the entire core cross-section was used as basis for calculation in both whole and fractured cores. Note that the injected brine mainly channels through the fracture in cores L1T - L5T (i.e. the cross-sectional area conducting flow which will vary between fracture types and locally within cores). Initial fracture conductivities (Table 2) are therefore more uncertain, but nevertheless provided to indicate whether flow occurs mainly in the fracture network (initial fracture conductivity » matrix permeability range) or is likely more evenly distributed in the core (initial fracture conductivity ≈ matrix permeability range). Each core plug was wrapped in aluminum foil to minimize exposure between CO_2 and the Viton rubber sleeve and mounted in a Hassler-type core holder connected to the flow system (Fig. 1). A confinement pressure of 92–105 Bar (12 bars above pore pressure) was maintained during all injections. The injected mixture during co-injections (80% CO_2 and 20% brine volumetric fractions) was flooded through the bypass, and pH was

Table 1
Fluids used in core flooding experiments. The brine composition was representative of a generic carbonate formation brine.

Fluid	Content	Density [g/ml]	Viscosity [cP]	pH
Brine	Distilled water with 4.0 wt% NaCl 3.4 wt% $CaCl_2$ 0.5 wt% $MgCl_2$ 0.01 wt% NaN_3	1.05 (20 °C, 1 bar)[1] 1.05 (40 °C, 90 bar)	1.09 (20 °C, 1 bar)[a] 0.65 (40 °C, 90 bar)	5.58
CO_2	>99.99% pure CO_2	0.49 (40 °C, 90 bar)[b]	0.03 (40 °C, 90 bar)[b]	–
Co-injection	Brine with 80% CO_2			4.28*

* Measured at ambient pressure, after the back pressure regulator (Fig. 1).
[a] Values from (Fernø et al., 2015).
[b] Values from (Lemmon et al., 2020).

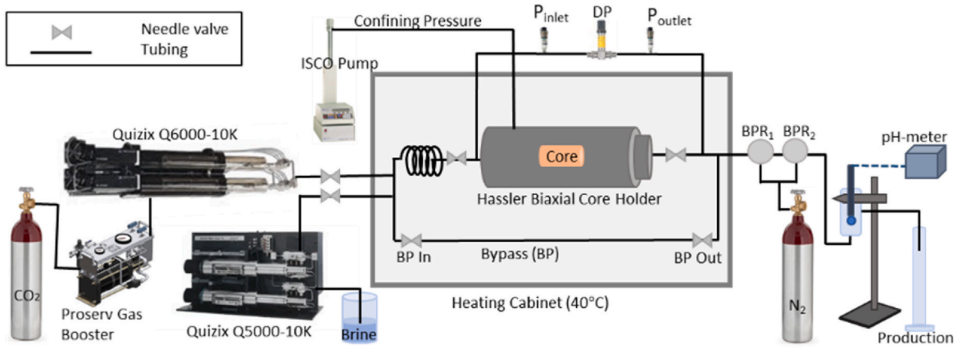

Fig. 1. Laboratory setup used during dissolution experiment. The Hassler biaxial core holder was mounted in a heating cabinet, and connected to a 10 m long coil upstream of the core inlet to ensure that injected fluids reached elevated temperature conditions prior to entering the core. The fracture plane was kept horizontal during co-injection to minimize gravitational effects. Temperature was kept constant at 40 °C. Quizix plunger pumps Q5000-10k and Q6000-10k were used for brine and CO_2 injections respectively, and an ISCO pump for confinement pressure. Absolute (ESI 0–400 bar) and differential pressure transducers (Aplisens 0–16 bar for whole cores and 0–2.5 bars for fractured cores) were used to monitor dynamic pressure developments during injections. Two back pressure regulators (Equilibar) maintained and stabilized the pore and system pressures. The inline pH meter (Ati q45p) measured effluent pH at ambient conditions.

Table 2
*Measured core properties including dimensions, porosity, absolute permeability. * For fractured cores (L1T – L5T)* $\mathbf{K_{w,inital}}$ *indicates the initial fracture conductivity. In core L5T a silicon strip was mounted longitudinally along the core to limit flow along the edges of the fracture.*

	Core ID	Length [cm] ±0.01	Diameter [cm] ±0.01	Porosity [%] ±0.05	$K_{w,inital}$ [mD] ±0.5
WHOLE	L2	7.33	3.80	22.2	48.1
	L3	7.00	3.78	27.1	78.0
	L4	7.26	3.79	21.4	21.8
	L7	7.64	3.80	21.9	31.5
	L8	7.04	3.80	23.2	43.4
FRACTURED	L1T	7.31	3.78	22.3	387*
	L2T	7.33	3.78	24.6	605*
	L3T	7.00	3.78	24.0	649*
	L4T	6.96	3.78	26.7	463*
	L5T	6.78	3.78	22.6	38*

measured at ambient conditions with an inline pH meter (*Ati q45p*) before flooding through the core. The produced effluent pH was also measured during co-injection (for fractured cores only). The differential pressure was continuously monitored (*Aplisens differential pressure* 0–16 bars, and ESI absolute pressure 0–400 bars) to assess core dissolution and the dynamic formation of preferred flow paths. The injectivity index J_{index} was used to monitor injectivity development during co-injection and is given by:

$$J_{index} = \frac{Q\left[\frac{ml}{h}\right]}{dP\ [bars]} \quad (1)$$

where Q is the volumetric flow rate though the core plug and dP is the pressure drop across the core plug. Minor pressure fluctuation is expected in this system due to rapid changes in local saturations and relative permeability (not accounted for in global measurements). The injectivity index was used to evaluate changes in flow potential over time. After injection of the desired pore volumes (PV inj, Table 3), CO_2 injection was stopped while brine injection continued for 24 h to displace CO_2 from the pore network and measure post-dissolution absolute permeability. The relation between pre- and post-dissolution absolute permeabilities, is given by the impedance factor:

$$J = \frac{K_0}{K} \quad (2)$$

where J is the impedance factor, Ko the absolute permeability of the core after dissolution, and K the initial permeability of the core. The cores were visually inspected after removal from the core holder and photographed (images may be found in the supplementary material, Figure A.5 and Figure A.6). The produced effluent was filtered (0.45 µm Supor filter) and the debris was analyzed with X-Ray Diffraction (*D8 ADVANCE ECO XRD*) to shed light on the crystalline phases present (only for cores L2T, L3T and L4)

Spatially resolved dissolution cannot be quantified by global measurements; a selection of cores (Table 3) were therefore imaged using high resolution µCT and µPET. µCT (ProCon X-ray CT-ALPHA) was used both pre- and post-dissolution to visualize and quantify structural changes caused by dissolution. The µCT images were obtained at no-flow static conditions and enabled micrometer scale investigation of dissolution patterns, vugs, cementation and visible wormholes. The µ-CT scanner used a 125 kV micro-focus tube with a 3000 x 3000 pixel

Table 3
Overview of flow parameters. The Darcy velocity is calculated using the whole core cross-section, hence the actual Darcy velocity in fractured cores is likely higher than reported.

	Core ID	P_{pore} [barg]	Q [ml/h]	Q_{Darcy} [cm/h]	PV inj	Fracture system	Imaging module Pre/post dissolution
WHOLE	L2	92	36	3.2	400	n.a.	μCT/μPET
	L3	93	72	6.4	400	n.a.	-/μPET
	L4	93	24	2.1	400	n.a.	-/μCT + μPET
	L7	80	48	4.3	392	n.a.	-/μPET
	L8	90	60	5.3	400	n.a.	-/-
FRACTURED	L1T	80	20,40,80,160	1.8–14.3	392	Open	μCT/μCT + μPET
	L2T	90	40	3.6	216	Open	μCT/-
	L3T	90	80	7.1	406	Open	μCT/μCT + μPET + PET
	L4T	90	80	7.1	368	Tight	μCT/-
	L5T	90	40	3.6	222	Tight	μCT/μCT

detector, and scanned each core with a continuous helix motion using 1600 projections for each rotation. The exposure time was set to 500ms, and the reconstructed images had a spatial resolution of 29.2 μm. Micro-Positron Emission Tomography (μPET) imaging was used to visualize flow in partly dissolved core plugs after co-injection using a traceable ^{18}FDG-brine (experimental setup and general procedure detailed in (Brattekås et al., 2023)). μPET imaging was performed during miscible brine-^{18}FDG-brine injections using the same total volumetric rate and core orientation as during co-injection. Reconstructed images had spatial and temporal resolutions of 0.42 mm (voxel size) and 60 s.

3. Results and discussion

This section presents multi-scale (Darcy and sub-Darcy) experimental results and analysis during and after co-injections, describing the temporal changes in injectivity index, impedance factor and pH, in addition to changes in rock structure (μCT) and flow paths (μPET) from the carbonate dissolution and precipitation processes (cf. Table 4).

3.1. Darcy-scale investigations

Darcy-scale measurements include pH and differential pressure measurements (dynamic during co-injection) and visual inspection of the core exterior and effluent analysis (after co-injection).

3.1.1. *Injectivity and impedance development during co-injection*

The injectivity index (Eq. (1)) was monitored during co-injection of supercritical CO_2 and brine (operational parameters in Table 4) for whole and fractured cores (see Fig. 2). The injectivity index behavior falls into two categories: *increasing* and *decreasing*. In open fracture cores (L1T, L2T and L3T) injectivity *increased* over time (injectivity index >1.0 relative to initial value, cf. Table 4), due to localized dissolution in the fracture plane, efficiently increasing the fracture aperture. In whole (L3 and L4) and tight fracture cores (L4T and L5T) injectivity *decreased* over time (injectivity index <1.0 relative to initial value, cf. Table 4), caused by dynamics in dissolution and precipitation mechanisms that were more pronounced within porous media and narrow fractures (further discussed in 3.2). Pressure fluctuations were observed throughout co-injection for all cores, as expected during two-phase flow, but with less fluctuations in open fracture cores compared to whole and tight fractures (the reader is referred to Figure A.1 and A.2 for all results).

The development in effluent pH during co-injection of supercritical CO_2 and brine (see Fig. 3) describes the Darcy-scale dissolution of $CaCO_3$ that leads to formation of bicarbonate ions (HCO_3^-) which re-increase the aqueous phase pH (Minto et al., 2017; Gaus, 2010). The pH development in fractured systems indicated an effect of initial fracture conductivity. In open fracture cores (L2T and L3T) the effluent pH relative to the injected phase increased before 1 PV injected, compared with tight fractures cores (L4T and L5T) where a pH increase was not observed until 3.5 PV injected. The effluent pH remained above the injected pH after gas breakthrough, indicating sustained (continuous) dissolution throughout co-injection.

Two further observations confirmed dissolution of core material in all studied systems: 1) calcite minerals (confirmed with XRD, see Figure A4) were observed in the effluent after gas breakthrough, and 2) up to 2.1% mass loss (cf. Table 4) was recorded post-dissolution for whole cores. Visual external inspection post co-injection (Figure A5 and A.6) also supported dissolution: *whole cores* were predominately dissolved at both end faces, cores with *tight fractures* were dissolved at the inlet face (less at outlet), whereas cores with *open fractures* showed dissolution along the pre-existing fracture plane.

Darcy-scale dissolution and precipitation data (injectivity, impedance, XRD, pH, weight and core exterior investigation) confirmed that CO_2 and brine co-injections altered the rock structure of all cores. Dissolution and the associated formation of high permeability pathways (wormholes) were expected to increase injectivity in all cores. Nevertheless, the injectivity increased only for open fracture cores, where the pre-existing conductive fracture plane concentrated reactive fluid flow in a limited area. The recorded mass loss confirmed that dissolution also occurred in whole cores, but the loss of injectivity suggests that

Table 4
Darcy velocity, injectivity, permeability, impedance and mass loss for studied systems during co-injections. End point weight was not recorded for fractured cores (i.e. mass loss not provided).

	Core ID	Darcy velocity [cm/h]	Injectivity index @ 200 PV (relative to start)	$K_{w,\ inital}$ [mD] ± 0.5	$K_{w,post\ dissolution}$ [mD]	Impedance factor	Mass loss [%]
WHOLE	L2	3.2	163 (0.4)	48.1	20	2.4	0.6
	L3	6.4	307 (0.5)	78.0	38	2.0	1.9
	L4	2.1	97 (0.5)	21.8	15	1.5	2.1
	L7	4.3	169 (0.7)	31.5	19	1.7	0.6
	L8	5.3	147 (0.7)	43.4	21	2.1	0.9
FRACTURED	L1T	1.8–14.3	2245 (8.2)	387	1370	0.3	n.a
	L2T	3.6	3863 (6.8)	605	716	0.8	n.a
	L3T	7.1	2944 (3.4)	649	655	1.0	n.a
	L4T	7.1	350 (0.7)	463	36	12.8	n.a
	L5T	3.6	275 (0.8)	38	26	1.5	n.a

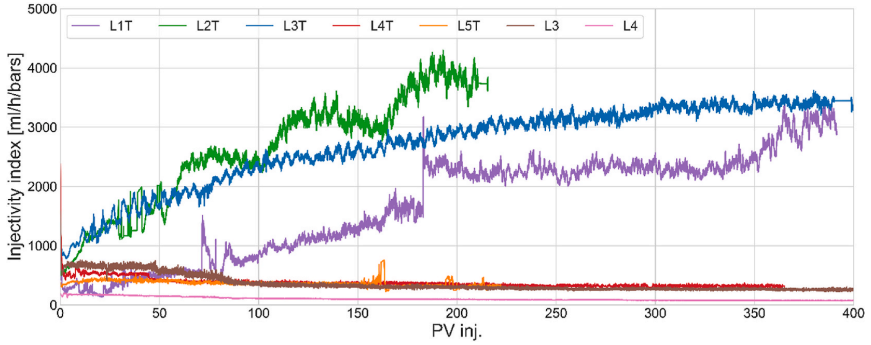

Fig. 2. Development in injectivity index for whole cores (L3 and L4), cores with tight fractures (L4T and L5T) and cores with open fractures (L1T, L2T and L3T) during co-injection of supercritical CO_2 and brine. An increasing injectivity was only observed in cores with open fractures, although dissolution occurred in all cores. Differential pressures fluctuated for all cores (detailed plot included in the supplementary material (Figure A.1)).

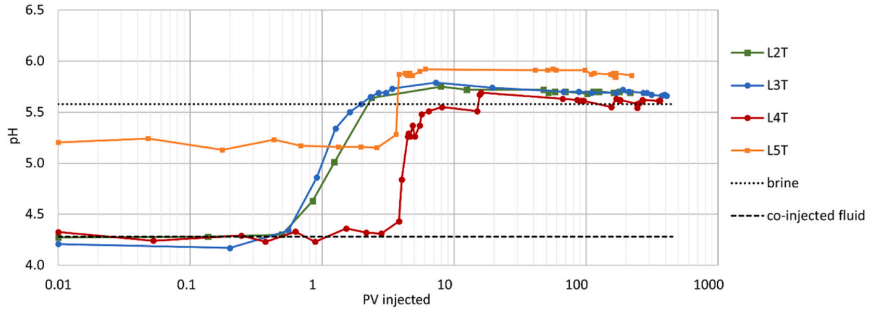

Fig. 3. Development in effluent pH during co-injection in fractured cores. The open fracture cores (L2T and L3T, pH was not measured in L1T) show a pH increase before 1 PV injected, compared with tight fracture cores (L4T and L5T) both with increased pH after 3.5 PV injected. The injected brine pH (grey dotted line) was 5.58 and the pH of co-injected fluid (20% brine and 80% CO_2; dashed black line) was 4.28. Note: The pH value for L5T prior to breakthrough was higher than the co-injected fluid due to contaminated outlet tubing: it is expected that the pH should be comparable to co-injected fluid before breakthrough. Also note the logarithmic x-axis. Differential pressure related to measured pH is presented in Figure A3.

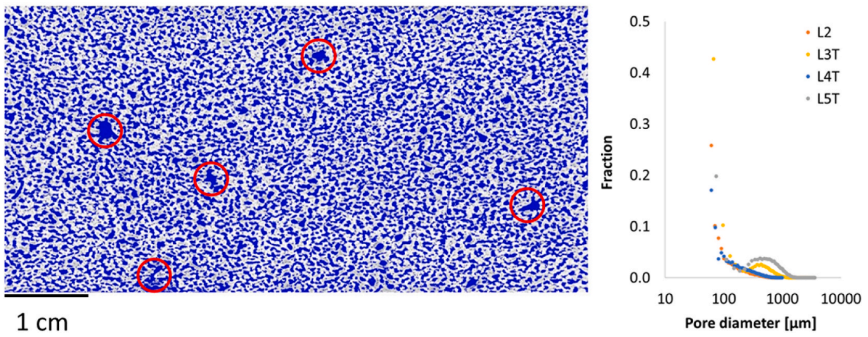

Fig. 4. Spatially resolved pore size distribution from µCT image (left, core L2), where blue represents the pores above the lower image resolution limit (31 ± 2 µm) with large pores (vugs) indicated in red circles. Distribution of pore diameters (µm) for four cores (right) show some variation, but also demonstrated that the majority of pores were small (20–40% of pores were close to the resolution limit for all cores), with few pores above 100 µm. Analysis is based on equal volumes in the interior of each core (2.5*2.5*5 cm in the x, y, z directions, respectively) to avoid beam hardening and end effects.

secondary precipitation may have occurred due to oversaturation and change in solubility. The decreased injectivity observed in whole and tight fracture cores may, therefore, be explained by 1) re-arrangement of partly dissolved calcite crystals blocking narrow pore-throats downstream, and/or 2) secondary precipitation or mineralization of dissolved ions, both of which may cause local changes in the flow pattern. Note the difference between tight fracture cores L4T and L5T: in L5T fluid flow along fracture edges was physically limited and initial

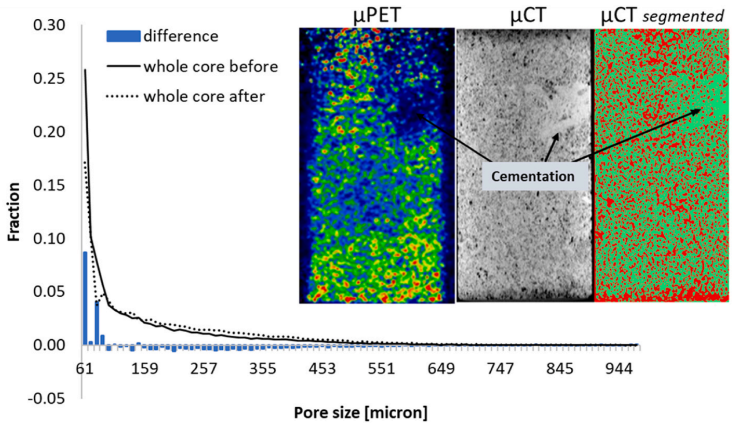

Fig. 5. Quantitative comparison of pore size distribution before (core L2) and after co-injection (core L4) and sub-Darcy multi-modal visualization (inset, core L4). The pore size distributions were obtained for the core interior (2 x 2 × 6.5 cm) to avoid artifacts from beam hardening and end effects. The difference (blue columns) between pore sizes before and after co-injection shows a loss of small pores (60–90 μm) and a gain in medium and larger pores (negative difference values). Hence, the dissolution and precipitation processes may have increased the size of some pores while clogging smaller pores by fines during transport. A 32% reduction in observable pores was found after co-injection. A similar trend was observed in whole core L3 (not included here). Inset: multi-modal imaging of water distribution (μPET) and rock structure (μCT) in the XZ plane. A cemented, low-porosity (2%, calculated from μPET) region with low water content (dark blue region, 'μPET' image) and high-density (bright, 'μCT' image) rock matrix was observed. Pore sizes were below image resolution (red pores and green matrix, 'segmented μCT' image). The water saturation was generally higher (warmer colors) in the inlet region compared with the outlet region, attributed to Darcy-scale dissolution heterogeneity. Porosity profiles for L3 and L4 are added to the supplementary material (Figure B1 and B.2 respectively) and show both cementation (L4) and dissolution (L3). Cores L2 and L7 did not exhibit structural changes quantifyable by μPET.

fracture conductivity, hence, significantly lowered compared to L4T. Post dissolution permeabilities are, however, comparable in the two cores, which supports that local particle re-arrangement and/or precipitation occurred in the fracture network: with fluid diversion into the core interior as a direct consequence for L4T. Determining where dissolution and/or clogging occurred within the core pore space is not possible from global Darcy-scale measurements.

3.2. Sub-Darcy scale investigation

To better understand where the carbonate reactive processes occurred within the core plugs, and how flow was influenced, *in-situ* imaging was applied after co-injection. The analysis was performed in fully brine-saturated conditions, under the assumption of static conditions with all reactive processes at equilibrium.

3.2.1. Pore size distribution

The rock material has trimodal distribution of pore sizes, with comparable size distribution for all studied core samples (see Fig. 4). The majority (80%) of pores were smaller than 200 μm, with most pores present close to the resolution limit. Sub-Darcy image analysis demonstrated a minority of vugs (larger pores; 2400–3000 μm), corroborating previous thin-section analysis (Tipura, 2008).

3.2.1.1. Local changes in pore space and flow. The effect of local rock structure changes on flow (see Fig. 5) may be studied with multi-modal imaging by comparing spatially resolved rock density (μCT images) with water distributions (μPET images). Whole cores where impedance factors increased during co-injection (>1, see Table 4) generally demonstrated a nonuniform porosity distribution after co-injection, where local regions of low porosity relative to surrounding rock matrix were prominent. A low-porosity region (i.e. region with high rock density) aligned with reduced water flow (i.e. low permeability) in core L4 (Fig. 5). Higher-porosity regions coincided with a preferential flow path of injected water post dissolution.

A quantitative comparison of pore size distribution before and after co-injection was used to inform the discussion of rock structural changes as a result of carbonate dissolution and precipitation processes (see Fig. 5). The quantitative analysis suggests that the core was partially clogged by calcite particles from dissolution downstream, leading to local areas with cementation. Note that cementation was not observed for any core prior to co-injection. Visible exterior changes (cf. Figure A6) were not seen at the outlet of this core; and the impedance factor was 1.5 (i.e. a 50% decrease in absolute permeability). Sub-Darcy structure changes after co-injection was resolved with μPET by evaluating the dynamics of a miscible water-water displacement.

3.2.2. Relationship between impedance factor and local dissolution

The fractured cores fall into two impedance-based categories: *increased* (>1.0, cores L5T and L4T) and *decreased* (≤1.0, L1T, L2T and L3T).

The decreased impedance factor observed in cores with open fractures (L1T, L2T and L3T) implied geometric changes in the pre-existing fracture plane, exemplified below for core L1T with the lowest (0.3) impedance factor (see Fig. 6). Post-dissolution visualization with multiple imaging modalities confirmed that dissolution occurred, with an average porosity increase of 13% in the fracture plane compared to 5.5% in the rock matrix (quantified by μCT). Although dissolution had occurred in most of the pore space, flow occurred exclusively in the fracture plane post-dissolution (quantified by μPET). Hence, the open fracture cores retained reactive flow in the irregular fracture aperture (mimicking a pre-existing wormhole), causing further local dissolution in the main flow path.

A different dissolution-impedance factor relationship was observed for open fracture core L3T, where an increase in porosity was also measured both in and around the fracture plane. The porosity change (by dissolution) was largest in the fracture area close to the inlet (first 3 cm core length) compared with the middle and outlet (see Fig. 7). In contrast to fractured core L1T (impedance factor 0.3), the impedance factor for core L3T was 1 (i.e., no change in Darcy scale permeability before and after dissolution), see Table 4. Local flow analysis showed that flow occurred both inside and outside of the pre-existing fracture

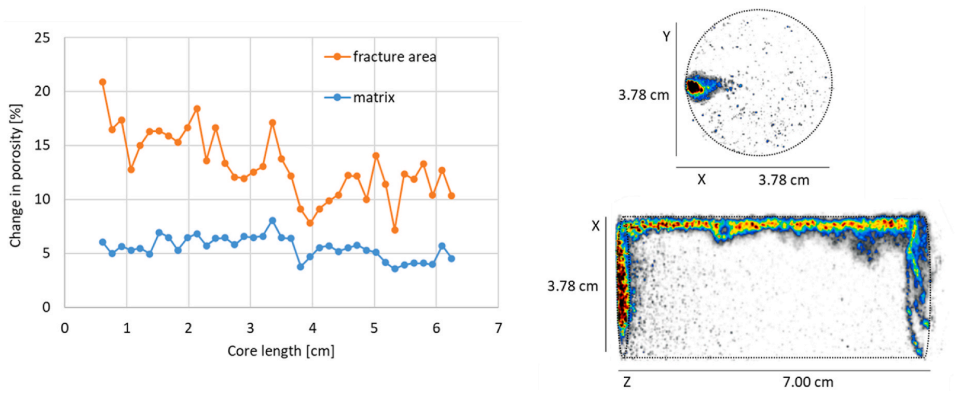

Fig. 6. Profiles of porosity change (left) and the localized fracture plane flow (right) after co-injection in open fracture core L1T. Left: The porosity increased both in the fracture region (orange, on average 13.2%) and in the rock matrix (blue, on average 5.5%). Hence, most of the dissolution occurred in the fracture plane, leading to increasing injectivity and reduced impedance. The porosity profiles are calculated by quantitative comparison of three-dimensional μCT images before and after co-injection. Right: The accumulated μPET signal (XY- and XZ plane) shows that the open, longitudinal fracture was the dominating flow conduit, with some dissolved regions near the inlet and outlet end faces. Warmer colors indicate more brine present. Note: for the porosity profiles the spatial resolution was XY-plane = 60 μm (two pixels) and slice thickness of Z = 1.5 mm. Five slices were omitted at the inlet and outlet to reduce the influence of end effects.

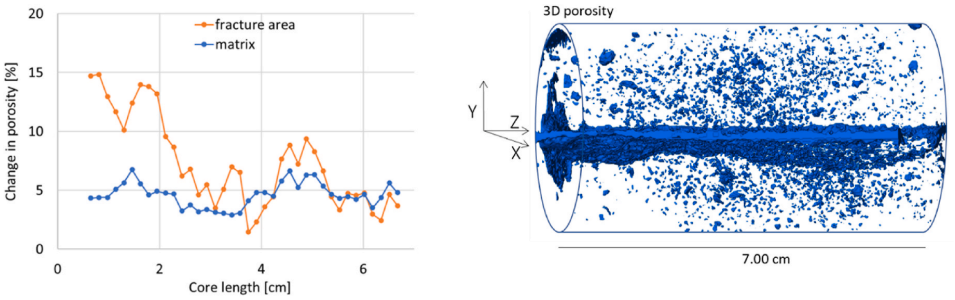

Fig. 7. Quantitative porosity change profiles and 3D resolved porosity change after co-injection in open fracture core L3T. Left: Porosity changes by dissolution in the fracture area (orange) and matrix (blue) after co-injection, visible by μCT. Dissolution in the fracture area was on average 7%, with more pronounced porosity change close to the inlet (0–3 cm). In the core middle and outlet (3–7 cm) both matrix and fracture porosity averaged 5%. Regions where the matrix porosity change exceeded the fracture area suggest that more dissolution occurred outside of the fracture plane. Right: Visualization of spatially resolved void (>50 μm, blue) calculated from μCT images show that dissolution occurred in the majority of the core, not only in the pre-existing fracture plane. (Additional micro-CT images available in supplementary material, Figure B3). Note: for the porosity profiles the spatial resolution was XY-plane = 60 μm (two pixels) and slice thickness of Z = 1.5 mm. Five slices were omitted at the inlet and outlet to reduce the influence of end effects.

plane post-dissolution (quantified by μPET). Hence, the anticipated reactive flow discrimination to the pre-existing fracture plane, which occurred in L1T, did not occur in L3T. Comparing structural changes (Fig. 7) with flow (Fig. 8) reveals the formation of a high porosity zone in the matrix due to dissolution, with connection to the fracture plane. We speculate that narrow restrictions in the initially heterogeneous fracture plane may have trapped particulates during transport and diverted reactive flow into the surrounding matrix, similar to formation and development of wormholes through gel (Brattekås et al., 2017).

In cores with tight fractures (L4T and L5T) increased impedance factors were observed (permeability decreased post-dissolution), which suggests that reactive flow, and consequently dissolution, predominantly occurred outside of the fracture plane. Note the difference in calculated impedance factor (Table 4), resulting from the presence/absence of initial flow along the fracture edges. Compact conical dissolution was observed in both cores (figure A5). Additional development of small wormholes was observed in a fractured core sample with increased impedance factor of 1.5 (L5T, Fig. 9). The formation of wormholes across the cross-sectional area suggested that reactive flow was not restricted to the fracture plane.

External structural changes, such as compact-conical dissolution at the inlet face, can be quantified by visual observations, but access to local changes in flow and structure within the opaque porous medium was only achieved by in-situ imaging. Post-dissolution visualization of structure and fluid flow properties in selected cores indicated that dissolution and precipitation reactions (and consequently impedance) were strongly affected by local heterogeneities in the fracture plane. Dissolution in the fracture plane was promoted in some cores (L1T), as expected. Dissolution in the adjacent matrix was, however, also observed in both open and tight fractures. It is likely that a locally decreased fracture conductivity, caused by secondary precipitation and trapped dissolved particles, promoted dissolution outside of the fracture plane; as observed by wormhole development (tight-fracture L5T) and dissolution adjacent to the fracture plane (open-fracture L3T). Reduced injectivity was, however, only observed for core L5T in global Darcy scale measurements. Wormhole development was only observed in one tight fracture core (L5T), but did not form in tight-fracture (L4T) or whole (L2) systems where co-injection was performed under similar

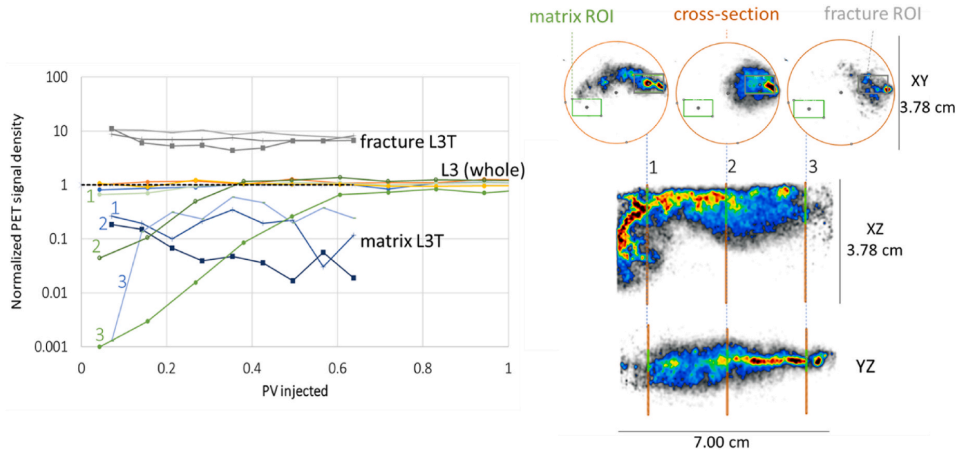

Fig. 8. Comparison of local flow paths in whole and fractured systems at three different positions along the core length (1, 2 and 3). Left: Development in local PET signal (labeling the brine) in whole (core L3) and fractured (core L3T) systems. The local PET signal is normalized to the XY-plane signal density (PET signal/volume) at each position. A piston-like displacement was observed in two small regions of interest (ROI) in L3, and both ROIs carried an equal volume of traced fluid (ROIs are indicated by small squares in the top right figure; both coincide with matrix in L3. In L3T the green square represents the matrix, and the grey represents the fracture). Traced water injection into L3T showed that flow occurred both within and outside of the pre-existing fracture plane: the signal in the fracture immediately increased upon injection of traced water. The signal in the matrix also increased to a maximum within 0.2 PV injected, although with a lower intensity. Our analysis shows that the L3T matrix conducts approximately 10% of flow, predominantly adjacent to the fracture plane.

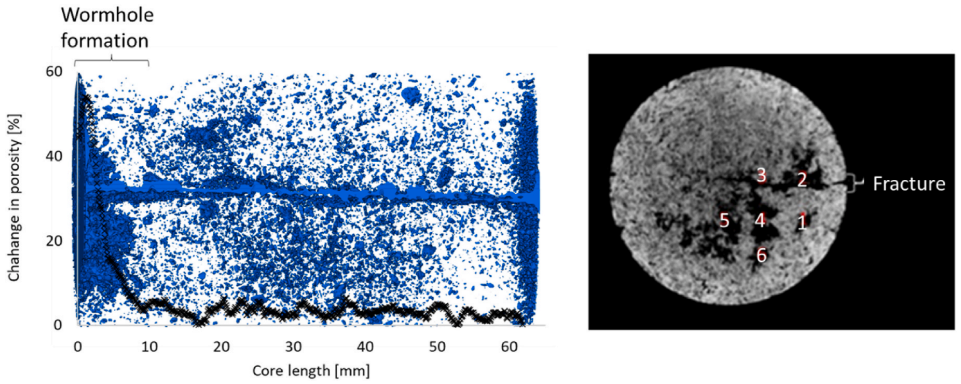

Fig. 9. Structural changes in rock structure in fractured core L5T after dissolution. Left: A 3D rendering of μCT images shows global dissolution (void >50 μm, blue), but predominantly at the end faces (inlet and outlet). Both compact-conical dissolution at the inlet and formation of multiple wormholes was observed. A porosity profile (showing the change from before and after co-injection, black) overlay the 3D image of the core porosity: up to 60% change in porosity was observed in the first 10 mm of the core, with minor changes (approximately 5%) in the remaining core. Right: 2D μCT image (XY-plane) close to the inlet (1.5 mm) showing the fracture plane and six wormholes. Smaller wormholes (1, 3–6) formed outside of the fracture plane, while the most prominent wormhole (2) extended 13.5 mm (20% of the core length) in proximity to the fracture. Note: The 2D XY μCT image was obtained 1.5 mm from the core inlet, where compact conical dissolution was not dominant. The reader is referred to supplementary material for additional images (Figure B4).

conditions.

3.3. Summarizing discussion

Dissolution of carbonate rock was observed in all studied systems during co-injection of supercritical CO_2 and water; and was confirmed by Darcy scale weight loss or effluent (calcite mineral production) measurements. Less than 2% of mass loss was recorded for the Edwards limestone rock material, during injection of 400 PV of CO_2 and brine. Injectivity development, accessed through dynamic pressure measurements, indicated two dissolution categories: *increasing* and *decreasing*. Injectivity decreased in whole and tight-fracture cores, presumably due to flow obstruction (lodged or precipitated minerals), limiting the initial flow path. Open-fracture cores presumably confined reactive flow in the fracture plane and efficiently produced dissolved particles (i.e. increased injectivity). The differences in injectivity were determined based on pressure measurements, but other global measurements (e.g. the produced effluent pH development (Fig. 3)) corroborated the existence of the two distinct injectivity categories. Darcy-scale behavior, hence, indicated similar and distinct dissolution properties within for whole, tight fracture and open fracture cores, respectively.

Access to local flow (μPET) and structural changes (μCT), however,

showed that dissolution and precipitation reactions were strongly affected by local heterogeneities and inconsistent within the pre-defined categories. *In-situ* imaging confirmed different dissolution patterns and significantly localized (mm scale) effects: in whole cores dissolution occurred predominantly at the inlet (all cores). Cementation (L4) and high-porosity regions (L3) irregularly occurred in the core interior, while other cores (L2 and L7) did not undergo quantifiable structural changes during CO_2 and brine co-injection. In one tight-fracture core (LT5) developing wormholes were observed across the fracture plane. Dissolution in open-fracture cores was visualized within the fracture plane (L1T), as expected, but also both within and around the fracture plane (L3T). Local dissolution within the core interior, e.g. outside of the fracture plane was not detectable in Darcy scale measurements, but clearly influential on fluid flow, as captured by μPET.

Our work shows that dissolution of heterogeneous limestone rock material depends on local rock/fluid interactions and localized features of the core samples (e.g. irregular fracture apertures or PSD). Coupled with reactive flow, these features become determining factors for localized dissolution and developing flow patterns. Darcy scale measurements of heterogeneity and dynamic development during co-injection did not sufficiently capture the dissolution properties within the core samples. The inconsistency in developing flow patterns at this relatively small scale implies that field scale dissolution prediction is an utterly complex task in heterogeneous carbonate. Carbonates on larger scale will likely include most of the features investigated in this study: matrix with varying permeability and both tight and open fractures: where this work highlights the significant variation in dissolution patterns formed within each of these categories. Channeling in carbonates is clearly a dynamic issue; where displacement patterns may shift during reactive flow, depending on the degree and localization of dissolution. This has implications for larger scale channeling of CO_2: in fractured reservoirs, where the reservoir rock is reactive and prone to dissolution, channeling may worsen (continuous erosion of fracture to larger aperture as in L1T) or improve (dissolved particles lodging in irregular fracture aperture and diverting fluid flow as in L3T) with time. By comparing μPET and μCT we can confirm that PET is able to capture mm-scale changes within the porous matrix, such as cementation and dissolution. Recent work (Kurotori et al., 2023) also showed the potential of PET imaging to quantify fracture structure. Multi-modal imaging of dynamic reactive fluid displacements in different fracture systems is possible with the system used in this work, and would provide important information about the development of dissolution and displacement patterns in complex rocks. The experiments presented in this work clearly shows that imaging is an important asset in determining dissolution flow patterns; whereas Darcy scale measurements should be more carefully interpreted.

4. Conclusions

The worldwide abundance of carbonate formations and reservoirs makes storage of CO_2 in such formations highly likely. However, the reactive nature of carbonate minerals increases the importance of understanding dynamics and dissolution processes, which occur during CO_2 injection, to enable long term safe storage. Study of the relationship between carbonate dissolution and Darcy-scale structural changes in core plugs (under relevant storage conditions) with and without pre-existing highly permeable fractures have resulted in the following main conclusions:

- Darcy scale measurements confirmed calcite dissolution by co-injection of brine and CO_2 in Edwards limestone outcrop cores. Measurements included visual inspection of core exteriors, weight changes, effluent analysis (pH and precipitates) and differential pressure development.
- Injectivity *increased* during two-phase injection of CO_2 and brine in cores with open fractures. *In-situ* imaging confirmed localized dissolution in (L1T) or around (L3T) the fracture plane.
- Injectivity *decreased* during two-phase injection of CO_2 and brine in cores with tight fractures. *In-situ* imaging revealed that reactive flow occurred across the core cross-section, and dissolution was, hence, not restricted to the fracture plane. Compact conical dissolution and wormhole formation was observed.
- Injectivity *decreased* during two-phase injection of CO_2 and brine in whole cores. *In-situ* imaging identified cementation in the core matrix as a possible mechanism for injectivity reduction. The changes in structure (μCT) influenced core scale flow (μPET).

Author contribution

Conceptualization: Martin A. Fernø; and Bergit Brattekås; Methodology: Malin Haugen, Olav Parelius Folkvord, Torunn Veien, Martin A. Fernø; and Bergit Brattekås; Formal analysis: Malin Haugen, Olav Parelius Folkvord, Torunn Veien, Martin A. Fernø; and Bergit Brattekås; Investigation: Malin Haugen, Olav Parelius Folkvord, Torunn Veien and Bergit Brattekås; Writing: Malin Haugen, Olav Parelius Folkvord, Torunn Veien, Martin A. Fernø; and Bergit Brattekås; Visualization: Malin Haugen, Olav Parelius Folkvord, Torunn Veien, Martin A. Fernø; and Bergit Brattekås; Funding acquisition: Martin A. Fernø

Declaration of competing interest

The authors declare that they have no known competing financial interests or personal relationships that could have appeared to influence the work reported in this paper.

Data availability

Data will be made available on request.

Acknowledgements

The authors thank Eivind Wilhelm Nagel Støren and Jan Magne Cederstrøm at the Department of Geoscience, UiB for assistance on the ProCon X-ray CT-ALPHA Computed Tomography (micro-CT) scanner and Andreas Lambach Viken for X-Ray Diffraction analysis (EarthLab). The PET-CT imaging was performed at the Molecular Imaging Center (MIC), Department of Biomedicine, University of Bergen. The authors thank Heidi Espedal for assistance. This work was partly funded by the Research Council of Norway under grants Subsurface Carbonate CO_2 Storage and Security (grant number 280341), In-situ quantification of CO_2 flow and mobility control for improved carbon utilization and storage (grant number 324818), and Centre for Sustainable Subsurface Resources (grant number 331841).

Appendix A. Supplementary data

Supplementary data to this article can be found online at https://doi.org/10.1016/j.jgsce.2023.205139.

References

Alcorn, Z., Graue, A., Karakas, M., 2022. CO2 Foam Pilot in a Heterogeneous Carbonate Reservoir: Analysis and Results. https://doi.org/10.2118/209359-MS.

Al-Khulaifi, Y., et al., 2019. Pore-scale dissolution by CO2 saturated brine in a multimineral carbonate at reservoir conditions: impact of physical and chemical heterogeneity. Water Resour. Res. 55 (4), 3171–3193. https://doi.org/10.1029/2018WR024137.

Benson, S.M., Cole, D.R., 2008. CO_2 sequestration in deep sedimentary formations. Elements 4 (5), 325–331. https://doi.org/10.2113/gselements.4.5.325.

Brattekås, B., M, S., Graue, A., Fernø, M.A., Espedal, H., Seright, R.S., 2017. New insight into wormhole formation in polymer gel during water chase floods with positron emission tomography. SPE J. 22 (1) https://doi.org/10.2118/180051-PA.

Brattekås, B., et al., 2020. Foam flow and mobility control in natural fracture networks. Transport Porous Media 131 (1), 157–174. https://doi.org/10.1007/s11242-019-01249-3.

Brattekås, B., et al., 2023. Of rats and rocks: using pre-clinical PET imaging facilities in core analysis. E3S Web Conf. 366, 01011 https://doi.org/10.1051/e3sconf/202336601011.

Fernø, M.A., et al., 2015. Mobility control during CO2 EOR in fractured carbonates using foam: laboratory evaluation and numerical simulations. J. Petrol. Sci. Eng. 135, 442–451. https://doi.org/10.1016/j.petrol.2015.10.005.

Gaus, I., 2010. Role and impact of CO2–rock interactions during CO2 storage in sedimentary rocks. Int. J. Greenh. Gas Control 4 (1), 73–89. https://doi.org/10.1016/j.ijggc.2009.09.015.

Hommel, J., Coltman, E., Class, H., 2018. Porosity–permeability relations for evolving pore space: a review with a focus on (Bio-)geochemically altered porous media. Transport Porous Media 124 (2), 589–629. https://doi.org/10.1007/s11242-018-1086-2.

IPCC, 2005. Special Report on Carbon Dioxide Capture and Storage, pp. 195–276 (Chapter 5): Underground geological storage.

Kurotori, T., Zahasky, C., Gran, M., et al., 2023. Comparative analysis of imaging and measurements of micrometer-scale fracture aperture fields within a heterogeneous rock using PET and X-ray CT. Transport Porous Media 147, 519–539. https://doi.org/10.1007/s11242-023-01922-8.

Laboratory, N.E.T., 2010. Carbon Dioxide Enhanced Oil Recovery.

Larkin, R., Creel, P., 2008. Methodologies and solutions to remediate inter-well communication problems on the SACROC CO2 EOR project – a case study. In: SPE Symposium on Improved Oil Recovery. OnePetro, Tulsa, Oklahoma, USA. https://doi.org/10.2118/113305-MS.

Lemmon, E., McLinden, M., Friend, D., 2020. Thermophysical Properties of Fluid Systems.

Luhmann, A.J., et al., 2014. Experimental dissolution of dolomite by CO2-charged brine at 100°C and 150bar: evolution of porosity, permeability, and reactive surface area. Chem. Geol. 380, 145–160. https://doi.org/10.1016/j.chemgeo.2014.05.001.

Luquot, L., Gouze, P., 2009. Experimental determination of porosity and permeability changes induced by injection of CO 2 into carbonate rocks. Chem. Geol. 265 (1), 148–159. https://doi.org/10.1016/j.chemgeo.2009.03.028.

Maheshwari, P., et al., 2013. 3-D simulation and analysis of reactive dissolution and wormhole formation in carbonate rocks. Chem. Eng. Sci. 90, 258–274. https://doi.org/10.1016/j.ces.2012.12.032.

Minto, J.M., et al., 2017. X-ray CT and multiphase flow characterization of a 'bio-grouted' sandstone core: the effect of dissolution on seal longevity. Int. J. Greenh. Gas Control 64, 152–162. https://doi.org/10.1016/j.ijggc.2017.07.007.

Oelkers, E.H., Gislason, S.R., Matter, J., 2008. Mineral carbonation of CO_2. Elements 4 (5), 333–337. https://doi.org/10.2113/gselements.4.5.333.

Ott, H., Oedai, S., 2015. Wormhole formation and compact dissolution in single- and two-phase CO2-brine injections. Geophys. Res. Lett. 42 (7), 2270–2276. https://doi.org/10.1002/2015GL063582.

Smith, D.D., MJ, G., Kemp, C.C., McBee, M., Taitano, J.A., Winfield, M.S., Portwood, J.T., Everett, D.M., 2006. The successful evolution of anton Irish conformance efforts. In: SPE Annual Technical Conference and Exhibition. OnePetro, San Antonio, Texas, USA. https://doi.org/10.2118/103044-MS.

Smith, M.M., et al., 2013. CO2-induced dissolution of low permeability carbonates. Part I: characterization and experiments. Adv. Water Resour. 62, 370–387. https://doi.org/10.1016/j.advwatres.2013.09.008.

Tipura, L., 2008. Wettability Characterization by NMR T2 Measurements in Edwards Limestone. Bergen: Department of Physics and Technology, University of Bergen, Master Thesis.

Paper 4

Journal of Natural Gas Science and Engineering 77 (2020) 103268

Contents lists available at ScienceDirect

Journal of Natural Gas Science and Engineering

journal homepage: http://www.elsevier.com/locate/jngse

Explicit tracking of CO_2-flow at the core scale using micro-Positron Emission Tomography (μPET)

Bergit Brattekås *, Malin Haugen

Department of Physics and Technology, University of Bergen, Norway

ARTICLE INFO

Keywords:
In-situ imaging
CO_2 flow
Carbonates
Explicit tracking of CO_2
Positron emission tomography

ABSTRACT

Safe subsurface sequestration of carbon dioxide (CO_2) is becoming increasingly important to meet climate goals and curb atmospheric CO_2 concentrations. The world-wide CO_2 storage capacity in carbonate formations is significant; within deep, saline aquifers and through several CO_2-enhanced oil recovery projects, with associated CO_2 storage. Carbonates are complex, both in terms of heterogeneity and reactivity, and improved core scale and sub core-scale analysis of CO_2 flow phenomena is necessary input to simulators, aiming to establish large-scale behavior. This paper presents a recent advancement in *in-situ* imaging of CO_2 flow, utilizing high-resolution micro-Positron Emission Tomography and radioactive tracer [^{11}C]arbon dioxide to explicitly track CO_2 during dynamic flow and subsequent trapping at the core scale. Unsteady state water injection (imbibition) and CO_2 injection (drainage) were performed in a low-permeable chalk core at elevated pressure conditions. Short-lived radioisotopes were used to label water and CO_2, respectively, and facilitated explicit tracking of each phase separately during single phase injection. Local flow patterns and dynamic spatial fluid saturations were determined from *in-situ* imaging during each experimental step. Initial miscible displacement revealed displacement heterogeneities in the chalk core, and dynamic image data was used to disclose and quantify local permeability variations. Radial permeability variations influenced subsequent flow patterns, where CO_2 predominantly flooded the higher-permeability outer part of the core, leaving a higher water saturation in the inner core volume. Injection of water after CO_2 flooding is proposed to be the most rapid and effective way to ensure safe storage, by promoting capillary trapping of CO_2. PET imaging showed that presence of CO_2 reduced the flow of water in higher-permeability areas, improving sweep efficiency and promoting a nearly ideal core-scale displacement. Alternate injections of water and gas is also expected to improve sweep efficiency and contribute to improved oil recovery and CO_2 storage on larger scales. Sub-core analysis showed that residually trapped CO_2 was evenly distributed in the chalk core, occupying 40% of the pore volume after ended water injection. Micro-Positron Emission Tomography yielded excellent small-scale resolution of both water and CO_2 flow, and may contribute to unlocking fluid flow dynamics and determining mechanisms on the millimeter scale; presenting a unique opportunity in experimental core-scale evaluations of CO_2 storage and security.

1. Introduction

Today there is little doubt that global warming is related to the increased CO_2 concentrations in the atmosphere. In the Paris Agreement from 2015 (COP21 Paris), the international community agreed to climate and energy goals limiting global warming to well below 2 °C above pre-industrial levels. Carbon capture, utilization and storage (CCUS) is identified as an important part of the portfolio of technologies needed to achieve these goals (IEA, 2019).

CO_2 can be injected in (active or depleted) hydrocarbon reservoirs, saline aquifers or non-mineable coal beds for long-term subsurface storage. Saline aquifer storage of CO_2 mostly targets sandstone formations, however; CO_2 injection to achieve enhanced oil recovery (EOR) is performed in several carbonate formations. Worldwide, more than 60% of proven oil reserves and 40% of gas reserves are found in carbonate formations (Akbar et al., 2000); hence a significant potential for CO_2 storage exist within carbonates. Carbonates represent complex flow systems, with fractures, small-scale heterogeneities and a wide range of pore sizes, in addition to being highly reactive (hence, dissolution may occur in parts of the formation during CO_2 injection due to

* Corresponding author.
E-mail address: bergit.brattekas@uib.no (B. Brattekås).

https://doi.org/10.1016/j.jngse.2020.103268
Received 20 December 2019; Received in revised form 17 February 2020; Accepted 17 March 2020
Available online 18 March 2020

acidification). Advanced laboratory methods are necessary to capture the properties of flow on the core and sub-core scales in such systems, to further map the controlling mechanisms of CO_2 storage in carbonate formations. In this paper we used micro-Positron Emission Tomography (μPET) to explicitly evaluate dynamic saturation development during brine and CO_2 injections in chalk at the core and sub-core scale. PET imaging, although primarily used in medicine and pre-clinical research as a diagnostic tool, is an up-and-coming imaging technology in porous media research. PET imaging is non-invasive and independent of experimental pressure and temperature conditions, and has high temporal and spatial resolutions at high signal to noise ratios. Recent advances in the imaging tool has spurred researchers to explore the limitations and possibilities associated with PET imaging during dynamic fluid flow in porous media (Kulenkampff et al., 2008; Fernø et al. 2015a, 2015b; Zahasky et al., 2019).

In-situ imaging has been extensively used to image fluid flow dynamics on the core scale, and the most used imaging modalities are Magnetic Resonance Imaging (MRI) and Computed Tomography (CT). MR imaging relies on spin detection from hydrogen atoms, and as such detects hydrogen-rich fluid phases, e.g. water and oil. MR imaging may implicitly monitor CO_2 injection by detecting the decrease in signal during injection into a core already saturated by water and/or oil (Ersland et al., 2010; Almenningen et al., 2018). CT monitors saturation based on attenuation measurements, and produce spatial representations of density contrasts through a porous medium. When the density contrast between injected and displaced fluids is high (e.g. between water and gas), CT may provide accurate and fast imaging at high resolution (Akin and Kovscek, 2003). CT or MR imaging also capture static rock structures, thus fluid flow behavior may be coupled with small scale heterogeneities in the core material. PET imaging represents an opportunity to image fluid flow without signal influence from the surrounding porous medium, and is often used in combination with CT or MRI. PET imaging only detects fluids labelled by positron-emitting radionuclides: in which emitted positrons will combine with an electron to balance atomic charge, and consequently send out photons of 511 keV energy in opposite directions. Annihilation events are detected by measuring photon coincidences versus time: to facilitate three-dimensional imaging, a ring consisting of several small detector elements encloses the porous medium. Post processing of the PET signal determine the position of each annihilation event in three dimensions, with high spatial and temporal accuracy. PET imaging, hence, offers the opportunity to visualize and quantify fluid flow *in-situ* at the core and local scale without signal influence from mineralogy, rock properties and initial saturation state. A range of radioisotopes are available for explicit labelling of different fluid phases, and new radioisotopes are continuously being developed: radioactive isotope ^{11}C–CO_2 facilitates explicit detection of CO_2 within the porous medium by PET imaging. Explicit quantification of CO_2 behavior is helpful for determining the potential of a storage formation, e.g. by measuring caprock capillary threshold pressure (Fernø et al., 2015a demonstrated that PET imaging could be used to determine CO_2 entry into very low-permeable shale), and porous media flow parameters including CO_2/brine relative permeability: parameters that are necessary input for numerical simulators and must be measured in controlled core-scale experiments (Busch and Müller, 2011).

The spatial resolution of PET imaging is limited by several parameters, including the distance between the annihilation event and the PET detector elements, and the area of the detector elements (Levin and Hoffman, 1999; Bailey et al., 2005; Zahasky et al., 2019). Small pre-clinical μPET scanners have been proposed to yield optimum resolution, and was previously used to investigate spontaneous imbibition (Ruth et al., 2016; Føyen et al., 2019), dynamic wormholing phenomena (Brattekås et al., 2017), fracture flow diversion by polymer gel (Brattekås and Seright, 2018), foam generation and flow in natural fracture networks (Brattekås et al., 2019) and single-and multiphase transport parameters during water and nitrogen gas injection in sandstone (Zahasky and Benson, 2018). μPET imaging was previously performed using the most common radioisotope for fluid flow studies: Fluorodeoxyglucose (^{18}F) (comprehensive overview may be found in Zahasky et al. (2019). ^{18}F may be dissolved in water, and can therefore be used for explicit imaging of water flow, and implicit imaging of other fluids by quantifying the loss of signal over time. The half-life (time it takes to decrease the original level of radioactivity to 50%) of ^{18}F is 109 min. Radioisotope ^{11}C, used to label CO_2, has a short half-life of 20 min, which pose additional experimental challenges; by limiting the time scale of experiments significantly, and in terms of safety regulations when handling high doses of radiation and produced radioactive gas. ^{11}C–CO_2 flow imaged by PET is therefore limited to only two previous studies: Fernø et al. (2015a) utilized ^{11}C to trace supercritical CO_2 propagation into shale at reservoir conditions, and Pini et al. (2016) mixed ^{11}C in an aqueous sodium bicarbonate solution to evaluate solute transport in a sandstone core at ambient conditions. Here we present, for the first time, explicit imaging of ^{11}C–CO_2 propagation into a chalk core at elevated pressure conditions, imaged by μPET. Alternate water and gas injections were performed, where each fluid was explicitly imaged during injection. Brine was labelled using ^{18}F, and CO_2 was labelled using ^{11}C. The signal of brine or gas was allowed to decay before the next injection, in the following cycle: ^{18}F-brine → ^{11}C–CO_2 → ^{18}F-brine. Spatial fluid saturations were calculated based on the registered activity of the labelled brine or gas phase at given time steps. Dynamic *in-situ* imaging presents an addition to global measurements, to more accurately determine local flow properties. This is particularly useful during unsteady-state experiments involving water/CO_2, where the results may be strongly influenced by heterogeneity, viscosity contrasts (fingering) and end effects (Busch and Müller, 2011).

2. Materials and methods

2.1. Preparations of the core and experimental set-up

A compact experimental setup (Fig. 1) was built to facilitate quick and safe imaging of high-pressure fluid injections in a CT 80 W Nanoscan PC imager μPET scanner. The setup was designed to minimize the risks for leakage, by reducing the number of connections and valves. The experimental set-up consisted mainly of: three piston pumps, a core holder, a back-pressure regulator, and several in-line pressure transducers, and is further described below.

A cylindrical Rørdal chalk core (Ekdale and Bromley, 1993) with 3.81 cm diameter and 8.44 cm length was washed and dried at elevated temperature. The core was fully saturated by brine (5 wt%NaCl, 5 wt% $CaCl_2$) under vacuum and the porosity was determined by weight measurements ($\varphi = 46.5\%$). Absolute permeability (K) was measured by injecting brine into the core at different volumetric flow rates while measuring the differential pressure across the core, and was calculated by Darcy's law [Eq. (1)] to 6.15 mD.

$$K = \frac{Q\mu L}{A\Delta P} \quad [1]$$

Eq. (1) gives a generalized form of Darcy's law, applicable to horizontally aligned, fully saturated and uniformly shaped porous media, such as the chalk core plug. All parameters on the right side of the equation are measured directly in the laboratory: the length (L) and cross-sectional area (A) of the core plug, and the pressure drop across the core (ΔP) during injection of an incompressible fluid, with a constant viscosity (μ) at different volumetric flow rates (Q).

The core was wrapped in aluminum foil and placed in a Viton sleeve with 1.5″ peek end pieces at each end. Distribution grooves in the end pieces ensured a uniform distribution of fluids across the core cross section during injections. The core was mounted in a custom-made core holder certified to 200 bar pressure (©RS Systems, Trondheim, Norway). Pump 3 (ISCO piston pump) contained light mineral oil and was used to apply and maintain confinement pressure around the core, held 10 bar above the line pressure for the duration of the experiment. The core

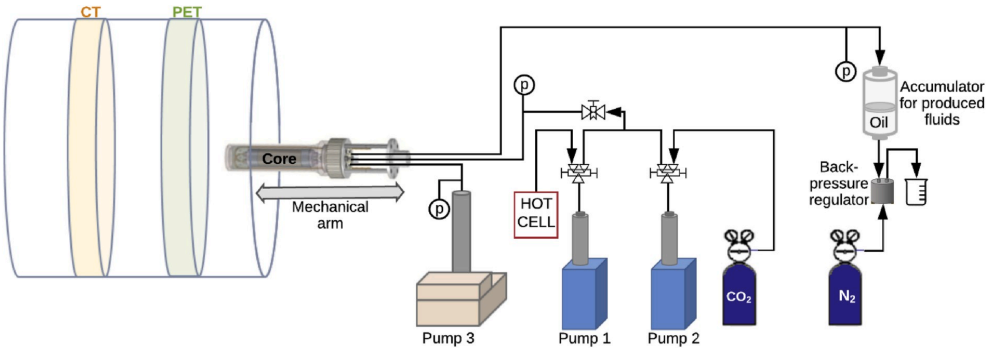

Fig. 1. Schematic of the experimental setup used for PET imaging of radiolabeled CO_2 and brine injections. Pump 1 was used to inject brine into the core, and also received $^{11}C–CO_2$ in gaseous state from the hot cell, and was used to inject CO_2 into the core. Pump 2 contained pressurized CO_2. Produced fluids were collected in an accumulator. The system pressure was controlled by a back-pressure regulator connected to a nitrogen tank. Line pressures (P) were measured using pressure gauges connected to the injection and production lines. Confining pressure was controlled by Pump 3. The mechanical arm moves the core holder horizontally into position for CT and PET imaging.

holder was attached to a mechanical arm outside the μPET scanner. The mechanical arm is controlled through the scanner software (©Nucline), and moves the core holder horizontally into the position determined by the operator. The core holder must be able to move freely along the z-axis to be positioned within the field of view detectable by μPET imaging. The core holder was therefore connected to flexible peek injection and production lines. The injection line was connected to two piston pumps (Sanchez Technologies): Pump 1 and 2 were connected by 1/8″ Hastelloy tubing (Swagelok) facilitating valves (Autoclave) and could easily be isolated from each other and/or the core system. Liquid ^{18}F-FDG was received before each water injection, and was mixed with brine and pressurized in Pump 1. Before CO_2 injection, Pump 1 was connected to the hot cell using 1/8″ plastic Swagelok tubing, and the radioactive isotope was transferred directly into the pump at a slightly elevated pressure (≈ 8 bar). $^{11}C–CO_2$ was mixed and pressurized to experimental conditions in the pump by transferring pressurized CO_2 from Pump 2. Radioactively labelled brine or CO_2 was injected from Pump 1 into the common, flexible injection line. The production line was connected to a piston accumulator, filled with mineral oil. The radioactive fluid was collected on the top side of the piston. Oil was produced at the lower end of the accumulator, which was connected to a back-pressure regulator controlled by a Nitrogen gas tank. The core system was pressurized to 68 bars by non-labelled brine before labelled injection started. Initial CT scans were acquired to determine the position of the core, and the core holder was thereafter moved into the PET field of view, ranging 8*8*9.47 cm in the x-, y-, z-directions. PET sequences were acquired, where the spatial resolution offered by the detector system was 0.4 mm^3. Three radiolabeled floods were monitored using PET acquisitions: the injection procedure for each flood is detailed in section 2.2.

2.2. Fluid injections

1st brine injection: Radioactively labelled brine was injected into the chalk core to miscibly displace the initial brine saturation and determine inherent displacement heterogeneities within the core. ^{18}F was produced by a local cyclotron and used to synthesize ^{18}F-fluorodeoxyglucose (^{18}F-FDG), which is a water-soluble fluorine radioisotope with a half-life of 109 min 350 MBq of ^{18}F-FDG was received in a syringe and mixed in brine (5 wt%NaCl, 5 wt%$CaCl_2$). The brine was transferred to the injection pump (Pump 1, Fig. 1) and pressurized to the experimental conditions. Pump 2 contained pressurized CO_2 and was not used during this stage. PET acquisition was performed while radioactive brine was injected into the core at a volumetric flow rate of 1 cm^3/min. Two pore volumes (PV) of brine were injected, and the core pore volume remained fully saturated by water during this flood. The back-pressure was kept constant at 68 Bar. After water injection, the core was shut-in and remaining radioactivity allowed to decay before further injections.

CO_2 injection: 2 PV of $^{11}C–CO_2$ was injected into the chalk core. Water was displaced by CO_2, thus the volume of water in the pore volume decreased and the volume of gas increased. When several immiscible fluids are present in the same pore space, their respective volumes are often expressed as saturation, S_i, which describes the fraction of the total pore volume filled with a fluid *i*. When gas invaded the chalk core, the fraction of water in the pore volume decreased from $S_w = 1$ (pore volume 100% water filled), to a lower, irreducible water saturation, S_{wi}. The gas saturation in the pore volume increased correspondingly, and could be explicitly quantified by PET imaging. Pump 1 was emptied and set to receive while [^{11}C]arbon dioxide was produced by the cyclotron and transferred at an elevated pressure through nylon tubings directly into the pump. 2 GBq of $^{11}C–CO_2$ was pressurized in Pump 1 by transferring 350 cm^3 of pre-pressurized CO_2 from Pump 2. Radioactive CO_2 was injected from Pump 1 into the chalk core using a volumetric injection rate of 1 ml/min, while the fluid distribution was continuously recorded by PET. The experimental pressure condition was 50 bars, thus CO_2 was compressed by a factor of 79 compared to atmospheric conditions and injected in vapor phase. After 2 PV of CO_2 had been injected, the core was shut in and $^{11}C–CO_2$ decayed swiftly. A second injection of ^{18}F-FDG labelled water was performed within a few hours.

2nd brine injection: Water was injected to promote capillary trapping of CO_2. ^{18}F- FDG labelled brine displaced CO_2 to the residual gas saturation (the fraction of the pore volume filled with water increased, and the fraction filled with gas decreased to a lower, immobile value, S_{gr}, which correspond to the volume of capillary trapped CO_2). The procedure was similar to the first brine injection; 350 MBq of ^{18}F-FDG was mixed in brine, pressurized to the experimental pressure condition (50 Bar, similar to CO_2 injection) and injected using a volumetric flow rate of 1 ml/min. The spatial distribution of fluids was continuously monitored by PET acquisitions.

2.3. Post-processing and analysis of in-situ saturations

Post-processing of the PET signal was necessary to determine the saturation and spatial distribution of each fluid. Three-dimensional PET images were reconstructed, where each image frame represented a time span of 5 min. It must be acknowledged that high volumetric injection rates coupled with long reconstruction frames implement a higher uncertainty in the images, in terms of localizing of the displacement front. For the purpose of this paper, the uncertainty was tolerable (within 6%

of the pore volume). Post-processing of the PET signal may be performed several times, using different time intervals. The images were reconstructed without attenuation correction from CT. Spatial fluid saturations could then be calculated based on the registered activity of the labelled brine or gas phase.

The three-dimensional core images were further sub-divided into sub-core sections, to evaluate discrepancies from ideal displacement that were observed during the first brine and CO_2 injections. Pini et al. (2016) and Zahasky and Benson (2018) previously performed sub-core scale analysis based on three-dimensional (3D) PET-data, where the core was subdivided into streamline tubes spanning the full core length, essentially collapsing three-dimensional saturation data to a two-dimensional (2D) bundle of tubes. The necessary assumptions for such sub-division, in addition to similar pressure boundary conditions for all tubes, is that flow within each element is one-dimensional with constant velocity, and that mixing or transverse dispersion between the tubes do not occur. Dynamic fluid flow data during water and gas injections showed that the best option to collapse the present 3D data to 2D was by sub-dividing the core into concentric shells (Fig. 2), due to a clear radial difference in the displacement. Four concentric shells were implemented on the core cross-section, at nine different core lengths.

3. Results and discussion

3.1. 1st brine injection

Miscible ^{18}F-FDG labelled brine injection (at $S_w = 1$), was first performed, where PET imaging revealed displacement heterogeneities within the chalk core (Fig. 3). Water breakthrough occurred at t = 0.67 PV water injected, hence the displacement deviated from ideal displacement, where the water breakthrough is anticipated to occur at 1 PV injected. Visualization by PET showed that the injected brine moved faster close to the core circumference, with a swift breakthrough at the production end.

PET visualization (Fig. 3) showed that the increase in radiolabeled water saturation was slower in the inner part of the core compared to the core circumference. Sub-core analysis was used to identify the cause for deviation from ideal displacement during miscible brine-brine displacement (Fig. 4): The accumulated volume of radiolabeled water ($V_{FDGbrine}$) across the core length increased linearly in all concentric shells before water breakthrough. Core scale development was near ideal (displaced volumes equal to displaced, as expected) with a faster development in the outer core region (Shell 4) and a slower development in the inner core (Shell 1, 2 and 3). The partial volume flow in each concentric shell could be determined from the slope of each line in Fig. 4, and Darcy's law was used to determine absolute sub-core permeabilities to 4.4 mD (inner core, Shell 1), 4.8 mD (Shell 2), 5.6 mD (Shell 3) and 7.1mD (core circumference, Shell 4). The permeability variation significantly impacted the water displacement. Further, each of the nine core positions were analyzed separately. Fig. 4 (right side) summarize the findings by showing two separate core positions; dimensionless length (Xd) 0.15 and 0.57. Displacement discrepancies between inner and outer core regions was more pronounced when the displacement front advanced further from the inlet, yielding a much slower development in core center saturation at higher X_d. The PET signal reached the same end point in all shells, which indicates that the pore volume of water is not spatially dissimilar-i.e. the porosity does not vary significantly within the core. Permeability variations can, hence, not be attributed to porosity directly. Pore size variations could cause a variation in permeability, but may not be determined by PET imaging. Rørdal chalk core material is expected to be relatively homogeneous; because globally measured porosity and permeability values are within the expected range, deviations from ideal displacement would not be determined (or expected) without *in-situ* imaging.

3.2. CO_2 injection

Radiolabeled CO_2 was injected into the core, reducing the water saturation towards irreducible (S_{wi}). Displacement heterogeneities were further amplified during CO_2 injection (Fig. 5), due to the unfavorable mobility ratio of gaseous CO_2 displacing higher-viscosity brine. CO_2 breakthrough was recorded at the production end after 0.5 PV injected. The average CO_2 saturation at the end point was calculated from the ^{11}C–CO_2 intensity to be 0.66, corresponding to an irreducible water saturation of 0.44. Quantitative core scale profiles (Fig. 5) show a clear gradient in saturation along the core length; with a significantly higher CO_2 saturation (i.e. higher signal) close to the inlet than further into the core. The CO_2 saturation range was measured to vary between 0.56 (close to the production end) and 0.87 (close to the inlet).

Sub-division of the core into sub-core concentric shells, as illustrated in Fig. 2, was performed. A gradient in CO_2 intensity (i.e. saturation) along the core length was also clearly visible in the sub-core analysis (Fig. 6), where the saturation end-points were significantly lower further into the core (X_d 0.57), than close to the inlet (X_d 0.15). A second, radial, gradient in CO_2 saturation was also revealed: although the CO_2 saturation increased in all shells, the saturation development was slower in the inner parts of the core (yellow lines in Fig. 6) compared to the outer parts of the core (blue lines in Fig. 6). Longitudinal and radial displacement discrepancies led to a poorer drainage by CO_2 in the core center and close to the production end. The core was shut-in after injection, and the signal from ^{11}C–CO_2 decayed.

3.3. 2nd brine injection

Radiolabeled brine was injected a second time to facilitate residual trapping of CO_2. PET imaging revealed an even displacement of CO_2 from the pore space, with no significant radial or longitudinal variations on the core or sub-core scale (Fig. 7). The water saturation at breakthrough averaged 0.60, hence capillary trapped CO_2 occupies 40% of the pore volume. The signal end points reached in each concentric shell

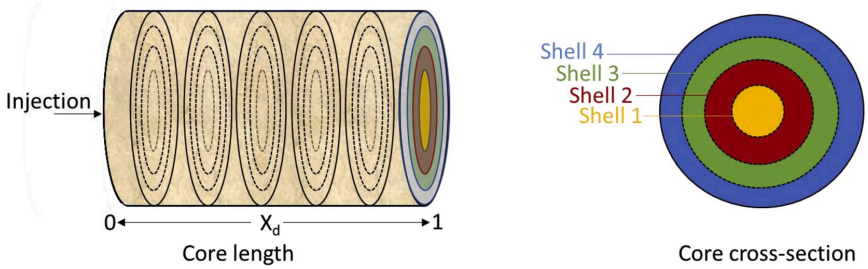

Fig. 2. Sub-core analysis was performed by dividing the core cross-section into concentric shells. Four concentric shells were analyzed in the axial direction, for nine different core lengths i.e. each cross-section represented 1 cm of the core. Dimensionless core length (X_d) was used.

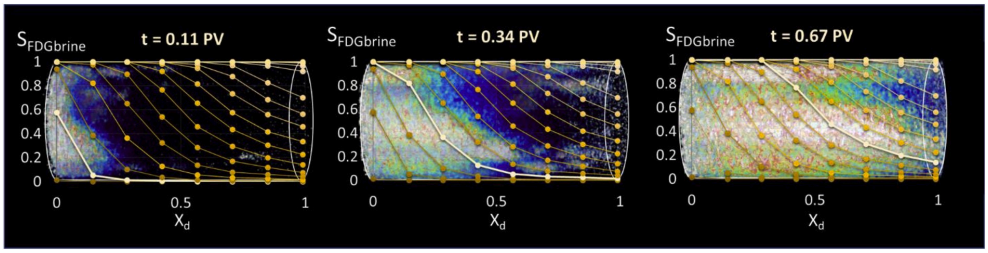

Fig. 3. Development of miscible FDG brine-brine displacement in a cylindrical chalk core sample. Qualitative 3D images of core saturation are overlaid by quantitative 1D profiles derived from the PET signal. In the three-dimensional images, bright colors correspond to a strong PET signal (high number of annihilation events). Three different time steps are shown: t = 0.11PV (left), t = 0.34 PV (middle) and t = 0.67 PV (right). Injected water broke through at the production end at t = 0.67 PV, due to flow heterogeneities.

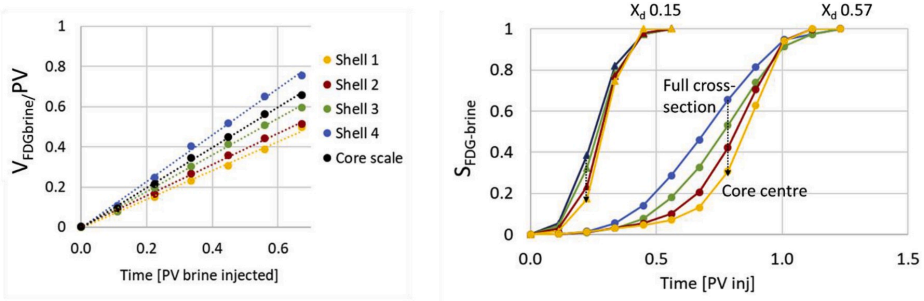

Fig. 4. Volume of radiolabeled water (V_w) in each concentric shell as a function of time (left). A linear displacement was seen in all core regions, with faster increase in the outer core (Shell 4), caused by a higher permeability. V_w was normalized to the pore volume, which gives water saturation. Dimensionless core lengths 0.15 and 0.57 are shown separately on the right, and emphasize that displacement discrepancies are more pronounced further into the core. The core was fully saturated by water at the end of injection, thus the same endpoint signal was reached in all shells.

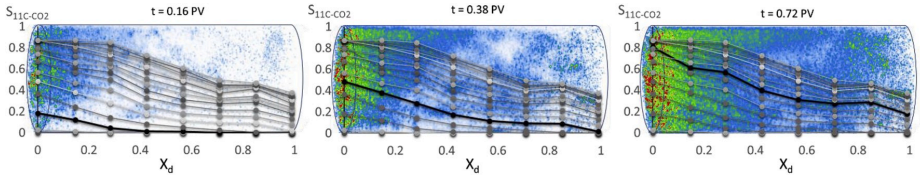

Fig. 5. Dynamic saturation development during $^{11}C–CO_2$ injection into a chalk core. Qualitative 3D images of core saturation are overlaid by quantitative 1D profiles derived from the PET signal. Three different time steps are shown: t = 0.16 PV (left), t = 0.38 PV (middle) and t = 0.72 PV (right). Injected CO_2 broke through at the production end at t = 0.5 PV, due to flow heterogeneities and an unfavorable mobility ratio. In the 3D images, red color represents the highest PET intensity (seen immediately after the inlet at t = 0.38 and t = 0.72), followed by green and blue. Areas with no signal from $^{11}C–CO_2$ are shown in white. -The mixed white/blue color close to the production end at t = 0.72 PV indicates large spatial variations in CO_2 saturation.

were similar, as were the end points for each core position, suggesting that capillary trapped CO_2 is evenly distributed in the core. This is surprising, because visualization showed a significantly uneven saturation distribution during CO_2 injection (Fig. 5). A redistribution of CO_2 may have occurred during shut-in, before the second waterflood. The CO_2 saturation was high during shut-in, and it is likely that capillary redistribution of water by spontaneous imbibition (from high-saturation to low-saturation pores) forced CO_2 to spread out within the core. Saturation redistribution during the period of shut-in cannot be identified by PET due to loss of signal as ^{11}C decays. Redistribution of CO_2 during core shut-in (no injection) likely had a positive effect on the relatively high degree of capillary trapped gas, as CO_2 appeared to be more uniformly distributed in the core plug at the onset of brine injection than immediately after CO_2 injection. Capillary trapping of CO_2 has been proposed as the most rapid and effective way to ensure safe storage of CO_2, and can be controlled by waterflooding (Qi et al., 2008).

3.4. *μPET addition to global data*

Global measurements of pressure and produced effluents, used in most laboratory core floods, yield important information and provide the basis for assessing average system properties. Differential pressure measurements for each injection are provided in Fig. 8. The differential pressure quickly reached plateau and remained stable during the first brine injection, when the core was fully saturated by water. During CO_2 injection and second brine injection, two phases were present in the pore space: hence, the pressure increased more slowly, reached a peak value and decreased to a stable value towards the end of injection when the

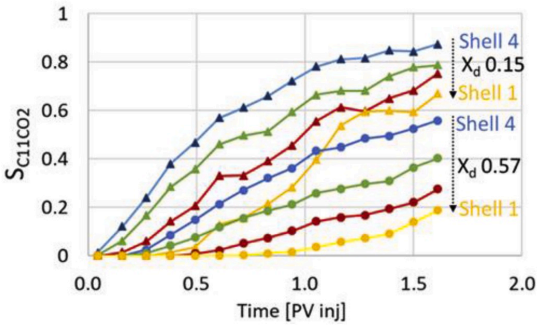

Fig. 6. Sub-core saturation development for core lengths 0.15 and 0.57 during CO_2 injection. The saturation development in shell 1 (inner core) is slower further into the core, and a wide variation in saturation end points were observed.

core saturation was stable. End point relative permeabilities can be calculated from the stabilized pressures at the end of each injection, and was 0.02 for CO_2 at the irreducible water saturation (CO_2 is the flowing phase, water is immobile). Low relative permeabilities for CO_2 were also previously observed (Busch and Müller, 2011). The end point relative permeability for water flowing through a partially CO_2-saturated core (presence of residually trapped CO_2) was 0.74.

Dynamic development of core saturation may also be determined from effluent measurements, although the inherent uncertainty may be high depending on the chosen laboratory method. *In-situ* imaging by PET provides spatially and temporally accurate saturation snap-shots (Fig. 9), where the resolution is not pre-determined but set during post-processing of the PET signal. Effluent measurements would show the deviation from ideal displacement early on during the first miscible brine and gaseous CO_2 floods, and the close to ideal development when brine was injected to trap CO_2, but without determining the cause for deviations. PET imaging revealed severe displacement heterogeneities during the first miscible brine injection and CO_2 injection, which could be quantified by sub-core analysis and attributed to a permeability variation within the chalk core. The high spatial resolution of μPET provided a sufficient number of voxels (each of 0.4 mm^3 volume) for sub-core analysis: ranging from 67 (shell 1) to 550 (shell 4), which is necessary to account for natural fluctuations in the PET instrument. For clinical PET scanners with lower spatial resolutions (2–3 mm), the same sub-core analysis would include only a few voxels and, hence, be more influenced by uncertainties. Although longitudinal discrepancies could be quantifiable, the radial displacement heterogeneities would not.

A clear advantage of most clinical PET scanners that must not be overlooked is the combination with another imaging modality, like CT or MRI: which may be used to gain insight into heterogeneities in the rock structure. CT included in preclinical μPET scanners are usually intended for small, less dense animals, hence the beam strength is not sufficient to accurately reproduce rock structure. Some structural information may, however, be available from PET imaging alone, as demonstrated during miscible brine-brine displacement.

By investigating flow dynamics in complex flow systems, such as carbonates, controlling mechanisms of CO_2 migration may be further mapped on larger scales. The possibility of using μPET to explicitly image fluid flow, and accurately quantify flow dynamics on mm-scale, unlocks significant potential in experimental work related to CO_2-EOR

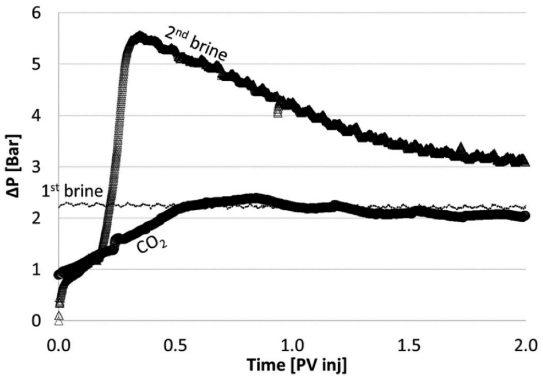

Fig. 8. Differential pressure development during brine injection when the core was fully water saturated, drainage by CO_2 and second water imbibition.

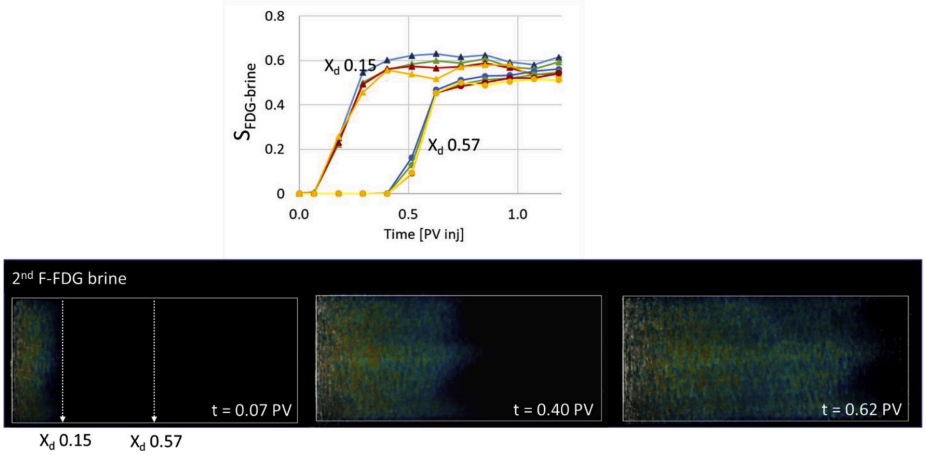

Fig. 7. Top: Sub-core saturation development for core lengths 0.15 and 0.57 during subsequent waterflooding, efficiently trapping CO_2. Bottom: 2D representation of core scale saturation development. No significant radial displacement differences were observed. Thus, during subsequent brine injection, an ideal and piston-like displacement was observed on the core and sub-core scales.

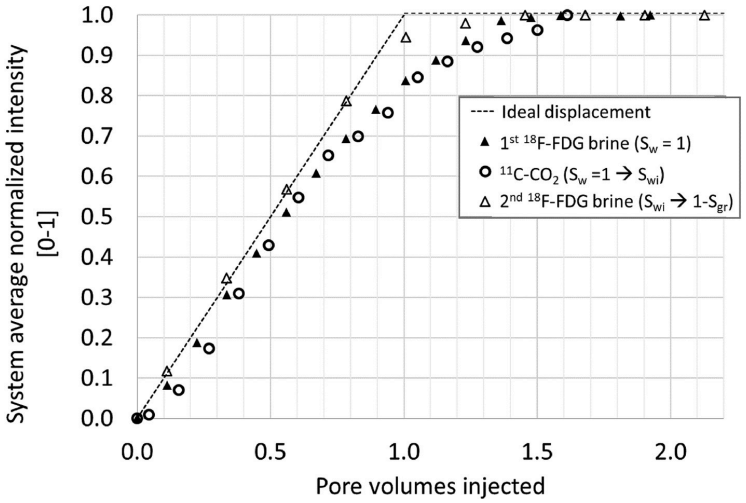

Fig. 9. Core scale saturation development from PET-imaging. The straight, dotted line shows an ideal displacement. The first brine injection and CO_2 injection deviates from ideal displacement early on, while the second brine injection (brine displacing CO_2) shows close to ideal development.

and storage. CO_2 capillary threshold pressure was previously measured using PET-imaging (Fernø et al., 2015a) and CO_2/brine relative permeabilities may be derived from unsteady-state core floods similar to the ones presented here. Positron Emission Tomography hence present a robust imaging approach to improve laboratory measurements that are important to geological CO_2 storage.

4. Conclusions

This paper demonstrated explicit and dynamic imaging of CO_2 during flow through a low-permeable chalk core at elevated pressure conditions. Short-lived radioisotopes were used to track the water and gas phases.

- Improved spatial resolution offered by preclinical μPET provided accurate quantification of spatial phase saturations during brine and CO_2 injections.
- Dynamic PET imaging revealed heterogeneous displacement patterns, which could be quantified at the mm-scale, and attributed to a sub-core variation in permeability. Sub-core permeabilities were calculated from PET displacement data.
- A CO_2 storage capacity of 66% pore volume was obtained by injecting CO_2 into a water-filled chalk core. The storage capacity was reduced to 40% after subsequent injection of water, which trapped and evenly distributed CO_2 in the pore volume.
- PET imaging may contribute to improved determination of basic flow parameters and saturation functions from core-scale experiments, which are essential to numerical simulations of CO_2 migration in the subsurface.

Declaration of competing interest

The authors declare that they have no known competing financial interests or personal relationships that could have appeared to influence the work reported in this paper.

CRediT authorship contribution statement

Bergit Brattekås: Methodology, Visualization, Formal analysis, Writing - original draft. **Malin Haugen:** Methodology, Visualization, Writing - original draft.

Acknowledgements

The PET imaging was performed at the Molecular Imaging Center in Bergen, Norway. The authors thank Heidi Espedal and Njål Brekke for help during experiments.

The authors thank the mechanical work shop at the Dept. of Physics and Technology for constructing a custom portable trolley to house the experimental equipment. The core holder was made by RS systems (Trondheim, Norway). The authors acknowledge the research council of Norway for financial support, through the "Subsurface Carbonate CO_2 Storage and Security" project no. 280341, and for funding PhD candidate Malin Haugen.

Nomenclature

^{18}F-FDG	18F-Fluorodeoxyglucose, glucose analog and radiopharmaceutical, miscible with water
^{11}C	Radioactive isotope of carbon, used to trace CO_2
$t_{1\backslash 2}$	Half-life of the decaying radioactive isotope
K	Absolute permeability [mD]
Φ	Effective porosity: [%]
L	Core length [cm]
X_d	Dimensionless core length [0-1]
Q	Volumetric flow rate [cm^3/s]
A	Cross-sectional area of core [cm^2]
μ	Fluid viscosity [Pa·s]
S_w	Fraction of water present relative to the pore volume (water saturation)
S_g	Fraction of gas present relative to the pore volume (gas saturation)
S_{wi}	Irreducible water saturation [0-1]
S_{gr}	Residual gas saturation [0-1]
V_w	Volume of water [cm^3]

Abbreviations

CO_2	Carbon dioxide
NaCl	Sodium Chloride
$CaCl_2$	Calcium chloride

EOR	Enhanced Oil Recovery
PET	Positron Emission Tomography
μPET	micro-Positron Emission Tomography
CCUS	Carbon, Capture, Utilization and Storage
MRI	Magnetic Resonance Imaging
CT	Computed Tomography
PV	Pore Volume
ΔP	Pressure drop across the unit length

References

Akbar, M., Vissapragada, B., Alghamdi, A.H., Allen, D., Herron, M., Carnegie, A., Dutta, D., Olesen, J.-R., Chourasiya, R.D., Logan, D., Stief, D., Netherwood, R., Duffy Russell, S., Saxena, K., 2000. A Snapshot of Carbonate Reservoir Evaluation, pp. 20–41. Oilfield Review, Winter 2000-2001.

Akin, S., Kovscek, A.R., 2003. Computed Tomography in Petroleum Engineering Research, vol. 215. Geological Society, London, Special Publications, pp. 23–38.

Almenningen, S., Gauteplass, J., Fotland, P., Aastveit, G.L., Barth, T., Ersland, G., 2018. Visualization of hydrate formation during CO2 storage in water-saturated sandstone. Int. J. Greenh. Gas Contr. 79, 272–278.

Bailey, D.L., Townsend, D.W., Valk, P.E., Maisey, M.N., 2005. Positron Emission Tomography. Springer.

Brattekås, B., Eide, Ø., Johansen, S.A., Vasshus, S.S., Polden, A.G., Fernø, M.A., 2019. Foam Flow and Mobility Control in Natural Fracture Networks. Transport in Porous Media.

Brattekås, B., Seright, R.S., 2018. Implications for improved polymer gel conformance control during low-salinity chase-floods in fractured carbonates. J. Petrol. Sci. Eng. 163, 661–670.

Brattekås, B., Steinsbø, M., Graue, A., Fernø, M.A., Espedal, H., Seright, R.S., 2017. New insight into wormhole formation in polymer gel during water chase floods with positron emission tomography. SPE J. 22 (1), 32–40.

Busch, A., Müller, N., 2011. Determining CO2/brine relative permeability and capillary threshold pressures for reservoir rocks and caprocks: recommendations for development of standard laboratory protocols. Energy Procedia 4, 6053–6060.

COP21, 2015. Paris: Conference of Parties 21st Meeting in Paris in December. Accessible at: https://unfccc.int/process-and-meetings/the-paris-agreement/the-paris-agreement.

Ekdale, A.A., Bromley, R.G., 1993. Trace fossils and ichnofabric in the Kjølby gaard Marl, uppermost creataceous, Denmark. Bull. Geol. Soc. Den. 31, 107–119.

Ersland, G., Fernø, M.A., Graue, A., Baldwin, B.A., Stevens, J., 2010. Complementary imaging of oil recovery mechanisms in fractured reservoirs. Chem. Eng. J. 158 (1), 32–38.

Fernø, M.A., Gauteplass, J., Hauge, L.P., Abell, G.E., Adamsen, T.C.H., Graue, A., 2015b. Combined positron emission tomography and computed tomography to visualize and quantify fluid flow in sedimentary rocks. Water Resour. Res.

Fernø, M.A., Hauge, L.P., Rognmo, A.U., Gauteplass, J., Graue, A., 2015a. Flow visualization of CO2 in tight shale formations at reservoir conditions. Geophys. Res. Lett. 42, 7414–7419.

Føyen, T.L., Fernø, M.A., Brattekås, B., 2019. The effects of nonuniform wettability and heterogeneity on induction time and onset of spontaneous imbibition. SPE J. 24 (3), 1192–1200.

IEA, 2019. The Role of CO2 Storage. IEA, Paris. https://www.iea.org/reports/the-role-of-co2-storage.

Kulenkampff, J., Gruundig, M., Richter, M., Enzmann, F., 2008. Evaluation of positron-emission-tomography for visualisation of migration processes in geomaterials. Phys. Chem. Earth 33 (14–16), 937–942.

Levin, C.S., Hoffman, E.J., 1999. Calculation of positron range and its effect on the fundamental limit of positron emission tomography system spatial resolution. Phys. Med. Biol. 44 (3), 781–799.

Pini, R., Vandehey, N.T., Druhan, J., O'Neil, J.P., Benson, S.M., 2016. Quantifying solute spreading and mixing in reservoir rocks using 3-D PET imaging. J. Fluid Mech. 796, 558–589.

Qi, R., LaForce, T.C., Blunt, M.J., 2008. Design of Carbon Dioxide Storage in Oil Fields. SPE Annual Technical Conference and Exhibition. Society of Petroleum Engineers, Denver, Colorado, USA.

Ruth, D., Fernø, M.A., Haugen, Å., Arabjamaloei, R., Brattekås, B., 2016. Matching experimental saturation profiles by numerical simulation of combined Co-/Counter-Current spontaneous imbibition. In: International Symposium of the Society of Core Analysts, Snowmass, CO, USA.

Zahasky, C., Benson, S.M., 2018. Micro-positron emission tomography for measuring sub-core scale single and multiphase transport parameters in porous media. Adv. Water Resour. 115, 1–16.

Zahasky, C., Kurotori, T., Pini, R., Benson, S.M., 2019. Positron emission tomography in water resources and subsurface energy resources engineering research. Adv. Water Resour. 127 (May 2019), 39–52.

Paper 5

Transport in Porous Media
https://doi.org/10.1007/s11242-023-02047-8

Physical Variability in Meter-Scale Laboratory CO_2 Injections in Faulted Geometries

Malin Haugen[1] · Lluís Saló-Salgado[2,3] · Kristoffer Eikehaug[1] · Benyamine Benali[1] · Jakub W. Both[4] · Erlend Storvik[4] · Olav Folkvord[1] · Ruben Juanes[2,3] · Jan Martin Nordbotten[4,5] · Martin A. Fernø[1,5]

Received: 16 January 2023 / Accepted: 11 December 2023

Abstract
Carbon, capture, and storage (CCS) is an important bridging technology to combat climate change in the transition toward net-zero. The FluidFlower concept has been developed to visualize and study CO_2 flow and storage mechanisms in sedimentary systems in a laboratory setting. Meter-scale multiphase flow in two geological geometries, including normal faults with and without smearing, is studied. The experimental protocols developed to provide key input parameters for numerical simulations are detailed, including an evaluation of operational parameters for the FluidFlower benchmark study. Variability in CO_2 migration patterns for two different geometries is quantified, both between 16 repeated laboratory runs and between history-matched models and a CO_2 injection experiment. The predicative capability of a history-matched model is then evaluated in a different geological setting.

Keywords Geologic carbon sequestration · CO_2 storage · FluidFlower · Laboratory · Numerical simulations

✉ Malin Haugen
malin.haugen@uib.no

[1] Department of Physics and Technology, University of Bergen, Bergen, Norway

[2] Department of Civil and Environmental Engineering, Massachusetts Institute of Technology, Cambridge, MA 02139, USA

[3] Earth Resources Laboratory, Department of Earth, Atmospheric and Planetary Sciences, Massachusetts Institute of Technology, Cambridge, MA 02139, USA

[4] Center for Modeling of Coupled Subsurface Dynamics, Department of Mathematics, University of Bergen, Bergen, Norway

[5] Center for Sustainable Subsurface Resources, Norwegian Research Center, Postboks 22 Nygårdstangen, 5838 Bergen, Norway

1 Introduction

As the prices of renewable energy are decreasing, carbon, capture, utilization, and storage represent a bridging technology to combat climate change in the transition period toward net zero. Geological carbon sequestration (GCS) could contribute to the energy transition by tackling emissions from existing energy assets, providing solutions in some of the sectors where emissions are hardest to reduce (like cement production), supporting the rapid scaling up of low-emissions hydrogen production, and enabling some CO_2 to be removed from the atmosphere through bio-energy and direct air capture with GCS (IEA 2021).

Carbon sequestration is based on the principle that the injected CO_2 becomes less mobile over time by porous media trapping mechanisms, where the relative importance between the governing processes depends on the subsurface conditions. In situ visualization of CO_2 injection and the trapping mechanisms are valuable for understanding the fluid flow and migration patterns during geological CO_2 sequestration (GCS), and the authors believe it is also important for enhancing public understanding and acceptance about CO_2 storage and security. The laboratory experiments presented in this paper are relevant for geological carbon storage as the main mechanisms are sustained, including capillarity, dissolution, and convective mixing, and it represents a unique possibility to test our simulation skills, because in contrast to the subsurface, here we can compare predictions to observations.

The FluidFlower concept links GCS research and dissemination through experimental rigs constructed at University of Bergen (UiB) that enable meter-scale, multiphase, quasi-two-dimensional flow on complex, yet representative geological geometries. Intermediate scale quasi-2D laboratory experiments are widely used to study multiphase porous media flow, including gravity unstable flows in the presence of heterogeneity (Glass et al. 2000; Van De Ven and Mumford 2018, 2020; Krishnamurthy et al. 2022), and CO_2 migration and dissolution (Kneafsey and Pruess 2010; Trevisan et al. 2017; Rasmusson et al. 2017). These approaches enable visualizing and studying a range of porous media flow dynamics in engineered representative porous media using unconsolidated beads or sand grains. A key feature of the FluidFlower rigs is the ability to repeat experiments in the same geometry, without the need to remove the sands between repeated runs. Different geological geometries are constructed using unconsolidated sands, and simulation models based on the experimentally studied geometry provide key input parameters for numerical simulations. Gaseous and aqueous forms of CO_2 are distinguished with pH-sensitive dyes, and the multiphase fluid flow dynamics is captured with time-lapse imaging. The Darcy Scale Image Analysis toolbox (DarSIA, Nordbotten et al. 2023) is utilized to analyze the images to quantify key parameters and variability in the experimentally observed CO_2 migration patterns.

The goal of this study is twofold: First, evaluate and discuss physical reproducibility in repeated experimental CO_2 injections in two different geometries. Second, perform dedicated laboratory experiments for history matching to determine the predicative capability of the validated and physics-based model in a different geological setting using the same sands (Saló-Salgado et al. 2023). The paper is divided into three sections: (1) laboratory protocols for measurements of petrophysical sand properties and CO_2 injections, (2) main laboratory results are discussed, including physical variability between repeated CO_2 injections in two geological geometries, and (3) numerical modeling of experimental CO_2 injections with history matching and simulation with comparison to physical experiments.

2 Methods and Materials

2.1 Fluids

Fluid properties are summarized below (Table 1), and the porous media was initially fully saturated with an aqueous pH-indicator mix, referred to as "formation water". The CO_2 was injected as dry gas and will partially partition into the formation water to form "CO_2 saturated water". The image analysis (Section 1.6) can distinguish between the different phases from the added pH sensitive dyes (gas and aqueous phases are originally transparent). Three different pH-indicator mixes (Fig. 1) were used to test visual impact on tracking CO_2 gas migration (as absence of color) and CO_2 saturated water, and further how this is influenced by the image segmentation using DarSIA (Nordbotten et al. 2023).

The pH of the formation water impacts the equilibrium between gaseous CO_2 and the aqueous phase, and it was expected pH-indicator mix 3 (pH approximately 10) would lead to higher CO_2 dissolution rate (and less mobile gaseous CO_2) compared with mix 1 and 2 (pH approximately 8). The rate of dissolution impacts migration patterns for both gaseous CO_2 and CO_2 saturated water, and the CO_2 concentration in CO_2 saturated water also influence gravitational-dominated flow processes due to density differences. At standard conditions (20 °C and 1013 millibar), the maximum solubility of CO_2 in water is about 1.7 g of CO_2 pr kg of water (The Engineering ToolBox 2008), corresponding to an increase in density of around 1–2%.

2.2 Physical Properties of the Quartz Sand—Experimental Protocol

When sediments (particles) accumulate they form sedimentary deposits which compose layers of rock. Within a deposit, the individual particles vary in size, shape, etc., and hence, the layer they constitute has certain macroscopic properties such as porosity and permeability (Krumbein and Monk 1942). These mass properties will vary with, among others, the combination of properties of the particles and the conditions of packing (Krumbein and Monk 1942). The geologically important characteristics of sediments might be described using six measurable quantities: size, shape (sphericity), roundness (angularity), mineral composition, surface texture and orientation. The following sections describe the procedures to measure the properties of the unconsolidated sands.

2.2.1 Sand preparation

The unconsolidated quartz sand used was purchased from a commercial Norwegian supplier. Based on the stated and available grain size ranges, desired grain size ranges for this study were chosen according to the Wentworth scale (Wentworth 1922) (Table 2). The received sands were sieved prior to building the geological geometries to achieve increased control of the used grain size ranges. Dry wire-mesh sieves (*Glenammer*) staked on a mechanical shaker were used, before the sands were washed in a two-step process: (1) Rinsed with tap water to remove fine material, (2) Acid washed using HCl until carbonate impurities were dissolved, and no more CO_2 bubbles were observed (varying from 24 to 72 h for the different sand types). The acid was then neutralized, and the sand was rinsed with tap water. After washing, the sands were dried at 60 °C

Table 1 Fluids and pH-indicator mixes with their expected pH values

Fluid (phase)	Composition	pH	Usage
Deionized water	H_2O	–	Petrophysical sand properties
Acid (aq)	Tap water with - Above 0.1 M hydrochloric acid (HCl)	< 2 *	Remove carbonate impurities during sand cleaning
pH-indicator mix 1 (aq)	Deionized water with - 0.14 mM bromothymol blue (BTB^-) - 0.43 mM methyl red (Mre^-) - 0.10 mM hydroxide (OH^-) - 0.67 mM sodium ions (Na^+)	~ 8.3	Initial formation fluid to enable detecting CO_2 dissolution in the aqueous phase
pH-indicator mix 2 (aq)	Deionized water with - 0.14 mM bromothymol blue (BTB^-) - 0.10 mM hydroxide (OH^-) - 0.24 mM sodium ions (Na^+)	~ 8.3	Initial formation fluid to enable detecting CO_2 dissolution in the aqueous phase
pH-indicator mix 3 (aq)	Deionized water with - 0.75 mM bromothymol blue (BTB^-) - 1.00 mM hydroxide (OH^-) - 0.67 mM sodium ions (Na^+)	< 10.4**	Initial formation fluid to enable detecting CO_2 dissolution in the aqueous phase
CO_2 (g)	99.999%—5.0 purity	–	Injected as gaseous phase
Lye solution (aq)	Deionized water with 0.48 mM sodium hydroxide (NaOH)	< 10.7**	Reset/clean the system after experiments (flush out CO_2 saturated water and trapped free gas)

*Maintained below pH 2 until stable. **Depending on exposure to air

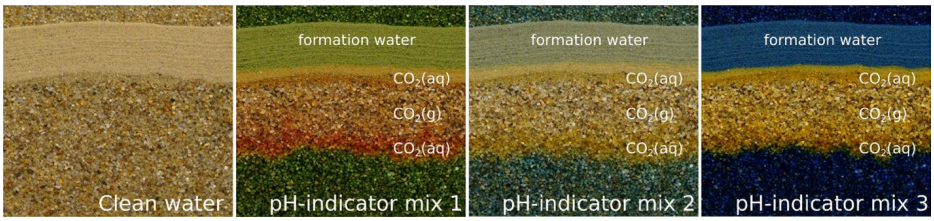

Fig. 1 Illustration of different pH-indicator mixes used in the experiments, and their colored response to gaseous and dissolved CO_2 as supposed to the formation water. From left to right: Image of a layered sand formation saturated with clean water; same formation but saturated with pH-indicator mixes 1–3 in the presence of CO_2

Table 2 Desired grain-size range of sand used in this study and size of wire-mesh sieves used

Sand ID	Desired grain size range[a] [mm]	Desired grain size range[a] [phi scale]	Grade[a]
ESF	0.13 to 0.36[b]	2.9 to 1.5	Fine sand
C	0.5 to 0.71	1.0 to 0.5	Coarse sand (lower)
D	0.71 to 1.0	0.5 to 0.0	Coarse sand (upper)
E	1.0 to 1.41	0 to -0.5	Very coarse sand (lower)
F	1.41 to 2.0	−0.5 to −1.0	Very coarse sand (upper)
G	2.0 to 2.8	−1.0 to −1.5	Granule gravel

[a]Sieved range and grade according to Wentworth class (Wentworth, C.K., 1922)

[b]Size range provided by supplier. Sand ESF was not sieved, only washed and dried to maintain fine particles

for at least 24 h and stored in clean 15 L plastic containers until use. Sands named ESF, C, E and F were used to build the geometries investigated here (Sect. 2.3), whereas all sand types were used in FluidFlower benchmark geometry (Fernø et al. 2023).

2.2.2 Protocol for petrophysical measurements

The petrophysical properties porosity (φ), absolute permeability (K) and endpoint relative permeability (kr) of the unconsolidated sand were measured using a sand column (Fig. 2). Custom-made end pieces (polyoxymethylene) with a Y-shaped passage enabled absolute pressure measurement (ESI, GSD4200-USB, −1 to 2.5 bara) at each end face, with milling for a round metal mesh and paper filter against the sand to maintain sand column integrity. A differential pressure transducer (Aplisens PRE-28, 0–2.5 bara) was positioned 154 mm from the top and bottom of the tube and measured the differential pressure across a 171 mm section of the sand column. The procedural steps for the petrophysical measurements are detailed below, and different fluids were injected through the sand column throughout the procedure. Note that all bottles and outlets were at the same height to ensure a stable system with no flow in or out of the sand column when fluid injection was stopped. Tubes were fixed in place to mitigate influence on measured sand column weight and produced fluids during endpoint relative permeability measurements.

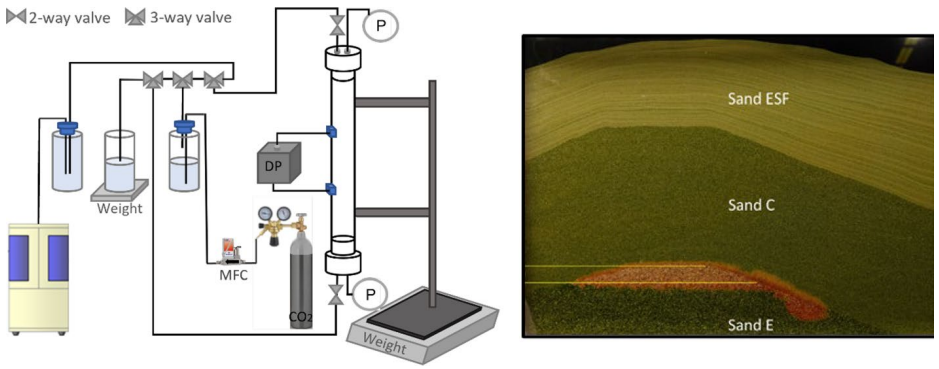

Fig. 2 Left: schematic of the experimental set-up used for measuring porosity, absolute permeability, and relative permeability (Sect. 2.2.3–2.2.5). A vertical Plexiglas tube (length 478.0 mm and diameter 25.8 mm) with metal mesh and 0.2 µm paper filter against the sand maintained sand column integrity. ESI pressure transducers (−1–2.5 bara) monitored inlet and outlet pressure and temperature. An Aplisens differential pressure transducer (0–2.5 bara) recorded the differential pressure in the middle of the sand column. Quizix QX pump controlled the volumetric rate of injected aqueous phases, whereas a Bronkhorst El-Flow Prestige mass flow controller with a maximum rate of 10ml/min was used for the CO_2 injection. Right: Example geometry used for gas column breakthrough experiments to obtain capillary entry pressure (height of gas column, distance between horizontal yellow lines), here for sand C

2.2.3 Porosity (φ) measurement

Porosity was calculated for all sand types using the following procedure:

1. The vertical tube, with bottom end-piece and filter attached, was filled with degassed, deionized (DI) water to a predetermined and known water height.
2. Dry sand was poured into the water-filled tube and settled at the bottom. Approximately 20 mm sand was added each time, and the tube was gently tapped during sand settling. Sand was added until the sand column height reached the predetermined level.
3. Water was constantly removed from the top of the tube during sand settling and the volume of the extracted water was measured cumulatively.
4. Prior to attaching the top end-piece, the tube was filled with DI (to minimize air between the end-piece and the sand) and the filter placed on top of the sand. Tubing attached to the end-piece was loosened to enable the displaced water to escape as the end-piece was placed into the tube without asserting force to the sand.

The extracted water volume in step 3 equals the sand grain volume, and the porosity was calculated from the ratio of the pore volume (bulk volume—grain volume) to bulk volume.

2.2.4 Absolute permeability (K) measurement

Absolute permeability was measured after the porosity measurement described above with the following procedure:

1. Degassed DI water was injected from the bottom with a high volumetric injection rate (650 ml/h for 3 h) to remove trapped gas bubbles, if any.
2. Flow direction was reversed (top endpiece used as inlet) and degassed DI water was injected using 5 ascending and descending constant volumetric injection rates between 200 and 600 ml/h, with 100 ml/h increments for 10 min. (Stable differential pressures were achieved.)
3. Differential pressures versus injection rate were recorded and used for calculation of absolute permeability using Darcy's law and is given by $Q = -K \bullet A \bullet \left(\frac{\Delta P}{L}\right)$, where Q is the flow rate, K is the absolute permeability, A is the cross-sectional area, ΔP is the differential pressure, and L is the unit length.

2.2.5 *Unsteady-state endpoint relative permeability (k_r) measurements*

The unsteady-state end-point relative permeabilities during both drainage and imbibition used CO_2-saturated water and CO_2. The average sand column end-point fluid saturation was calculated from volumetric and weight measurements. The following procedure was followed:

1. After absolute permeability measurements (Sect. 2.2.4), degassed DI water was miscibly displaced with CO_2-saturated DI water. This step was performed to avoid dissolution of gaseous CO_2 gas in the water phase during drainage CO_2 injection.
2. End-point drainage: CO_2 gas was injected from the top with a constant rate of 10 ml_s/min (10 ml/min @ standard conditions: 20 °C + 1013 millibar). The absolute inlet and outlet pressure (sands E, F, G) or differential pressure (sands ESF, C, D), were recorded during drainage. Water production was monitored during drainage (by weight), and CO_2 was injected until no further water production was recorded. The weight of the partially water saturated sand column was recorded. Endpoint relative permeability to CO_2 was calculated based on the pressure differential between 10 and 0 ml/min.
3. End-point imbibition: After the drainage process was completed, the injection was switched back to CO_2 saturated water and ramped up to a constant volumetric rate of 600 ml/h, also injected from the top. The pressures and weight of sand column were recorded during injection. When no additional gas was produced for 60 min, the final sand column weight was recorded and an injection cycle to measure water endpoint permeability was conducted.

2.2.6 Capillary Entry Pressure Measurement

The capillary entry pressure to gas was experimentally measured for each sand type based on observed gas column break-through experiments in the FluidFlower rig (Fig. 3). Different geometries were investigated, including anticlines with an "inverse V shape" top to an "inverse U shape" top, constructed using the sedimentary protocol detailed in Sect. 1.5. The porous media was saturated with pH-indicator mix 1 (see Table 1), and gaseous CO_2 was injected at 10 ml_s/min (10 ml/min @ standard conditions: 20 °C and 1013 millibar). The gas accumulation and column height were monitored with time-lapsed imaging to detect the maximum gas column height between the different sand layers and under the sealing layer (ESF). The observed gas column height (in meter) was converted to pressure to provide the entry pressure for each sand type, by: $P_C = \rho \bullet g \bullet h$, where P_C is the

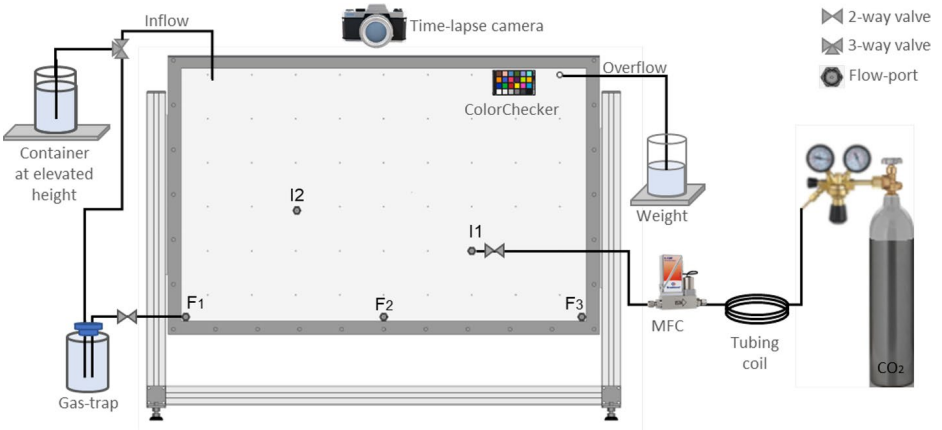

Fig. 3 Schematic overview of a tabletop FluidFlower (920×575 mm visible width x height within the frame) and the associated equipment. Liquids are injected through gravity (container at elevated height) or using a pump. During flushing and resetting the flow-cell, the flush-ports (F1–F3) are utilized, and as a preventive measure to avoid unwanted air bubbles trapped in tubing to enter the rig, a gas-trap was included. For gas injection (through port I1 or I2), the set-up consists of a CO_2 calibrated mass flow controller (MFC), CO_2 tank with regulator and a coil of tubing mitigate pressure fluctuations caused by the gas regulator. Inflow (tubing end) and outflow (always-open port) provide a constant hydraulic head and provide information about volume displaced if logged. A camera with time lapse function is used to acquire high-resolution images of the dynamics, and the ColorChecker ensure correction of colors during image analysis to mitigate changes in illumination. All flow ports are 1/8-inch NPT to 1/8 Swagelok, with inner diameter of 1.8 mm

capillary pressure, ρ is the density of the non-wetting phase, and h is the height of the non-wetting phase column.

2.3 Laboratory Injections of Carbon Dioxide

The FluidFlower enables engineering of meter-scale geological geometries using unconsolidated sands, and its design allows for repeated injections to evaluate reproducibility without removing the sand and rebuilding the geometry. The porous media was constructed using unconsolidated sands and held in place by two optically transparent panels in the front and the back, glued together to an aluminum frame with spacing of 10 mm. The flow cell has no-flow boundaries in the bottom and sides, whereas the top is open and in contact with atmospheric pressure. The size (920×575 mm visible width×height) and design of the tabletop rig allow evaluate physical reproducibility between operationally identical experiments, and rapid testing of key operational conditions, e.g., different pH-indicator mixes, injection protocols, constructing different geological structures and the effect of degassed aqueous phase. Technical and mechanical properties of the FluidFlower rigs are detailed in Eikehaug et al. 2023.

Two different geometries (termed ‘Albus’ and ‘Bilbo’) were studied in this work (see Sect. 2.3). The experimental set-up consists of throttle valve and Swagelok valves (2- and 3-way), mass flow controller (MFC) (EL-FLOW Prestige FG-201CV 0–10 mls/min, BronkHorst) calibrated for CO_2, pressurized CO_2 canister including pressure regulator, gas trap, ColorChecker (X-Rite), and camera with time-lapse function (Albus geometry: Sony ZV-1, 5472×3080 pixels; Bilbo geometry: Sony A7III, lens SAMYANG AF 45 mm F1.8,

7952 × 4472 pixels). The high-resolution images enable monitoring and analysis of multiphase flow dynamics with single grain identification and are one of the main measurements in this set-up.

2.4 Fluid Injection Protocols and Initial Conditions

The protocol to prepare for CO_2 injection experiments used the following steps, with reference to Fig. 3:

1. Inject the preferred pH-indicator mix according to the experimental protocol, using the three injection ports (F1–F3) along the bottom of the rig.
2. Initiate inflow with open overflow port to ensure constant hydrostatic pressure during the experiment.
3. Bleed tubing/valves for CO_2 injection with fluid from the rig (and collect samples for pH measurements). Stabilize overflow before continuing.
4. Run a warm-up MFC sequence (100% open valve for 30 min) to reduce rate fluctuations.
5. At a low CO_2 injection rate, connect tubing to valve and let it pressurize according to protocol before the valve is opened.
    a. Some backflow of pH-indicator is expected; record time when the injected CO_2 displace the backflow fluid into the valve.
    b. Continue CO_2 injection as described in the protocol (Table 3).
    c. Log inflow and outflow rate (mass per timestep) to determine displaced volume.
6. Inject degassed lye solution to reset the fluids in the porous media.

We note that gas injection should follow a scripted MFC protocol, with sufficiently high injection rate to maintain gaseous CO_2 in the injection point. All experiments utilize two ports for CO_2 injection (except experiments AC06 and AC07 that used one port) at room temperature (approximately 23 °C) and atmospheric pressure at the free water table at the top of the rig (cf. Table 4). Temperature fluctuations were minimized, but not eliminated, in the laboratory space, and added some uncertainty.

Table 3 Condensed CO_2 injection protocol used in geometry Albus and geometry Bilbo. Comprehensive protocol found in SI. Table 1. I1 and I2 refer to injection in flow port 1 and port 2, respectively (Fig. 3)

Objective	Albus geometry		Bilbo geometry	
	Rate [ml_s/min][a]	Duration [hh:mm:ss]	Rate [ml_s/min][a]	Duration [hh:mm:ss]
I1 rate ramp-up	0.1–1.5	00:05:00	1.0–1.5	00:02:00
I1 injection	**2.0**	**00:45:00**	**2.0**	**01:03:13**
I1 rate ramp-down	1.5–0.1	00:05:00	1.5–0.5	00:03:00
I2 rate ramp-up	0.1–1.5	00:05:00	1.0–1.5	00:02:00
I2 injection	**2.0**	**01:15:00**	**2.0**	**01:12:52**
I2 rate ramp-down	1.5–0.1	00:04:42	1.5–0.5	00:03:00

[a]CO_2 injection rate in ml_s/min @ standard conditions: 20 °C and 1013 millibar

Table 4 Initial conditions for CO_2 injection experiments in the Albus (AC) and Bilbo (BC) geometries

Experiment	pH-indicator mix[a]	CO_2 inj. 1st/2nd port [g]	P [mbar] [b] 48 h avg. $\pm\sigma$	CO_2 inj. Started	State of formation water degassing
AC02	1	0.179/0.283	999 ± 5	Oct 13th, 2021	Insufficient
AC03	1	0.176/0.283	994 ± 12	Oct 18th, 2021	Insufficient
AC04	1	0.176/0.283	996 ± 11	Oct 21st, 2021	Insufficient
AC05	1	0.176/0.283	995 ± 2	Oct 26th, 2021	Insufficient
AC06	1	0.459/0	989 ± 3	Oct 29th, 2021	Insufficient
AC07	1	0.981/0	993 ± 2	Dec 7th, 2021	Insufficient
AC08	1	0.176/0.284	1015 ± 2	Apr 21st, 2022	Insufficient
AC09	2	0.176/0.284	1010 ± 2	May 3rd, 2022	Insufficient
AC10	3	0.176/0.284	1018 ± 6	May 6th, 2022	Sufficient
AC14	1	0.176/0.284	1003 ± 1	Jun 10th, 2022	Sufficient
AC19	3	0.176/ 0.284	1020 ± 3	Oct 18th, 2022	Sufficient
AC22	3	0.176/ 0.284	1000 ± 1	Nov 15th, 2022	Sufficient
BC01	1	0.240/0.275	1020 ± 4	May 7th, 2022	Sufficient
BC02	1	0.240/0.275	992 ± 3	May 23rd, 2022	Sufficient
BC03	2	0.240/0.275	1006 ± 2	Aug 17th, 2022	Sufficient
BC04	3	0.240/0.275	1019 ± 3	Aug 31st, 2022	Sufficient

[a]Ref Table 4

[b]Atmospheric pressure from metrological data in Bergen (Norway) during each cycle (SI. Figure 4) (Geophysical Institute, 2022)

2.5 Procedure for Constructing Geometries

The size and operational capabilities of the tabletop FluidFlower make it a valuable asset to test and develop procedures and tools for constructing geometric features. A detailed sketch of the desired geological geometry is drawn on the front panel (Fig. 4), and dry sand with predetermined grain size is poured from the top into the water-filled flow cell.

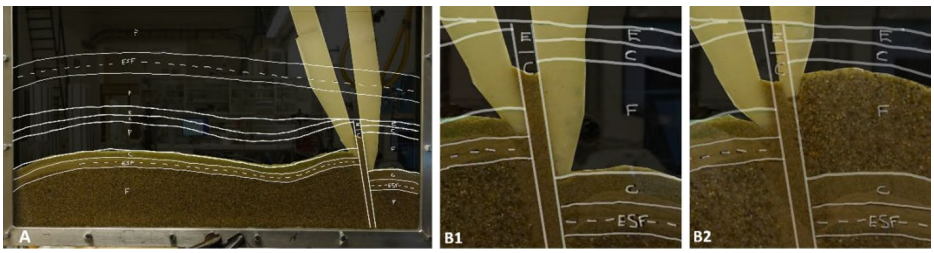

Fig. 4 Example of how to build features using unconsolidated sand. **A** The geological geometry is sketched on the transparent front panel. In this example the sand outside the fault was different from inside the fault, and two "angle-tools" (observed as off-white structures in the image series) separate the sands. **B** Details from fault construction. The fault and adjacent facies are deposited in a layer-by-layer approach for each sand type to match planned geometry. B1 show sand C added into the fault zone before sand F is added on the right (B2). The angle tool represents the boundary of the fault, and the sand to the right of the fault replaces the angle tool as it is lifted to maintain the sand within the fault

Hence, the geometry is built from bottom to top, and excess water is produced through the "overflow" port (cf. Figure 3) to maintain a constant water level during construction. For improved control during geometry building, the grain sizes in adjacent layers should be comparable in size to reduce mixing of grains. Increased complexity may be achieved by (1) increasing the number of sand types and creating sequences with many layers (i.e., each layer consists of one sand type), or (2) adding features such as faults or heterogeneities with different properties.

In this work, three tools were designed to construct a fault using unconsolidated sand:

- 'Angle tools' for sharp edges/faults made from pre-cut polycarbonate covered with polyester fiber mats. The fiber mats compress when inserted and "self-hold" to separate settling sand on either side.
- Pipette filler bulb attached to a steel pipe to smooth layered surfaces with gentle water puffs.
- A large diameter stiff tubing with a funnel on top for accurate direction of the sand.

2.6 Image Acquisition and Analysis

2.6.1 Camera Settings

Because the two geometries were operated in parallel in two FluidFlower rigs, two different cameras were used. For the Albus geometry the camera (Sony ZV-1) used the following settings: exposure time ¼ sec, F number 2.5, ISO 200, and manual focus. Standard light conditions were used to illuminate the rig, and light fluctuations were accounted for in the image analysis. Ideally, controlled light settings should be applied (Eikehaug et al. 2023). The camera was positioned in front of the rig. Images were captured at 5472×3080 pixels every 20 or 30 s during CO_2 injection, and every 300 s afterward until 48 h after CO_2 injection was initiated. While for the Bilbo geometry, the camera (Sony A7III, lens SAMYANG AF 45 mm F1.8) used the following settings: exposure time 1/6 s, F number 2.2, ISO 100, and manual focus. Images were captured at 7952×4472 pixels every 30 s during CO_2 injection and every 300 s afterward until the end of the experiment at 48 h.

Because of the image interval used to capture dynamics during each experiment, the full dataset consists of ~ 4800 images for each experiment. A subset that captures most of the flow dynamics was generated and used for the analysis presented here. These subsets consist of 214 images with the following intervals: 10 images prior to CO_2 injection start, images every 5 min during the first 360 min (6 h), images every 10 min from 360 min until 1440 min (24 h), and images every 60 min from 1440 min until end of experiment at 2880 min (48 h).

2.6.2 Phase Segmentation Through Image Analysis

The high-resolution images, acquired as described above, allow for a detailed visual examination of the fluid displacement along the front panel; fluid flow inside the reservoir remains unnoticed, yet the low depth of the geometry suggests relatively small deviations averaged over time. Micro-scale features such as gas bubbles or sand grain motion as well as macro-scale features as the phase segmentation of the CO_2-water mixture into the phases of water, CO_2 saturated water, and CO_2 gas can be identified from the photographs. The latter is possible due to the use of pH sensitive dyes. To analyze

the large and varying dataset for all experiments, the image analysis toolbox DarSIA (Nordbotten et al. 2023) is used. Altogether, the combination of photographs and image analysis software constitutes one of the main measurement instruments used in this work.

Prior to any analysis, DarSIA is used to unify the environment including the aligning of images and restricting to a fixed region of interest, normalizing temporal color and illumination fluctuations, as well as monitoring and correcting for small sand settling events. Having a cleaned representation of each image allows for comparing it to a fixed baseline image and therefore tracking advancing fluids as differences to the baseline.

A range of assumptions was made to quantitatively describe the multiphase flow from the FluidFlower rig, and a summary is included below:

I. we assume that gas-filled regions are 100% saturated with the gas (CO_2)
II. we assume a constant CO_2 concentration in the CO_2 saturated water
III. we do not account for the dynamics of the gas partitioning in the gas accumulation
IV. we can accurately calculate the volume of CO_2 injected during each run
V. we have accurate information about porosity and depth

Based on these assumptions, a tertiary phase segmentation of the images, identifying the formation water, dissolved CO_2 and mobile CO_2 phases, also locates the presence of all CO_2 within the geometry. The algorithmic phase segmentation boils down to thresholding both in terms of color and signal intensity. Depending on the pH-indicator used, two suitable monochromatic color channels are picked aiming at identifying first all CO_2 within the water, and then the gaseous CO_2 within all CO_2. Each sand type, saturated or unsaturated, reflects light differently. Thus, the thresholding algorithm is designed to take into account the heterogeneous nature of the geometry. It automatically dissects the analysis into sub-analyses of the different sand layers including choosing dynamic thresholding parameters for the different phases and layers. With this, an accurate segmentation of CO_2 and water is possible. The detection of gaseous CO_2 occurs on the Darcy scale. It should be emphasized that this possibly leads to ignoring single gas bubbles while at other times enlarging them due to the averaging procedure and specific choice of thresholding parameters, used for converting the fine scale images to coarse scale data. On the larger scale, this effect is noticeable but plays only a minor role. The segmentation and its accuracy are illustrated in Fig. 5.

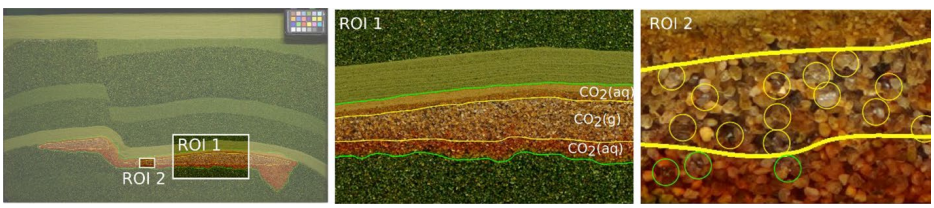

Fig. 5 Left: Illustration of the phase segmentation for BC01 after one hour of CO_2 injection. Center (ROI1): Segmentation with the transition zones of mobile to dissolved CO_2 as well as from dissolved CO_2 to water being entirely associated to the mobile and dissolved CO_2 phases, respectively. Right (ROI2): Highlighted, manually detected gas bubbles associated to dissolved (green circles) and mobile (yellow circles) CO_2 phases, illustrating the accuracy of the segmentation algorithm

3 Results and Discussion

3.1 Textural Sand Properties

The most important textural properties of natural clastic sediments can be expressed as five quantities: (1) grain size, (2) sorting, (3) sphericity, (4) roundness (angularity), and (5) packing (Beard and Weyl 1973). The grain size and sorting are measurable, and important factors in the porosity and permeability, however, packing (grain arrangement) of unconsolidated sand is difficult to measure and to assess its impact on porosity and permeability (Beard and Weyl 1973). Key sand grain properties were derived from segmented, binary microscopic images (Zeiss, Axio Zoom.V16) to obtain the distributions of sand grain width, length, and sphericity using Python and OpenCV functions (see Table 5). The grain size (mm) was converted to phi scale, where $(grain\ size)_{in\ phi} = -log_2 * (grain\ size)_{in\ mm}$ (Krumbein 1936). The grain size measurements and sphericity demonstrate that many grains were noncircular, and each sand type had a larger distribution (SI. Fig. 1) than expected from the sieving process. According to Folk and Ward (1957), standard deviation (std) of grain size in phi-scale is a measure of sorting, and according to their classification, std of 0.71–1.00 (sand ESF) is moderately sorted, while 0.35–0.50 (sand G) is well sorted and < 0.35 (sand C, D, E and F) is very well sorted.

3.2 Petrophysical Properties

Measurements of the petrophysical properties were performed as detailed in Sect. 1.2, and the results are presented in Table 6. The petrophysical properties are used as input to simulation models for performing history match (Sect. 3) of the CO_2 injection experiments presented here, and in and associated numerical simulations (Saló-Salgado et al. 2023).

Comparing grain size versus sorting, sand ESF, C and D is within the range of grain sizes studied by Beard and Weyl 1973, and for wet-packed sand they observed that the porosity remained about the same regardless of grain size, which is the same as observed in the measured porosity presented here (Table 6). The permeability for unconsolidated sand varies with the square of an average diameter (Krumbein and Monk (1942), and references therein), and this is also the case for the measured values presented here (Table 6). Dataset from the literature is compared to the measured values in SI. Fig. 2. The capillary entry pressure was influenced by grain orientation and packing, and we observe differences between horizontal layers and vertical features (like a fault zone) in the studied geometries (see SI. Fig. 3). The sensitivity is used in the history matching of capillary entry pressures in the numerical modeling of the experimental CO_2 injections.

The inner diameter of the cylindrical tube used during permeability measurements should be minimum 8–10 times the maximum particle size of the tested sand column (Chapuis 2012). The geometric mean width and length for sand F and sand G (Table 5) are on this threshold value (8–10 times) with an inner tube diameter of 25.8 mm. Hence, this adds to the uncertainty to the measured permeability values as the relatively large grain size versus tube diameter may lead to poor packing conditions and preferential flow along tube walls (Chapuis 2012). We did not observe preferential flow paths along the walls in this work but note that our confidence in reported parameters for sands F and G is lower than other sands.

Table 5 Calculated properties of samples of the sieved sand, including width, length, and sphericity

Sand ID	# Grains analyzed	Grain size width		Grain length		Sphericity[a]	
		Geomean ± std [mm]	Mean phi scale ± std	Geomean ± std [mm]	Mean phi scale	Geomean	Std
ESF[b]	100	0.16 ± 0.12	2.62 ± 0.82	0.26 ± 0.17	1.94	–	–
C	1127	0.67 ± 0.09	0.58 ± 0.18	0.86 ± 0.17	0.21	0.69	0.10
D	1190	1.05 ± 0.14	−0.07 ± 0.19	1.36 ± 0.23	−0.45	0.68	0.11
E	1000	1.44 ± 0.17	−0.53 ± 0.17	1.87 ± 0.31	−0.90	0.64	0.14
F	1112	1.78 ± 0.26	−0.83 ± 0.22	2.25 ± 0.43	−1.17	0.59	0.18
G	959	2.56 ± 0.56	−1.35 ± 0.38	3.27 ± 0.70	−1.71	0.39	0.26

[a]Two-dimensional sphericity where circular = 1.0. Calculated as $(4 * \pi * Area)/(Circumference^2)$, where area and circumference are calculated using the OpenCV functions contourArea and arclength, respectively

[b]ESF grains were measured manually using a distance functionality in the Zeiss software because the grains were not possible to separate due to electrostatic forces

Table 6 Calculated porosity, absolute permeability, endpoint relative permeability for gas and water and capillary entry pressure for each sand

Sand ID	Porosity[a]	K [D][b]	Endpoint gas (CO_2)		Endpoint water		Capillary entry pressure
			S_{wi}	$k_{rel.gas}$	$1\text{-}S_g$	$k_{rel.water}$	Pc [mbar]
ESF	0.44	44	0.32	0.09	0.86	0.71	15.0
C	0.44	473	0.14	0.05	0.90	0.93	3.3
D	0.44	1110	0.12	0.02	0.92	0.95	0.9
E	0.45	2005	0.12	0.10	0.94	0.93	0.26[c]
F	0.44	4259	0.12	0.11	0.87	0.72	0.10[c]
G	0.45	9580	0.10	0.16	0.94	0.75	0.01[c]

[a]average based on constructing each sand pack twice with the same sand sample

[b]average calculated from one ascending and descending cycle (9 data points) for each sand

[c]calculated from the power function of the trendline in the log–log plot of Pc against geometric mean grain width for ESF, C and D sand because gas accumulation was not detectable during the capillary entry pressure measurements

3.3 Geological geometries

The geological geometries (Fig. 6) were motivated by the relationship between fluid flow and the presence of folds and faults in sedimentary rocks and basins. Two layered geometries with folds and faults with different properties (detailed below) were used to evaluate our ability to incorporate and investigate such geological features using unconsolidated sand, following three guiding principles: (1) enable realistic CO_2 flow pattern and trapping scenarios with increasing modeling complexity, (2) being sufficiently idealized so that the sand facies can be reproduced numerically with high accuracy, and (3) be able to operate, monitor and reset the fluids within a reasonable time frame.

Both geometries include two main reservoir sections separated by a lower seal (sand ESF) unit overlain by a regional sealing unit at the top of the geometry. For geometry Albus (Fig. 6, top), the layers are folded and have two anticlines, one toward the left edge of the rig and one to the right. The right anticline is offset by a listric normal fault, causing a discontinuity in the lower sealing unit. The fault is represented by a fault plane (~ 28 mm, sand C) with an 80 ° dip angle and lower permeability compared with the main reservoir (sand F). Features of the listric normal fault cause a rollover anticline on the footwall (right side of the fault), representing another structural trap. The upper reservoir section consists of layers of high permeability sand (*Upper F and E, and Middle F*) intersected by a layer of lower permeability sand (*Upper C*), and the lower reservoir section consists of uniform high permeability sand (*Lower F*). For geometry Bilbo (Fig. 6, bottom), one can imagine that there has been folding that created an anticline across the field of view, which later has been faulted. The structure has an erosional surface overlayed by a *Top Regional Sealing* unit (sand ESF). Note that the fault zone is not included, and the dip (70–80 degrees) and throw changes downwards in the reservoir layers. In contrast to geometry Albus, the *Lower Sealing* layer between the two reservoir sections in geometry Bilbo is continuous, and the sealing properties are therefore expected to be maintained. This could be described as smearing or drag folding and is a common feature when the clay content is high and is a feature which could have a

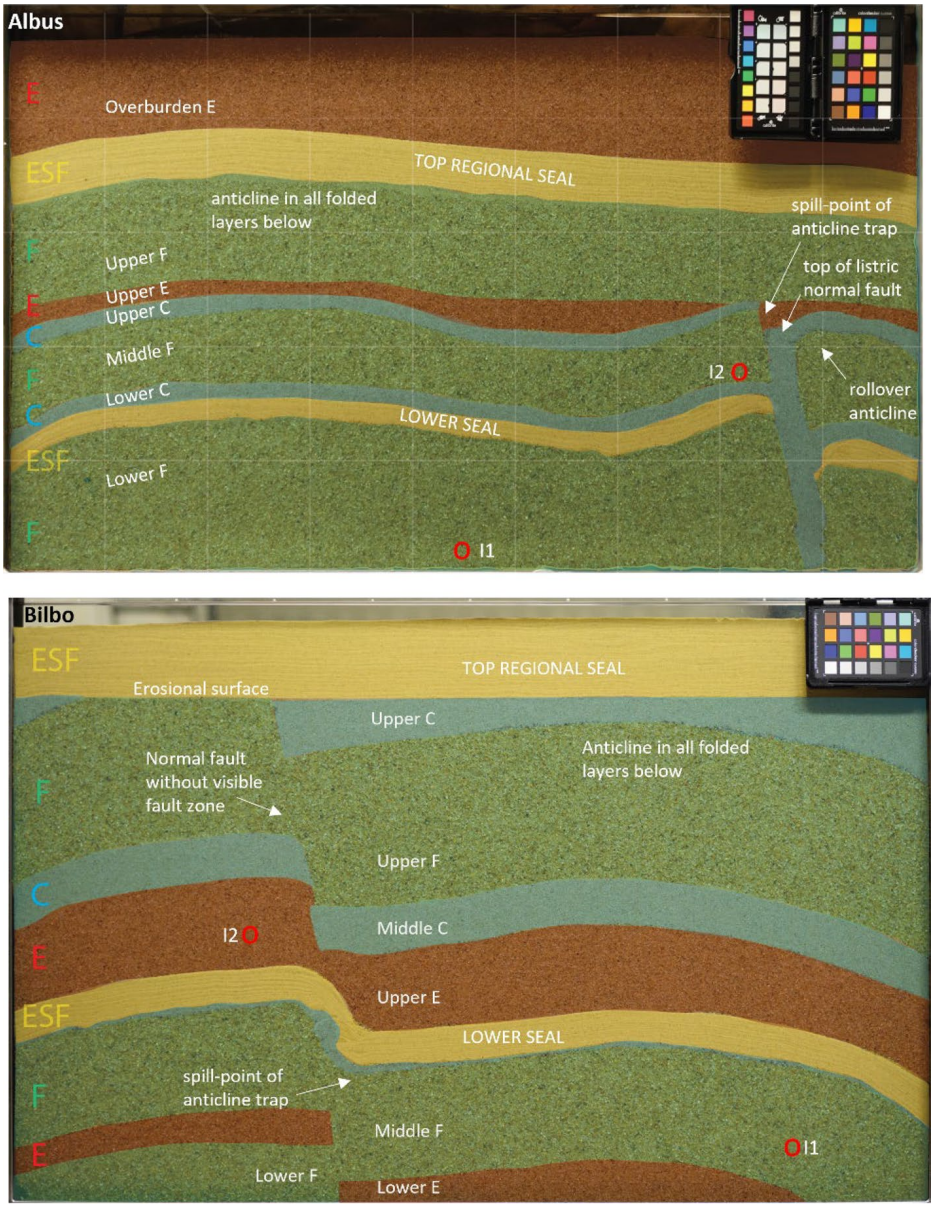

Fig. 6 The Albus (top) and Bilbo (bottom) geological geometries. Colors represent each sand type (red: sand E; green: sand F; yellow: sand ESF; blue: sand C) with grain size distributions and petrophysical properties listed in Table 2 and 5, respectively. A free water table of a few centimeters can be seen at the top of each geometry. Ports used for CO_2 injection are marked with red circles. Albus geological model is overlain with a 1000×1000 mm Cartesian grid with [0,0] in the lower left corner

large impact on fault transmissibility and fluid flow in the reservoir. Note that the drag/smear feature does not contain clay in geometry Bilbo, and because of increased leakage potential along the vertical no-flow boundaries, the layers dip downwards toward the edges to reduce this risk.

3.4 Image Analysis Sensitivity

The different pH-indicator mixes (Table 1) constitute the visual markers for the image analysis, and threshold parameters must be chosen to properly identify the different phases. As shown from Fig. 1, the responses of the different pH-indicators to the presence of CO_2 span different ranges of color variations. Comparing the chemically similar pH-indicator mixes 1 and 2, the first shows a larger span of colors than the latter. As a consequence of the latter, the thresholding algorithm is more sensitive with respect to the threshold parameters, resulting in systematic over-detection of the gaseous phase (Fig. 7). A similar conclusion can be drawn for the comparison of the chemically different pH-indicator mixes 1 and 3. Across the different experiments using the same pH-indicator mix, the same thresholding algorithms and parameters have been used. The calibration of the three sets of parameters was performed based on visual examination, without comparison across the mixes.

3.4.1 Mass Calculations

After an image is segmented into formation water, CO_2-saturated water and mobile CO_2, the total mass of each CO_2 phase can be determined. The total CO_2 mass $m^{total}_{CO_2}$ is known at any time, cf. injection profile in Table 3. Thus, assuming that all CO_2 in the rig either is mobile or dissolved, cf. assumption III, it is sufficient to determine the mass of mobile CO_2, $m^{mobile}_{CO_2}$, while the mass of dissolved CO_2 is given by $m^{dissolved}_{CO_2} = m^{total}_{CO_2} - m^{mobile}_{CO_2}$.

The mass of mobile CO_2, $m^{mobile}_{CO_2}$, is determined as pixel-wise sum of the pixel-wise defined mass density of mobile CO_2, $\rho^{mobile}_{CO_2} = \phi \cdot d \cdot A \cdot s_g \cdot \chi^g_{CO_2}$. Here, ϕ, d, A denote the local porosity and depth as well as the pixel area, respectively, constituting together the local pore volume, which according to assumption V can be determined accurately, cf. also SI. Fig. 4. Based on assumption I, the saturation s_g, takes the value 1 in the region of detected mobile CO_2 and 0 otherwise and is thereby fully prescribed by the phase segmentation. It remains to identify the mass concentration of CO_2 in the gaseous phase $\chi^g_{CO_2}$ which is given by the density of gaseous CO_2 under operational conditions, obtained from the NIST database (Lemmon et al.2022) Here, a uniform temperature distribution of 23 °C is assumed in the rigs; in addition, the fluid pressure is determined from local

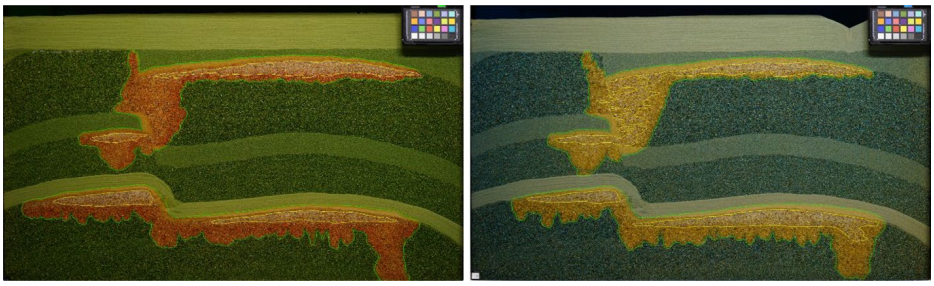

Fig. 7 Phase segmentation for the same experimental set-up under the same conditions, only differing the use of the pH-indicator mix. Left: pH-indicator mix 1 is used, and the segmentation detects gaseous regions (yellow contours) based on variations in the red color and tuned to detect dry sand. Right: pH-indicator mix 2 is used, and the segmentation detects gaseous regions (yellow contours) based on the variations in the yellow color, which are less pronounced compared to the left image. As a result, residual trapped and rising mobile CO_2 is detected in the upper zone on the right image

meteorological weather measurements, cf. SI. Fig. 2, taking into account the local height difference between the FluidFlower rigs (~ 29 m corresponding to increase of 3.625 mbar) and additional hydrostatic pressure of 1013.25 mbar/m from the free water level. This finally determines $m_{CO_2}^{mobile}$.

3.5 Experimental Results and Variations in CO_2 Migration Patterns

Here, we compare the 16 CO_2 injection experiments (12 in the Albus geometry, and four in the Bilbo geometry), describe the observed multi-phase flow and CO_2 migration patterns, evaluate physical reproducibility and discuss the impacts from key operational conditions, including the effect of degassed aqueous phase and different pH-indicator mixes.

3.5.1 *CO_2 Migration Patterns in the Albus and Bilbo Geometries*

The CO_2 migration for 10 operationally comparable CO_2 injection experiments in the Albus geometry follows a similar pattern, which is described next with reference to Fig. 8: The gaseous CO_2 injected in the *Lower F* layer (I1) quickly dissolves in the formation water and changes the color of the pH-indicator. With continued CO_2 injection, the CO_2 saturated water spreads out in a U-shape from the injection port, upwards until it reaches the *Lower seal*. At this stage both gaseous CO_2 and CO_2 saturated water are observed and distinguished. CO_2 migrates to the left, below the *Lower seal,* and accumulates in the anticlinal fold trap (contour 1—light blue). As the gas accumulation increases in the trap, the U-shape above the injection port expands, and gravitational fingers develop under the gas accumulation when CO_2 injection in port 1 stops (contour 2—dark blue). The migration from the second CO_2 injection port (I2) is initially characterized with a small gas accumulation in the small anticlinal trap below the *Upper C* layer on the left side of the fault

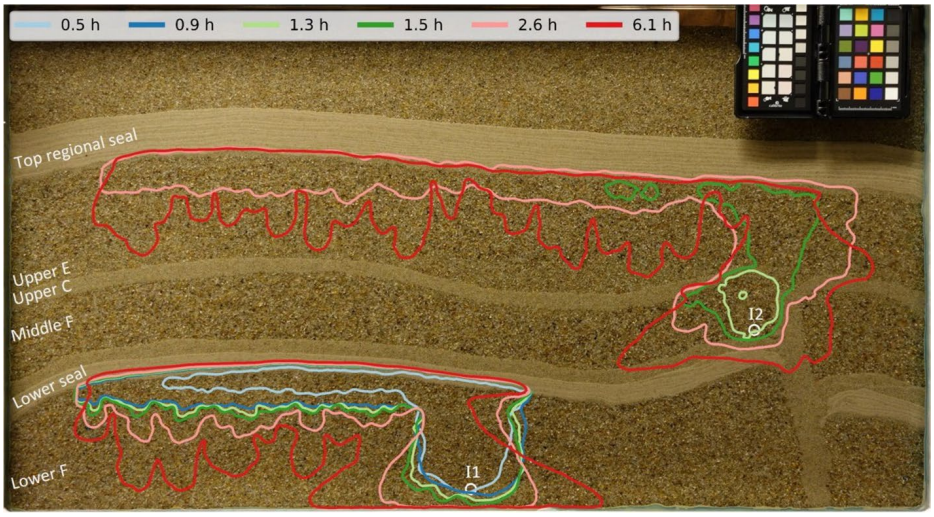

Fig. 8 The migration pattern of CO_2 in the Albus geometry during experiment AC10, representing the general pattern observed for all 10 experiments (AC01–AC10). The contours represent the distribution of gaseous and aqueous CO_2 at different times: 0.9 h represent end of first injection (I1) and 2.6 h represent end of second injection (I2)

(contour 3-light green). When the gas reaches the anticlinal trap spill point (cf. Figure 6, top), buoyancy forces cause the gas to continue through the *Upper E* layer and upwards until it reaches the *Top Regional seal* (contour 4-dark green). The gas migrates stepwise upwards under the sealing unit and sequentially fills the anticlinal trap with gas. Meanwhile, the gravitational fingers below the lower gas accumulation grow (contour 2–5); after the second injection ceased (contour 5-pink) fingers develop below the *Top Regional seal* (contour 6-red). The fingers moved laterally when reaching the *Upper C* layer, before some fingers eventually continue downwards in the *Middle F* layer below.

The CO_2 migration for four CO_2 injection experiments in the Bilbo geometry follows a similar pattern (differences will be discussed later in this section), see Fig. 9: The gaseous CO_2 injected in the *Middle F* layer (I1) migrates upwards with a U-shaped accumulation of CO_2 saturated water, similar to the Albus geometry. Both residually trapped CO_2 bubbles and CO_2 saturated water occur above the injection point, with gas migrating to the left when reaching the *Lower seal* unit (contour 1—light blue). Residually trapped gas bubbles are observed from the injector to the front of the advancing gas as it fills the anticline trap. The gas accumulation slightly exceeds the spill-point (contour 2—dark blue) before it "burst" leftwards into the smeared fault trap, a process that is repeated multiple times (see discussion in Fernø et al. 2023). Some residually trapped gas bubbles are observed in the vicinity of the smeared *Lower seal* area, and a new gas accumulation develops in the smeared fault trap when CO_2 injection in port I1 stopped (contour 3- light green). The CO_2 injection continues in the second port (I2), located in the footwall of the *Upper E* layer. A small gas accumulation is observed before the gas exceeds the spill-point below the footwall of the faulted *Middle C* layer above (contour 4—dark green). Some gas flows left of the fault plane and into the footwall of the *Upper F layer,* but most of the CO_2 migrates right and accumulates under the anticline

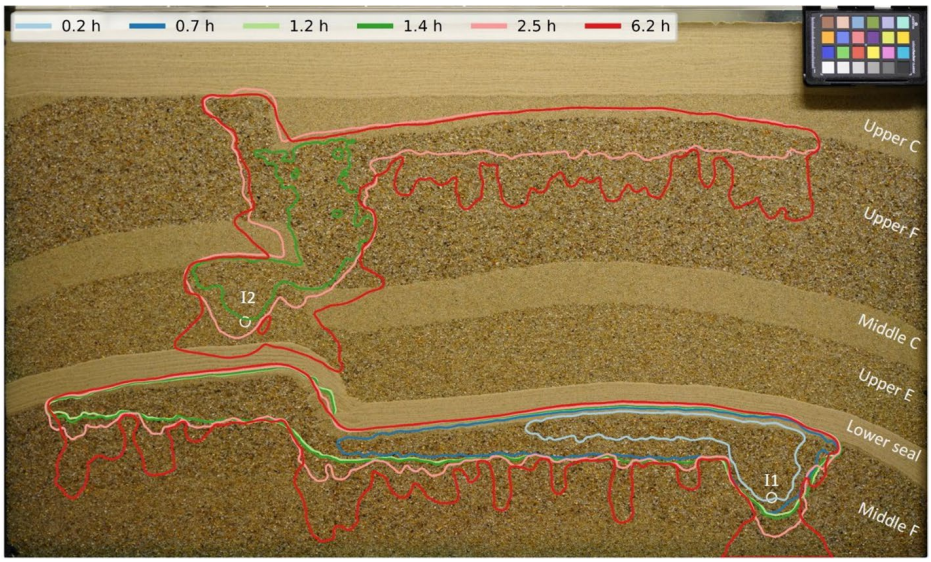

Fig. 9 The migration pattern of CO_2 during experiment BC02, representing the general pattern observed for all four (BC01-04) experiments in the Bilbo geometry. The contours represent the distribution of gaseous and aqueous CO_2 at different times: 1.2 h represent end of first injection (I1), and 2.5 h represent end of second injection (I2)

trap in the hanging wall of the *Upper F* layer. As seen in the Albus geometry, after injection has ceased in the Bilbo geometry (contour 5—pink), gravitational fingers of CO_2-saturated water develop and sink downwards (contour 6—red).

3.5.2 Quantitative Analysis of Physical Variability

To compare different experiments and assess physical variability, the phase segmentations are utilized by DarSIA to provide visualizations and convert images to data**.** To compute the overlap percentages, we first weight all pixels in the segmented images with their corresponding volume. Then, the ratio between the number of volume-weighted pixels where CO_2 (gaseous and dissolved) overlap is reported. The 10 repeated CO_2 injections in the Albus geometry (Fig. 10) illustrate the impact from variable degassing of the formation water. Of the 10 experiments with the same injection protocol, six experiments have pH-indicator mix 1 (Table 1). Development of calculated mass of mobile CO_2 and dissolved CO_2 over time shows a wide spread, where the effect of insufficient degassing was evident for the mobile gas at later times: with sufficient degassing, the mass of mobile CO_2 is zero for later times (AC14) because all of the injected CO_2 is dissolved in the formation water. In contrast, with insufficient degassing (atmospheric gases present in the aqueous phase) a gaseous phase remains in the geometry and is included in the mass calculations of mobile CO_2. The remaining gas at late times (observed in AC02-05 and AC08) is decreasing amounts of air, and not CO_2.

The degree of degassing influences the distribution of mobile and dissolved CO_2 in Albus geometry. Nevertheless, the overlap in spatial distribution of mobile and dissolved CO_2 for six experiments in the Albus geometry has an overall average of 65% overlapping (Fig. 11). Operational inconsistencies that reduce the overlap include (1) some CO_2 was injected in AC02 prior to starting the experiment (ramp-up), and (2) CO_2 injection was not scripted in the first experiments, causing deviation in time between CO_2 injection in port 1 and port 2 (SI. Table 1). The spatial distribution is included in supplementary information (SI. Fig. 6).

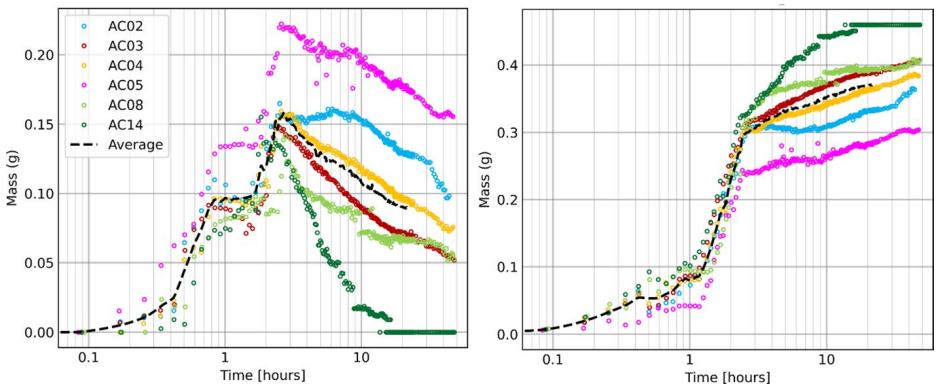

Fig. 10 Comparison of CO_2 injection experiments in the Albus geometry with the same injection protocol and pH-indicator mix. Left plot: development of calculated mass of mobile CO_2 over time, and right plot: development of calculated mass of dissolved CO_2

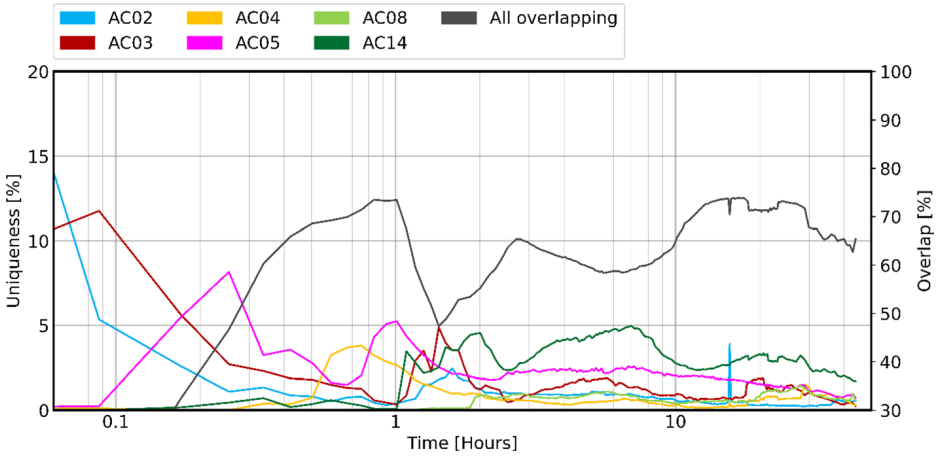

Fig. 11 Development of uniqueness of phase segmentations of dissolved CO_2 for six CO_2 injection experiments in the Albus geometry. Most of the injections have less than 5% uniqueness. The degree of overlap between all six experiments (gray, secondary y-axis) reaches a maximum (approximately 75%) after one hour, with an average of 65% for the duration of the experiments. Note that the x-axis is logarithmic

3.5.3 Impact from Different pH-Indicator Mixes

Three different pH-indicator mixes are used in the Bilbo geometry, varying in parts in their chemical properties (Table 1), as well as their interaction with the image analysis (detailed in Sect. 1.6). The development in uniqueness and overlap (Fig. 12, top) demonstrates that the experiments are comparable with less than 5% uniqueness for most of the time, where changes originate from variations in atmospheric pressure (SI. Fig. 4) or methylene red precipitation (SI. Fig. 7). The depth map of the rig (SI. Fig. 5) is also considered when computing the fractions with DarSIA, such that it really becomes volume fractions and not area fractions. Different colors are assigned to appearances of different segmentations and their overlaps (Fig. 12, bottom). Moreover, the fractions that each color represents in reference to the total covered area are calculated (and printed in the legends). As expected, the gas dissolves faster with less spreading of dissolved CO_2 in the BC04 experiment (pH ~ 10.4) compared to the experiments BC01– 03 (pH ~ 8.3), which is reflected in the low overlap of "BC01 + BC04" compared to "BC01 + BC03" (Fig. 12, top). Furthermore, the observation is supported by the evolution of the masses of the different CO_2 phases (Fig. 13). In the same figure, a clear difference between BC01 and BC03 can be observed which is directly connected to the sensitivity of the image analysis and the detection of mobile and residual trapped gaseous phase, as discussed in Sect. 1.6.

Similar material for CO_2 injection experiments in the Albus geometry, comparing results from pH-indicator mix 1–3 are included in supplementary information (SI. Figs. 8 and 9). To summarize, the results follow the same trends as for the CO_2 injection experiments in the Bilbo geometry, as presented above. We highlight the comparison of pH-indicator mix 1 and 2 (AC14 and AC09), showing an average overlap of only 81% (SI. Fig. 9), which again is attributed to the interplay of the mixes as visual markers and the image analysis. Furthermore, for the two experiments with higher degree of vacuuming of initial fluids (AC19 and AC22), an increase of the dissolution rate results in earlier attaining zero mobile/residual gas compared to the other experimental runs (SI. Fig. 8).

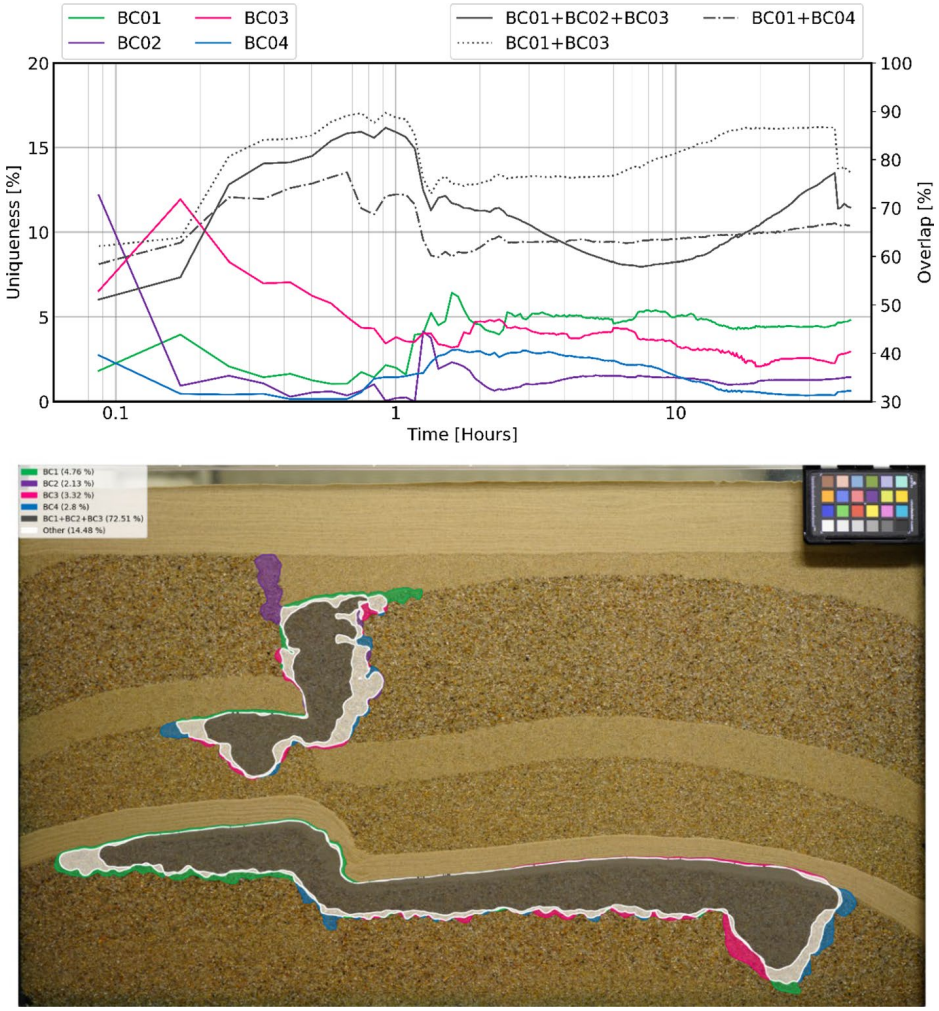

Fig. 12 The development in uniqueness and overlap for experiments BC01-04. Top: quantitative uniqueness for BC01-04 and overlap for combinations of experiments. Bottom: Spatial uniqueness after 1.5 h in BC01 (green), BC02 (purple), BC03 (pink) and BC04 (blue); overlap for BC01-03. Other overlap combinations are lumped together (white). Each color represents the spatial distribution of mobile and dissolved CO_2. Additional timesteps are shown in SI. Figure 7

4 Numerical Modeling of Experimental CO_2 Injection

Safe geologic storage of CO_2 requires numerical modeling for forecasting CO_2 migration in complex geological structures. The computational models used are typically physics-based and are expected to include all dominant processes. Nevertheless, the accuracy of these models is hard to quantify due to lack of direct observations in field conditions. The FluidFlower benchmark study (Flemisch et al. 2023) provides an insight into the accuracy of numerical models for CO_2 storage. Furthermore, Saló-Salgado et al. (2023) aim to refine our understanding of the accuracy of numerical models by systematically

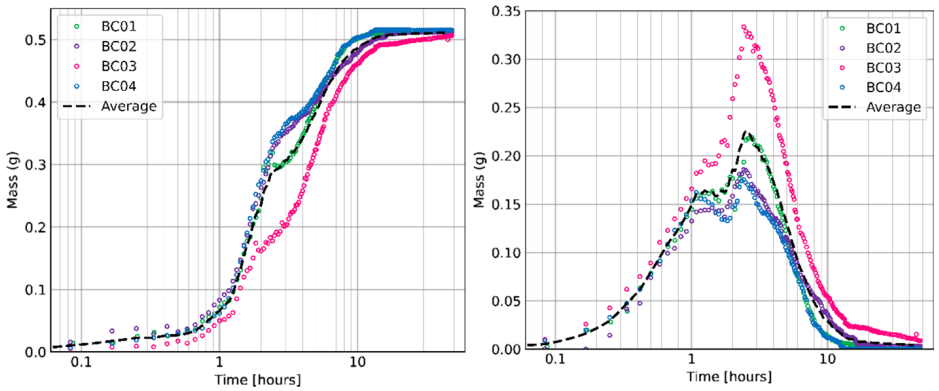

Fig. 13 Development in mass [g] of dissolved CO_2 (left) and mobile CO_2 (right) for four CO_2 injection experiments (BC01-04) in the Bilbo geometry. The overall behavior of dissolved CO_2 is comparable for all experiments, the deviation of BC03 relates to sensitivity of the image analysis with respect to threshold parameters (discussed in Sect. 2.5). Experiment with pH-indicator mix number 3 (BC04) has faster CO_2 dissolution compared to pH-indicator mix number 1 (BC01, BC02) and 2 (BC03)

evaluating the value of increasing amount of local data in predicting the CO_2 migration in FluidFlower experiments. This provides a unique opportunity to evaluate both the measurements of the petrophysical properties of the unconsolidated sand (Sect. 2.2) and CO_2 migration during injection experiments in the two studied geometries (Sect. 3).

Saló-Salgado et al. (2023) present three different versions of a numerical model (denoted Model 1 through Model 3), with, respectively, increasing amount of experimentally measured petrophysical data, while keeping all other model characteristics constant:

- Model 1 considers only grain size width as provided by the experimental measurements (Table 5) to estimate petrophysical data from published data on similar silica sand.
- Model 2 furthermore considers single-phase data from the experimental measurements, while the multiphase data remain based on published data.
- Model 3 uses all the data provided from the experimental measurements (Table 6).

To set up the simulation models, Saló-Salgado et al. (2023) complemented the experimental data made available to each model with published data to estimate the petrophysical parameters (porosity, permeability, relative permeability and capillary pressure) for each sand. History matching Models 1–3 using the AC02 experiment in the Albus geometry is detailed in Saló-Salgado et al. (2023). To history match the models, Saló-Salgado et al. (2023) used a manual iterative procedure. After a given simulation run, they quantitatively compared areas with free-phase CO_2 and water with dissolved CO_2, as well as convective finger migration times. Using the differences between estimates from experimental images and simulation values, they manually updated sand permeabilities and capillary pressure curves to be used in the next simulation run. This process required 11, 8 and 7 iterations for Model 1 to Model 3, respectively. To test the robustness of the simulation model, the petrophysical values obtained from history match in the respective Models 1–3 are used to predict migration development during CO_2 injection in the Bilbo geometry (Fig. 6), and this is detailed below.

4.1 Model Properties used for the Geometry in the Bilbo rig

4.1.1 Numerical Model Set-up

Simulation results presented here are performed with the black oil module in the MATLAB Reservoir Simulation Toolbox (MRST) (Lie 2019), where properties of the water are assigned to the oleic phase. Structural trapping, dissolution trapping and residual trapping (Juanes et al. 2006) are included, and details about their implementation can be found elsewhere (Saló-Salgado et al. 2023). Due to the buoyancy of CO_2 at atmospheric conditions and high permeability of the sand, very small timesteps are required for convergence of the nonlinear solver. PVT properties used in the simulations are according to atmospheric conditions (25 °C), with CO_2 in gaseous phase. The thermodynamic model is the same as applied in Saló-Salgado et al. (2023).

Dimensions of computational grid used to model the porous medium in the Bilbo rig are: $93.4 \times 53.3 \times 1.05$ cm. Layer contact coordinates are extracted from a 2D image, and our composite Pebi grid (Heinemann et al. 1991; Berge et al. 2019) has a cell size of 5 mm and a total of 20,470 cells, with a single cell layer to account for thickness and volume and obtain a 3D grid (SI. Fig. 10). The grid cell size is very similar to the one used in Saló-Salgado et al. (2023); their analysis shows that (1) this resolution is fine enough to achieve very good concordance to the AC02 experiment, and (2) model calibration is cell size dependent. There are no-flow boundary conditions everywhere except at the top surface, where there is constant pressure consistent with atmospheric pressure and a fixed-height water table. The model is initialized with 100% water saturation and hydrostatic pressure. Injection is conducted using injector wells with 1.8 mm diameter completed in a single cell at the respective coordinates (e.g. chapter 4.3.2 in Lie 2019; Fig. 6). The CO_2 injection schedule in the simulations is the same as in the Bilbo experiments (Table 3).

4.1.2 Petrophysical Input Parameters

The input values for porosity, absolute permeability and relative permeability used in the Bilbo model are identical to the ones used to match the AC02 experiment Model 1 to 3 (SI. Table 2), detailed in Saló-Salgado et al. (2023). During CO_2 injection in AC02, the sealing capacity of the C-sand was not critical due to the location of the injection ports and the injection protocol used. Hence, the calibration based on history matching this injection retains a high degree of uncertainty for the C-sand. This becomes prominent when simulating the Bilbo-geometry, where the second injection port is in the *Upper E* layer, overlayed by the faulted *Middle C* layer (Fig. 6). When the Albus AC02 HM values are used for capillary entry pressure for sand C in the Bilbo geometry, free-phase CO_2 migrates through the *Middle C* layer in the footwall instead of filling the fault trap to the spill-point. To mitigate this effect, we choose to decrease the gas saturation at which the capillary entry pressure is defined (Sge) and increase the capillary entry pressure (Pc) in the C-sand (Table 7). The increased capillary entry pressure for the vertical fault zone was also observed experimentally (see SI. Fig. 3). The Pce values in Table 7 are slightly higher than the maximum value in SI. Fig. 3 (about 7 mbar), given that a run with Pce = 7 mbar still showed entry of gaseous CO_2 in the middle C-sand. The capillary pressure curves for all other sands remain identical to the ones used to history match Model 1–3 to AC02.

Table 7 C-sand values for gas saturation where the capillary entry pressure is defined (Sge) and capillary entry pressure (Pc) obtained from history match of CO_2 injection experiment in the Albus geometry, compared to values needed to match the CO_2 injection experiment in the Bilbo geometry. All other parameters are kept the same as obtained from HM of the Albus experiment for the three models

Model	Albus HM: sand C		Bilbo HM: sand C	
	Sge	Pc [mbar]	Sge	Pc [mbar]
1	1e-3	4.6	1e-4	9.3
2	1e-3	2.6	1e-4	10.0
3	1e-3	4.5	1e-4	9.6

4.2 Simulation Results

When evaluating the simulation results there are known deviations between the set-up of the numerical simulations and the physical geometry that should be kept in mind: (1) discrepancy between the temperature value used in mass calculation from experimental results and model input, which contributes to the small difference in total injected mass (SI. Fig. 11), and (2) variations in flow cell depth, where calculations from experimental results include the depth map (SI. Fig. 5) with expansion of up to ~ 40%, while in the model a constant expansion of 5% is used.

A qualitative comparison of gas saturation and concentration of dissolved CO_2 shows that all three models provide similar, and fairly accurate, results for the CO_2 migration during CO_2 injection experiment in the Bilbo geometry (Fig. 14). The relative differences between the models appear to be comparable to the difference between the model and the experiment. However, there are subtle differences:

- After 3 h, Model 1 shows CO_2 in the footwall of the *Upper F* layer (top left corner in Fig. 14) equal to the experiment. However, this is due to CO_2 spilling out of the

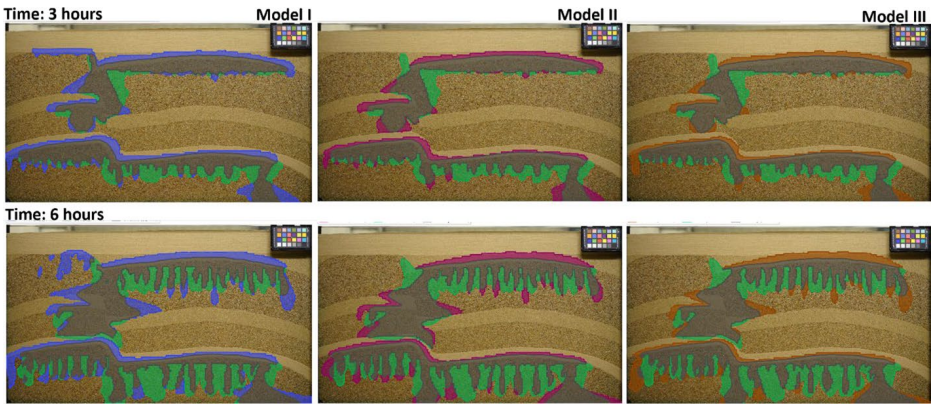

Fig. 14 Spatial uniqueness after 3 and 6 h for Model 1 (I; blue) Model 2 (II; dark pink), Model 3 (III; brown) and experiment BC01 (green); overlap between each model and experiment in gray. Each color represents the spatial distribution of mobile and dissolved CO_2. Contours of the simulation results are obtained from gas concentration maps, and a threshold value of 0.21 kg/m3 (15% of the maximum value around 1.4 kg/m3) is used

anticline from the right, rather than pore variability and diverging path possibilities observed experimentally.
- The models show CO_2 concentration reaching higher elevation within the middle-left and top-right C sands, with respect to the experiment.

The spatial distribution of mobile CO_2 (gas phase) and dissolved CO_2 over time (SI. Fig. 12) is quantified in Table 8, where the unique (for each case) and overlapping phase segmentations for the three Models (1, 2, 3) and experiment BC01 is compared. Note that lower uniqueness indicates better match with experiment. The distribution of mobile CO_2 for Model 2 and 3 overlaps with BC01, demonstrated as zero uniqueness for time steps in Table 8.

Quantitatively, Models 2 and 3 perform similarly and correlate better with the experimental results than Model 1, particularly regarding the amount of mobile CO_2. This is consistent with results obtained by Saló-Salgado et al. (2023) when applying the history matched models to different setting (e.g. see their Fig. 17). However, the numerical model is missing some physics compared to the experiment. An example of this is the compact sinking front with very thick and only moderately protruding fingers seen in the experiment, whereas the model shows thinner fingers sinking from a receding front, even when the diffusion coefficient is increased. We expect that this deviation between model and experiment can be reduced by incorporating hydrodynamic dispersion in the numerical model (see discussion in Saló-Salgado et al. 2023).

5 Conclusions and Future Outlook

Key learnings for constructing geological geometries (using unconsolidated sand) include: The grain sizes in adjacent layers should be close to avoid mixing as fines fall into the coarser sand; (horizontal) layers may be adjusted using a ladle in the water table using smooth movements along the whole unit length (especially important for fine-grain sand with longer settling time); faults require a minimum of one "angle tool" to depending on the fault design (with or without fault zone). For fluid injection protocol key learning includes: CO_2 injection rate should follow a scripted MFC protocol, with sufficiently high injection rate during ramp up to maintain CO_2 as a gas phase in the initial stages of injection. The development of DarSIA was important to quantify key parameters and variability in the experimentally observed CO_2 migration patterns. The results show anticipated behavior of injected CO_2, however, with physical variabilities induced by design (different formation water chemistry) and because the system is sensitive (atmospheric pressure). Numerical modeling of CO_2 injection experiments has predicted fairly accurate results for the CO_2 migration and has demonstrated the value of including measured petrophysical properties of the porous media in the simulation models. Hence, the rig represents a unique possibility to test our simulation skills because here we can compare predictions to observations.

Future outlook. The FluidFlower rig represents a fast-prototyping tool to evaluate the parameter and operational space and has been an essential part in development and planning of FluidFlower Benchmark initiative (Nordbotten et al. 2022). The presented workflows provide an excellent opportunity to address various research and particularly modeling questions. The range of possible phase configurations combined with the quick (and if needed recyclable) set-up allows for conducting a series of varying experiments

Table 8 Model-experiment comparison of the unique and overlapping spatial distribution of mobile and dissolved CO_2. Numbers are % of all regions with CO_2

Time [hours]	Mobile CO_2[a]					Dissolved CO_2[b]				
	Uniqueness				Two or more overlap	Uniqueness				Two or more overlap
	Model 1	Model 2	Model 3	BC01		Model 1	Model 2	Model 3	BC01	
3	11.4	0.0	0.0	4.3	84.2	7.4	0.9	0.8	13.9	77.0
6	28.1	0.0	0.0	0.5	71.4	6.6	1.1	1.3	19.2	71.9
9	31.2	0.0	0.0	0.2	68.6	4.1	0.9	0.7	18.4	75.9
12	38.9	0.0	0.0	0.4	60.7	3.4	0.8	0.3	17.1	78.4
18	66.8	0.0	0.0	0.0	33.2	2.8	0.4	0.2	13.4	83.2
24	71.1	0.0	0.0	0.0	28.9	2.3	0.4	0.3	11.1	85.9

[a]For simulations, gas saturation of 0.001 was used as threshold during segmentation with DarSIA

[b]For simulations, concentration of 0.21 kg/m^3 (15% of the maximum value around 1.4 kg/m^3) was used as threshold during segmentation with DarSIA (numbers from SI. Fig. 12)

and thereby performing a comprehensive physical sensitivity study, aiming at studying isolated phenomena. The access to dense observation data and a comparison with corresponding simulation data open up for better understanding and the possibility for improved modeling.

Supplementary Information The online version contains supplementary material available at https://doi.org/10.1007/s11242-023-02047-8.

Acknowledgements The authors would like to acknowledge Ida Louise Mortensen and Mali Ones for their contribution in the laboratory during their UiB internship.

Funding Open access funding provided by University of Bergen (incl Haukeland University Hospital). The work of JWB is funded in part by the UiB Academia-project «FracFlow» and the Wintershall DEA-funded project «PoroTwin». MH is funded from Research Council of Norway (RCN) project no. 280341. KE and MH are partly funded by Centre for Sustainable Subsurface Resources, RCN project no. 331841. BB is funded from RCN project no. 324688. LS gratefully acknowledges the support of a fellowship from "la Caixa" Foundation (ID 100010434). The fellowship code is LCF/BQ/EU21/11890139.

Declarations

Conflict of interest The authors have not disclosed any competing interests.

References

Beard, D.C., Weyl, P.K.: Influence of texture on porosity and permeability of unconsolidated sand. AAPG Bull. **57**(2), 349–369 (1973)

Berge, R.L., Klemetsdal, Ø.S., Lie, K.A.: Unstructured Voronoi grids conforming to lower dimensional objects. Comput. Geosci. **23**, 169–188 (2019). https://doi.org/10.1007/s10596-018-9790-0

Chapuis, R.P.: Predicting the saturated hydraulic conductivity of soils: a review. Bull. Eng. Geol. Env. **71**(3), 401–434 (2012)

Eikehaug, K., Haugen, M., Folkvord, O., Benali, B., Bang Larsen, E., Tinkova, A., Rotevatn, A., Nordbotten, J.M., Fernø, M.A.: Engineering meter-scale porous media flow experiments for quantitative studies of geological carbon sequestration. Transp. Porous Med (2024). https://doi.org/10.1007/s11242-023-02025-0

Fernø, M.A., Haugen, M., Eikehaug, K., Folkvord, O., Benali, B., Both, J.W., Storvik, E., Nixon, C.W., Gawthrope, R.L., Nordbotten, J.M.: Room-scale CO_2 injections in a physical reservoir model with faults. Transp. Porous Med (2023). https://doi.org/10.1007/s11242-023-02013-4

Flemisch, B., Nordbotten, J.M., Fernø, M.A., Juanes, R., Both, J.W., Class, H., Delshad, M., Doster, F., Ennis-King, J., Franc, J., Geiger, S., Gläser, D., Green, C., Gunning, J., Hajibeygi, H., Jackson, S.J., Jammoul, M., Karra, S., Li, J., Matthäi, S.K., Miller, T., Shao, Q., Spurin, C., Stauffer, P., Tchelepi, H., Tian, X., Viswanathan, H., Voskov, D., Wang, Y., Wapperom, M., Wheeler, M.F., Wilkins, A., Youssef, A.A., Zhang, Z.: The FluidFlower validation benchmark study for the storage of CO_2. Transp. Porous Med. (2023). https://doi.org/10.1007/s11242-023-01977-7

Folk, R.L., Ward, W.C.: Brazos river bar: a study in the significance of grain size parameter. J. Sediment. Petrol. **27**, 3–27 (1957)

Geophysical Institute, University of Bergen, https://veret.gfi.uib.no/?action=download

Glass, R.J., Conrad, S.H., Peplinski, W.: Gravity-destabilized nonwetting phase invasion in macroheterogeneous porous media: Experimental observations of invasion dynamics and scale analysis. Water Resour. Res. **36**(11), 3121–3137 (2000). https://doi.org/10.1029/2000WR900152

Heinemann, Z., Brand, C., Munka, M., Chen, Y.: Modeling reservoir geometry with irregular grids. SPE Reserv. Eng. **6**(2), 225–232 (1991). https://doi.org/10.2118/18412-PA

IEA, Net Zero by 2050. 2021: Paris

Juanes, R., Spiteri, E.J., Orr, F.M., Blunt, M.J.: Impact of relative permeability hysteresis on geological CO_2 storage. Water Resour. Res. **42**, W12418 (2006). https://doi.org/10.1029/2005WR004806

Kneafsey, T.J., Pruess, K.: Laboratory flow experiments for visualizing carbon dioxide-induced Density-Driven Brine Convection. Transp. Porous Med. **82**, 123–139 (2010). https://doi.org/10.1007/s11242-009-9482-2

Krishnamurthy, P. G., DiCarlo, D. & Meckel, T.: Geologic heterogeneity controls on trapping and migration of CO_2. Geophys. Res. Lett. 49, 1–208 (2022) https://doi.org/10.1029/2022GL099104

Krumbein, W.C.: Application of logarithmic moments to size frequency distributions of sediments. Jnl. Sed. Petrol. **6**, 35–47 (1936)

Krumbein, W.C., Monk, G.D.: Permeability as a Function of the Size Parameters of Unconsolidated Sand. Petroleum Technology (1942)

Lemmon, E.W., Bell, I.H., Huber, M.L., McLinden, M.O.: Thermophysical Properties of Fluid Systems, NIST Chemistry WebBook, NIST Standard Reference Database Number 69, Eds. P.J. Linstrom and W.G. Mallard, National Institute of Standards and Technology, Gaithersburg MD, 20899, https://doi.org/10.18434/T4D303, (retrieved September 2, 2022).

Lie, K.-A.: An introduction to reservoir simulation using MATLAB/GNU Octave: User guide for the MATLAB Reservoir Simulation Toolbox (MRST). Cambridge University Press, 2019

Nordbotten, J.M., Fernø, M.A., Flemisch, B., Juanes, R., Jørgensen, M.: Final benchmark description: fluidflower international benchmark study. Zenodo (2022). https://doi.org/10.5281/zenodo.6807102

Nordbotten, J.M., Benali, B., Both, J.W., Brattekås, B., Storvik, E., Fernø, M.A.: DarSIA: An open-source Python toolbox for two-scale image processing of dynamics in porous media. Transp. Porous Med. (2023). https://doi.org/10.1007/s11242-023-02000-9

Rasmusson, M., Fagerlund, F., Rasmusson, K., Tsang, Y., Niemi, A.: Refractive-light-transmission technique applied to density-driven convective mixing in porous media with implications for geological CO_2 storage. Water Resour. Res. **53**, 8760–8780 (2017). https://doi.org/10.1002/2017WR020730

Saló-Salgado, L., Haugen, M., Eikehaug, K., Fernø, M.A., Nordbotten, J.M., Juanes, R.: Direct comparison of numerical simulations and experiments of CO_2 injection and migration in geologic media: value of local data and forecasting capability. Transp. Porous Media (2023). https://doi.org/10.1007/s11242-023-01972-y

The Engineering ToolBox (2008). *Solubility of Gases in Water vs. Temperature*. Available at: https://www.engineeringtoolbox.com/gases-solubility-water-d_1148.html [Accessed 05.07.2023].

Trevisan, L., Pini, R., Cihan, A., Birkholzer, J.T., Zhou, Q., González-Nicolás, A., Illangasekare, T.H.: Imaging and quantification of spreading and trapping of carbon dioxide in saline aquifers using meter-scale laboratory experiments. Water Resour Res. **53**, 485–502 (2017). https://doi.org/10.1002/2016WR019749

Van De Ven, C.J.C., Mumford, K.G.: Visualization of gas dissolution following upward gas migration in porous media: Technique and implications for stray gas. Adv. Water Resour. (2018). https://doi.org/10.1016/j.advwatres.2018.02.015

Van De Ven C.J.C., Mumford, K.G.: Intermediate-scale laboratory investigation of stray gas migration impacts: transient gas flow and surface expression. Environ. Sci. Technol (2020) https://doi.org/10.1021/acs.est.0c03530

Wentworth, C.K.: A scale of grade and class terms for clastic sediments. J. Geol. **30**(5), 377–392 (1922)

Paper 6

Transport in Porous Media
https://doi.org/10.1007/s11242-023-02013-4

Room-Scale CO_2 Injections in a Physical Reservoir Model with Faults

M. A. Fernø[1,4] · M. Haugen[1] · K. Eikehaug[1] · O. Folkvord[1] · B. Benali[1] · J. W Both[2] · E. Storvik[2] · C. W. Nixon[3] · R. L. Gawthrope[3] · J. M. Nordbotten[2,4]

Received: 10 January 2023 / Accepted: 12 August 2023

Abstract
We perform a series of repeated CO_2 injections in a room-scale physical model of a faulted geological cross-section. Relevant parameters for subsurface carbon storage, including multiphase flows, capillary CO_2 trapping, dissolution and convective mixing, are studied and quantified. As part of a validation benchmark study, we address and quantify six predefined metrics for storage capacity and security in typical CO_2 storage operations. Using the same geometry, we investigate the degree of reproducibility of five repeated experimental runs. Our analysis focuses on physical variations of the spatial distribution of mobile and dissolved CO_2, multiphase flow patterns, development in mass of the aqueous and gaseous phases, gravitational fingers and leakage dynamics. We observe very good reproducibility in homogenous regions with up to 97% overlap between repeated runs, and that fault-related heterogeneity tends to decrease reproducibility. Notably, we observe an oscillating CO_2 leakage behavior from the spill point of an anticline and discuss the observed phenomenon within the constraints of the studied system.

Keywords Carbon storage · Image analysis · Quantitative data analysis · Physical variability and reproducibility · Fault leakage dynamics

1 Introduction

In its simplest form, geological carbon storage (GCS) involves the injection of captured carbon dioxide (CO_2) into deep subsurface porous and permeable sedimentary rocks, overlain by an impermeable sealing layer. The migration of the buoyancy-driven CO_2 is determined by: (i) the intrinsic rock and fluid properties (e.g., porosity, permeability, fluid

✉ M. A. Fernø
Martin.Ferno@uib.no

[1] Department of Physics and Technology, University of Bergen, Bergen, Norway

[2] Department of Mathematics, Center for Modeling of Coupled Subsurface Dynamics, University of Bergen, Bergen, Norway

[3] Department of Earth Science, University of Bergen, Bergen, Norway

[4] Norwegian Research Center, Postboks 22 Nygårdstangen, 5838 Bergen, Norway

density and viscosity) and (ii) the distribution and properties of geological structures such as faults and fracture networks that are inherent to both reservoir and seal rocks. Faults are discontinuities that form at a range of scales; they can act as conduits or barriers for flow, and they generally have directionally dependent flow properties (Bastesen and Rotevatn 2012). Large sealing faults control storage site geometries and compartmentalization, whereas networks of small faults and fractures may affect reservoir flow and seal integrity (Ogata et al. 2014).

1.1 Faults, Fractures and Flow

The properties of the fracture networks (i.e., topology, connectivity and permeability) that form damage zones around faults as they evolve (Nixon et al. 2020) are particularly important to CO_2 flow. Subsurface faults are discerned from reflection seismic data, but descriptions suffer from limitations in seismic resolution and coverage. Geologically analogous outcrops and dedicated laboratory experiments provide a means to investigate smaller structures around faults and shed light on flow and sealing properties. Being able to identify and forecast the behavior of potential subsurface bypass structures during GCS operation is essential; understanding the interplay between multiphase flow and fault evolution is critically needed for carbon storage projects. Despite this, the flow properties of faults and their damage zones remain insufficiently understood, and little is known about how their flow behavior evolves in the different stages of a carbon storage project. Our current understanding of large-scale CO_2 plume migration is mainly from time-lapse seismic surveys with limited a priori knowledge (Furre et al. 2017). With increases in reservoir pressures during CO_2 injection, there is a greater risk of reactivation and potential generation of new fracture networks that can enhance seal permeability and capillary flow and provide pathways for fluid escape to shallower reservoirs or the surface (e.g., Ogata et al. 2014; Karstens and Berndt 2015; Karstens et al. 2017).

1.2 The Laboratory FluidFlower Rig

The FluidFlower concept links research and dissemination through a new experimental rig constructed at University of Bergen (UiB) that enables repeatable, meter-scale, multiphase, quasi-two-dimensional (2D) flow on model geological geometries with high-accuracy data acquisition. Intermediate-scale (decimeter to meter) quasi-2D laboratory experiments are widely used to study multiphase porous media flow, including gravity unstable flows in the presence of heterogeneity (Glass et al. 2000; Van De Ven and Mumford 2018, 2020; Krishnamurthy et al. 2022) and CO_2 migration and dissolution (Kneafsey and Pruess 2010; Trevisan et al. 2017; Rasmusson et al. 2017). These approaches enable visualizing and studying a range of porous media flow dynamics in engineered representative porous media using beads or sand grains. For the present study, we built a multi-scale heterogenous geometry motivated by geological features found on the Norwegian Continental Shelf (cf. Fig. 1). A key feature of the FluidFlower rig is the ability to repeat experiments in the same geometry, without the need to remove the sands between repeated runs. The five repetitions reported here are defined as 'physical ground truth' in a double-blind validation benchmark study (outlined below and detailed in Flemisch et al. 2023). Structurally, the benchmark geometry is characterized by broad open folds and normal faults: a major normal fault breaches the lower reservoir-seal system and terminates upward at the base of the upper reservoir. A broad open anticline, in the footwall of the fault, forms the main

trap to the lower reservoir-seal system and has a spill point in the immediate footwall of the fault. The broad open anticline is also the main trap geometry for the upper reservoir-seal system, but this is affected by a graben bounded by two oppositely dipping normal faults.

1.3 The FluidFlower Validation and Forecasting Study

Accurate modeling and simulation of multiphase flow in porous media is central to GCS operation, risk assessment and mitigation strategies. Forecasts of large-scale GCS deployment, including injectivity, field-scale CO_2 migration and reservoir pressure response, heavily rely on modeling and numerical simulation studies. Only a few dozen large-scale GCS projects are currently active globally (Steyn et al. 2022), and none of these are in a post-injection phase following a multi-decadal injection period. Hence, the modeling and simulation community does not have robust datasets to assess their forecasting skill, and significant uncertainty is associated with our ability to accurately capture the dominant physical GCS processes. As a partial remedy to this, several code comparison studies have been conducted (Pruess et al. 2004; Class et al. 2009; Nordbotten et al. 2012), none of which, however, were conducted in the presence of a physical ground truth. The FluidFlower forecasting and validation study (Flemisch et al. 2023) aims to provide a first assessment of the predictive skills of the GCS modeling and simulation community. Active academic GCS research groups around the world were invited to participate in a double-blind forecasting study. The participants of the forecasting study were asked to provide independent forecasts and then subsequently invited to update their forecasts in view of group interactions. The forecasts were compared to each other and to the experimental FluidFlower data ('physical ground truth') by means of various indicative qualitative and quantitative measures with relevance to both the CO_2 injection and post-injection dynamics of the GCS operations.

1.4 Relevance to Subsurface GCS

While the present study is set at ambient conditions at intermediate (meter) scale, the most important subsurface CO_2 trapping mechanisms are present in the laboratory experiment: *structural trapping* occurs under the sealing sand layers and within different reservoir zones; *dissolution trapping* occurs almost instantaneously when the injected CO_2 dissolves into the water phase initially saturating the porous media; *residual trapping* is observed in regions with intermediate water saturation, but is temporary because of rapid dissolution; *convective mixing* occurs when the CO_2-saturated water migrates downward and generate gravitational fingers. *Mineral trapping* is by design not part of the current study for increased control of active chemistry (using silica sand rendered inert by hydrochloric acid, with the pressure and temperature conditions set outside mineralization thresholds in the experimental time series). The fundamental physical processes of multiphase, multi-component flows and trapping behavior in the FluidFlower rig to a large degree represents the porous media physics in a subsurface system, even if the petrophysical properties like porosity, permeability and small-scale heterogeneity, as well as the pressure and temperature conditions, are not directly comparable to subsurface conditions. Furthermore, we remark that the structural trapping in the FluidFlower relies more on capillary entry pressure and less on permeability contrast, than expected at the field scale. Overall, we argue that the findings and observations in this study are indicative of field-scale simulation, although several observed phenomena scale differently in the FluidFlower compared

with subsurface systems. The proper identification of key scaling parameters for a 2D flow in a complex geology is non-trivial and is detailed elsewhere (see Kovscek et al. 2023, this issue).

Despite the physical similarities, actual field-scale simulation will deviate from this study in several important aspects, of which we highlight (see Flemisch et al. 2023 for a comprehensive discussion):

- *Heterogeneity.* The facies in the benchmark geometry were built with a single sand type aiming for homogenous petrophysical properties and, hence, emphasizing larger-scale structural heterogeneities. On the field scale, it is expected that there will be significant subscale heterogeneity also within each geological structure.
- *Quality of geological characterization.* A high-resolution image of the geological geometry, with accompanying thicknesses before CO_2 injections, was issued to the benchmark participants (cf. Nordbotten et al. 2022). At the field scale, the initial geological characterization will be associated with higher uncertainty and lower spatial resolution data from seismic surveys.
- *Pressure and temperature conditions.* The laboratory conditions in the reported study yield a gaseous CO_2 phase when injected, compared with liquid or supercritical phase at field conditions in typically reservoirs. The difference in phase condition has a minor impact on viscosity, but leads to a denser and less compressible CO_2 phase at the field scale.

The importance of forecasting, risk assessment and mitigation strategies for carbon storage, with many of the critical coupled subsurface processes remaining poorly understood, merits a continued broad interdisciplinary engagement. The utility of numerical modeling and simulation as a key decision-making tool for industrial application of CO_2 storage is scrutinized in the FluidFlower validation benchmark study for the storage of CO_2 (Flemisch et al. 2023).

2 Materials and Methods

This section briefly describes the key operational considerations and methodology developed to perform the experimental part of the forecasting study. It provides an overview of all procedural steps, a description of the geological geometry and parameters. The description is not exhaustive, and the reader is referred to supplementary materials (SM) and cited work for more detailed descriptions.

2.1 Fluids

The main fluids and their composition and usage are listed in Table 1.

Throughout the article we refer to the gaseous form of CO_2 as '*gas*'- the dry gas injected will partially partition into the aqueous phase saturating the porous media and will have a positive, nonzero water content due to solubility of water in CO_2. The water content in CO_2 was not explicitly quantified in this work. We refer to the aqueous phase partially saturated with dissolved CO_2 as the '*CO_2-saturated water*', and the aqueous phase without CO_2 as '*formation water*'. The aqueous, pH-sensitive solution ('formation water') was in equilibrium with the atmosphere when injected and contained dissolved atmospheric

Table 1 Fluid compositions and role in benchmark study

Fluid	Phase	Composition	Usage
pH-sensitive solution, termed 'formation water'	Aqueous	Deionized water with – 0.14 mM bromothymol blue (BTB^-) – 0.43 mM methyl red (MRe^-) – 0.10 mM hydroxide (OH^{-1}) – 0.67 mM sodium ions (Na^+)	Saturate the pore space and enable detecting of dissolved CO_2 in the aqueous phase
CO_2	Gaseous	99.999% – 5.0 purity	Injected as gaseous phase
Lye solution	Aqueous	Deionized water with 0.48 mM sodium hydroxide (NaOH)	Cleaning fluid to remove CO_2-saturated water and trapped free gas
Acid	Aqueous	Tap water with > 0.1 M hydrochloric acid (HCl) and pH < 1.0	Sand cleaning

gases (predominantly nitrogen and oxygen). The presence of other gases influences the CO_2-to-water mass transfer due to differences in gas-to-water Henry's constant (Van De Ven and Mumford 2020): the CO_2 mass transfer to the formation water releases nitrogen and oxygen into the gaseous phase. Hence, over time the gaseous phase in the system becomes deprived of CO_2, with reduced solubility in water. This effect was predominately observed toward the later-life of the gas accumulation under the anticlines and is discussed more below.

2.2 Sand Handling and Porous Media Flow Properties

Danish quartz sand was purchased (in total 3.5 tons) and systematically treated to achieve the required properties. Six different sand types were used (see Table 2). Before use, each sand was manually sieved from the supplied sand stock and treated with a strong acid (HCL) to remove impurities (predominately calcite). The acid was neutralized with sodium hydroxide, rinsed with tap water while manually agitating to remove precipitates and dust until no visible particles and then rinsed in tap water multiple times until clear solution without particles. The sand was then dried at 60 °C until dry and stored in cleaned plastic containers with lid until use. The absolute permeability was measured for each sand, all with nominal porosity 0.44. Detailed sand description, properties and procedural steps are outlined in (Haugen et al. 2023, this issue).

2.3 The FluidFlower rig and Building the Geometry

The *FluidFlower* enables meter-scale, multiphase, quasi-two-dimensional flow experiments on model geological geometries with quantitative data acquisition. Time-lapsed images are acquired to monitor dynamic, multiphase flow patterns with high spatial resolution where single sand grains may be identified. CO_2-saturated water is distinguished from formation water by a color shift of aqueous pH sensitive solution, whereas the gas phase is observed by reduction in colored aqueous phase (formation or CO_2-saturated water). The design allows for repeated injections tests with near identical initial conditions, allowing physical uncertainty and variability to be addressed using the same geological geometry. The model geological geometry is constructed using unconsolidated sands (cf. Table 2)

and held in place between an optically transparent front panel and an opaque back panel. The rig has 56 perforations that enable a range of well configurations (injector, producer, monitoring, or plugged) for porous media flow studies.

The FluidFlower rig is curved to sustain internal forces and capable of porous media up to approximately 6 m^2 (3 m length x 2 m height). The validation benchmark and forecasting study (Flemisch et al. 2023) monitored four wells (two for CO_2 injection and two for pressure measurements), but several other wells were active during the experiments. Technical wells/ports at the bottom and top enabled resetting the fluids between CO_2 injections and to maintain a fixed water column during experiments. Technical considerations and mechanical properties of the FluidFlower rig are detailed elsewhere (Eikehaug et al. 2023a, this issue). The FluidFlower has no-flow boundaries at the bottom and both sides, whereas the top is open with a fixed free water column (constant hydrostatic head). Relevance for subsurface carbon storage processes is maintained as dominant multiphase flow parameters and trapping mechanisms are present in the room-scale laboratory flow rig, including capillarity, dissolution and convective mixing.

The dry, unconsolidated sands were manually poured from the top into the water-filled void between the front and back panels. Each layer (consisting of one sand type, except the heterogeneous fault) was constructed from the bottom and upward, and faults and large dipping angle were created by manipulating the layer during pouring using guiding polycarbonate rectangles, funnels and plastic hoses. Mechanical manipulation (raking/scratching) was kept to a minimum and only in some areas in the vicinity of the faults. Faults were constructed though an iterative process, detailed in (Haugen et al. 2023, this issue), and the sealed fault was created using a silicone rubber rectangle. The hydrostatic pressure during geometry assembly was 100 mm above operating conditions. When the geometry was complete, the water-level was lowered to operating water-level (kept constant during all injections). Multiple flushing sequences using injection rates 10% higher than the injection protocols (cf. SM 4) were performed to achieve an initial, pre-injection sand settling to improve conditions for reproducibility during CO_2 injections. The nominal porous media depth was 19 mm, but depth variations were observed and accounted for with a spatially resolved depth map (cf. SM 2).

Table 2 Key parameters for each of the six sand types

	Grade	<grain size> [a] ± σ (mm)	Nominal K (D)	P_{C_entry} [b] (mbar)
Sand ESF	Fine	0.20 ± 0.11	50	15.0
Sand C	Coarse (lower)	0.66 ± 0.09	500	3.3
Sand D	Coarse (upper)	1.05 ± 0.14	1 000	0.9
Sand E	Very coarse (lower)	1.45 ± 0.19	2 000	*0.26*
Sand F	Very coarse (upper)	1.77 ± 0.31	4 000	*0.10*
Sand G	Granules	2.51 ± 0.63	10 000	*0.01*

[a] Averaged smallest grain width reported for each sand. Grains are not circular.

[b] Capillary entry pressures measured from gas column height (in mm) sustained under each sand and converted to mbar. Italic numbers extrapolated from trend, no observable gas column.

2.4 The Rationale Behind the Benchmark Geometry

The geological geometry of the physical room-scale model (cf. Fig. 1) was motivated by typical North Sea reservoirs. It was developed in close interdisciplinary collaboration between UiB researchers from reservoir physics, earth science and applied mathematics based on the following four principles:

1. Incorporate relevant features frequently encountered in subsurface geological carbon sequestration.
2. Enable realistic CO_2 flow patterns and trapping scenarios with increasing modeling complexity.
3. Sufficiently idealized for the sand facies to be reproduced numerically with high accuracy.
4. Be able to operate, monitor and reset the fluids within a reasonable time frame.

The geometry was designed to achieve realistic CO_2 flow and trapping mechanisms to evaluate the modeling capability of the porous media community. The anticipated CO_2 flow, migration and phase behavior from each of the two CO_2 injection wells are described below, along with a geological interpretation of the benchmark geometry where geological features described are found in Fig. 1 and highlighted in *italic* below.

2.5 Geological interpretation of benchmark geometry

The benchmark geometry is a compromise between geological realism, building a physical model from unconsolidated sand, and accurate gridding for numerical simulations of the geometry. The benchmark geometry comprises two stacked reservoir-seal systems, each capped by regional seals (represented by sand ESF). The lower reservoir is a homogeneous, high permeability reservoir (sand F) overlain by a laterally continuous seal. In contrast, the upper reservoir is stratigraphically more heterogeneous, forming an overall upward fining succession, but with permeability variations within the coarse sand layers (alternation of sands E, F, D and C), and additional stratigraphic complexity around a *sealed fault* associated with the local development of sands C and D.

Structurally, the benchmark geometry is relatively simple, characterized by broad open folds and normal faults. The major left-dipping normal fault (*heterogeneous fault*) breaches the lower reservoir-seal system and terminates upward at the base of the upper reservoir (within sand F). A broad open anticline, in the footwall of the fault, forms the main trap to the lower reservoir-seal system and has a spill point in the immediate footwall of the fault. The broad open anticline is also the main trap geometry for the upper reservoir-seal system, but this is affected by a graben bounded by two oppositely dipping normal faults; one *sealed fault* and one *open fault*. An additional, subtle, low relief anticline forms an additional trap in the footwall of the graben-bounding sealed fault. The graben-bounding faults tips-out downdip into the basal layer of the upper reservoir (sand E) and updip into the base of the top regional seal (the uppermost sand layer in the model), as such they only affect the stratigraphy in the uppermost reservoir. The *sealed* and *open faults* have different properties and sealing potential: the *sealed fault* is designed as a sealing fault with a low permeability fault core, whereas the *open fault* has a high permeability fault core and would potentially act as a conduit for cross-formational fluid flow.

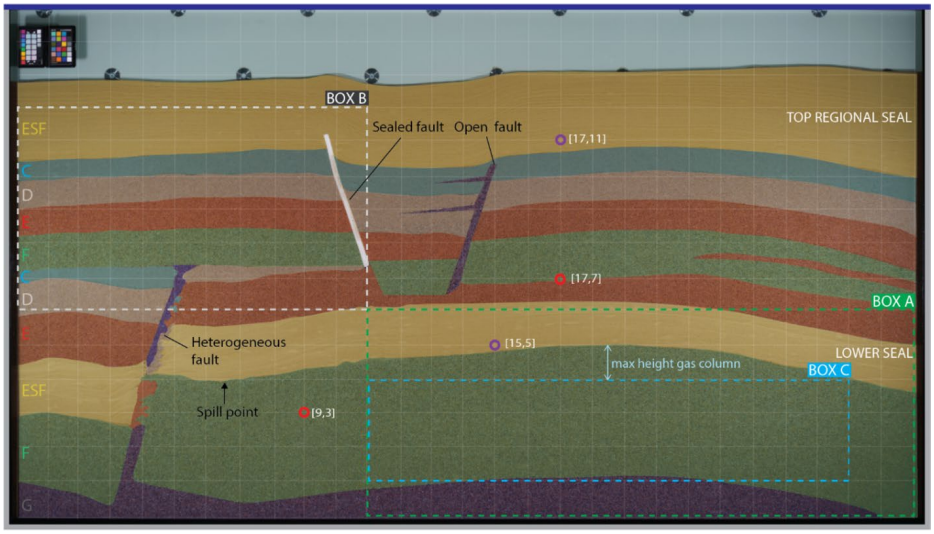

Fig. 1 The benchmark geometry with color enhanced layers for facies identification. Each sand type (ESF, C, D, E, F and G; cf. Table 2) has a separate color indicated to the left. Sand/color correlation: ESF/yellow; C/light blue; D/light brown; E/red; F/green; G/dark blue. The geometry includes three faults: *sealed* (silicone strip), *open* (sand G) and *heterogeneous* (sands G, F, D and C). Total length of visible porous media is 2800 mm, and porous media height is nominally 1300 mm. Edge shadows visible on the left and right, and the active porous extends 30 mm behind the black metal frame on each side. The three no-flow boundaries (left, right and bottom) are indicated gray, whereas the open boundary is blue (top). A 100×100 mm Cartesian grid with the origin [0,0] in the lower left corner with the x-axis positively oriented toward the right and the y-axis positively oriented toward the top aids the following coordination. Four monitored ports: two CO_2 injection well (red circles, coordinates [9,3] and [17,7]) and pressure ports (purple circles, coordinates [15,5] and [17,11]). Areas for reporting (Box A, B and C) are defined with the following coordinates (top right = TR; top left = TL; bottom right = BR; bottom left = BL): Box A: TL [11,6] -> TR [28,6], BL [11,0] -> BR [28,0]; Box B: TL [0,12] ->TR [11, 12], BL [0,6] -> BR [11,6]; Box C: TL [11, 4] ->TR [26,4], BL [11,1] ->BR [26,1]

Anticipated flow from well [9,3]. The buoyant gas phase flows upward and reaches the anticline sealing layer (sand ESF) above the injection point [9,3]. CO_2-saturated water is observed in the near-well region directly after onset of CO_2 injection. The anticline dipping angle facilitates gas migration into *Box A* and accumulation at the highest point of the CO_2 trap. The trap fills with gas and a layer with CO_2-saturated water forms underneath the downward expanding gas accumulation. The CO_2-saturated water flows downward into *Box C* over time due to (i) the positive pressure gradient from the expanding gas and (ii) convection because of the increased density relative to formation water. The gas accumulation increases upon continued injection until the gas-water interface aligns with the *spill point;* the excess gas flows through the *heterogeneous fault* and into *Box B* containing the fining upward sequence and upper fault zone. The layered sequence (sands F, E, D and C, bottom to top) temporarily traps buoyant gas and laterally spreads the gas phase at the capillary barriers between layers. The increased density of CO_2-saturated water relative to the formation water leads to gravitational fingers. The CO_2 injection ends (after 305 min) when the gas reaches the upper sand layer (sand C) under the seal, and CO_2 in all forms is contained between the left no-flow boundary and the *sealed fault*.

Anticipated flow from well [17,7]. The gas phase (injected in sand F) flows upward and spreads laterally at layer boundaries in the fining upward sequence (except between sand

F and E, cf. Table 2). The gas phase advances upward sequentially when it exceeds the capillary entry pressure in each layer. The CO_2-saturated water flows downward due to increased density and the pressure gradient of the gas accumulation—its flow pattern is influenced by the permeability variations in the layered sequence. The gas phase accumulates under the top seal above the injection well and migrates laterally until CO_2 injection is terminated (after 165 min). Depending on the volume of CO_2 injected, the gas phase will reach the *open fault*, and CO_2 in all forms will be contained between the *open fault* and the right no-flow boundary.

2.6 Image Acquisition and Analysis

The camera (Sony A7III, lens SAMYANG AF 45 mm F1.8) used the following settings (kept constant through all injections): shutter speed 1/30 sec; F number F2.8; ISO 100; color temperature 4100 K; and manual focus. The camera was positioned in the curve focal point with a 3.6 m distance from the center point in the rig, halfway up the window height. Images were captured at high spatial (7952×4472 pixels, for a total of 35.5 megapixels) and temporal (between 10 s and 5 min intervals, depending on active experimental phase) resolution to capture displacement and mass transfer dynamics. Each run consists of more than 1000 images; a subset that captures key events, displacement processes and mass transfer dynamics is available for open-access download (Eikehaug et al. 2023b). The subset contains 137 high-resolution images with the following intervals: 10 images before CO_2 injection at 20 s intervals; images every 5 min during the first 360 min (6 h) of the experiment (73 images); images every hour until 48 h (42 images); images every 6 h until end of experiment (12 images).

2.6.1 Phase Identification

The image analysis toolbox was used to separate between the different CO_2 phases (gaseous and aqueous) present in the experiments, and a set of assumptions enabled the quantification of each phase to be calculated during the CO_2 injection and associated mixing. Four main phases are anticipated:

1. Free gas (potentially flowing gas phase with nonzero gas permeability, referred to as mobile gas).
2. Trapped gas (residually trapped CO_2 with zero gas permeability, referred to as immobile gas).
3. CO_2-saturated water (aqueous phase with a nonzero CO_2 content).
4. Formation water (aqueous solution with zero CO_2 content).

Several assumptions were needed to quantitatively describe the observed multiphase flow phenomena during repeated CO_2 injections in the physical flow rig (these and further assumptions required for the data processing are discussed in more detail in SM 3):

SM3.I we assume that gas-filled regions are 100% saturated with the gas (CO_2).
SM3.II we assume a constant CO_2 concentration in the CO_2-saturated water.
SM3.III we do not account for the dynamics of the gas partitioning in the gas accumulation.

Based on these assumptions, a two-staged geometric separation of the formation water from any CO_2 in the system and of the gaseous CO_2 from the CO_2-saturated water is sufficient. This separation was possible due to the use of the pH-indicator mix (cf. Table 1; Fig. 2). Through pixel-wise image comparison to the image corresponding to the injection start, a thresholding approach first in the CMYK color space restricted to the key (black) channel, indicating any sort of change, and subsequently in the blue channel of the RGB color space, highlighting the gaseous phase, accomplishes the separation. The threshold parameters are carefully tuned through visual identification of the respective distinct plumes and their boundaries, based on several calibration images from all experimental runs. The heterogeneous nature of the geometry is considered in the analysis by choosing facies-based threshold parameters and thereby allows for tailored and relatively accurate phase segmentation, cf. Fig. 2. The parameters are chosen such that transition zones are included as demonstrated. In addition, further techniques are used to convert the resulting thresholded scalar images to Darcy-scale quantities, cf. (Nordbotten et al. 2023). The same unified setup has been used for analyzing all experimental runs.

It must be noted that based on the choice of the assumptions and the resulting image analysis, the identification of gaseous phases for which assumption SM 3.I is not satisfied may be erroneous; transition zones smear out and the saturation decays which leads to a sudden disappearance of the post-processed gaseous phase due to the use of fixed threshold parameters. In all experimental runs, two gaseous regions are detected, cf. Fig. 2, and the described effect takes place for the upper gaseous region, whereas the lower region is detected stably. While the upper region fully dissolves, the lower region results in remaining gas, cf. SM 3.III, which is detected as gaseous CO_2. Consequently, the subsequent quantitative analysis reports on a small amount of non-vanishing gas accumulation toward the end of the experimental runs.

2.6.2 Procedure in the Quantitative Analysis

The subsequent quantitative analysis results from post-processing the phase identification. We briefly elaborate on the procedure of key computations.

1. *Mass calculations and concentration maps.* Total CO_2 mass of dissolved and mobile CO_2 are determined through integration of the pixel-wise defined areal densities of mobile CO_2, $m^g_{CO_2} = \varphi \cdot d \cdot s_g \cdot \chi^g_c$, and dissolved CO_2, $m^w_{CO_2} = \varphi \cdot d \cdot s_w \cdot \chi^w_c$, with the single components determined as follows. Based on assumption SM 3.V, the porosity φ and the depth d can be accurately determined. Resulting from assumption SM 3.I, the phase identification provides saturation maps s_g for the gaseous phase and s_w for the aqueous phase, taking values either 0 or 1. It remains to quantify the mass concentrations of CO_2, χ^g_c and χ^w_c in gaseous and aqueous phases, respectively. Based on assumption SM 3.I, χ^g_c is provided as the density of gaseous CO_2 under operational conditions, cf. SM 1, obtained from the NIST database (Lemmon et al. 2022). With that, the pixel-wise areal density $m^g_{CO_2}$ is known. Assumption SM 3.II allows now for obtaining the remaining mass concentration χ^w_c through sparsification, as follows. As illustrated in Fig. 2, two CO_2 plumes originating from the two injection ports remain unconnected throughout almost the entire run time (until 84 h). The total CO_2 mass in each plume is known at any point in time based on the injection protocol, cf. SM 4, while the respective total mass of mobile CO_2 is determined through integration of $m^g_{CO_2}$ over the area of the plumes. Subtraction of both provides the total mass of dissolved CO_2 for each plume.

Finally, by assumption SM 3.II, χ_c^w set to be 0 in the formation water; constant and equal to the proportionality constant between the total volume and the total mass of dissolved CO_2 in each connected region of CO_2-saturated water χ_c^w; and not relevant for the mass calculations, yet for the discussion of convective mixing, in the remaining gaseous regions, χ_c^w is set to $\chi_{c,\max}^w = 1.8$ kg/m^3.

2. *Physical variability.* Given a set of phase segmentations, associated to different configurations, the intersections and complements of phase segmentations can be directly determined. Furthermore, we introduce metrics based on volume-weighted ratios of these, to quantify corresponding overlap and unique appearances of detected regions.
3. *Fronts and fingers.* When restricted to a region of interest, the internal interface between the detected water formation and the CO_2-saturated water can be interpreted as propagating front. Its length can be determined by making use of the Cartesian coordinate system attached to the images. Extremal points can be identified as fingertips, allowing to count them over time. Due to the use of regularization in DarSIA, when converting grain-scale data to Darcy scale, fingers are slightly smeared out. This affects the detection of the free space in between fingers, cf. Fig. 2. Thus, in these regions the resulting interface between the formation water and CO_2-saturated water can be understood as approximating non-convex hull of the fingers with its length being a lower estimate to the actual contour length of the fingers. The detection of single fingertips is, however, not affected resulting in lower uncertainty.

2.7 Image Analysis Toolbox

To use the high-resolution images as measurement data, image analysis is required. As part of the benchmark study, the open-source image analysis software *DarSIA* (short for Darcy Scale Image Analysis, Both et al. 2023a) has been developed, detailed in [Nordbotten et al.

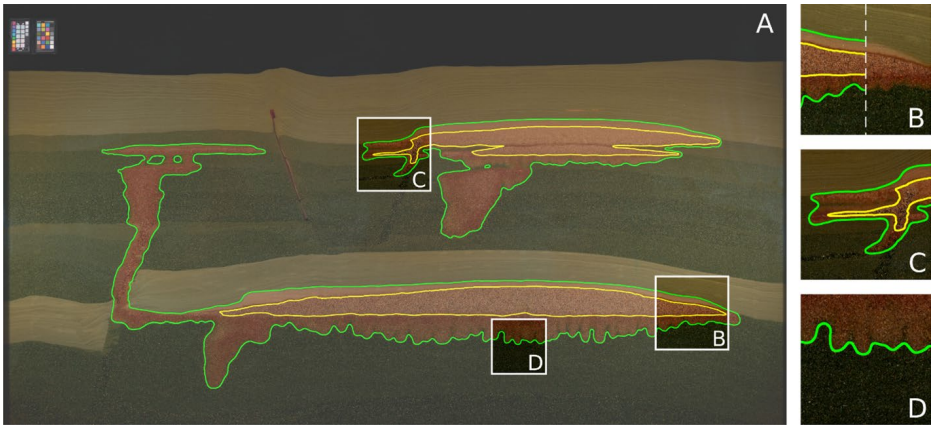

Fig. 2 Resulting phase identification of formation water, CO_2-saturated water and free gas using DarSIA, at injection stop; two plumes are identified, containing free gas regions (yellow contour) and CO_2-saturated water (green contour). Subfigure B: The pH-indicator mix (left and right, with and without contours, resp.) allows for visual separation of the different phases based on color spectra. Subfigure C: Detection of free gas in the open fault. Subfigure D: Due to the use of regularization in the upscaling, DarSIA smears out fingers and thus merely detects fingertips for fingers that are closer than a few grain diameters

2023, this issue]. DarSIA provides the capability to extract physically interpretable data from images for quantitative analysis of the image sequences of the time-lapsed CO_2 injection and storage experiments. In particular, DarSIA includes preprocessing tools to align images; project suitable regions of interest of images onto two-dimensional Cartesian coordinate systems; correcting for geometrical discrepancies due to, e.g., the curved nature of the physical asset; as well as correcting white balance fluctuations and perform color correction utilizing the color checker attached to the physical asset, overall, resulting in unified image sequences. Furthermore, additional analysis tools are available to, e.g., determine spatial deformation maps comparing different configurations and extract concentration profiles or identify phases, to mention a few. The latter aims at a Darcy-scale interpretation of the high-resolution images taken of the physical asset, effectively, removing sand grains and upscaling fluid quantities.

3 Results and Discussion

This section is divided into two parts: Part 1 relates to the sparse dataset requested in the benchmark study (Flemisch et al. 2023) and includes a discussion on temporal behavior for studied parameters across repeated runs; Part 2 expands our analysis and focuses on physical variability between repeated injections and drivers for the observed variability.

3.1 The Benchmark Sparse dataset

The sparse dataset (defined in Nordbotten et al. 2022) requested six data points to assess the ability of the participating modeling groups to forecast relevant properties of the physical system. The CO_2 phase was to be reported in the following three categories: *mobile free phase* (gas at saturations with a positive gas relative permeability), *immobile free phase* (gas at saturations with zero gas relative permeability), *dissolved* (mass of CO_2 in CO_2-saturated water). The sum of the *mobile*, *immobile* and *dissolved* phases equals the total mass of CO_2. The sparse dataset is included for completeness here, but the reader is referred to (Flemisch et al. 2023) for comprehensive analysis and discussion.

The following sparse data were requested (cf. Fig. 1 for described regions and pressure ports):

1. *As a proxy for assessing risk of mechanical disturbance of the overburden*: Maximum pressure [N/m^2] at pressure port (a) [15,5] and (b) [17,11].
2. *As a proxy for when leakage risk starts declining*: Time [s] of maximum mobile CO_2 [g] in Box A.
3. *As a proxy for our ability to accurately forecast near-well phase partitioning*: CO_2 mass [g] of (a) mobile; (b) immobile; (c) dissolved; and (d) total in seal in Box A at 72 h after injection start.
4. *As a proxy for our ability to handle uncertain geological features*: CO_2 mass [g] of (a) mobile; (b) immobile; (c) dissolved; and (d) total in seal in Box B at 72 h after injection start.
5. *As a proxy for our ability to capture onset of convective mixing*: Time [s] for which the quantity.

$$M(t) \equiv \int_C \left| \nabla \left(\frac{\chi_c^w(t)}{\chi_{c,\max}^w} \right) \right| dx$$

first exceeds 110% of the width of Box C, where χ_c^w is the mass fraction of CO_2 in the CO_2-saturated water.

6. *As a proxy for our ability to capture migration into low-permeable seals*: Total mass of CO_2 [g] in the top seal facies (sand ESF) at final time within Box A.

Here we report laboratory sparse dataset (cf. Table 3) using the dataset (Eikehaug et al. 2023b) and dedicated DarSIA scripts (Both et al. 2023b) with assumptions (cf. SM 3). The CO_2 distribution after 72 h with locations of Box A, Box B and Box C is included to aid interpretation (see Fig. 3).

3.1.1 Maximum Pressure at Ports [15,5] and [17,11] (parameters 1a and 1b)

The maximum pressures at the pressure ports ([15,5] and [17,11]) located in the sealing structures (sand ESF, cf. Fig. 1) were initially recorded with five pressure transducers (ESI, GSD4200-USB, -1 to 2 bara) because single digits millibar pressure gauges were not available for the benchmark study. The results were, however, discarded because 75% of the transducers recorded pressures less than the atmospheric pressure in the room. Hence, we use historical atmospheric pressure data reported from a nearby meteorological weather station (here Geophysical Institute, SM 1) and adjust for differences in elevation between the two locations. We then added the calculated hydrostatic pressures (see Table 3) to the recorded atmospheric pressure to get an estimate for the maximum value in each port. We apply an uncertainty of ± 1 mbar, five times stated instrument accuracy, to account for the possible overpressure during CO_2 injections.

3.1.2 Time of Maximum Mobile CO_2 in Box A (parameter 2)

The development in mobile gas in Box A for all five runs (cf. Fig. 4) increased linearly with the injection until the gas accumulation aligned with the spill point (defined in Fig. 1). On average, the maximum mass of mobile gas was observed after 4.11 ± 0.17 h. While there appears to be some noise in the identification of the maximum mobile gas, the time of maximum value is a clearly defined peak in the time series. Seen together with temporal resolution of the image series (20 s per frame), we expect identification of the time for maximum mobile CO_2 have an uncertainty of no more than three frames, i.e., $\pm$ 1 min. The nature behind the fluctuating mass after the initial spill (cf. black rectangle, Fig. 4) is discussed in more detail in Section 3.2.

3.1.3 Mobile, Immobile and Dissolved CO2 in Box A and Box B (parameters 3, 4 and 6)

The mass of mobile gas in Box A (parameter *3a* in Table 3) was on average 0.232 ± 0.047 g and is considered an upper bound for this parameter. The lower bound was found indirectly from the observation of nonzero mass of mobile gas at the end of the experiments (cf. Fig. 4), related to atmospheric gases in the formation water due to insufficient degassing

Table 3 Benchmark Sparse dataset

Parameter	1.		2.	3 [a].				4 [a].	5.		6.
Units	10^5 (N/m^2)		10^3 (s)	10^{-2} (g)				10^{-2} (g)	10^3 (s)		10^{-2} (g)
Sub parameter	1a	1b	2	3a upper	3a lower	3c	3d	4c	5 upper	5 lower	6
C1	1.106	1.046	15.4	16.3	2.9	320	37.6	76.3	12.9	12.2	54.3
C2	1.115	1.055	14.7	27.2	10.1	307	36.7	76.0	14.1	12.4	62.2
C3	1.136	1.076	14.9	28.1	12.5	313	40.4	71.5	14.9	12.8	59.1
C4	1.110	1.050	15.1	18.9	5.0	313	38.5	74.6	15.4	13.3	55.4
C5	1.108	1.048	13.7	25.3	6.9	298	37.8	90.5	17.3	12.3	52.6
Average ± 1 std	1.11 ±0.01	1.05 ±0.01	14.8 ±0.6	23.2 ± 4.7	7.5 ± 3.5	310 ± 7	38.2 ± 1.2	77.8 ± 6.6	14.9 ± 1.5	12.6 ±0.4	56.7 ± 3.5
Uncertainty	$\pm 10^{-3}$	$\pm 10^{-3}$	±0.06	–		±20%[b]	±20%[b]	±20%[b]	–		±20%[b]

[a]Parameters 3b, 4a, 4b and 4d are reported as zero and not included in Table 3. Rationale provided in main text below

[b]Stated uncertainties are discussed in the main text below

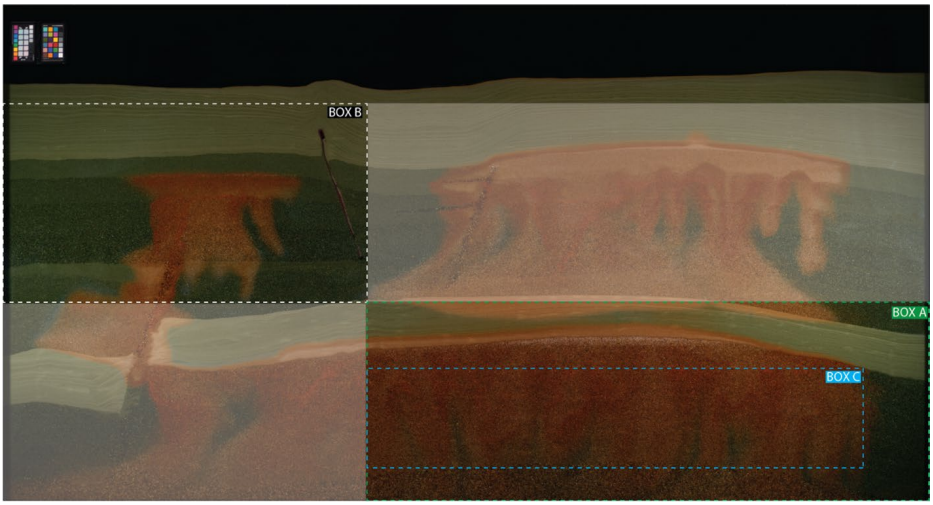

Fig. 3 Distribution of CO_2 after 72 h for run C3. The positions of Box A (green, dashed line), Box B (white, dashed line) and Box C (blue, dashed line) are used to populate the sparse benchmark dataset. The shaded regions in the benchmark geometry (top right and bottom left) are outside the defined boxes. CO_2 (in any form) in the shaded regions was not included in the analysis for the sparse dataset

(cf. Chapter 2.1 and Haugen et al. 2023). Based on our physical understanding of the studied system, we anticipate that the mass of mobile CO_2 should be zero at the end of the experiment. Hence, we subtract the end point mass from the upper bound to find an estimate of the lower bound, cf. Table 3. An alternative, but also physically plausible, lower bound for parameter 3a is zero, where all the mobile gas (CO_2) is dissolved in the CO_2-saturated water. The mass of mobile gas in Box B after 72 h (parameter 4a) is reported as zero because mobile gas was not observed in the segmented images.

The mass of immobile gas in Box A and Box B (parameters *3b* and *4b* in Table 3) were reported as zero because the formation water did not generate a unique and characteristic color for immobile gas. Hence, DarSIA and its color-based segmentation (cf. Section 2.5) are not able to distinguish immobile gas from the other phases. Careful visual inspection identified small amounts of immobile gas at early times, but visual inspection at 72 h did not identify any immobile gas. This is consistent with our physical understanding of the system, where isolated bubbles of CO_2 are expected to dissolve quickly.

The mass of dissolved gas in the CO_2-saturated water in Box A and Box B after 72 h (parameters *3c* and *4c* in Table 3) were 3.10 ± 0.07 g (Box A) and 0.778 ± 0.066 g (Box B), see Fig. 5. The mass calculations use the known injected CO_2 mass in well [9,3] for Box A and well [17,11] for Box B and apply DarSIA to segment the separate plumes originating from each well to calculate the mass of mobile and dissolved gas (cf. Section 2.5). The two plumes remain unconnected throughout almost the entire run time (until 84 h), and the total CO_2 mass in each plume is known at any point in time based on the injection protocol. After 84 h the plumes merge and the plots are extrapolated to 120 h (end of experiment) based on current trends. The mass of CO_2 in the sealing structures in Box A and Box B after 72 h (parameters *3d* and *4d* in Table 3) were 0.382 ± 0.012 (Box A, cf. Fig. 5) and 0.00 (Box B). Mobile and dissolved gas did not enter the top regional seal confined within Box B, but minute amounts of dissolved gas (in the order of 10^{-3} g) entered the sealing structure in the lower, right corner of Box B after 72 h. Hence, the final mass of CO_2 in the sealing

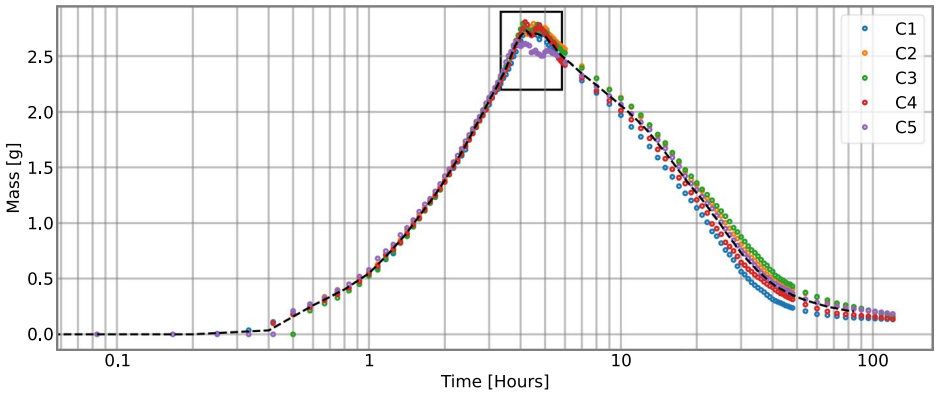

Fig. 4 Development in mass (g) of mobile gas in Box A for the whole experimental time (120 h) for all five runs (C1–C5) and the average (black, dashed line). The mass increased linearly with the injection rate until spill time (cf. Table 3) and then decreased because the mobile gas dissolved into the formation water. The development in mobile mass associated with the spill point (black rectangular) is discussed in detail below

structure confined within Box A (parameter *6*, cf. Fig. 6) was on average 0.567 ± 0.035. For the parameters discussed here (3c, 3d, 4c, 4d and 6), we attribute a nominal measurement uncertainty of $\pm 20\%$ based on the limitations and influence of underlying assumptions (cf. SM 3), stated weakness in the analysis of the color scheme (cf. Section 2.5), extrapolating trends and operational difficulties with mineralization of methylene red.

3.1.4 Development in M (t) Relative to the Width of Box C (parameter 5)

The $M(t)$ (parameter 5 in Table 3) is a measure of the total variation of the concentration field. As such, it is related to the contour lengths of the density-driven fingers, and we normalize it relative to the length of Box C, so that a value of $M_{\text{norm}}(t) = 1$ corresponds to no fingers below a gas cap spanning the whole length of the top of Box C. As CO_2-saturated water migrated downward due to gravity, the contour lines and the $M_{\text{norm}}(t)$ increase (see Fig. 7). On average for the five runs $M_{\text{norm}}(t)$ exceeds 110% of the width of Box C after 4.14 ± 0.4 h, where the stated times for each run may be considered as an upper bound due to the assumption that the concentrations are constant, which decreases the measure of the gradient in the integral. A lower bound is the time when $M_{\text{norm}}(t)$ reached 100% of the length of Box C, which is closely correlated to gas filling the upper boundary of Box C, a necessary prerequisite for $M_{\text{norm}}(t)$ exceeding 110%.

3.2 Physical Repeatability of Multiphase flow During Laboratory Carbon Sequestration runs

The benchmark study consisted of five operationally identical CO_2 injection experiments using the same geological geometry and initial conditions. The experiments were designed to generate physical data for model comparison, with the motivation to achieve a physical 'ground truth'. Here we discuss physical repeatability between the five runs (C1–C5) by comparing the degree of areal sweep overlap incorporating all forms of CO_2 (mobile, immobile, dissolved) in three regions (Box A, Box B' and Box D, cf. Fig. 8) with increasing geological complexity. We quantify the degree of overlap of runs C2, C3 and C4 and discuss the uniqueness of each run.

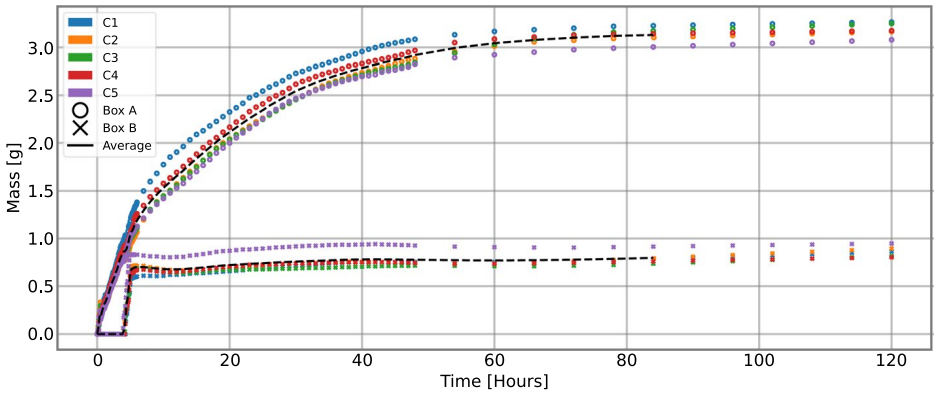

Fig. 5 The development in mass of dissolved CO_2 (g) in CO_2-saturated water in Box A (open circles) and Box B (crosses) for runs C1–C5 during the whole experimental time (120 h). All mass curves increase from the onset because mobile gas dissolved into the formation water to form CO_2-saturated water and reach plateau values when most of the gas within each box is dissolved. The curves in Box B remain zero until the gas exceeds the spill point and flow into the fault (after approximately 4 h). The somewhat different development for run C1 in Box A (blue circles) and run C5 in Box B (purple crosses) relates to the inconsistencies for these runs, discussed in Section 3.2. Note that the average curves (black, dashed lines) are calculated until 84 h

3.2.1 Physical Reproducibility with Increasing Reservoir Complexity

We investigate the reproducibility between five runs in the same geometry, with the hypothesis that increased reservoir complexity tends to reduce the degree of physical reproducibility. As mentioned above, our motivation to achieve a physical "ground truth"

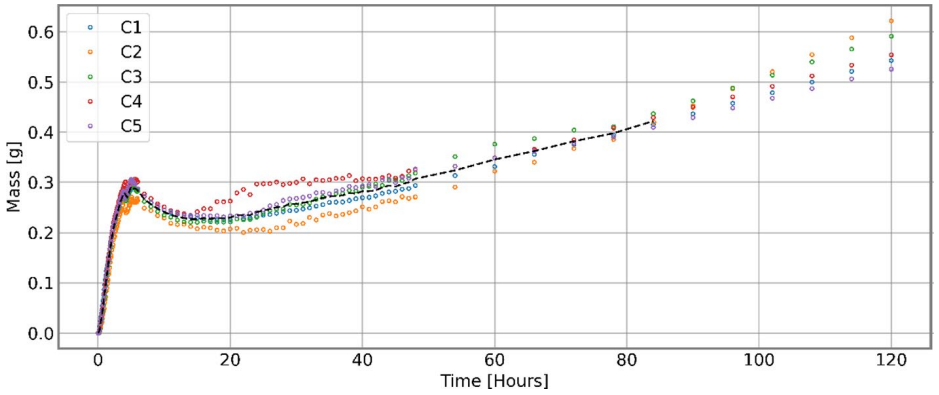

Fig. 6 Development of CO_2 (in any form) in sealing layer (sand ESF) confined within Box A during the whole experimental time (120 h) for all five runs (C1–C5). Only CO_2-saturated water (no gas) was observed in the sealing layer in Box A, and advection from the underlaying gas was the main driving force for increased mass initially. After gas injection stopped (after approximately 5 h), there was a slight decrease of CO_2 mass in the sealing layer, explained by gravity of the denser CO_2-saturated water and diminishing advective forces due to a reducing gas cap under the anticline. After approximately 20 h, the mass increases again because CO_2-saturated water from injector [17,7] flows downward and enters the top boundary of Box A (cf. Fig. 4 after 72 h)

was not fully achieved. This was because our 'identical' experiments indeed were not truly identical, even if the gas injection protocol was (within measurement uncertainty, cf. SM 4). Next, we describe the two known variables that influence the displacement patterns:

1. *Inconsistent water chemistry*. The formation water (cf. Table 1) in run C1 unintentionally used tap water instead of deionized water. The inconsistent water chemistry for C1 resulted in a unique dissolution rate and convective mixing behavior (cf. Figure SM.3). Run C1 is thus omitted from the analysis of physical reproducibility.
2. *Atmospheric pressure variations.* The atmospheric pressure variations in Bergen (cf. Figure SM.1) resulted in a low-pressure outlier for run C5 (968 mbar) compared with the other runs (on average 999 mbar during the injection period, cf. Table SM 1). Hence, the larger volume of the injected CO_2 (equal mass injected for all runs) influenced key parameters in the experiment (most prominently parameter 2 in Table 3, but also rate of dissolution). Run C5 is thus omitted from the analysis of physical reproducibility.

The described operational (water chemistry) and environmental (atmospheric pressure) inconsistencies provide the rationale for excluding C1 and C5 in our analysis of physical reproducibility for operationally identical experiments with comparable pressure and temperature conditions. An analysis of sand settling between runs showed only minor changes (cf. SM 6). Hence, we focus on runs with comparable system parameters and report the development in overlap between runs C2, C3 and C4 (cf. Fig. 9). To compute the overlap percentages, we first weight all pixels in the segmented images with their corresponding volume (see SM 2). Then, the ratio between the number of volume-weighted pixels where CO_2 (gas and dissolved) in C2, C3 and C4 overlap and the number of volume-weighted pixels where CO_2 (gas and dissolved) in any of the three runs appear is reported. Next, we describe the development in physical overlap within Box A, Box B' and Box D.

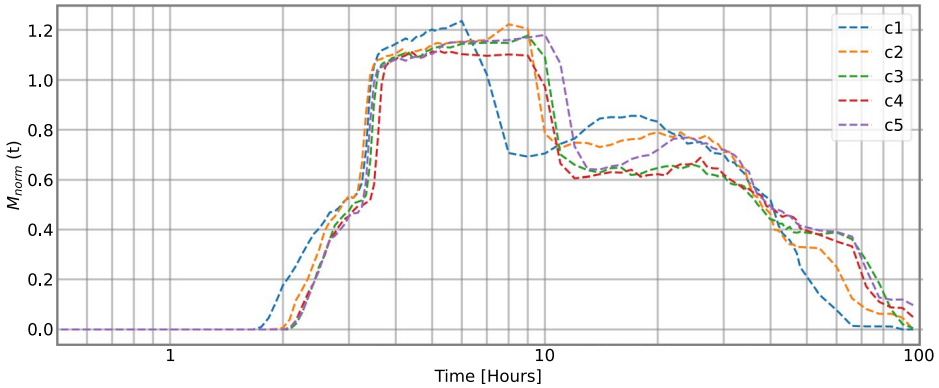

Fig. 7 Development in $M_{\text{norm}}(t)$ for all five runs from injection start until end of experiment (120 h). For the initial state of a zero CO_2 concentration within Box C, $M_{\text{norm}}(t)$ takes the value 0. Run C1 (blue) is ahead of the other runs, both in the start and at the end (fingers start to leave Box C). The rapid increase between 3 and 4 h arises because the mobile gas fills the top of Box C. The reverse is true after approximately 10 h (6 h for run C1) when the gas accumulation (due to shrinking by dissolution) exits the upper boundary of Box C and the parameter $M_{\text{norm}}(t)$ rapidly decreases. This is counterbalanced to some extent by the further development of the density-driven fingers, as seen around 20 h, until dissolution and diffusion eventually leads to a more uniform distribution of dissolved CO_2, and $M_{\text{norm}}(t)$ approaches 0 again

The development in physical overlap in Box A may be divided into four intervals: *i. pre-spilling*; *ii. gravitational fingers*, *iii. dissolution-driven flow* and *iv. homogenization.* The *pre-spilling* interval (from the injection start to approximately 4 h) occurred before the gas column height exceeded the spill point. The onset of gravitational fingers occurred in this interval, but they were still only minor and did not develop into pronounced gravitational fingers. The overlap increased from injection start and reached a global maximum (97% overlap) after approximately 4 h, with an average 92% $C_{2,3,4}$ overlap for the whole interval. The uniqueness of runs C2, C3 and C4 were on average 0.14% (cf. Figure SM.4) during the *pre-spilling* period. The *gravitational fingers* interval (approximately 4 to 30 h) was characterized by development of pronounced gravitational fingers in the gas accumulation under the anticline trap in Box A. The physical overlap of $C_{2,3,4}$ decreased from 97 to 79% (local minimum), dominated by the differences in number of fingers and individual finger dynamics (discussed in more detail below). The *dissolution-driven flow* interval (approximately 30 to 70 h) describes the period when the gravitational fingers reached the no-flow at the lower Box A boundary, and fingers started to move lateral and merge as the gas accumulation dissolved and pulled aqueous phase from surrounding regions into Box A. The physical overlap increased to above 95% in this period. The *homogenization* interval (approximately 70 to 120 h) was characterized by a constant physical overlap (above 95%) with only minor movement of aqueous phases confined in Box A.

Box B' generally follows the overall behavior of Box A in the four intervals defined above. Importantly, the reduction in physical overlap observed in the *gravitational fingers* interval (after approximately 4 h) was related to variable spilling times for runs C2, C3 and C4, not related to finger development (cf. parameter 2, Table 3 that approximates the spilling time for each run). The variation in spill times resulted initially in reduced overlap with slight variation in fault migration and displacement patterns for runs C2,C3 and C4. The sustained reduction of physical overlap stems from an apparent stochastic variation for run C3 (cf. Figure SM.3; 10 h), corroborated with development of the uniqueness for each

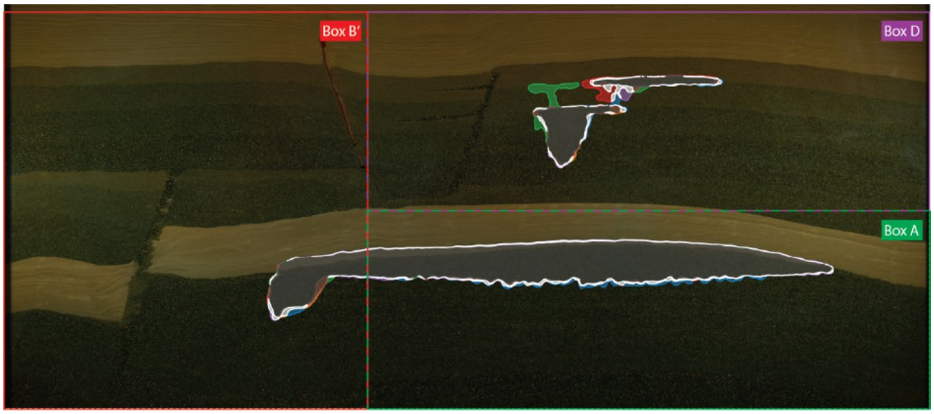

Fig. 8 Degree of physical overlap and description of Box A, Box B' and Box D with increasing geological complexity. Box A is identical to Fig. 1; Box B' is an extension of Box B (cf. Fig. 1) and includes the lower part of the geometry left to the heterogenous fault; Box D includes the fining upward sequence associated with injector [17,7] and the open fault (cf. Fig. 1). The CO_2 distribution (all forms) for all five runs (C1–C5) in three boxes (Box A, Box B' and Box D) after 155 min of CO_2 injection is shown. Spatially distributed overlap for all runs, with the following color scheme: gray (overlap C2 + C3 + C4); blue (unique C1); orange (unique C2); green (unique C3); red (unique C4); purple (C5 unique); brown (combinations all runs with at least one of C2, C3 or C4), white (other combinations). The reader is referred to SM 5 for additional time steps

run (cf. Figure SM.4; middle). The physical explanation for the observed variation in run C3 is not clear, but this only occurred for that single run, with subsequent runs (C4 and C5) reverting to the flow patterns seen for the earlier runs (C1 and C2). Hence, we do not expect the deviation in run C3 to stem from any physical alterations within the experiment (sand settling or chemical alterations). Remaining explanations could be related to variations in atmospheric pressure, or factors outside our experimental control.

The development in Box D was delayed in time relative to Box A and Box B' due to the later injection start of well [17,11], but follows the overall trend: initially increasing overlap, slight reduction due to finger development and convective mixing, then increase through homogenization. Small amounts of dissolved gas were observed in a localized point the top regional seal contained in Box D for most runs (cf. Figure SM 3). The seal breach occurred around a plugged port (CO_2 migrated along the sealing silicone), resembling a of CO_2 leakage scenario along a poorly abandoned well.

3.2.2 Dynamics of Gravitational Fingers in Box C

Box C is the homogenous zone under the lower anticline under the main gas accumulation and where most of the gravitational fingers emerged during and after CO_2 injection. From image analysis it was possible to extract the development of fingers as a function of time for all runs (cf. Fig. 10). Noticble fingers appear after an onset time of approximately 3 h, and the number was reasonably stable around 25–30, which corresponds to a characteristic spacing of about 5–6 cm. The stability of the number of fingers was an indication that the system is near the regime of the "maximally unstable" fingers spacing, predicted by theoretical considerations (see, e.g., Riaz et al. 2006; Elenius et al. 2012). This observation is supported by the finger lengths, which indicated a linear growth regime after onset. Repeatability was observed in terms of onset location and finger dynamics, even at time significantly after onset (cf. Figure SM.5 and Table SM.3).

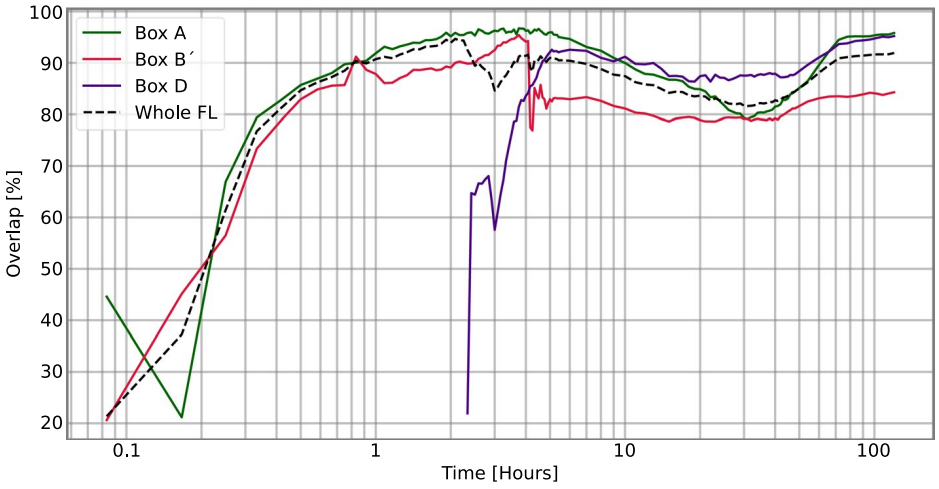

Fig. 9 Degree of physical reproducibility between operationally identical CO_2 injection runs with comparable pressure and temperature conditions (runs C2, C3 and C4). Box A (green line) represents the most homogenous case; Box B' (red line) represents the case with the heterogenous fault zone and fining upward sequence; Box D (purple line) represents the middle case with a fining upward sequence. Overlap considering the whole geometry (dashed line) is included for comparison

3.2.3 Oscillating CO_2 Leakage from Anticline

The benchmark geometry and injection protocol were designed to achieve realistic displacement processes relevant for subsurface carbon storage, where most observed phenomena and mass transfer dynamics were anticipated; showcased in the description of expected behavior (cf. Section 2.4) and benchmark description (Nordbotten et al. 2022). An oscillating CO_2 spilling event from the lower anticline was observed in our study, something that was not anticipated. Non-monotonic leakage behavior has previously been suggested in the literature (Preuss 2005) and in natural analogues (Shipton et al. 2004), attributed to the interplay between multiphase flow, Joule–Thomson cooling and heat transfer effects in the fault plane. Pulsating non-wetting CO_2 invasion has also been studied experimentally in tanks with heterogeneous geometries (Glass et al. 2000), focusing on buoyant-driven flow through capillary barriers. Intermittent non-wetting flows with repeated fragmentation (snap-off) and reconnection during buoyancy-driven flows (Wagner et al. 1997; Islam et al. 2014), with pulsation in the capillary pressure (Geistlinger et al. 2006; Mumford et al. 2009) has previously been discussed. Flow pulsation in fingers under buoyancy can occur regardless of grain sizes, with stepwise invasion of the non-wetting phase as new pathways form (Geistlinger et al. 2006). To our knowledge, oscillating CO_2 leakage behavior from an anticline spill point into a fault zone in the absence of thermal effects has not previously been observed experimentally nor received attention in the literature. Below we discuss the displacement dynamics during multiphase flow in the fault plane generating the observed oscillating anticline CO_2 leakage behavior.

The mass of mobile gas in Box A oscillated after the initial spilling event for all runs (cf. Fig. 11). The gas escapes the anticline trap in bursts and flows into the narrow restriction at the bottom of the fault (aligned in height with the spill point). When gas migrates upward in the fault zone (essentially a localized permeable pathway) it displaces resident aqueous fluids downward. The inflow of aqueous phase effectively reduces and ultimately blocks the upward migration of gas. This is in essence because the localized pathway in the inlet region of the fault cannot accommodate stable counter-current flow (upward gas flow and downward water flow), possibly due to viscous coupling effects (see, e.g., the review paper

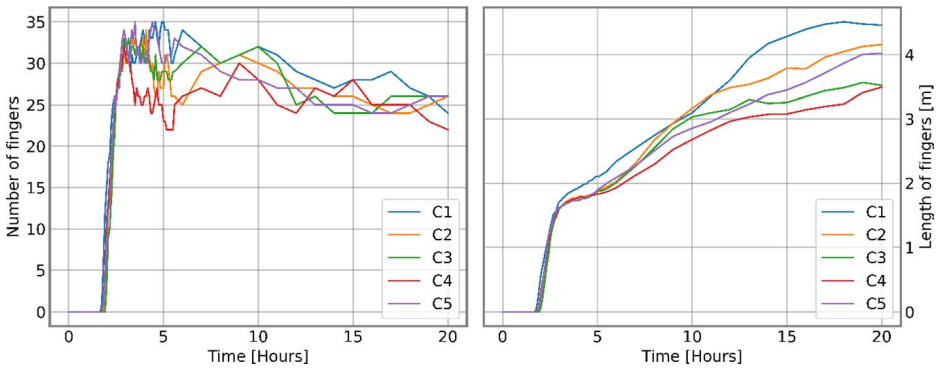

Fig. 10 Dynamics of convective mixing and gravitational fingers in Box C for all runs C1–C5. Left: Number of gravitational fingers, all runs follow the general trend: a rapid increase until a maximum is reached, followed by a declining number as some fingers merge. Right: The length (m) of the boundary of the phase segmentation, also identifying (an approximation) of the fingers. Note that the contour length only considers the boundary inside Box C. Both graphs end when the first finger reached the lower boundary of Box C (20 h)

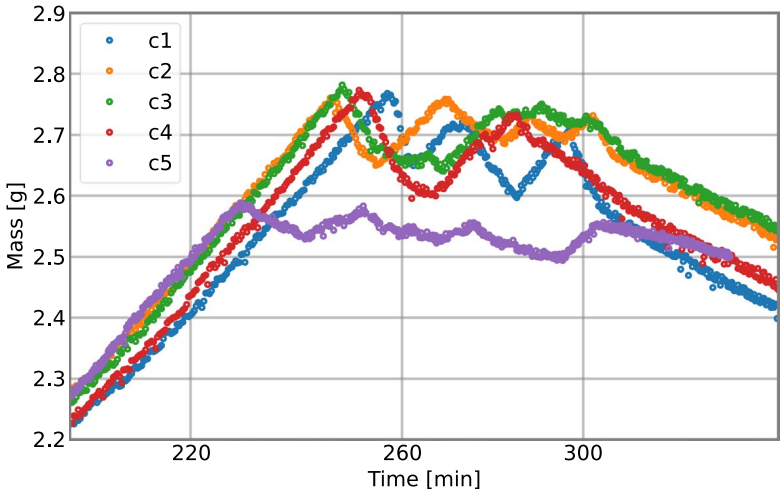

Fig. 11 Fluctuations in mass of mobile gas (g) in Box A after initial spilling event. The mass curves all demonstrate oscillations due to recurring spilling events from the anticline to the adjacent fault. For all runs, the maximum mass was observed before the initial gas escape. The lower atmospheric pressure for run C5 (purple circles) results in a lower initial spilling time

by Ayub and Bentsen 1999). When the upward migration of gas is temporarily blocked, the anticline gas column height increases again with continued CO_2 injection. The process then repeats itself when the aqueous phase flow dissipates. A secondary effect is that the inflowing aqueous phase increases the local water saturation between the spill point and the inlet point of the fault and traps gas. The gas quickly dissolves into aqueous phase, and the subsequent spilling events (up to four events per run) are essentially local drainage processes, characterized by oscillating mass of mobile gas under the anticline (Box A). Interestingly, the process appears hysteretic in nature, with decreasing peak mass values for each event, most likely related either to increased gas relative permeability between the spill point and the fault, or changes in the local CO_2 concentration in the aqueous phase. The fluctuations stopped when the CO_2 injection terminated (after approximately 300 min, cf. SM 4), and the gas column height (and, hence, the mass of mobile gas) decreased under the spilling point.

To generalize the underlying causes for the observed phenomenon is difficult based on the reported experiments alone, but pulsation behavior of buoyant gas accumulations underneath capillary barriers has been observed in similar tank experiments (Glass et al. 2000). In their work, pulsation occurs when the gas breaks through the capillary barrier through a finger that cannot be sustained (due to reinvasion of the wetting phase in the capillary barrier) when the gas column height decreases. The cycle repeated itself with continued CO_2 injection as the gas accumulation height increased again. Although Glass et al. (2000) concluded that the pulsation behavior would not significantly impact large-scale CO_2 flow, the pulsation behavior may accelerate upward plume migration through capillary barriers, especially in a relatively homogeneous formation with sparse capillary barriers (Ni and Meckel 2021). In our work, the observations are to some degree influenced by the physical system (no-flow boundaries in the vicinity of the spill point and fault, and the fault geometry aligned with the spill point acting as a restriction of upward migration of gas) and presence and shape of the gas accumulation effectively reducing the area available for

water flow. A systematic evaluation of the cyclic behavior including coupled processes and parameters of the problem remains a task for future work.

4 Concluding Remarks

The open-access, high-quality laboratory dataset, accompanied with dedicated analysis tools, represents an asset and opportunity for the carbon storage community to expand the current analysis in future studies. The physical data, describing many of the relevant processes for subsurface carbon storage, may also be used for model validation, comparison and data-driven forecasts for different stages of a carbon storage operation. Blueprints of the experimental infrastructure enhance reproducibility of scientific research and enable the porous media community at large to build physical assets and collectively join our efforts.

Our outlook, based on the observations identified in this study, is to probe the origin and premises for establishing non-thermally induced oscillating flows and to broaden the understanding of at what length scales and to what accuracy multiphase flows in porous media are deterministic.

In conclusion, the observed processes and phenomena qualitatively corroborate the physical understanding and knowledge within the carbon storage community. This supports the assertion that we have a sufficient understanding to claim that industrial carbon storage operations can be conducted in an efficient and safe manner.

Supplementary Information The online version contains supplementary material available at https://doi.org/10.1007/s11242-023-02013-4.

Acknowledgements The work of JWB is funded in part by the UiB Akademia-project «FracFlow» and the Wintershall DEA-funded project «PoroTwin». MH is funded from Research Council of Norway (RCN) Project No. 280341. KE and MH are partly funded by Centre for Sustainable Subsurface Resources, RCN Project No. 33184. BB is funded from RCN Project No. 324688.

Funding Open access funding provided by University of Bergen (incl Haukeland University Hospital).

Declarations

Conflict of interest The authors have not disclosed any competing interests.

References

Ayub, M., Bentsen, R.G.: Interfacial viscous coupling: A myth or reality? J. Pet. Sci. Eng. (1999). https://doi.org/10.1016/S0920-4105(99)00003-0

Bastesen, E., Rotevatn, A.: Evolution and structural style of relay zones in layered limestone–shale sequences: insights from the Hammam Faraun Fault Block, Suez rift, Egypt. J. Geol. Soc. (2012). https://doi.org/10.1144/0016-76492011-100

Both, J.W., Storvik, E., Nordbotten, J.M., Benali, B.: DarSIA v1.0, (2023a). https://doi.org/10.5281/zenodo.7515016

Both, J.W., Benali, B., Folvord, O., Haugen, M., Storvik, E., Fernø, M.A., Nordbotten, J.M.: Image analysis of the international FluidFlower benchmark dataset. Zenodo (2023b). https://doi.org/10.5281/zenodo.7515038

Class, H., Ebigbo, A., Helmig, R., Dahle, H.K., Nordbotten, J.M., Celia, M.A., Audigane, P., Darcis, M., Ennis-King, J., Fan, Y., Flemisch, B., Gasda, S.E., Jin, M., Krug, S., Labregere, D., Naderi Beni, A., Pawar, R.J., Sbai, A., Thomas, S.G., Trenty, L., Wei, L.: A benchmark study on problems related to CO_2 storage in geologic formations. Comput. GeoSci. **13**(4), 409–434 (2009). https://doi.org/10.1007/s10596-009-9146-x

Eikehaug, K., Haugen, M., Folkvord, O., Benali, B., Bang Larsen, E., Tinkova, A., Rotevatn, A., Nordbotten, J.M., Fernø, M.A.: Engineering meter-scale porous media flow experiments for quantitative studies of geological carbon sequestration, Transp. Porous Med. (2023a) (In Press)

Eikehaug, K., Bang Larsen, E., Haugen, M., Folkvord, O., Benali, B., Both, J.W., Nordbotten, J.M., Fernø, M.A.: The international FluidFlower benchmark study dataset https://doi.org/10.5281/zenodo.7510589 (2023b)

Elenius, M.T., Nordbotten, J.M., Kalisch, H.: Effects of a capillary transition zone on the stability of a diffusive boundary layer. IMA J. Appl. Math. (2012). https://doi.org/10.1093/imamat/hxs054

Flemisch, B., Nordbotten, J.M., Fernø, M.A., Juanes, R., Class, H., Delshad, M., Doster, F., Ennis-King, J., Franc, J., Geiger, S., Gläser, D., Green, C., Gunning, J., Hajibeygi, H., Jackson, S.J., Jammoul, M., Karra, S., Li, J., Matthäi, S.K., Miller, T., Shao, Q., Spurin, C., Stauffer, P., Tchelepi, H., Tian, X., Viswanathan, H., Voskov, D., Wang, Y., Wapperom, M., Wheeler, M.F., Wilkins, A., Youssef, A.A., Zhang, Z.: The FluidFlower Validation Benchmark Study for the Storage of CO_2. Transp. Porous Med. (2023). https://doi.org/10.1007/s11242-023-01977-7

Furre, A.K., Eiken, O., Alnes, H., Vevatne, J.N., Kiær, A.F.: 20 years of Monitoring CO_2-injection at Sleipner. Energy Procedia. (2017). https://doi.org/10.1016/j.egypro.2017.03.1523

Geistlinger, H., Krauss, G., Lazik, D., Luckner, L.: Direct gas injection into saturated glass beads: transition from incoherent to coherent gas flow pattern. Water Resour. Res. (2006). https://doi.org/10.1029/2005WR004451

Geophysical, Institute: University of Bergen, https://veret.gfi.uib.no/?action=download

Glass, R.J., Conrad, S.H., Peplinski, W.: Gravity-destabilized nonwetting phase invasion in macroheterogeneous porous media: experimental observations of invasion dynamics and scale analysis. Water Resour. Res. **36**(11), 3121–3137 (2000). https://doi.org/10.1029/2000WR900152

Haugen, M., Saló-Salgado, L., Eikehaug, K., Benali, B., Both, J.W., Storvik, E., Folkvord, O., Juanes, R., Nordbotten, J.M., Fernø, M.A.: Physical variability in meter-scale laboratory CO_2 injections in faulted geometries, Transp. Porous Med. (2023) (In Press)

Islam, A., Chevalier, S., Ben Salem, I., Bernabe, Y., Juanes, R., Sassi, M.: Characterization of the crossover from capillary invasion to viscous fingering to fracturing during drainage in a vertical 2D porous medium. Int. J. Multiph. Flow. **58**, 279–291 (2014). https://doi.org/10.1016/j.ijmultiphaseflow.2013.1

Karstens, J., Berndt, C.: Seismic chimneys in the southern viking graben–implications for palaeo fluid migration and overpressure evolution. Earth Planet. Sci. Lett. (2015). https://doi.org/10.1016/j.epsl.2014.12.017

Karstens, J., Ahmed, W., Berndt, C., Class, H.: Focused fluid flow and the sub-seabed storage of CO_2: evaluating the leakage potential of seismic chimney structures for the Sleipner CO_2 storage operation. Marine Pet. Geol. (2017). https://doi.org/10.1016/j.marpetgeo.2017.08.003

Kneafsey, T.J., Pruess, K.: Laboratory Flow experiments for visualizing carbon dioxide-induced, density-driven brine convection. Transp. Porous Med. **82**, 123–139 (2010). https://doi.org/10.1007/s11242-009-9482-2

Kovscek, A.R., Nordbotten, J.M., Fernø, M.A.: Scaling up FluidFlower results for carbon dioxide storage in geological media, TiPM SI submitted. (2023)

Krishnamurthy, P.G., DiCarlo, D., Meckel, T.: Geologic heterogeneity controls on trapping and migration of CO_2. Geophys. Res. Lett. **49**, 1–208 (2022). https://doi.org/10.1029/2022GL099104

Lemmon, E.W., Bell, I.H., Huber, M.L., McLinden, M.O.: *Thermophysical Properties of Fluid Systems*, NIST Chemistry WebBook, NIST Standard Reference Database Number 69, Eds. P.J. Linstrom and W.G. Mallard, National Institute of Standards and Technology, Gaithersburg MD, 20899, (2022). https://doi.org/10.18434/T4D303

Mumford, K.G., Dickson, S.E., Smith, J.E.: Slow gas expansion in saturated natural porous media by gas injection and partitioning with non-aqueous phase liquids. Adv. Water Resour. **32**(1), 29–40 (2009). https://doi.org/10.1016/j.advwatres.2008.09.00

Ni, H., Meckel, T.A.: Characterizing the effect of capillary heterogeneity on multiphase flow pulsation in an intermediate-scale beadpack experiment using time series clustering and frequency analysis. Water Resour. Res. **57**, e2021WR030876 (2021). https://doi.org/10.1029/2021WR030876

Nixon, C.W., Nærland, K., Rotevatn, A., Dimmen, V., Sanderson, D.J., Kristensen, T.B.: Connectivity and network development of carbonate-hosted fault damage zones from western Malta. J. Struct. Geol. (2020). https://doi.org/10.1016/j.jsg.2020.104212

Nordbotten, J.M., Flemisch, B., Gasda, S.E., Nilsen, H.M., Fan, Y., Pickup, G.E., Wiese, B., Celia, M.A., Dahle, H.K., Eigestad, G.T., Pruess, K.: Uncertainties in practical simulation of CO_2 storage. Int. J. Greenhouse Gas Control. **9**, 234–242 (2012). https://doi.org/10.1016/j.ijggc.2012.03.007

Nordbotten, J.M., Fernø, M.A., Flemisch, B., Juanes, R., Jørgensen, M.: Final benchmark description: FluidFlower international benchmark study. Zenodo. (2022). https://doi.org/10.5281/zenodo.6807102

Nordbotten, J.M., Benali, B., Both, J.W., Brattekås, B., Storvik, E., Fernø, M.A.: DarSIA: An open-source Python toolbox for two-scale image processing of dynamics in porous media, Transp. Porous Med. (2023). https://doi.org/10.1007/s11242-023-02000-9

Ogata, K., Senger, K., Braathen, A., Tveranger, J.: Fracture corridors as seal-bypass systems in siliciclastic reservoir-cap rock successions: Field-based insights from the jurassic Entrada formation (SE Utah, USA). J. Struct. Geol. (2014). https://doi.org/10.1016/j.jsg.2014.05.005

Pau, G.S.H., Bell, J.B., Pruess, K., Almgren, A.S., Lijewski, M.J., Zhang, K.: High-resolution simulation and characterization of density-driven flow in CO. storage in saline aquifers, Adv. Water Resour. (2010). https://doi.org/10.1016/j.advwatres.2010.01.009

Pruess, K.: Numerical studies of fluid leakage from a geologic disposal reservoir for CO_2 show self-limiting feedback between fluid flow and heat transfer. Geophys. Res. Lett. (2005). https://doi.org/10.1029/2005GL023250

Pruess, K., Garciia, J., Kovscek, T., Oldenburg, C., Rutqvist, J., Steefel, C., Xu, T.: Code intercomparison builds confidence in numerical simulation models for geologic disposal of CO_2. Energy. **29**(9–10), 1431–1444 (2004). https://doi.org/10.1016/j.energy.2004.03.077

Rasmusson, M., Fagerlund, F., Rasmusson, K., Tsang, Y., Niemi, A.: Refractive-light-transmission technique applied to density-driven convective mixing in porous media with implications for geological CO_2 storage. Water Resour. Res. **53**, 8760–8780 (2017). https://doi.org/10.1002/2017WR020730

Riaz, A., Hesse, M., Tchelepi, H., Orr, F.: Onset of convection in a gravitationally unstable diffusive boundary layer in porous media. J. Fluid Mech. **548**, 87–111 (2006). https://doi.org/10.1017/S0022112005007494

Shipton, Z.K., Evans, J.P., Kirschner, D., Kolesar, P.T., Williams, A.P., Heath, J.: Analysis of CO_2 leakage through 'low-permeability' faults from natural reservoirs in the Colorado Plateau, east-central Utah, Geological Storage of Carbon Dioxide (2004), edited by S. J. Baines and R. H.Worden,Geol. Soc. London Spec. Publ.,233, 43–58

Steyn, M., Oglesby, J., Turan, G., Zapantis, A., Gebremedhin, R., Zapantis, A., Amer, N.A., Havercroft, I., Ivory-Moore, R., Steyn, M., Yang, X., Gebremedhin, R., Zahra, M.A., Pinto, E., Rassool, D., Williams, E., Consoli, C., Minervini, J.: Global Status of CCS 2022 (2022). https://status22.globalccsinstitute.com/wp-content/uploads/2022/11/Global-Status-of-CCS-2022 Download.pdf

Trevisan, L., Pini, R., Cihan, A., Birkholzer, J.T., Zhou, Q., González-Nicolás, A., Illangasekare, T.H.: Imaging and quantification of spreading and trapping of carbon dioxide in saline aquifers using meter-scale laboratory experiments. Water Resour. Res. **53**, 485–502 (2017). https://doi.org/10.1002/2016WR019749

Van De Ven, C.J.C., Mumford, K.G.: Visualization of gas dissolution following upward gas migration in porous media: Technique and implications for stray gas. Adv. Water Resour. (2018). https://doi.org/10.1016/j.advwatres.2018.02.015

Van De Ven, C.J.C., Mumford, K.G.: Intermediate-Scale Laboratory Investigation of Stray Gas Migration Impacts: Transient gas Flow and Surface expression. Environ. Sci. Technol. (2020). https://doi.org/10.1021/acs.est.0c03530

Wagner, G., Birovljev, A., Meakin, P., Feder, J., Jøssang, T.: Fragmentation and migration of invasion percolation clusters: Experiments and simulations. Physical Rev. E Stat. Phys. Plasmas Fluids Related Interdiscip. Topics **55**(6), 7015–7029 (1997). https://doi.org/10.1103/PhysRevE.55.7015

Graphic design: Communication Division, UiB / Print: Skipnes Kommunikasjon AS

uib.no

ISBN: 978-82-308-6419-7 (PRINT)
978-82-308-6455-5 (PDF)